



ANALYSIS OF FLOW MIGRATION
IN AN ULTRA-COMPACT COMBUSTOR

THESIS

Brian T. Bohan, Captain, USAF

AFIT/GAE/ENY/11-M02

DEPARTMENT OF THE AIR FORCE
AIR UNIVERSITY

AIR FORCE INSTITUTE OF TECHNOLOGY

Wright-Patterson Air Force Base, Ohio

DISTRIBUTION A. APPROVED FOR PUBLIC RELEASE; DISTRIBUTION IS UNLIMITED.

The views expressed in this thesis are those of the author and do not reflect the official policy or position of the United States Air Force, the Department of Defense, or the United States Government. This material is declared a work of the U.S. Government and is not subject to copyright protection in the United States.

AFIT/GAE/ENY/11-M02

ANALYSIS OF FLOW MIGRATION
IN AN ULTRA-COMPACT COMBUSTOR

THESIS

Presented to the Faculty

Department of Aeronautics and Astronautics

Graduate School of Engineering and Management

Air Force Institute of Technology

Air University

Air Education and Training Command

In Partial Fulfillment of the Requirements for the
Degree of Master of Science in Aeronautical Engineering

Brian T. Bohan, BAE

Captain, USAF

March 2011

DISTRIBUTION A. APPROVED FOR PUBLIC RELEASE; DISTRIBUTION IS UNLIMITED.

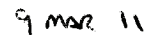
ANALYSIS OF FLOW MIGRATION
IN AN ULTRA-COMPACT COMBUSTOR

Brian T. Bohan, BAE
Captain, USAF

Approved:



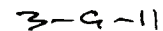
M. Polanka, PhD (Chairman)



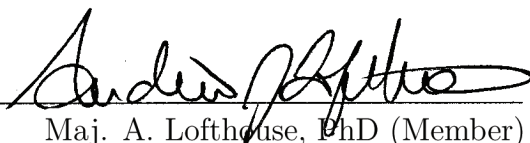
date



P. King, PhD (Member)



date



Maj. A. Lofthouse, PhD (Member)



date

Abstract

One of the major efforts for turbine engine research is to improve the thrust to weight of the system. One novel concept for accomplishing this is the use of an Ultra Compact Combustor (UCC). The UCC attempts to shorten the overall combustion length (thereby reducing weight) by performing the combustion in the circumferential direction along the outside diameter of the core flowpath. One of the major benefits of this design is enhanced combustion due to the establishment of a high-g field in the circumferential cavity. AFIT and the Air Force Research Laboratory (AFRL) have been teamed for several years in understanding the fundamental aspects of this design. Prior to the research presented in this report, work has focused around small-scale missile-sized combustors. There is a current push within AFRL to investigate this system for a larger, fighter-sized engine. AFIT has led this push by performing Computational Fluid Dynamic (CFD) simulations to scale the UCC. This thesis outlines this overall effort. Increasing the diameter of the UCC presents several challenges including how to control the fluid velocity in the circumferential cavity and how to turn the centrifugal combustion flow back to the axial direction into the high-pressure turbine rotor while presenting a uniform temperature across the turbine blades. Several numerical parameter studies have been conducted to establish relationships to predict tangential velocity based on cavity inlet conditions and determine a configuration that minimizes pressure losses through the combustor section. As a result of these investigations a 0.75m diameter UCC combustor design has been developed along with a hybrid turning vane which replaces the last compressor vane and high-pressure turbine vane. Furthermore, the issue of cooling the hybrid vane in the exhaust of the UCC, where not all the fuel is combusted within the circumferential cavity causing additional reactions within the vane section, was investigated. A film cooling experimental study was conducted in an effort to reduce or remove the negative effects that result from secondary combustion of unburned fuel with oxygen in the film coolant.

Acknowledgements

I would like to thank my advisor, Dr. Marc Polanka, for allowing me to take on such an ambitious project with meaningful real world applications. His guidance and feedback throughout this process have helped shape the research to its final form. I have enjoyed the opportunity to play with both numerical and real world fire.

The CFD analysis could have been far more challenging without the help of Maj. Andrew Lofthouse and Mr. Hugh Thornburg who let me bounce ideas off them and provided many time saving tips. Thank you both for all your help.

I would like to thank the sponsor of my research, Dr. Joe Zelina AFRL/RZTC, for supporting the manpower and expenses in operating the WSR and film cooling test rig. To Dr. Scott Stouffer, Dr. David Blunck and Mr. Mike Arstingstall my sincere thanks for all your help, guidance and support in getting through the experimental testing.

Most of all, I could never have completed the program here without the endless support of my wonderful wife who let me vent when I needed it and took care of everything at home to let me focus on school. She has shared my successes and picked me up when things weren't going well. The contribution and sacrifice she made for my education did not go unnoticed. My daughter also supported me throughout this process and was very understanding that Daddy needed to work late and on the weekend to complete 'pre-school'. To you both, thank you.

Brian T. Bohan

Table of Contents

	Page
Abstract	iv
Acknowledgements	v
List of Figures	ix
List of Tables	xxix
List of Symbols	xxxix
List of Abbreviations	xxxiv
I. Introduction	1
1.1 Ultra-Compact Combustor	1
1.2 Turbine Film Cooling	4
1.3 Potential for Heat Release in Film Cooling	5
1.4 Objectives	6
II. Background	7
2.1 Ultra-Compact Combustor	7
2.2 Secondary Flows	11
2.3 Computational Fluid Dynamics (CFD)	14
2.4 Film Cooling	17
2.4.1 Convective Heat Transfer	17
2.4.2 Flow Physics	19
2.4.3 Slot Cooling	26
2.5 Heat Transfer and Surface Temperature Calculations . .	28
2.6 Calculation of Stoichiometric Fuel-to-Air and Equivalence Ratios	30
2.7 Experimental Analysis of Film Cooling	31
2.8 Limitations of Previous Research	35
III. UCC Numerical Analysis Methodology	37
3.1 UCC Geometry	37
3.2 CFD Solver Settings	40
3.3 Secondary Flow Study (Turbulence Model Selection) . .	41
3.4 Computational Domain	43
3.5 Preliminary Analysis	49

	Page
3.5.1	Grid Independence Check 49
3.5.2	Test Conditions 50
3.6	5-Species Reacting Flow Analysis 53
3.6.1	Reacting Flow Grid Independence Check 53
3.6.2	Test Conditions 54
3.7	12-Species Reacting Flow Analysis 58
3.8	Domain Modification Analysis 60
3.9	Engine Condition Domain Modification 61
3.10	Uncertainty 62
IV.	UCC Numerical Analysis Results 63
4.1	Preliminary Analysis 63
4.2	5-Species Reacting Flow Analysis 86
4.3	12-Species Reacting Flow Analysis 96
4.4	Domain Modification Analysis 106
4.5	Engine Condition Domain Modification 119
V.	Experimental Film Cooling Test Methodology 124
5.1	Test Setup 124
5.1.1	Well Stirred Reactor 125
5.1.2	Test Rig 127
5.2	Air, Nitrogen and Fuel Supply 139
5.3	Data Acquisition 140
5.4	Test Plan 143
5.4.1	Single Cooling Scheme 143
5.4.2	Cooling Schemes in Series 143
VI.	Experimental Film-Cooling Test Results 145
6.1	Single Film Cooling Scheme 146
6.2	Film Cooling Schemes in Series 155
6.2.1	Upstream Slot, Downstream Fan-Shaped Laid-back Holes 155
6.2.2	US: Offset Normal Holes, DS: Fan-Shaped Laid-back Holes 165
6.3	Comparisons Between Cooling Schemes 172
VII.	Conclusions 178
7.1	Overview 178
7.2	Numerical Analysis Results Summary 178
7.3	Film Cooling Analysis Results Summary 179
7.4	Conclusions 180
7.5	Recommendations for Future Work 181

	Page
Appendix A. Numerical Starting Sequences	182
A.1 Preliminary Analysis Solver Starting Sequence	182
A.2 Reacting Flow Analysis Solver Starting Sequence	182
Appendix B. Detailed Schematic Drawings of Film Cooling Inserts . .	184
Appendix C. Detailed Drawing of Design 5 Flow Straightener	189
Appendix D. Numerical Analysis Supporting Results	190
D.1 Preliminary Analysis	190
D.1.1 Circumferentially-Averaged Total Temperature Profiles	190
D.1.2 Total Temperature Contour Plots	194
D.2 12-Species Reacting Flow Analysis	197
Appendix E. Experimental Film Cooling Supporting Results	199
E.1 Surface Temperature	199
E.1.1 $\Phi = 0.6$	199
E.1.2 Surface Temperature, $\Phi = 1.1$	201
E.1.3 Surface Temperature, $\Phi = 1.3$	203
E.1.4 Surface Temperature, $\Phi = 1.5$	205
E.2 Heat Flux	207
E.2.1 $\Phi = 0.6$	207
E.2.2 Heat Flux, $\Phi = 1.1$	210
E.2.3 Heat Flux, $\Phi = 1.3$	214
E.2.4 Heat Flux, $\Phi = 1.5$	218
E.3 Heat Transfer Coefficient	222
E.3.1 $\Phi = 0.6$	222
E.3.2 Heat Transfer Coefficient, $\Phi = 1.1$	225
E.3.3 Heat Transfer Coefficient, $\Phi = 1.3$	229
E.3.4 Heat Transfer Coefficient, $\Phi = 1.5$	233
E.4 Comparison Plots	237
E.4.1 $\Phi = 0.6$	237
E.4.2 Comparison Plots, $\Phi = 1.1$	238
E.4.3 Comparison Plots, $\Phi = 1.3$	240
E.4.4 Comparison Plots, $\Phi = 1.5$	241
E.4.5 Comparison Plots as a function of Φ	243
Bibliography	245
Vita	248

List of Figures

Figure		Page
1.1.	Traditional combustor and ultra-compact combustor	2
1.2.	Comparison of turbine inlet temperature to material limits . .	4
1.3.	Secondary combustion reaction from a traditional combustor .	5
2.1.	Bubble velocity controlled flame propagation (Left) and turbulent flame speed controlled reaction (Right)	7
2.2.	Flame propagation rate and bubble velocity as a function of g-loading	9
2.3.	Flame propagation at 10g's (Left), Flame propagation at 500g's (Right)	9
2.4.	UCC cavity equivalence ratio at blowout as a function of cavity g-loading	10
2.5.	Illustration of secondary flows	11
2.6.	Comparison of turbulence models to experimental LDV measurements along the stagnation plane of a turbine vane	13
2.7.	Spatial distribution of film cooling effectiveness at various blowing ratios	20
2.8.	Effect of injection angle on film cooling effectiveness	21
2.9.	Three common coolant hole shapes	22
2.10.	Local Effectiveness for cylindrical (left), fanshaped (center) and laidback fanshaped (right) at three blowing ratios	22
2.11.	Comparison of spatially averaged film effectiveness of shaped holes and cylindrical holes for two turbulence levels and varied blowing ratios	23
2.12.	Thermal profiles along coolant hole centerline for (a) attached, (b) detached then reattached and (c) fully separated coolant flow	24
2.13.	Coolant hole exit plane vorticity and corresponding velocity vectors highlighting secondary flows	26
2.14.	Radial Film Hole Geometries	27

Figure		Page
2.15.	Shallow Trench Geometry and Results	27
2.16.	Least squares linear fit of thermal conductivity of Hastelloy-X .	29
2.17.	Previous Research Test Rig (left) and film cooling inserts (right)	32
2.18.	Angled hole visible burning for (a) $M=0$, (b) $M=0.5$, air, (c) $M=1.0$, air, (d) $M=1.0$, N_2 , and (e) $M=1.5$, air	33
2.19.	Graphical relationship of blowing ratio to heat flux for three equivalence ratios at $x/D = 20$	33
2.20.	Velocity vectors above and downstream of cooling hole highlighting secondary flow structure	34
2.21.	Temperature contours (left) and cooling effectiveness (right) for $\Phi = 1.5$ and $M = 1.0$. a-c) N_2 injection d-f) air injection . . .	35
3.1.	Cross-sectional view of UCC section used in the current analysis (Dimensions are in centimeters)	38
3.2.	Origin of the hybrid vane design	39
3.3.	UCC turbine vane designs tested	40
3.4.	Secondary flow test domain	41
3.5.	Resulting horseshoe and passage vortices with surface trace on the vane surface	42
3.6.	Computational domain relative to full array	44
3.7.	Computational domains	45
3.8.	Fuel injector positioning relative to air inlet ports	47
3.9.	Gaseous fuel nozzle specifications (cm)	47
3.10.	Air inlet port size variations (Shown for 20-vane configuration)	48
3.11.	Grid independence check - Variation of circumferential cavity tangential velocity with grid resolution	50
3.12.	Reacting flow grid independence check - Variation of circumferential cavity tangential velocity with grid resolution	54
3.13.	20 hybrid vane domain with core flow divider plate	60
3.14.	20 hybrid vane domain with cavity inlet splitter duct	61

Figure		Page
4.1.	Tangential velocity as a function of vane count and cavity mass flow inlet percentage (engine conditions)	63
4.2.	Tangential velocity as a function of cavity mass flow inlet percentage	65
4.3.	Cavity cross-sectional mass flow rate as a function of vane count (100% cavity inlet mass flow rate)	65
4.4.	Streamlines and contours of total temperature for typical style vane domains	67
4.5.	Circumferentially-averaged total temperatures at combustor section exit (100% cavity inlet \dot{m})	69
4.6.	Circumferentially-averaged total temperatures at combustor section exit with core mass flow rate variations using 20-vane, hybrid vane style domain (engine conditions)	72
4.7.	Plot of tangential velocity vs. cavity air inlet velocity for the 20 hybrid vane domain	74
4.8.	Plot of tangential velocity vs. cavity air inlet velocity for the 30 hybrid vane domain	74
4.9.	Plot of tangential velocity vs. cavity air inlet velocity for both hybrid vane domains	75
4.10.	Plot of tangential velocity vs. cavity air inlet area for the 20 hybrid vane engine condition	75
4.11.	Circumferentially-averaged total temperatures at combustor section exit with air inlet variations using the 20 hybrid vane domain (engine conditions)	77
4.12.	Circumferentially-averaged total temperatures at combustor section exit with air inlet variations using the 30 hybrid vane domain (engine conditions)	77
4.13.	Circumferentially-averaged total temperatures at combustor section exit with air inlet variations using the 20 hybrid vane domain (rig conditions)	78
4.14.	Circumferentially-averaged total temperatures at combustor section exit with air inlet variations using the 30 hybrid vane domain (rig conditions)	78

Figure		Page
4.15.	Total temperature contours on UCC components using 100% cavity inlet mass flow, 20 hybrid vane domain under engine conditions	79
4.16.	Streamlines from the 3x area air inlet, 20 hybrid vane domain under engine conditions	80
4.17.	Time lapse sequence of fluid exiting the circumferential cavity during small-scale UCC experimental testing	81
4.18.	Contours of total temperature in the 30 hybrid vane domain with baseline air inlet diameters under rig conditions. Velocity ratio = 4.45	82
4.19.	Streamlines in the circumferential cavity for the 20 vane domain using baseline air inlets (above) and 3x air inlets (below)	83
4.20.	Relationship of cavity inlet velocity to cavity tangential velocity and hole diameter for the 5-species analysis	86
4.21.	Circumferentially-averaged total temperatures at combustor section exit using the 5-species model and ideal air inlet diameters for each test configuration	89
4.22.	Total temperature contours on UCC components for ideal tangential velocity in the 20 hybrid vane domain under engine conditions	89
4.23.	Total temperature contours on UCC components for ideal tangential velocity in the 20 hybrid vane domain under rig conditions	90
4.24.	Total temperature contours on UCC components for ideal tangential velocity in the 30 hybrid vane domain under engine conditions	90
4.25.	Total temperature contours on UCC components for ideal tangential velocity in the 30 hybrid vane domain under rig conditions	90
4.26.	Absolute (static) pressure contours on UCC components in the 20 hybrid vane domain under engine conditions	92
4.27.	Total pressure contours on UCC components in the 20 hybrid vane domain under engine conditions	93
4.28.	Absolute (static) pressure contours on UCC components in the 20 hybrid vane domain under rig conditions	93

Figure		Page
4.29.	Total pressure contours on UCC components in the 20 hybrid vane domain under rig conditions	93
4.30.	Comparison of circumferentially-averaged total temperatures at combustor section exit using the 5-Species model and ideal air inlet diameter for the 20 vane domain under rig conditions with and without variable C_p values	94
4.31.	Total temperature contours on UCC components for ideal tangential velocity in the 20 hybrid vane domain under rig conditions using different definitions of C_p	95
4.32.	Relationship of cavity inlet velocity to cavity tangential velocity and hole diameter	97
4.33.	Circumferentially-averaged total temperatures at combustor section exit using the 12-species combustion model and ideal air inlet diameters with piecewise-polynomial C_p values	98
4.34.	Iso-surface of $C_{12}H_{23}$ colored by total temperature using the 12-species combustion model and ideal air inlet diameters with a 20 hybrid vane engine configuration	100
4.35.	Iso-surface of H_2 colored by total temperature using the 12-species combustion model and ideal air inlet diameters with a 20 hybrid vane engine configuration	100
4.36.	Iso-surface of CO colored by total temperature using the 12-species combustion model and ideal air inlet diameters with a 20 hybrid vane engine configuration	101
4.37.	Iso-surface of OH colored by total temperature using the 12-species combustion model and ideal air inlet diameters with a 20 hybrid vane engine configuration	101
4.38.	Iso-surface of C_3H_8 colored by total temperature using the 12-species combustion model and ideal air inlet diameters with a 20 hybrid vane rig configuration	102
4.39.	Iso-surface of H_2 colored by total temperature using the 12-species combustion model and ideal air inlet diameters with a 20 hybrid vane rig configuration	102

Figure		Page
4.40.	Iso-surface of CO colored by total temperature using the 12-species combustion model and ideal air inlet diameters with a 20 hybrid vane engine configuration	103
4.41.	Iso-surface of OH colored by total temperature using the 12-species combustion model and ideal air inlet diameters with a 20 hybrid vane rig configuration	103
4.42.	Circumferentially-averaged mass fractions of species at combustor section exit using the 12-species combustion model and ideal air inlet diameters with a 20 hybrid vane engine configuration .	104
4.43.	Circumferentially-averaged mass fractions of species at combustor section exit using the 12-species combustion model and ideal air inlet diameters with a 20 hybrid vane engine configuration .	105
4.44.	Circumferentially-averaged mass fractions of species at combustor section exit using the 12-species combustion model and ideal air inlet diameters with a 20 hybrid vane rig configuration . . .	105
4.45.	Circumferentially-averaged mass fractions of species at combustor section exit using the 12-species combustion model and ideal air inlet diameters with a 20 hybrid vane rig configuration . . .	106
4.46.	Circumferentially-averaged total temperatures at combustor section exit using the 5- and 12-species combustion model and ideal air inlet diameters with piecewise-polynomial C_p values for a domain with and without the divider plate	108
4.47.	Total temperature contours on domain exit plane for 5- and 12-species combustion models with and without the divider plate .	108
4.48.	Total temperature contours on UCC components for ideal tangential velocity in the 20 hybrid vane domain under rig conditions with and without the divider plate	109
4.49.	Cross-sectional view of UCC section with the divider plate (Dimensions are in centimeters)	110
4.50.	Plan view of domain showing streamlines of the vortex formed from the divider plate, contours are colored by total temperature	111

Figure		Page
4.51.	Plan view of domain without the divider plate showing streamlines through the same points in the domain as Figure 4.50, contours are colored by total temperature	111
4.52.	Upstream view of UCC turbine vanes with divider plate showing streamlines and a vector plane positioned downstream of the circumferential cavity	112
4.53.	Iso-surface of C_3H_8 colored by total temperature using the 12-species combustion model and ideal air inlet diameters with a 20 hybrid vane rig configuration with divider plate	114
4.54.	Iso-surface of H_2 colored by total temperature using the 12-species combustion model and ideal air inlet diameters with a 20 hybrid vane rig configuration with divider plate	114
4.55.	Iso-surface of CO colored by total temperature using the 12-species combustion model and ideal air inlet diameters with a 20 hybrid vane engine configuration with divider plate	115
4.56.	Iso-surface of OH colored by total temperature using the 12-species combustion model and ideal air inlet diameters with a 20 hybrid vane rig configuration with divider plate	115
4.57.	Circumferentially-averaged mass fractions of species at combustor section exit using the 12-species combustion model and ideal air inlet diameters with a 20 hybrid vane rig configuration . . .	116
4.58.	Circumferentially-averaged mass fractions of species at combustor section exit using the 12-species combustion model and ideal air inlet diameters with a 20 hybrid vane rig configuration . . .	116
4.59.	Streamlines around UCC turbine vane for the 20 hybrid vane domain under rig conditions with and without the divider plate	118
4.60.	Relationship of cavity inlet velocity to cavity tangential velocity and hole diameter for the ducted cavity inlets	121
4.61.	Streamlines into the circumferential cavity for the 20 hybrid vane domain under engine conditions with and without a ducted cavity inlet	122
5.1.	Experimental test setup	124

Figure		Page
5.2.	Lower half of the toroid with the jet ring in the WSR housing .	126
5.3.	Complete toroidal setup with the jet ring in the WSR housing .	126
5.4.	Test rig with sections and assemblies labeled	127
5.5.	Test section, flat plate design	128
5.6.	Test section, instrument block	129
5.7.	Test section, forward facing step	129
5.8.	Film cooling inserts	130
5.9.	Schematic of the fan-shaped laidback holes (in inches)	131
5.10.	Film cooling assemblies	131
5.11.	Heat transfer gauge assembly	132
5.12.	Heat transfer gauge labels and positions	133
5.13.	Transition section assembly	134
5.14.	Single machined flow straightener disc (left), flow straightener stack sitting on WSR exhaust port (right)	135
5.15.	Flow straightener designs considered	136
5.16.	Numerical ‘test rig’ for flow straightener testing	137
5.17.	Design 5 flow straightener numerical test results	138
5.18.	Flow controls for air, nitrogen and fuel supplied to the WSR and test rig film cooling plena	140
5.19.	Screen shot of LabView system monitor and data logging interface	141
5.20.	Sample of manual log and blowing ratio calculation spreadsheet	142
6.1.	Exhaust exiting the test rig for various WSR equivalence ratios ($\dot{m}_{air} = 425$ SLPM)	145
6.2.	Reactor exhaust temperature at the entrance to the test rig as a function of equivalence ratio. Current study ($\dot{m}_{air}=425$ SLPM) with polyfit line. Evans data and comparison data ($\dot{m}_{air}= 850$ SLPM)	146
6.3.	Heat flux comparison to Evans, $\Phi = 0.6$, $\dot{m}_{air}=850$ SLPM, Fan- shaped holes, Coolant=Air, M=Variable	147

Figure		Page
6.4.	Convective heat transfer coefficient comparison to Evans, $\Phi = 0.6$, $\dot{m}_{air}=850$ SLPM, Fan-shaped holes, Coolant=Air, M=Variable	148
6.5.	Heat flux comparison to Evans, $\Phi = 1.5$, $\dot{m}_{air}=850$ SLPM, Fan-shaped holes, Coolant=Air, M=Variable	148
6.6.	Convective heat transfer coefficient comparison to Evans, $\Phi = 1.5$, $\dot{m}_{air}=850$ SLPM, Fan-shaped holes, Coolant=Air, M=Variable	149
6.7.	Gauge surface temperature, $\Phi = 0.6$, $\dot{m}_{air}=425$ SLPM, Fan-shaped holes, Coolant=Air/N ₂ , M=Variable	150
6.8.	Gauge heat flux, $\Phi = 0.6$, $\dot{m}_{air}=425$ SLPM, Fan-shaped holes, Coolant=Air/N ₂ , M=Variable	150
6.9.	Gauge heat transfer coefficient, $\Phi = 0.6$, $\dot{m}_{air}=425$ SLPM, Fan-shaped holes, Coolant=Air/N ₂ , M=Variable	151
6.10.	Gauge surface temperature, $\Phi = 1.3$, $\dot{m}_{air}=425$ SLPM, Fan-shaped holes, Coolant=Air/N ₂ , M=Variable	152
6.11.	Gauge heat flux, $\Phi = 1.3$, $\dot{m}_{air}=425$ SLPM, Fan-shaped holes, Coolant=Air/N ₂ , M=Variable	152
6.12.	Gauge heat transfer coefficient, $\Phi = 1.3$, $\dot{m}_{air}=425$ SLPM, Fan-shaped holes, Coolant=Air/N ₂ , M=Variable	153
6.13.	Heat flux difference, $\Phi = 1.3$, $\dot{m}_{air}=425$ SLPM, Fan-shaped holes, Coolant=Air/N ₂ , M=Variable	154
6.14.	Heat transfer coefficient difference, $\Phi = 1.3$, $\dot{m}_{air}=425$ SLPM, Fan-shaped holes, Coolant=Air/N ₂ , M=Variable	154
6.15.	Cherry red sections of the stainless steel pipe housing the flow straightener and transition section caused by cracks in the ceramic components	155
6.16.	Gauge surface temperature, $\Phi = 0.6$, $\dot{m}_{air}=425$ SLPM, US: Slot, Coolant=Air, M=Variable, DS: Fan, Coolant=Air/N ₂ , M=2 . .	156
6.17.	Gauge heat flux, $\Phi = 0.6$, $\dot{m}_{air}=425$ SLPM, US: Slot, Coolant=Air, M=Variable, DS: Fan, Coolant=Air/N ₂ , M=2	157
6.18.	Gauge heat transfer coefficient, $\Phi = 0.6$, $\dot{m}_{air}=425$ SLPM, US: Slot, Coolant=Air, M=Variable, DS: Fan, Coolant=Air/N ₂ , M=2	157

Figure		Page
6.19.	Gauge surface temperature, $\Phi = 1.5$, $\dot{m}_{air}=425$ SLPM, US: Slot, Coolant=Air, M=Variable, DS: Fan, Coolant=Air/N ₂ , M=2 . .	158
6.20.	Gauge heat flux, $\Phi = 1.5$, $\dot{m}_{air}=425$ SLPM, US: Slot, Coolant=Air, M=Variable, DS: Fan, Coolant=Air/N ₂ , M=2	159
6.21.	Heat flux difference, $\Phi = 1.5$, $\dot{m}_{air}=425$ SLPM, US: Slot, Coolant=Air, M=Variable, DS: Fan, Coolant=Air/N ₂ , M=2	159
6.22.	Gauge heat transfer coefficient, $\Phi = 1.5$, $\dot{m}_{air}=425$ SLPM, US: Slot, Coolant=Air, M=Variable, DS: Fan, Coolant=Air/N ₂ , M=2	160
6.23.	Heat transfer coefficient difference, $\Phi = 1.5$, $\dot{m}_{air}=425$ SLPM, US: Slot, Coolant=Air, M=Variable, DS: Fan, Coolant=Air/N ₂ , M=2	160
6.24.	Visible burning in slot film coolant ($\Phi = 1.5$), scale is in inches	162
6.25.	Gauge surface temperature, $\Phi = 1.5$, $\dot{m}_{air}=425$ SLPM, US: Slot, Coolant=N ₂ , M=Variable, DS: Fan, Coolant=Air/N ₂ , M=2 . .	163
6.26.	Gauge heat flux, $\Phi = 1.5$, $\dot{m}_{air}=425$ SLPM, US: Slot, Coolant=N ₂ , M=Variable, DS: Fan, Coolant=Air/N ₂ , M=2	163
6.27.	Heat flux difference, $\Phi = 1.5$, $\dot{m}_{air}=425$ SLPM, US: Slot, Coolant=N ₂ , M=Variable, DS: Fan, Coolant=Air/N ₂ , M=2	164
6.28.	Gauge heat transfer coefficient, $\Phi = 1.5$, $\dot{m}_{air}=425$ SLPM, US: Slot, Coolant=N ₂ , M=Variable, DS: Fan, Coolant=Air/N ₂ , M=2	164
6.29.	Heat transfer coefficient difference, $\Phi = 1.5$, $\dot{m}_{air}=425$ SLPM, US: Slot, Coolant=N ₂ , M=Variable, DS: Fan, Coolant=Air/N ₂ , M=2	165
6.30.	Gauge surface temperature, $\Phi = 0.6$, $\dot{m}_{air}=425$ SLPM, US: Offset normal, Coolant=Air, M=Variable, DS: Fan, Coolant=Air/N ₂ , M=2	166
6.31.	Gauge heat flux, $\Phi = 0.6$, $\dot{m}_{air}=425$ SLPM, US: Offset normal, Coolant=Air, M=Variable, DS: Fan, Coolant=Air/N ₂ , M=2 . .	166
6.32.	Gauge heat transfer coefficient, $\Phi = 0.6$, $\dot{m}_{air}=425$ SLPM, US: Offset normal, Coolant=Air, M=Variable, DS: Fan, Coolant=Air/N ₂ , M=2	167

Figure		Page
6.33.	Gauge surface temperature, $\Phi = 1.1$, $\dot{m}_{air}=425$ SLPM, US: Offset Normal, Coolant=Air, M=Variable, DS: Fan, Coolant=Air/N ₂ , M=2	168
6.34.	Gauge heat flux, $\Phi = 1.1$, $\dot{m}_{air}=425$ SLPM, US: Offset Normal, Coolant=Air, M=Variable, DS: Fan, Coolant=Air/N ₂ , M=2 . .	168
6.35.	Heat flux difference, $\Phi = 1.1$, $\dot{m}_{air}=425$ SLPM, US: Offset Normal, Coolant=Air, M=Variable, DS: Fan, Coolant=Air/N ₂ , M=2	169
6.36.	Gauge heat transfer coefficient, $\Phi = 1.1$, $\dot{m}_{air}=425$ SLPM, US: Offset Normal, Coolant=Air, M=Variable, DS: Fan, Coolant=Air/N ₂ , M=2	169
6.37.	Heat transfer coefficient difference, $\Phi = 1.1$, $\dot{m}_{air}=425$ SLPM, US: Offset Normal, Coolant=Air, M=Variable, DS: Fan, Coolant=Air/N ₂ , M=2	170
6.38.	Visible burning in offset normal hole film coolant ($\Phi = 1.1$), scale is in inches	171
6.39.	Visible burning in offset normal hole and fan-shaped hole film coolant ($\Phi = 1.5$), scale is in inches	173
6.40.	Gauge surface temperature comparison, $\Phi = 1.1$, $\dot{m}_{air}=425$ SLPM, US: Blank/Slot/Offset, Coolant=Air, M=Variable, DS: Fan, Coolant=Air, M=2	174
6.41.	Heat flux comparison, $\Phi = 1.1$, $\dot{m}_{air}=425$ SLPM, US: Blank/Slot/Offset, Coolant=Air, M=Variable, DS: Fan, Coolant=Air, M=2	175
6.42.	Gauge heat transfer coefficient comparison, $\Phi = 1.1$, $\dot{m}_{air}=425$ SLPM, US: Blank/Slot/Offset, Coolant=Air, M=Variable, DS: Fan, Coolant=Air, M=2	175
6.43.	Gauge surface temperature comparison, $\Phi = \text{Variable}$, $\dot{m}_{air}=425$ SLPM, US: Blank/Slot/Offset, Coolant=Air, M=2, DS: Fan, Coolant=Air, M=2	176
6.44.	Heat flux comparison, $\Phi = \text{Variable}$, $\dot{m}_{air}=425$ SLPM, US: Blank/Slot/Offset, Coolant=Air, M=2, DS: Fan, Coolant=Air, M=2 . .	176

Figure		Page
6.45.	Gauge heat transfer coefficient comparison, Φ = Variable, $\dot{m}_{air}=425$ SLPM, US: Blank/Slot/Offset, Coolant=Air, M=2, DS: Fan, Coolant=Air, M=2	177
B.1.	Normal blank	184
B.2.	Fan-shaped laidback holes	185
B.3.	Angled slot	186
B.4.	Offset normal holes	187
B.5.	Solid blank	188
C.1.	Design 5 flow straightener (inches)	189
D.1.	Circumferentially-averaged total temperatures at combustor sec- tion exit for varying cavity inlet mass flow rates for the 0 hybrid vane domain	190
D.2.	Circumferentially-averaged total temperatures at combustor sec- tion exit for varying cavity inlet mass flow rates for the 0 typical vane domain	190
D.3.	Circumferentially-averaged total temperatures at combustor sec- tion exit for varying cavity inlet mass flow rates for the 20 hybrid vane domain	191
D.4.	Circumferentially-averaged total temperatures at combustor sec- tion exit for varying cavity inlet mass flow rates for the 20 typical vane domain	191
D.5.	Circumferentially-averaged total temperatures at combustor sec- tion exit for varying cavity inlet mass flow rates for the 30 hybrid vane domain	192
D.6.	Circumferentially-averaged total temperatures at combustor sec- tion exit for varying cavity inlet mass flow rates for the 30 typical vane domain	192
D.7.	Circumferentially-averaged total temperatures at combustor sec- tion exit for varying cavity inlet mass flow rates for the 45 typical vane domain	193

Figure		Page
D.8.	Circumferentially-averaged total temperatures at combustor section exit for varying cavity inlet mass flow rates for the 60 typical vane domain	193
D.9.	Total temperature contours on UCC components using 100% cavity inlet mass flow, 20 hybrid vane domain, rig conditions . . .	194
D.10.	Total temperature contours on UCC components using 100% cavity inlet mass flow, 30 hybrid vane domain, engine conditions .	195
D.11.	Total temperature contours on UCC components using 100% cavity inlet mass flow, 30 hybrid vane domain, rig conditions . . .	196
D.12.	Circumferentially-averaged mass fractions of species at combustor section exit using the 12-species combustion model and ideal air inlet diameters with a 30 hybrid vane engine configuration .	197
D.13.	Circumferentially-averaged mass fractions of species at combustor section exit using the 12-species combustion model and ideal air inlet diameters with a 30 hybrid vane engine configuration .	197
D.14.	Circumferentially-averaged mass fractions of species at combustor section exit using the 12-species combustion model and ideal air inlet diameters with a 30 hybrid vane rig configuration . . .	198
D.15.	Circumferentially-averaged mass fractions of species at combustor section exit using the 12-species combustion model and ideal air inlet diameters with a 30 hybrid vane rig configuration . . .	198
E.1.	Gauge surface temperature, $\Phi = 0.6$, $\dot{m}_{air}=425$ SLPM, US: Blank, Coolant=N/A, M=N/A, DS: Fan, Coolant=Air/N ₂ , M=Variable	199
E.2.	Gauge surface temperature, $\Phi = 0.6$, $\dot{m}_{air}=425$ SLPM, US: Slot, Coolant=Air, M=Variable, DS: Fan, Coolant=Air/N ₂ , M=2 . .	200
E.3.	Gauge surface temperature, $\Phi = 0.6$, $\dot{m}_{air}=425$ SLPM, US: Offset Normal, Coolant=Air, M=Variable, DS: Fan, Coolant=Air/N ₂ , M=2	200
E.4.	Gauge surface temperature, $\Phi = 1.1$, $\dot{m}_{air}=425$ SLPM, US: Blank, Coolant=N/A, M=N/A, DS: Fan, Coolant=Air/N ₂ , M=Variable	201
E.5.	Gauge surface temperature, $\Phi = 1.1$, $\dot{m}_{air}=425$ SLPM, US: Slot, Coolant=Air, M=Variable, DS: Fan, Coolant=Air/N ₂ , M=2 . .	201

Figure		Page
E.6.	Gauge surface temperature, $\Phi = 1.1$, $\dot{m}_{air}=425$ SLPM, US: Slot, Coolant= N_2 , M=Variable, DS: Fan, Coolant=Air/ N_2 , M=2 . . .	202
E.7.	Gauge surface temperature, $\Phi = 1.1$, $\dot{m}_{air}=425$ SLPM, US: Offset Normal, Coolant=Air, M=Variable, DS: Fan, Coolant=Air/ N_2 , M=2	202
E.8.	Gauge surface temperature, $\Phi = 1.3$, $\dot{m}_{air}=425$ SLPM, US: Blank, Coolant=N/A, M=N/A, DS: Fan, Coolant=Air/ N_2 , M=Variable	203
E.9.	Gauge surface temperature, $\Phi = 1.3$, $\dot{m}_{air}=425$ SLPM, US: Slot, Coolant=Air, M=Variable, DS: Fan, Coolant=Air/ N_2 , M=2 . . .	203
E.10.	Gauge surface temperature, $\Phi = 1.3$, $\dot{m}_{air}=425$ SLPM, US: Slot, Coolant= N_2 , M=Variable, DS: Fan, Coolant=Air/ N_2 , M=2 . . .	204
E.11.	Gauge surface temperature, $\Phi = 1.3$, $\dot{m}_{air}=425$ SLPM, US: Offset Normal, Coolant=Air, M=Variable, DS: Fan, Coolant=Air/ N_2 , M=2	204
E.12.	Gauge surface temperature, $\Phi = 1.5$, $\dot{m}_{air}=425$ SLPM, US: Blank, Coolant=N/A, M=N/A, DS: Fan, Coolant=Air/ N_2 , M=Variable	205
E.13.	Gauge surface temperature, $\Phi = 1.5$, $\dot{m}_{air}=425$ SLPM, US: Slot, Coolant=Air, M=Variable, DS: Fan, Coolant=Air/ N_2 , M=2 . . .	205
E.14.	Gauge surface temperature, $\Phi = 1.5$, $\dot{m}_{air}=425$ SLPM, US: Slot, Coolant= N_2 , M=Variable, DS: Fan, Coolant=Air/ N_2 , M=2 . . .	206
E.15.	Gauge surface temperature, $\Phi = 1.5$, $\dot{m}_{air}=425$ SLPM, US: Offset Normal, Coolant=Air, M=Variable, DS: Fan, Coolant=Air/ N_2 , M=2	206
E.16.	Gauge heat flux, $\Phi = 0.6$, $\dot{m}_{air}=425$ SLPM, US: Blank, Coolant=N/A, M=N/A, DS: Fan, Coolant=Air/ N_2 , M=Variable	207
E.17.	Gauge heat flux difference, $\Phi = 0.6$, $\dot{m}_{air}=425$ SLPM, US: Blank, Coolant=N/A, M=N/A, DS: Fan, Coolant=Air/ N_2 , M=Variable	207
E.18.	Gauge heat flux, $\Phi = 0.6$, $\dot{m}_{air}=425$ SLPM, US: Slot, Coolant=Air, M=Variable, DS: Fan, Coolant=Air/ N_2 , M=2	208
E.19.	Gauge heat flux difference, $\Phi = 0.6$, $\dot{m}_{air}=425$ SLPM, US: Slot, Coolant=Air, M=Variable, DS: Fan, Coolant=Air/ N_2 , M=2 . . .	208

Figure		Page
E.20.	Gauge heat flux, $\Phi = 0.6$, $\dot{m}_{air}=425$ SLPM, US: Offset Normal, Coolant=Air, M=Variable, DS: Fan, Coolant=Air/N ₂ , M=2 . .	209
E.21.	Gauge heat flux difference, $\Phi = 0.6$, $\dot{m}_{air}=425$ SLPM, US: Offset Normal, Coolant=Air, M=Variable, DS: Fan, Coolant=Air/N ₂ , M=2	209
E.22.	Gauge heat flux, $\Phi = 1.1$, $\dot{m}_{air}=425$ SLPM, US: Blank, Coolant=N/A, M=N/A, DS: Fan, Coolant=Air/N ₂ , M=Variable	210
E.23.	Gauge heat flux difference, $\Phi = 1.1$, $\dot{m}_{air}=425$ SLPM, US: Blank, Coolant=N/A, M=N/A, DS: Fan, Coolant=Air/N ₂ , M=Variable	210
E.24.	Gauge heat flux, $\Phi = 1.1$, $\dot{m}_{air}=425$ SLPM, US: Slot, Coolant=Air, M=Variable, DS: Fan, Coolant=Air/N ₂ , M=2	211
E.25.	Gauge heat flux difference, $\Phi = 1.1$, $\dot{m}_{air}=425$ SLPM, US: Slot, Coolant=Air, M=Variable, DS: Fan, Coolant=Air/N ₂ , M=2 . .	211
E.26.	Gauge heat flux, $\Phi = 1.1$, $\dot{m}_{air}=425$ SLPM, US: Slot, Coolant=N ₂ , M=Variable, DS: Fan, Coolant=Air/N ₂ , M=2	212
E.27.	Gauge heat flux difference, $\Phi = 1.1$, $\dot{m}_{air}=425$ SLPM, US: Slot, Coolant=N ₂ , M=Variable, DS: Fan, Coolant=Air/N ₂ , M=2 . .	212
E.28.	Gauge heat flux, $\Phi = 1.1$, $\dot{m}_{air}=425$ SLPM, US: Offset Normal, Coolant=Air, M=Variable, DS: Fan, Coolant=Air/N ₂ , M=2 . .	213
E.29.	Gauge heat flux difference, $\Phi = 1.1$, $\dot{m}_{air}=425$ SLPM, US: Offset Normal, Coolant=Air, M=Variable, DS: Fan, Coolant=Air/N ₂ , M=2	213
E.30.	Gauge heat flux, $\Phi = 1.3$, $\dot{m}_{air}=425$ SLPM, US: Blank, Coolant=N/A, M=N/A, DS: Fan, Coolant=Air/N ₂ , M=Variable	214
E.31.	Gauge heat flux difference, $\Phi = 1.3$, $\dot{m}_{air}=425$ SLPM, US: Blank, Coolant=N/A, M=N/A, DS: Fan, Coolant=Air/N ₂ , M=Variable	214
E.32.	Gauge heat flux, $\Phi = 1.3$, $\dot{m}_{air}=425$ SLPM, US: Slot, Coolant=Air, M=Variable, DS: Fan, Coolant=Air/N ₂ , M=2	215
E.33.	Gauge heat flux difference, $\Phi = 1.3$, $\dot{m}_{air}=425$ SLPM, US: Slot, Coolant=Air, M=Variable, DS: Fan, Coolant=Air/N ₂ , M=2 . .	215
E.34.	Gauge heat flux, $\Phi = 1.3$, $\dot{m}_{air}=425$ SLPM, US: Slot, Coolant=N ₂ , M=Variable, DS: Fan, Coolant=Air/N ₂ , M=2	216

Figure		Page
E.35.	Gauge heat flux difference, $\Phi = 1.3$, $\dot{m}_{air}=425$ SLPM, US: Slot, Coolant= N_2 , M=Variable, DS: Fan, Coolant=Air/ N_2 , M=2 . . .	216
E.36.	Gauge heat flux, $\Phi = 1.3$, $\dot{m}_{air}=425$ SLPM, US: Offset Normal, Coolant=Air, M=Variable, DS: Fan, Coolant=Air/ N_2 , M=2 . . .	217
E.37.	Gauge heat flux difference, $\Phi = 1.3$, $\dot{m}_{air}=425$ SLPM, US: Offset Normal, Coolant=Air, M=Variable, DS: Fan, Coolant=Air/ N_2 , M=2	217
E.38.	Gauge heat flux, $\Phi = 1.5$, $\dot{m}_{air}=425$ SLPM, US: Blank, Coolant=N/A, M=N/A, DS: Fan, Coolant=Air/ N_2 , M=Variable	218
E.39.	Gauge heat flux difference, $\Phi = 1.5$, $\dot{m}_{air}=425$ SLPM, US: Blank, Coolant=N/A, M=N/A, DS: Fan, Coolant=Air/ N_2 , M=Variable	218
E.40.	Gauge heat flux, $\Phi = 1.5$, $\dot{m}_{air}=425$ SLPM, US: Slot, Coolant=Air, M=Variable, DS: Fan, Coolant=Air/ N_2 , M=2	219
E.41.	Gauge heat flux difference, $\Phi = 1.5$, $\dot{m}_{air}=425$ SLPM, US: Slot, Coolant=Air, M=Variable, DS: Fan, Coolant=Air/ N_2 , M=2 . . .	219
E.42.	Gauge heat flux, $\Phi = 1.5$, $\dot{m}_{air}=425$ SLPM, US: Slot, Coolant= N_2 , M=Variable, DS: Fan, Coolant=Air/ N_2 , M=2	220
E.43.	Gauge heat flux difference, $\Phi = 1.5$, $\dot{m}_{air}=425$ SLPM, US: Slot, Coolant= N_2 , M=Variable, DS: Fan, Coolant=Air/ N_2 , M=2 . . .	220
E.44.	Gauge heat flux, $\Phi = 1.5$, $\dot{m}_{air}=425$ SLPM, US: Offset Normal, Coolant=Air, M=Variable, DS: Fan, Coolant=Air/ N_2 , M=2 . . .	221
E.45.	Gauge heat flux difference, $\Phi = 1.5$, $\dot{m}_{air}=425$ SLPM, US: Offset Normal, Coolant=Air, M=Variable, DS: Fan, Coolant=Air/ N_2 , M=2	221
E.46.	Gauge heat transfer coefficient, $\Phi = 0.6$, $\dot{m}_{air}=425$ SLPM, US: Blank, Coolant=N/A, M=N/A, DS: Fan, Coolant=Air/ N_2 , M=Variable	222
E.47.	Gauge heat transfer coefficient difference, $\Phi = 0.6$, $\dot{m}_{air}=425$ SLPM, US: Blank, Coolant=N/A, M=N/A, DS: Fan, Coolant=Air/ N_2 , M=Variable	222
E.48.	Gauge heat transfer coefficient, $\Phi = 0.6$, $\dot{m}_{air}=425$ SLPM, US: Slot, Coolant=Air, M=Variable, DS: Fan, Coolant=Air/ N_2 , M=2	223

Figure		Page
E.49.	Gauge heat transfer coefficient difference, $\Phi = 0.6$, $\dot{m}_{air}=425$ SLPM, US: Slot, Coolant=Air, M=Variable, DS: Fan, Coolant=Air/N ₂ , M=2	223
E.50.	Gauge heat transfer coefficient, $\Phi = 0.6$, $\dot{m}_{air}=425$ SLPM, US: Offset Normal, Coolant=Air, M=Variable, DS: Fan, Coolant=Air/N ₂ , M=2	224
E.51.	Gauge heat transfer coefficient difference, $\Phi = 0.6$, $\dot{m}_{air}=425$ SLPM, US: Offset Normal, Coolant=Air, M=Variable, DS: Fan, Coolant=Air/N ₂ , M=2	224
E.52.	Gauge heat transfer coefficient, $\Phi = 1.1$, $\dot{m}_{air}=425$ SLPM, US: Blank, Coolant=N/A, M=N/A, DS: Fan, Coolant=Air/N ₂ , M=Variable	225
E.53.	Gauge heat transfer coefficient difference, $\Phi = 1.1$, $\dot{m}_{air}=425$ SLPM, US: Blank, Coolant=N/A, M=N/A, DS: Fan, Coolant=Air/N ₂ , M=Variable	225
E.54.	Gauge heat transfer coefficient, $\Phi = 1.1$, $\dot{m}_{air}=425$ SLPM, US: Slot, Coolant=Air, M=Variable, DS: Fan, Coolant=Air/N ₂ , M=2	226
E.55.	Gauge heat transfer coefficient difference, $\Phi = 1.1$, $\dot{m}_{air}=425$ SLPM, US: Slot, Coolant=Air, M=Variable, DS: Fan, Coolant=Air/N ₂ , M=2	226
E.56.	Gauge heat transfer coefficient, $\Phi = 1.1$, $\dot{m}_{air}=425$ SLPM, US: Slot, Coolant=N ₂ , M=Variable, DS: Fan, Coolant=Air/N ₂ , M=2	227
E.57.	Gauge heat transfer coefficient difference, $\Phi = 1.1$, $\dot{m}_{air}=425$ SLPM, US: Slot, Coolant=N ₂ , M=Variable, DS: Fan, Coolant=Air/N ₂ , M=2	227
E.58.	Gauge heat transfer coefficient, $\Phi = 1.1$, $\dot{m}_{air}=425$ SLPM, US: Offset Normal, Coolant=Air, M=Variable, DS: Fan, Coolant=Air/N ₂ , M=2	228
E.59.	Gauge heat transfer coefficient difference, $\Phi = 1.1$, $\dot{m}_{air}=425$ SLPM, US: Offset Normal, Coolant=Air, M=Variable, DS: Fan, Coolant=Air/N ₂ , M=2	228
E.60.	Gauge heat transfer coefficient, $\Phi = 1.3$, $\dot{m}_{air}=425$ SLPM, US: Blank, Coolant=N/A, M=N/A, DS: Fan, Coolant=Air/N ₂ , M=Variable	229

Figure		Page
E.61.	Gauge heat transfer coefficient difference, $\Phi = 1.3$, $\dot{m}_{air}=425$ SLPM, US: Blank, Coolant=N/A, M=N/A, DS: Fan, Coolant=Air/N ₂ , M=Variable	229
E.62.	Gauge heat transfer coefficient, $\Phi = 1.3$, $\dot{m}_{air}=425$ SLPM, US: Slot, Coolant=Air, M=Variable, DS: Fan, Coolant=Air/N ₂ , M=2	230
E.63.	Gauge heat transfer coefficient difference, $\Phi = 1.3$, $\dot{m}_{air}=425$ SLPM, US: Slot, Coolant=Air, M=Variable, DS: Fan, Coolant=Air/N ₂ , M=2	230
E.64.	Gauge heat transfer coefficient, $\Phi = 1.3$, $\dot{m}_{air}=425$ SLPM, US: Slot, Coolant=N ₂ , M=Variable, DS: Fan, Coolant=Air/N ₂ , M=2	231
E.65.	Gauge heat transfer coefficient difference, $\Phi = 1.3$, $\dot{m}_{air}=425$ SLPM, US: Slot, Coolant=N ₂ , M=Variable, DS: Fan, Coolant=Air/N ₂ , M=2	231
E.66.	Gauge heat transfer coefficient, $\Phi = 1.3$, $\dot{m}_{air}=425$ SLPM, US: Offset Normal, Coolant=Air, M=Variable, DS: Fan, Coolant=Air/N ₂ , M=2	232
E.67.	Gauge heat transfer coefficient difference, $\Phi = 1.3$, $\dot{m}_{air}=425$ SLPM, US: Offset Normal, Coolant=Air, M=Variable, DS: Fan, Coolant=Air/N ₂ , M=2	232
E.68.	Gauge heat transfer coefficient, $\Phi = 1.5$, $\dot{m}_{air}=425$ SLPM, US: Blank, Coolant=N/A, M=N/A, DS: Fan, Coolant=Air/N ₂ , M=Variable	233
E.69.	Gauge heat transfer coefficient difference, $\Phi = 1.5$, $\dot{m}_{air}=425$ SLPM, US: Blank, Coolant=N/A, M=N/A, DS: Fan, Coolant=Air/N ₂ , M=Variable	233
E.70.	Gauge heat transfer coefficient, $\Phi = 1.5$, $\dot{m}_{air}=425$ SLPM, US: Slot, Coolant=Air, M=Variable, DS: Fan, Coolant=Air/N ₂ , M=2	234
E.71.	Gauge heat transfer coefficient difference, $\Phi = 1.5$, $\dot{m}_{air}=425$ SLPM, US: Slot, Coolant=Air, M=Variable, DS: Fan, Coolant=Air/N ₂ , M=2	234
E.72.	Gauge heat transfer coefficient, $\Phi = 1.5$, $\dot{m}_{air}=425$ SLPM, US: Slot, Coolant=N ₂ , M=Variable, DS: Fan, Coolant=Air/N ₂ , M=2	235

Figure		Page
E.73.	Gauge heat transfer coefficient difference, $\Phi = 1.5$, $\dot{m}_{air}=425$ SLPM, US: Slot, Coolant= N_2 , M=Variable, DS: Fan, Coolant=Air/ N_2 , M=2	235
E.74.	Gauge heat transfer coefficient, $\Phi = 1.5$, $\dot{m}_{air}=425$ SLPM, US: Offset Normal, Coolant=Air, M=Variable, DS: Fan, Coolant=Air/ N_2 , M=2	236
E.75.	Gauge heat transfer coefficient difference, $\Phi = 1.5$, $\dot{m}_{air}=425$ SLPM, US: Offset Normal, Coolant=Air, M=Variable, DS: Fan, Coolant=Air/ N_2 , M=2	236
E.76.	Gauge surface temperature comparison, $\Phi = 0.6$, $\dot{m}_{air}=425$ SLPM, US: Blank/Slot/Offset, Coolant=Air, M=Variable, DS: Fan, Coolant=Air, M=2	237
E.77.	Heat flux comparison, $\Phi = 0.6$, $\dot{m}_{air}=425$ SLPM, US: Blank/Slot/Offset, Coolant=Air, M=Variable, DS: Fan, Coolant=Air, M=2	237
E.78.	Gauge heat transfer coefficient comparison, $\Phi = 0.6$, $\dot{m}_{air}=425$ SLPM, US: Blank/Slot/Offset, Coolant=Air, M=Variable, DS: Fan, Coolant=Air, M=2	238
E.79.	Gauge surface temperature comparison, $\Phi = 1.1$, $\dot{m}_{air}=425$ SLPM, US: Blank/Slot/Offset, Coolant=Air, M=Variable, DS: Fan, Coolant=Air, M=2	238
E.80.	Heat flux comparison, $\Phi = 1.1$, $\dot{m}_{air}=425$ SLPM, US: Blank/Slot/Offset, Coolant=Air, M=Variable, DS: Fan, Coolant=Air, M=2	239
E.81.	Gauge heat transfer coefficient comparison, $\Phi = 1.1$, $\dot{m}_{air}=425$ SLPM, US: Blank/Slot/Offset, Coolant=Air, M=Variable, DS: Fan, Coolant=Air, M=2	239
E.82.	Gauge surface temperature comparison, $\Phi = 1.3$, $\dot{m}_{air}=425$ SLPM, US: Blank/Slot/Offset, Coolant=Air, M=Variable, DS: Fan, Coolant=Air, M=2	240
E.83.	Heat flux comparison, $\Phi = 1.3$, $\dot{m}_{air}=425$ SLPM, US: Blank/Slot/Offset, Coolant=Air, M=Variable, DS: Fan, Coolant=Air, M=2	240

Figure		Page
E.84.	Gauge heat transfer coefficient comparison, $\Phi = 1.3$, $\dot{m}_{air}=425$ SLPM, US: Blank/Slot/Offset, Coolant=Air, M=Variable, DS: Fan, Coolant=Air, M=2	241
E.85.	Gauge surface temperature comparison, $\Phi = 1.5$, $\dot{m}_{air}=425$ SLPM, US: Blank/Slot/Offset, Coolant=Air, M=Variable, DS: Fan, Coolant=Air, M=2	241
E.86.	Heat flux comparison, $\Phi = 1.5$, $\dot{m}_{air}=425$ SLPM, US: Blank/Slot/Offset, Coolant=Air, M=Variable, DS: Fan, Coolant=Air, M=2	242
E.87.	Gauge heat transfer coefficient comparison, $\Phi = 1.5$, $\dot{m}_{air}=425$ SLPM, US: Blank/Slot/Offset, Coolant=Air, M=Variable, DS: Fan, Coolant=Air, M=2	242
E.88.	Gauge surface temperature comparison, $\Phi = \text{Variable}$, $\dot{m}_{air}=425$ SLPM, US: Blank/Slot/Offset, Coolant=Air, M=2, DS: Fan, Coolant=Air, M=2	243
E.89.	Heat flux comparison, $\Phi = \text{Variable}$, $\dot{m}_{air}=425$ SLPM, US: Blank/Slot/Offset, Coolant=Air, M=2, DS: Fan, Coolant=Air, M=2	243
E.90.	Gauge heat transfer coefficient comparison, $\Phi = \text{Variable}$, $\dot{m}_{air}=425$ SLPM, US: Blank/Slot/Offset, Coolant=Air, M=2, DS: Fan, Coolant=Air, M=2	244

List of Tables

Table		Page
2.1.	Summary of Thermal Conductivity of Hastelloy-X	29
3.1.	Vane spacing, throat width and axial solidity for all test configurations	44
3.2.	Circumferential cavity fuel and air inlet specifications per test section	46
3.3.	Hybrid vane domain air inlet port variations	49
3.4.	Mesh volume for each test domain	50
3.5.	Operating parameters used in preliminary analysis for engine condition and rig condition for complete annulus	51
3.6.	Core and circumferential cavity inlet mass flow rates for engine conditions, per section	52
3.7.	Operating parameters used in 5-species reacting flow analysis for engine condition and rig condition for complete annulus	55
4.1.	100% mass flow rate into the circumferential cavity test results for varied geometry (engine conditions)	70
4.2.	Result for 100% mass flow rate into the cavity using the 20 and 30 hybrid vane domains (rig conditions)	70
4.3.	Results for core mass flow rate variations. 20-vane, hybrid style vane domain, engine conditions	71
4.4.	Results for air inlet area variations, 100% cavity inlet mass flow rate, 20-vane, hybrid style vane domain	73
4.5.	Results for air inlet area variations, 100% cavity inlet mass flow rate, 30-vane, hybrid style vane domain	73
4.6.	Residence time for 20 and 30-vane domains	84
4.7.	Circumferential cavity flow properties using different cavity sizes	84
4.8.	Values of the exponent, Q , for each test configuration	87
4.9.	Inlet port diameters and fluid properties for 5-species, ‘ideal’ tangential velocity analysis	88

Table		Page
4.10.	Calculated pressures for ‘ideal’ test configurations using a 5-species combustion model	91
4.11.	Fluid properties for 5-species ‘ideal’ tangential velocity analysis for constant and variable C_p values using the rig condition . . .	95
4.12.	Inlet port diameters and fluid properties for 12-species analysis using ‘ideal’ inlet diameters determined from 5-species analysis	96
4.13.	Calculated pressures and losses for ‘ideal’ cavity inlet diameters using a 12-species combustion model	99
4.14.	Comparison of fluid properties within the circumferential cavity for 5- and 12-species combustion models with ‘ideal’ inlet diameters with and without the divider plate	112
4.15.	Calculated pressures and losses for ‘ideal’ cavity inlet diameters using a 5- and 12-species combustion model with and without the divider plate	117
4.16.	Calculated static pressures at the domain inlet, cavity inlet port and domain exit for the ducted domain	119
4.17.	Fluid properties in the ducted domain	121
4.18.	Calculated versus actual cavity inlet diameters	123
5.1.	Flow straightener design specifications for all designs considered	135

List of Symbols

Symbol		Page
T_4	Turbine Inlet Temperature	4
T_{4max}	Maximum Turbine Inlet Temperature	4
S_B	Bubble Velocity	7
g_c	Newtons Constant, 9.82 m/s ²	8
r_{cavity}	Radius of Cavity	8
U_{tan}	Tangential Velocity	8
β	Tangent Angle	8
\dot{m}_{cavity}	Mass Flow in UCC Cavity	8
ρ_{cavity}	Density in the Circumferential Cavity	8
A_{exit}	Area of UCC Exit	8
u_τ	Friction Velocity	15
ν	Kinematic Viscosity	15
y	Distance to the Wall	15
μ_t	Turbulent or Eddy Viscosity	16
k	Turbulent Kinetic Energy	16
ε	Turbulent Dissipation Rate	16
ω	Specific Dissipation Rate	16
q''	Heat Flux Per Unit Area	17
h	Convective Heat Transfer Coefficient	17
T_{ref}	Reference Temperature	17
T_s	Surface Temperature	17
T_c	Coolant Temperature	17
T_∞	Coolant Temperature	17
T_f	Film Temperature	17
T_{aw}	Adiabatic Wall Temperature	17

Symbol		Page
η	Adiabatic Effectiveness	18
$T_{c,exit}$	Coolant Temperature at Coolant Hole Exit	18
ϕ	Overall Effectiveness	18
T_m	Metal Temperature	18
$T_{c,i}$	Internal Coolant Temperature	18
h_f	Convection Coefficient With Film Cooling	19
h_{eff}	Effective Convection Coefficient	19
M	Mass Flux Ratio, Blowing Ratio	19
ρ_c	Coolant Density	19
ρ_∞	Free Stream Density	19
U_c	Coolant Velocity	19
U_∞	Free Stream Velocity	19
\dot{m}	Mass Flow Rate	20
A	Cross-Sectional Area	20
$\dot{m}_{c,total}$	Total Mass Flow Rate in all Coolant Holes	20
$A_{c,total}$	Total Area of all Coolant Holes	20
A_∞	Cross-Sectional Area of the Free Stream Inlet	20
\dot{m}_∞	Mass Flow Rate of the Free Stream Fluid	20
I	Momentum Flux	23
θ	Normalized Temperature	24
k	Thermal Conductivity	28
T	Temperature	28
x	Distance From Reference Location	28
a_0	Constant From Least Squares of Thermal Conductivity . .	28
a_1	Constant From Least Squares of Thermal Conductivity . .	28
C	Constant of Integration	30
Φ	Equivalence Ratio	30
stoic	Stoichiometric	31

Symbol		Page
\dot{m}_{fuel}	Mass Flow Rate of Fuel	31
\dot{m}_{air}	Mass Flow Rate of Oxidizer	31
MW	Molecular Weight	31
s	Vane Spacing	38
b	Vane Chord	38
β_1	Vane Inlet Angle	38
β_2	Vane Exit Angle	38
σ	Axial Solidity	43
c	Chord	43
$A_{ellipse}$	Elliptic Area	48
ϕ	Inlet Diameter	48
λ	Injection Angle	48
C_p	Constant Pressure Specific Heat	52
$\dot{m}_{section}$	Mass Flow Rate Into Domain Section	87
I	Number of Inlet Ports	87

List of Abbreviations

Abbreviation		Page
UCC	Ultra-Compact Combustor	1
AFRL	Air Force Research Lab	1
OD	Outside Diameter	2
ID	Inside Diameter	3
ITB	Inter-Turbine Burner	3
CFD	Computational Fluid Dynamics	6
UNICORN	Unsteady Ignition and Combustion with Reactions	8
LBO	Lean Blowout	9
LDV	Laser Doppler Velocimeter	13
DNS	Direct Numerical Simulation	15
RANS	Reynolds-Averaged Navier-Stokes	15
SST	Shear Stress Transport	16
REF	Reference	25
ISHAP	Inlet-Shaped Film Hole	25
FDIFF	Forward-Diffused Film Hole	25
LDIFF	Laterally-Diffused Film Hole	25
WSR	Well Stirred Reactor	30
EDC	Eddy-Dissipation-Concept	33
AFIT	Air Force Institute of Technology	55
DPM	Discrete Phase Modeling	56
PDF	Probability Density Function	59
SLPM	Standard Leters Per Minute	137
GPM	Gallons Per Minute	143
US	Upstream	156
DS	Downstream	156

ANALYSIS OF FLOW MIGRATION IN AN ULTRA-COMPACT COMBUSTOR

I. Introduction

1.1 *Ultra-Compact Combustor*

A large majority of the current axial turbine engines in operation today utilize a combustor design that in principle has not changed much since the creation of the jet engine in 1929 by Sir Frank Whittle. The materials in the combustor have been updated to handle higher temperatures and with the introduction of film cooling, the combustion temperatures can exceed the material failure temperature of the combustor liner. The concept of the traditional combustor uses axial flow straightened by the compressor exit guide vane and a long combustion region on the order of 25-50 centimeters to fully combust the fuel prior to entering the high-pressure turbine inlet guide vane (IGV). Historically, turbine engine combustion has taken place at an overall fuel-to-air ratio much less than stoichiometric [1]. Combining the low fuel-to-air ratio and the long combustor sections allowed the fuel and air to mix, evaporate and fully burn prior to exiting the combustor section. To improve engine efficiency and specific thrust the value of the turbine inlet temperature (T_4) has been steadily increased over the past many years. Increased combustion temperatures can be achieved by increasing the fuel-to-air ratio closer to stoichiometric.

In recent years, the effort to improve the thrust-to-weight ratio of turbine engines has led to advanced combustors which are more compact than the traditional combustor discussed above [2]. An ultra-compact combustor, UCC, could be the solution to an increase in T_4 and a decrease in the length of the combustor which could lead to improved efficiency and an increased specific thrust. The UCC is a revolutionary combustor design under development at the Air Force Research Lab, AFRL, which has the potential to meet thrust-to-weight and efficiency goals of future turbine

engines. The UCC shortens the combustor section compared to traditional engines by combining the combustor, compressor exit guide vane and turbine inlet guide vane in one package. Figure 1.1 shows an illustration of a traditional combustor and a UCC. The UCC reduces axial length by burning a swirling fuel-air mixture in a cavity in the circumferential direction around the outside diameter, OD, of the engine. The idea behind combustion in the circumferential cavity is to provide the fuel ample residence time like that provided in a traditional combustor while drastically reducing axial length. Additional length is saved using a UCC by integrating the compressor exit guide vane and turbine inlet guide vane into a single vane located directly below the circumferential cavity. Overall the UCC is estimated to shorten the combustion section by 66% [2] which results in significant weight savings as well.

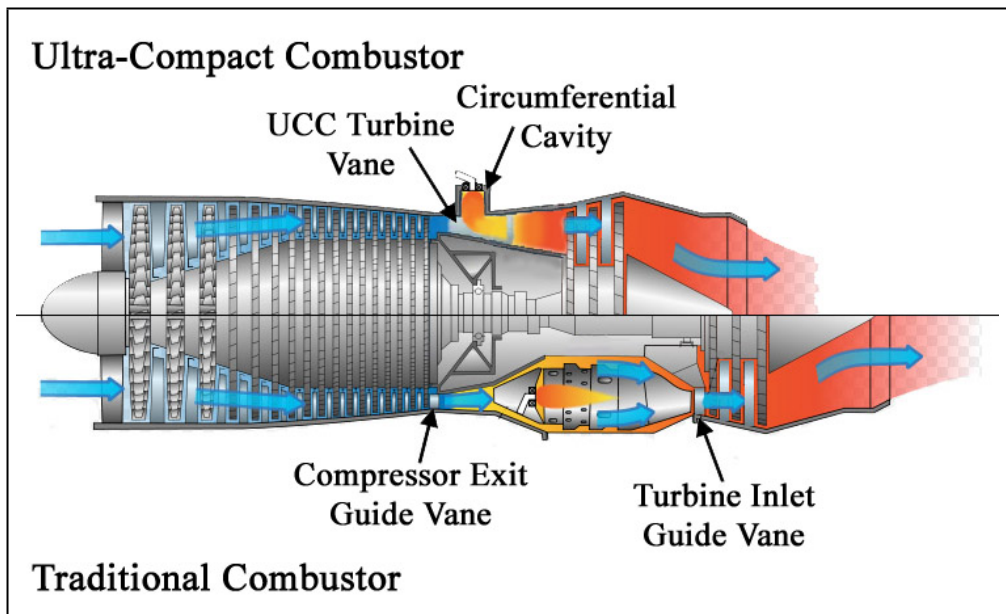


Figure 1.1: Traditional combustor (below), Ultra-Compact Combustor (above)

In a traditional combustor, air flow is in the axial direction where residence time is a function of the flow velocity and combustor length. To allow complete combustion, the combustor must be long enough to allow the fuel to completely mix with air and burn before exiting.

In a UCC, fuel and air are injected into the cavity at an angle to force the fuel-air mixture to flow in a circumferential direction. This circumferential versus axial burning increases the g-loading on the fluid and provides two benefits. The first benefit is that combustion products burned under increased g-loading experience increased flame speeds as introduced by Lewis [3] in 1973. An increase in the reaction rate results in a decrease in the combustor volume. The second benefit is that the heavier, unburned fuel particles are forced to the OD of the circumferential cavity by the g-force. This migration ensures that these particles stay in the cavity until they are consumed and converted to lighter exhaust products. The lighter exhaust products are pushed toward the inside diameter, ID, of the circumferential cavity where they exit the cavity and interact with the turbine vanes. Allowing the heavy unburned fuel to remain in the circumferential cavity until it is fully broken down is the equivalent of an infinite combustion section which only occupies about 5 cm of axial length.

Due to the compressed size and light weight design of the UCC, the concept is being investigated for use as a second-stage combustor as well. A second-stage combustor is also referred to as an inter-turbine burner, ITB, and is located between the high-pressure and low-pressure turbines. Large amounts of low-pressure energy can be extracted from the low-pressure turbine with a moderate temperature increase across the ITB [4]. The additional energy could be used to drive a large fan for an ultra-high bypass ratio engine or a number of other applications.

The UCC design presents a significant challenge to cooling the turbine vanes below the circumferential cavity and presenting a uniform temperature in the radial direction to the first turbine stage for fighter size engines. The cooling challenge arises due to the integrated nature of the vanes into the combustor and the high design fuel-air ratio. Introducing oxygen rich cooling flow to combustion products immediately after exiting the circumferential cavity increases the potential for a combustion reaction to occur with unburned fuel on the surface of the vanes, significantly reducing component life. The temperature distribution challenge is to extract the combustion

gases from the circumferential cavity and evenly distribute and mix the hot gases with the core flow prior to impacting the turbine, a distance of approximately 10.5 centimeters.

1.2 Turbine Film Cooling

As mentioned in Section 1.1, the desire to achieve improved efficiency and specific thrust have led to an increase in the turbine inlet temperature, T_4 . Common sense would say that T_{4max} should not be higher than those temperatures above which turbine material failure can occur. However, beginning in 1960 cooling methods used on turbine airfoils allowed T_{4max} to be higher than the turbine airfoil material could handle. These cooling methods involved convective cooling schemes focused on cooling the inside of the turbine blade with high-pressure compressor bleed air. In the 1970s holes were drilled into the airfoil surface to allow the bleed air to escape the internal cooling passages, forming a cooling film on the airfoil surface and film cooling technology was born [5].

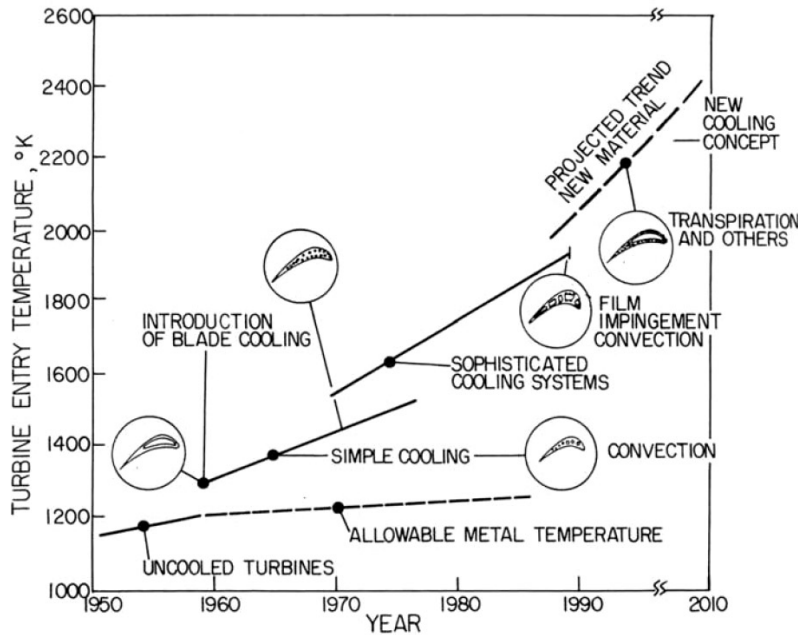


Figure 1.2: Comparison of turbine inlet temperature to material limits [6]

Figure 1.2 shows the relationship between T_4 and turbine material limits over the past 60 years. The gap between turbine inlet temperatures and the turbine material temperature limit highlights the necessity for cooling. In recent years, improvements in turbine materials have resulted in more heat tolerant structures but even with these improvements the requirement for cooling still exists.

1.3 Potential for Heat Release in Film Cooling

Until the time when engine components can be made from a material that can directly handle the heat of a turbine engine, manufacturers will depend on film cooling to prevent catastrophic material failure. However, with modern engines operating with elevated fuel-to-air ratios and less time and combustor volume to burn the fuel, the likelihood of heat release in the cooling film due to fuel streaks reacting with oxygen rich cooling film in the turbine section is high. This secondary reaction of fuel with the turbine cooling film is illustrated in Figure 1.3 which shows the process of burning in the turbine as described by Lukachko et al. [7].

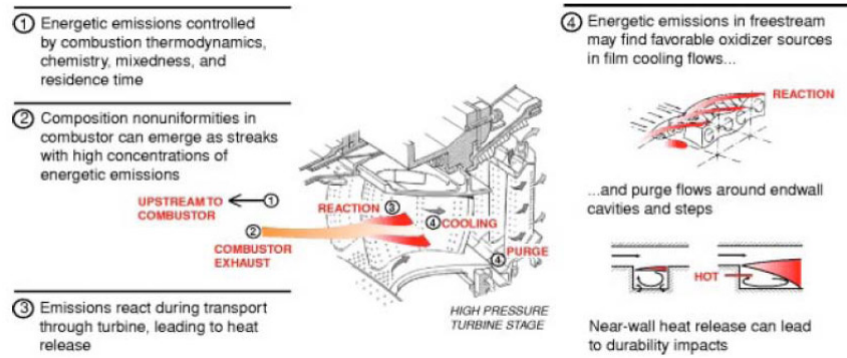


Figure 1.3: Secondary combustion reaction from a traditional combustor [7]

There is still another challenge to turbine cooling beyond reacting fuel streaks. With modern combustor temperatures rising, some of the combustion energy will be stored in the flow in the form of dissociated highly energetic species such as carbon monoxide rather than as increased exhaust temperature [8]. The energy stored in the dissociated molecules could be released in the relatively cool turbine section of the

engine where cooler temperatures promote molecular recombination. The likelihood of recombination is even greater in the turbine cooling film due to the low temperature relative to the mainstream gas. If energy is released in the cooling film, regardless of whether it is the result of a secondary combustion reaction or molecular recombination of dissociated gas, the result is a drastically decreased cooling effectiveness of the turbine cooling scheme. Since modern engines operate with T_4 well exceeding the material temperature limit, a reduction in the cooling scheme effectiveness will result in a severe reduction in engine component durability or immediate component failure.

1.4 Objectives

The objectives of this research were to incorporate several aspects of UCC research into a single design. The primary objective was to migrate the hot combustion products from the circumferential cavity and evenly mix it with the cooler core flow to present a uniform temperature fluid to the high-pressure turbine. There were several sub-objectives and research that played into meeting the primary objective. The first was to obtain a full understanding of the UCC geometry and inlet flow conditions that control the tangential velocity of the fluid in the circumferential cavity. By understanding the parameters that impact the tangential velocity, correlations could be drawn to achieve any desired cavity velocity and thus any g-load to maximize the benefits available from g-loaded combustion. The second sub-objective was to investigate UCC turbine vane modifications to aid in achieving the most desirable temperature distribution at the turbine inlet. The third sub-objective was to experimentally investigate film cooling techniques that could be used in high fuel-to-air environments since the UCC turbine vane located below the circumferential cavity will require cooling in the presence of fuel rich exhaust. Evans [8] researched the topic of heat release in turbine film cooling but the current research attempted to mitigate the negative effects of secondary reactions in the cooling film. The UCC analysis was accomplished using computational fluid dynamics, CFD, while the film cooling analysis was performed experimentally.

II. Background

2.1 *Ultra-Compact Combustor*

The UCC was initially conceived by Sirignano [9]. The design takes advantage of circumferential combustion versus axial combustion supplemented with an additional benefit of g-loaded combustion which results in an increased flame speed. This finding was originally documented by Lewis [3] who reported that beginning at 200 g's the flame speed began to increase. From 500 to 3,500 g's there was a steady increase in flame speed with increasing centrifugal force. In this range, Lewis found that the burning rate of the fuel-air mixture was proportional to the square root of the g-loading. Lewis attributed the increase in flame speed to the presence of bubbles or eddies that traveled ahead of the flame front and resulted from the centripetal acceleration. If the bubble velocity (S_B) exceeds the turbulent flame speed, the flame propagates at the bubble velocity given by Equation 2.1 [3]. If the bubble velocity is slower than the turbulent flame speed the turbulent flame speed controls the reaction. These two cases are shown in Figure 2.1 where the dark circles are the flame bubbles that travel at velocity S_B in the time Δt and the dashed lines represent the turbulent flame front at the time $t + \Delta t$.

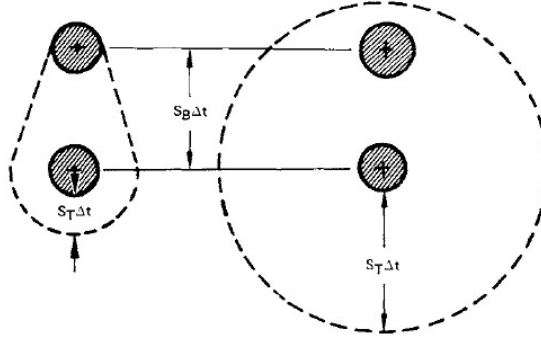


Figure 2.1: Bubble velocity controlled flame propagation (Left) and turbulent flame speed controlled reaction (Right) [3], [2].

$$S_B = 1.25\sqrt{g} \quad (2.1)$$

In Equation 2.1, g is the g-loading with units of ft/s. Lewis noted that 1.25 coincidentally is the 1g bubble velocity in ft/s. Below 200 g's the turbulent flame speed controls the flame propagation and the velocity is independent of g-loading. The g-loading value as defined by Zelina et al. [4] is given in Equation 2.2.

$$g = \frac{U_{tan}^2}{g_c r_{cavity}} \quad (2.2)$$

Here, g_c is Newtons constant with a value of 9.82 m/s², r_{cavity} is the radius of the UCC cavity and U_{tan} is the tangential velocity and is defined by Equation 2.3 [10]

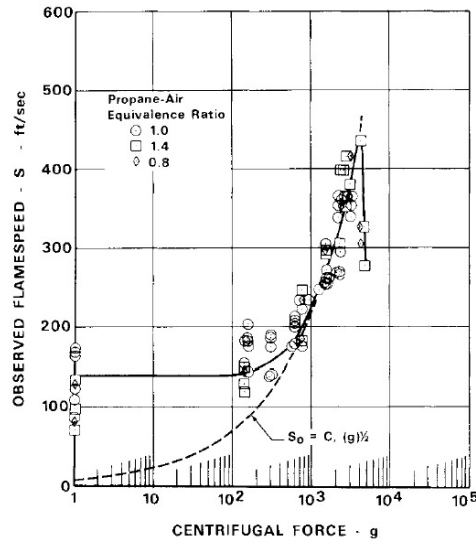
$$U_{tan} = \frac{\dot{m}_{cavity}}{\rho_{cavity} A_{exit} \tan\beta}, \quad (2.3)$$

where β is the angle from the tangent line to the surface of the circumferential cavity, \dot{m}_{cavity} is the mass flow through the circumferential cavity, ρ_{cavity} is the density in the circumferential cavity and A_{exit} is the area of the circumferential cavity exit.

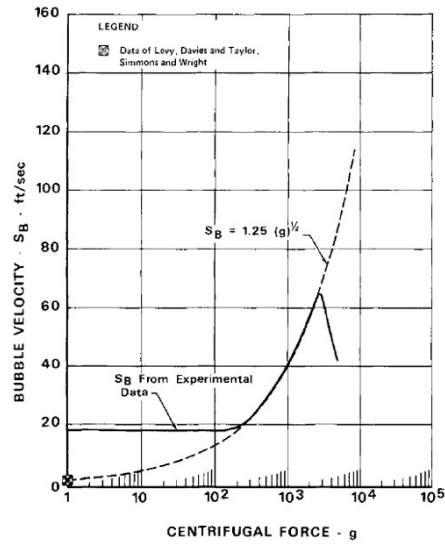
Lewis found that there was also a maximum value of g (3500 g's) above which the flame speed and bubble velocity quickly decreased for increased g-loading until blowout occurred between 7,000 and 8,000 g's. Figure 2.2 shows the relationship of flame speed and bubble velocity (given in ft/sec) as a function of g-loading.

Zelina et al [2] showed the magnitude of enhanced flame speeds due to g-loading using the UNICORN CFD code. The study examined flame propagation for a hydrogen-air mixture in a 50-mm by 1000-mm two-dimensional tube using a laminar, time-dependent solver. The solution was run for a number of applied gravitational loads between 0g and 500g's. Figure 2.3 shows the flame propagation at three time steps for an applied g-load of 10g's and 500g's. It can easily be seen that the higher g-loading case had a significantly increased flame speed shown by the enhanced flame propagation at each time step compared to the lower g-load case.

Additionally, initial experimental studies by Zelina et al. [2] on small scale UCC systems operating at atmospheric and increased pressures showed a combustion effi-



(a) Propane Flame Propagation Rate



(b) Bubble Velocity

Figure 2.2: Flame propagation rate and bubble velocity as a function of g-loading [3], [2]

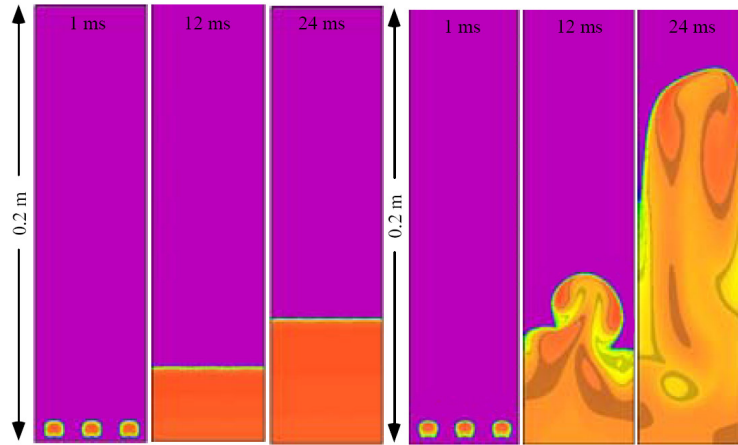


Figure 2.3: Flame propagation at 10g's (Left), Flame propagation at 500g's (Right) [2].

ciency between 95 and 99% over a wide range of operating conditions burning JP-8 +100 fuel. This study noted that the axial flame length from the UCC was approximately 50% shorter than conventional combustion systems which could help reduce or eliminate any burning in the turbine problems. A series of lean blowout, LBO,

tests conducted by Zelina et al. [2] which recorded the equivalence ratio in the cavity at blowout for varying g-loading found that a stable flame could be maintained over a wide range of operating conditions with a maximum g-loading value approximated between 7,000 and 8,000 g's. The maximum g-loading value is supported by the data presented by Lewis [3]. Figure 2.4 shows the results of the LBO study.

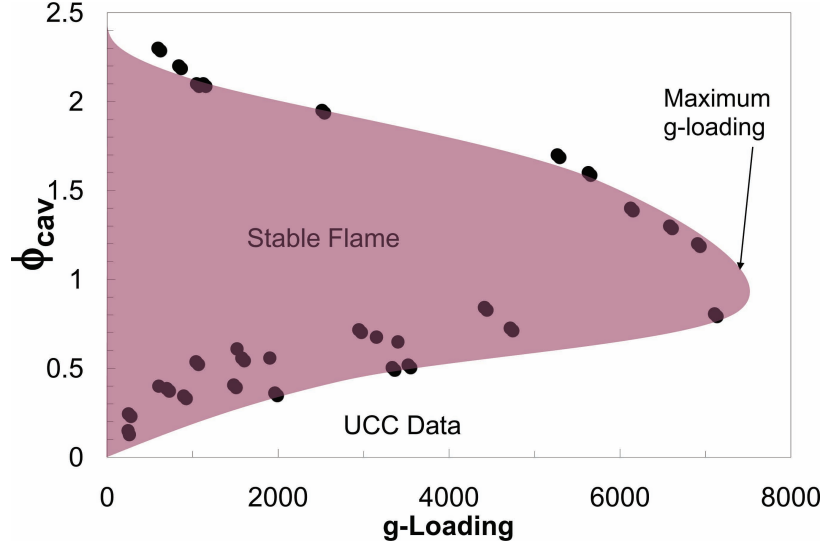


Figure 2.4: UCC cavity equivalence ratio at blowout as a function of cavity g-loading [2]

A study by Anderson et al. [10] was performed on a small scale UCC combustor section which observed the effects of main swirl direction on high-g combustion. The study found that there was a difference in the stability of the flame by varying the flow direction, however, it appeared that the main differences in the flow were a result of the fuel and air injector locations relative to the UCC turbine vanes. The positioning of the fuel injectors and vanes was not symmetric and the relative distances between these components varied depending on the direction of flow. In one cavity flow direction the fuel exited the cavity almost immediately after striking a UCC turbine vane, while the reverse direction allowed the fuel to remain in the cavity longer and exited after passing over the vane. This study confirmed that the air and fuel injector placement can impact the stability and usefulness of the system.

2.2 Secondary Flows

The UCC turbine vanes experience fluid interactions from two directions, one of which is a cross flow. When a body with an endwall exists in cross flow, the effects of secondary flows must be considered. A secondary flow is comprised of the three-dimensional, vortical structures that develop around obstructions in the flow such as turbine vanes. Langston [11] provided much of the early work regarding secondary flows and identified two dominant vortical structures that result from the flow around a body protruding from a surface. His research identified the vortex structures referred to as a horseshoe and passage vortex. An illustrated diagram of secondary flows as related to turbine vanes is shown in Figure 2.5. As flow passes over the surface, a boundary layer is developed resulting in low speed flow near the wall and high speed flow away from the wall. As the fluid approaches the protruding body the higher momentum fluid travels down the face of the obstruction into the lower momentum fluid. The downwash rolls up into a vortex that is then swept around the obstruction and grows as it convects downstream. These structures are primarily seen in the endwall regions of three-dimensional structures due to the presence of large gradients in velocity and fluid properties.

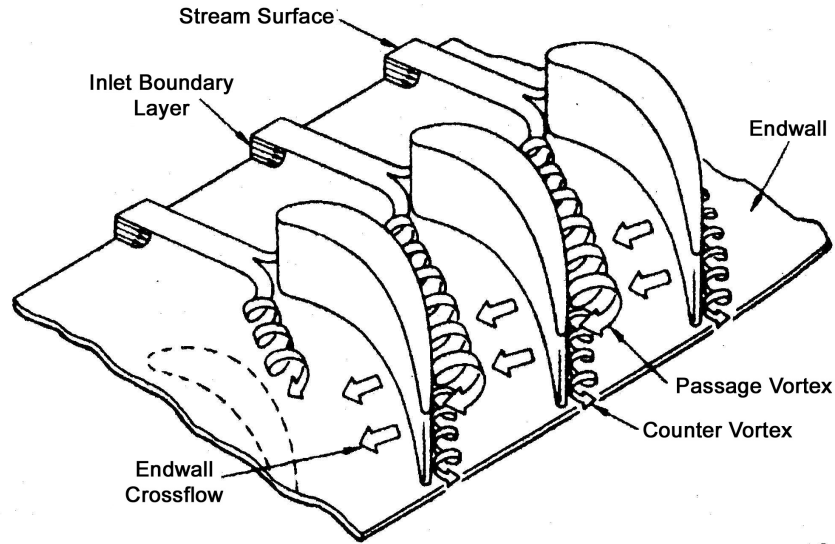


Figure 2.5: Illustration of secondary flows [11]

The presence of secondary flows has both positive and negative effects on the current study. From a positive point of view these structures could be a driving factor in achieving a uniform temperature profile at the exit to the UCC section. In particular, the secondary flows along the OD endwall of the vane which will encounter the shear from the cavity circumferential flow. This interaction could be exploited to aid in the migration of the hot flow exiting the cavity. The migration across taller vanes than previously experimented with is one of the key aspects of the current study. Understanding the flow properties across taller vanes will be an important factor as the UCC transitions from small scale testing to a larger fighter scale. To the knowledge of the author no research has been performed on a UCC for a fighter scale engine.

The negative impact of secondary flows is that the same motion that enhances mixing also hinders film cooling of the turbine vanes as the vortical structures entrain fluid near the wall sweeping away cooling flows [6]. Lethander [6] researched techniques to mitigate the effects of the secondary flows by effectively removing or reducing the vortical structures by adding a fillet to round the endwall into the turbine vane.

Much of the research regarding secondary flows as applied to turbine engines has been directed to the turbine region of an engine that uses a conventional combustion system. The long can-type combustor provides an undisrupted surface where a boundary layer could form. Hermanson and Thole [12] [13] studied the effect of inlet conditions and Mach number on the formation of secondary flows. The inlet in their study was the exit properties of the combustor section. Their research showed that larger boundary layers resulted in a horseshoe vortex that spread further around the leading edge. Additionally, they showed that when no stagnation pressure gradient was present, no horseshoe or passage vortex formed. Based on these results it can be concluded that knowing the compressor exit conditions (for a UCC), or combustor exit conditions (for a conventional combustor) directly impacts the ability to predict the secondary flow properties around the turbine vanes.

Hermanson and Thole [13] also provided an excellent comparison of experimental results using a laser Doppler velocimeter, LDV, to numerical flowfield predictions from the $k-\varepsilon$ and RNG $k-\varepsilon$ turbulence models along the stagnation plane of a turbine vane. Figure 2.6 shows the results obtained by Hermanson and Thole. This study was specifically concerned with the ability of the turbulence models to replicate horseshoe and passage vortex secondary flow structures around the turbine vane. Anticipating a secondary flow dominated regime and the importance these structures could play in mixing hot fluid from the circumferential cavity with cooler core flow, this study was of particular interest.

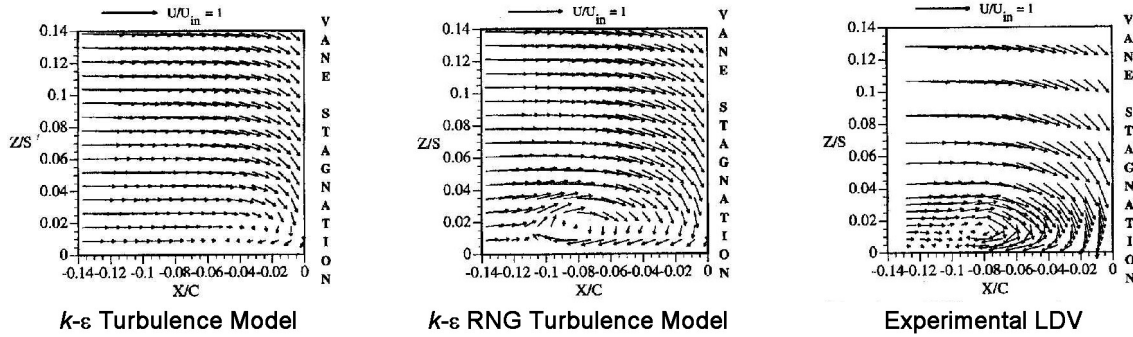


Figure 2.6: Comparison of turbulence models to experimental LDV measurements along the stagnation plane of a turbine vane [13]

From Figure 2.6 it can be seen that the RNG $k-\varepsilon$ turbulence model most closely matched the experimental result. The vortex structure was located in the same X/C location and only slightly higher in the Z/S position. An additional comparison for this model showed the predicted magnitude of the y-vorticity to be equal to the experimental levels. Hermanson and Thole also compared the RNG $k-\varepsilon$ simulation to the experimental results in six additional planes around the turbine vane. The largest difference between the numerical results and the experimental data was that in each plane the model predicted the vortex to be 1-3% higher off the endwall. The standard $k-\varepsilon$ turbulence model predicted the vortex to be too close to the endwall and the stagnation plane and did not capture the rotation. The RNG $k-\varepsilon$ turbulence model was anticipated to provide the most accurate results due to the presence of additional

terms in the transport equations for k and ε which can handle stagnation flows and high streamline curvature. Hermanson and Thole [13] completed the remainder of their study using the RNG k - ε turbulence model.

2.3 Computational Fluid Dynamics (CFD)

Prior to 1970, designs for vehicles and systems involving fluid mechanics and heat transfer were developed using a combination of experimental and theoretical methods [14]. Development of computational fluid dynamics began in the 1970's to simulate fluid flows, thus adding a third method to engineering design, numerical analysis. In the 1980's CFD advanced to solve the first two-dimensional and later three-dimensional Euler based solutions. In the mid-1980's development of more complex viscous flows using the Navier-Stokes equations became the focus of CFD research. At this same period turbulence models began to emerge with various levels of numerical complexity [15]. In current times, computational fluid dynamics is routinely used and has a wide range of applications including, but not limited to, fluid dynamics of internal and external flows, combustion analysis and heat transfer; all of which are applicable to the current study.

Proper grid development is the key to achieving realistic results in any CFD solution. A well constructed mesh can remove problems that could ultimately lead to instability and greatly increases the likelihood to achieving a solution [16]. Grid generation is not a trivial exercise and becomes more challenging with more complex flow physics. The required grid spacing at the wall is dependent on the type of solution (viscous or inviscid) and the turbulence model used, if any. In general, to resolve the viscous sublayer of a viscous flow down to the wall, the y^+ value of the first cell should be ≤ 1 [15] with a smooth growth rate of approximately 20% for each successive cell. The function y^+ is a non-dimensional relationship involving the properties of the fluid and the distance of the cell to the wall as shown in Equation 2.4 [17].

$$y^+ = \frac{u_\tau y}{\nu} \quad (2.4)$$

The symbol u_τ is the friction velocity, ν is the kinematic viscosity and y is the distance to the wall. The definition of u_τ is given in Equation 2.5 where τ_w is the wall shear and ρ is the density.

$$u_\tau = \sqrt{\frac{\tau_w}{\rho}} \quad (2.5)$$

For cases where the solution does not need to be integrated to the wall, wall functions can be used. A wall function is based on the logarithmic “law-of-the-wall” relationship and the understanding that the viscous sublayer is fairly universal across all flows. Through the use of wall functions the boundary layer equations are solved using a turbulence model on a relatively course grid and an approximate solution for the near-wall region is found using the “law-of-the-wall” relationship. The “law-of-the-wall” is assumed valid when the first cell away from the wall is within the range $30 < y^+ < 200$ [14].

In addition to the size of the cells, the type of mesh used, whether structured or unstructured, must be selected. In general a structured mesh is desired from a computational point of view, however, for complex three-dimensional geometries a structured mesh is not practical. Depending on the solver, a combination of structured and unstructured cells can be used, producing a hybrid grid which typically enhances grid quality when using structured cells to resolve boundary layers and triangular or tetrahedral cells for the remainder of the domain [16].

Turbulence models range in increasing computational demand from simple algebraic models up to the very computationally expensive Direct Numerical Simulations, DNS. Somewhere in between these extremes there are a class of turbulence models referred to as RANS models or Reynolds-Averaged Navier-Stokes models. This class of models breaks the variables in the Navier-Stokes equations into a mean and fluctuating component and solves for the mean values which are typically most important to engineering applications while modeling the fluctuations [15]. These models provide a sufficient level of fidelity while limiting the computational expense. In all of the RANS models the common goal is to solve the closure problem caused by the Reynolds

stresses in the averaged form of the Navier-Stokes equations by solving for the value of the turbulent or eddy viscosity, μ_t . Within the RANS category there are still several sub-categories of turbulence models including first-order models (0-2 equations) and second-order models. The most common models in use today are the two-equation models, specifically the k - ε and k - ω models. Both of these models are based on the solution to equations for the turbulent kinetic energy, k , and the turbulent dissipation rate, ε , or the specific dissipation rate, ω . There are benefits and drawbacks for each of these models. The k - ε model performs best away from walls in a constant pressure or favorable pressure gradient. This model requires a damping function through the viscous sublayer to remain valid which results in turbulence equations with stiff source terms [15]. Typically the k - ε model is not integrated to the wall, it takes advantage of wall functions for a near wall solution. Since the solution is usually not directly solved in the viscous sublayer, this model is not the best choice for wall flows. Additionally, the k - ε model should not be used in adverse pressure gradients or separated flows. The k - ω model on the other hand is seemingly just the opposite. This model performs well in adverse pressure gradients and at the wall and does not require a damping function. k - ω is, however, very sensitive to the free stream value of ω and thus can vary significantly in the wake region of the flow. The k - ω SST model, or Shear Stress Transport model, combines the positive features of the k - ε and k - ω models. The k - ω equations are used in the sublayer and logarithmic regions of the flow (near the wall where k - ω performs best) while the k - ε equations are used in the wake region and in free shear layers where k - ε performs best. Variations of the k - ε equations also exist, most notably k - ε RNG which is tuned to handle stagnation flows and conditions with high streamline curvature. This model can be used for internal, wall-bounded flows but requires that the first computational point away from the wall occurs within the range of $30 < y^+ < 60$.

2.4 Film Cooling

2.4.1 Convective Heat Transfer. The mathematics of heat transfer and convection have been around for many years. Over the past 40 years the equations have been adapted to further understand the concept of film cooling. Film cooling in turbine engines works by buffering the engine surfaces from the hot freestream gases with a thin film of coolant air ejected from discrete holes or slots. Even with the coolant flow protecting the engine components it is still important to know the heat transfer to the surface. Equation 2.6 shows the definition of convective heat flux to the surface per unit area, q'' . While these equations can be found in many sources, Bogard and Thole [5] provides an excellent overview of the equations of heat transfer as applied to film cooling.

$$q'' = h(T_{ref} - T_s) \quad (2.6)$$

In the above equation, h is the convective heat transfer coefficient, T_{ref} is an appropriate reference temperature (temperature above the surface) and T_s is the surface temperature. Determining the value of q'' in a film cooling flow is challenging due to a fluctuating heat transfer coefficient and variable temperature located directly above the surface. The temperature variation above the surface is due to the mixing of coolant air at temperature T_c and the freestream fluid at temperature T_∞ . If the coolant fluid ejected from the component surface remained attached to the surface and no mixing took place, the temperature driving the convective heat transfer would be T_c . Since separation and mixing do occur, the driving temperature is the film temperature, T_f , which ranges between T_c and T_∞ depending on the distance from the coolant ejection site and the amount of mixing taking place.

Under experimental conditions where the film temperature and flow conditions are known, the adiabatic wall temperature, T_{aw} , can be found. The adiabatic wall temperature is the temperature of the wall with no heat transfer to the surface, it is also the temperature of the fluid directly above the adiabatic surface. Due to the discrete distribution of coolant holes, the adiabatic wall temperature and local

convection coefficient can vary widely over the entire component surface. If T_{aw} is known, the film cooling performance can be determined in the form of the non-dimensional adiabatic effectiveness, η , as shown in Equation 2.7.

$$\eta = \frac{(T_{\infty} - T_{aw})}{(T_{\infty} - T_{c,exit})} \quad (2.7)$$

In Equation 2.7, $T_{c,exit}$ is the coolant temperature at the coolant hole exit. In many cases T_{aw} is not known or the surface is not an adiabatic surface. Additionally, $T_{c,exit}$ is a difficult temperature to measure because the presence of a temperature probe at the exit of a small hole disrupts airflow out of the hole and impacts the temperature at the exit. Another non-dimensional parameter known as the overall effectiveness, ϕ , is used to determine the impact of film cooling without requiring the adiabatic wall temperature or coolant temperature at the coolant hole exit. Equation 2.8 shows the relationship of the overall effectiveness.

$$\phi = \frac{(T_{\infty} - T_m)}{(T_{\infty} - T_{c,i})} \quad (2.8)$$

Here T_m is the metal temperature of the cooled component and $T_{c,i}$ is the internal coolant temperature prior to entering the coolant hole. There is a limitation to using this parameter. If the metal surface is actively cooled by other means, such as water in the case of the experimental tests conducted within this report and Evans [8], the value of ϕ is calculated to be significantly higher than would be achieved without the water cooling. Therefore, the results can not be directly compared to other reports that did not use water cooling and can not be directly applied to performance in an engine.

The value of h fluctuates widely over the component surface and is highly dependent on flow conditions. In many cases the disturbance to the flow caused by the coolant hole or coolant jet can increase the value of the convection coefficient. Under certain circumstances the increase in h can actually accelerate the heat transfer to

the surface for a constant T_{ref} . The designation of h is changed from Equation 2.6 to h_f designating the convection coefficient with film cooling. This change is shown in Equation 2.9.

$$q'' = h_f(T_{ref} - T_s) \quad (2.9)$$

Since the film temperature is very difficult to measure, the reference temperature used in this report will be T_∞ . Additionally, to account for heat release in the cooling film, the convective coefficient is replaced by the effective convection coefficient, h_{eff} . Equation 2.10 shows the final form of the convective heat transfer equation used in this report.

$$q'' = h_{eff}(T_\infty - T_s) \quad (2.10)$$

2.4.2 Flow Physics. There are several factors within the geometry and flow properties of a cooling scheme that greatly impact the cooling effectiveness. The mass flux ratio, M , also referred to as the blowing ratio, is the first important fluid factor to mention. Equation 2.11 shows the relationship to calculate the value of M .

$$M = \frac{\rho_c U_c}{\rho_\infty U_\infty} \quad (2.11)$$

In Equation 2.11, ρ_c is the coolant density, ρ_∞ is the free stream density, U_c is the coolant velocity and U_∞ is the free stream velocity. The relationship in Equation 2.11 does have the limitation that it requires knowledge of the exact density and velocity for each fluid and it is extremely difficult to measure these properties in a fluctuating flow field. For experimental purposes the inlet area of the coolant holes and free stream channel is known and the mass flow can be measured. The relationship in Equation 2.12 shows how the mass flow and area are related to density and velocity.

$$\frac{\dot{m}}{A} = \rho U \quad (2.12)$$

In the above equation, \dot{m} is the mass flow rate and A is the cross-sectional area of the coolant hole or channel. Using the relationship in Equation 2.12 and substituting into Equation 2.11 yields Equation 2.13:

$$M = \frac{\dot{m}_{c,total} A_{\infty}}{\dot{m}_{\infty} A_{c,total}} \quad (2.13)$$

where $\dot{m}_{c,total}$ is the total mass flow rate through all coolant holes or the mass flow rate into the coolant plenum assuming no pressure rise in the plenum, $A_{c,total}$ is the total area of all coolant holes, A_{∞} is the cross-sectional area of the free stream fluid inlet and \dot{m}_{∞} is the mass flow rate of the free stream fluid.

The effect of M on η downstream of a cooling hole has been documented in many sources, several of which reference the research of Baldauf et al. [18]. Figure 2.7 shows the results obtain by Baldauf et al. for a cooling hole with an incidence angle of 30° to the surface for several blowing ratios.

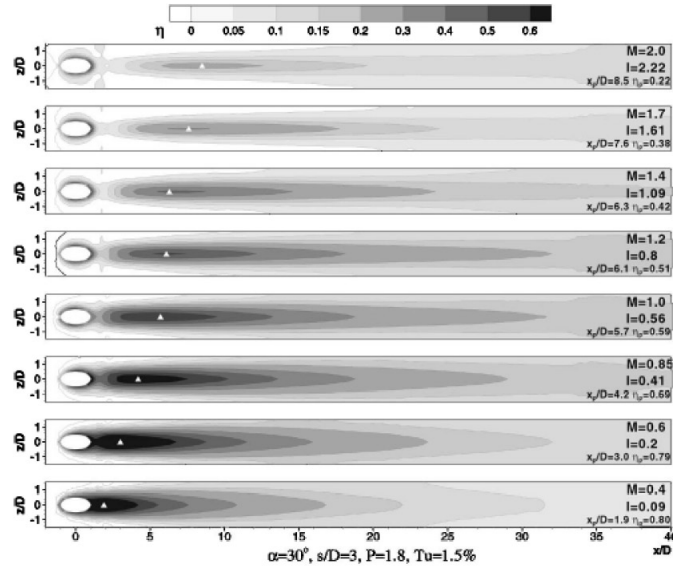


Figure 2.7: Spatial distribution of film cooling effectiveness at various blowing ratios [18]

Looking at Figure 2.7 it can be seen that the test cases with higher blowing ratios have a minimum effectiveness immediately after the coolant hole. The reduced

effectiveness surrounding the hole is likely due to the tendency for higher blowing ratio coolant jets to separate from the surface. In the cases shown in the figure that did separate ($M=1.2 - 2.0$), the flow appeared to reattach to some degree further downstream in the region with an increase in effectiveness. Based on the lack of dark gray regions with the higher blowing ratio test cases it is shown that higher blowing ratios have a reduced area averaged effectiveness due to separation. As the blowing ratio decreased, the region of peak effectiveness moved closer to the coolant hole with the effective length of the coolant jet also decreased.

The injection angle of the coolant flow also plays a role in the downstream effectiveness. Baldauf et al. [18] performed an additional study to compare the results of a 30° injection angle relative to the surface and coolant holes that were normal to the surface. The results shown in Figure 2.8 show that for low blowing ratios the angled holes achieved a significantly higher effectiveness across a larger area while at high blowing ratios the flow from both holes appeared to separate resulting in minimal effectiveness over the test area.

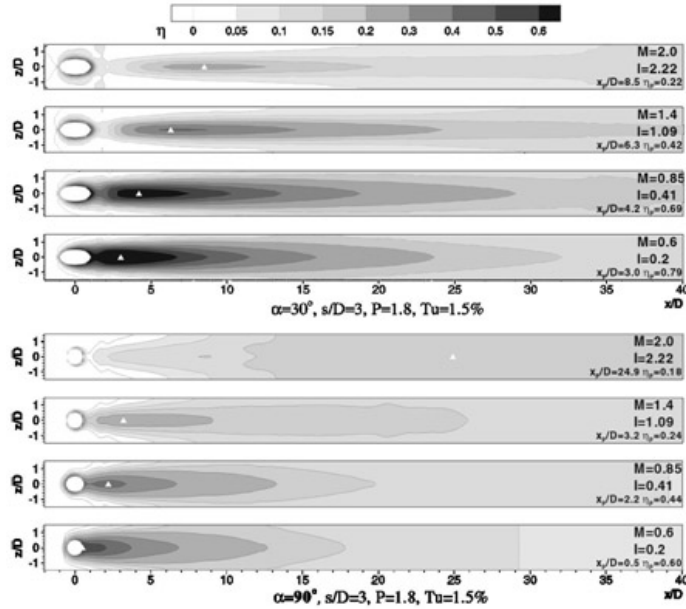


Figure 2.8: Effect of injection angle on film cooling effectiveness [18]

Shaped coolant holes offer improvements to film cooling effectiveness and the ability for the coolant to spread cross-wise after exiting the coolant hole. The three primary hole shapes are shown in Figure 2.9 and include cylindrical (normal or angled), fanshaped and laidback fanshaped.

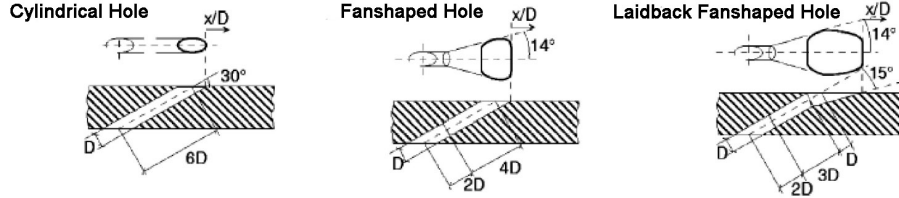


Figure 2.9: Three common coolant hole shapes [5]

The primary benefit to using a shaped hole over a cylindrical hole is that the velocity of the fluid is decreased at the exit of the hole due to the increase in area, and thus a higher blowing ratio can be pushed through a shaped hole while avoiding separation. Figure 2.10 shows how the effectiveness downstream of each hole type varies with increased blowing ratio as presented by Gritsch et al. [19].

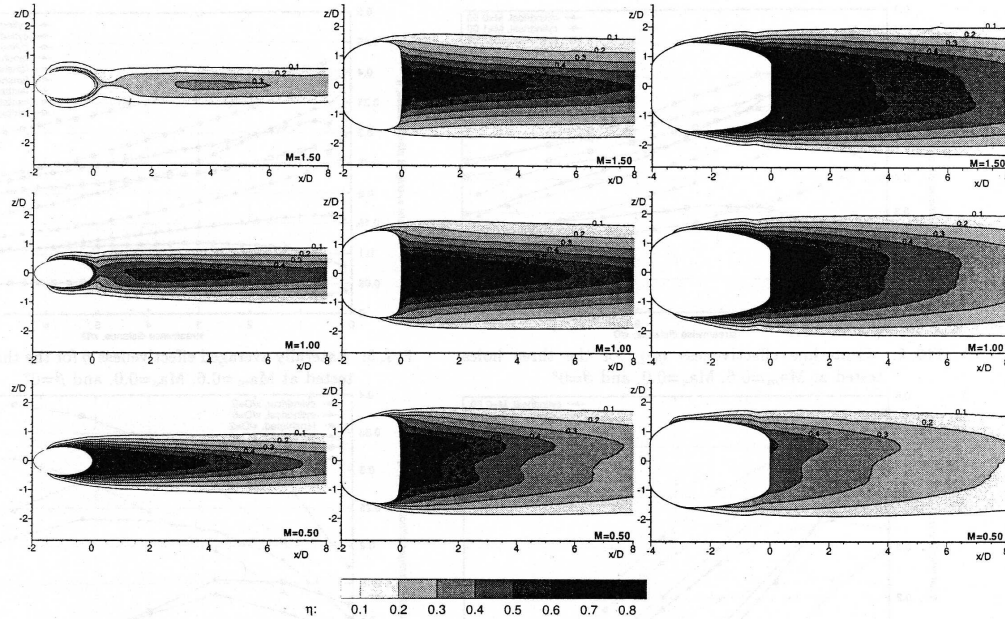


Figure 2.10: Local Effectiveness for cylindrical (left), fanshaped (center) and laid-back fanshaped (right) at three blowing ratios [19]

As expected, the shaped holes performed better than the cylindrical holes at higher blowing ratios and impacted a substantially larger surface area. The cylindrical hole had a higher effectiveness than the shaped holes at the $M=0.5$ blowing ratio while the shaped hole covered a larger area with a slightly reduced effectiveness. Figure 2.11 shows a comparison of spatially averaged film cooling effectiveness for cylindrical holes and fanshaped holes across a range of blowing ratios. This plot also highlights the impact free stream turbulence plays in the film cooling effectiveness. Higher free stream turbulence reduced the effectiveness of the cooling scheme due to the increased mixing of coolant with the free stream fluid. These results are also supported by Dittmar et al. [20].

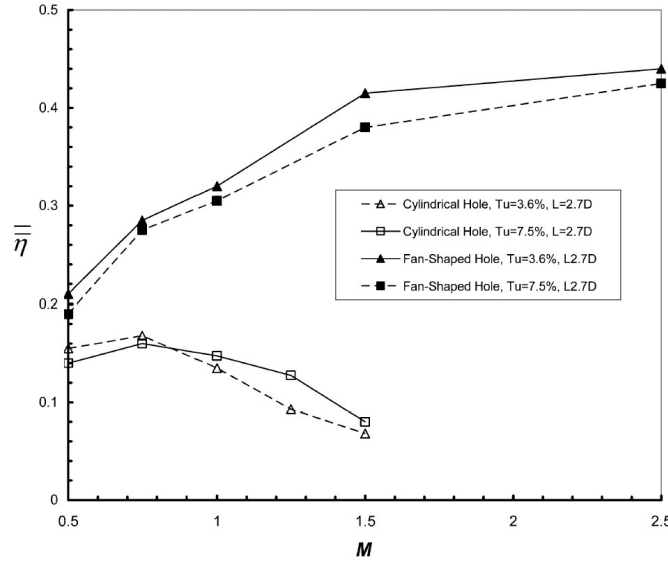


Figure 2.11: Comparison of spatially averaged film effectiveness of shaped holes and cylindrical holes for two turbulence levels and varied blowing ratios [5], [21]

The momentum flux, I , of the coolant film is an important factor in determining whether the coolant jet will separate from the component surface. In fact the momentum flux is a better indicator that separation will occur than the blowing ratio. Equation 2.14 shows the relationship of I .

$$I = \frac{\rho_c U_c^2}{\rho_\infty U_\infty^2} \quad (2.14)$$

The determination of whether separation will occur is based on how forcefully the coolant ejects from the coolant hole relative to how forcefully the free stream flow can push the coolant jet downstream and turn it into the wall. The coolant jet separates for $I > 0.8$, remains attached for $I < 0.4$ and initially separates then reattaches downstream for $0.4 < I < 0.8$ [5]. Figure 2.12 shows results presented by Thole et al. [22] of thermal profiles along the centerline of a coolant hole for a situation where the coolant remains attached (a), coolant detached then reattached (b) and fully separated (c) from the wall.

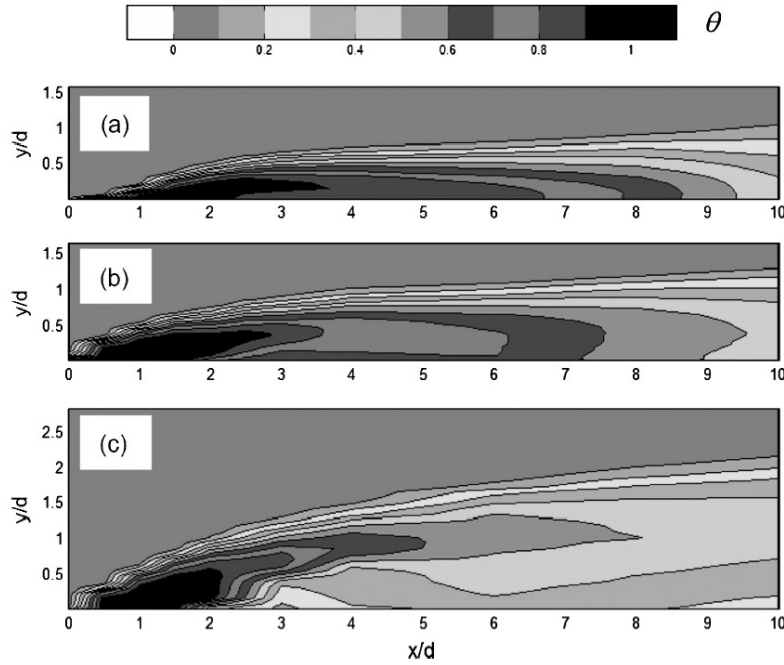


Figure 2.12: Thermal profiles along coolant hole centerline for (a) attached, (b) detached then reattached and (c) fully separated coolant flow [22]

In Figure 2.12, θ is the normalized temperature defined by:

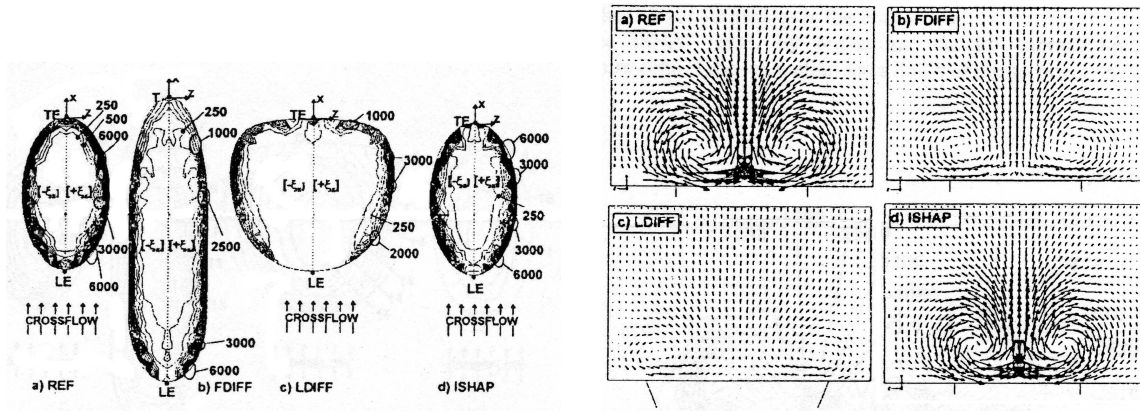
$$\theta = \frac{(T_{\infty} - T)}{(T_{\infty} - T_c)} \quad (2.15)$$

Teekaram et al. [23] and Liess [24] both performed studies into the effect of pressure gradients on film cooling. Both papers agree that there is a negligible impact on

film cooling due to weak pressure gradients. The papers also discuss a decreased heat transfer coefficient and increased film cooling effectiveness in the presence of accelerated flow due to strong favorable pressure gradients. In the case of the UCC there is a small pressure drop across the entire combustion section and a weak favorable gradient on the suction surface of the turbine vane.

The series of papers by Leylek's group at Clemson [25], [26], [27] and [28] provide a detailed investigation of CFD modeling of non-reacting film cooling schemes including discrete-jet film cooling, streamwise injection with cylindrical holes, compound-angle injection with cylindrical holes and streamwise injection with shaped holes, respectively.

The study of discrete-jet film cooling [25] found that the flow inside a film cooling hole is very complex and contains counter-rotating vortices and jetting effects. The strength of the vortical structures and jet effects were controlled by the cooling hole length-to-diameter ratio, blowing ratio and injection angle. The other three papers on the subject all performed similar experiments applied to different cooling schemes and provided the corresponding results. A review of all three papers allowed the differences between the different cooling schemes to be observed. One finding was that regardless of the cooling hole orientation and shape, all schemes produced a pair of counter-rotating vortices on the component surface starting at the coolant hole exit and sweeping downstream. The strength of the vortices varied based on the geometry of the holes. Figure 2.13a shows the vorticity at the exit plane for four different shaped holes while 2.13b shows the corresponding velocity vectors at a distance of $x/D = 2$ downstream from the hole. The secondary flow vortical structures for the cylindrical film hole used as a reference (REF) and the ISHAP case were clearly the strongest while the elongated (FDIFF) and wide (LDIFF) holes had significantly reduced vortex strength.



(a) Vorticity at coolant hole exit plane

(b) Velocity vectors at $x/D = 2$

Figure 2.13: Coolant hole exit plane vorticity and corresponding velocity vectors highlighting secondary flows [28]

2.4.3 Slot Cooling. Based on the work of Hartnett et al. [29], among others, it has been shown that in almost all cases a large continuous slot yields higher film cooling effectiveness levels over a much larger area than those achieved by discrete cooling holes. The problem with slot cooling is that the size of the slot itself leaves the component to be cooled structurally unsound. Under the temperatures and pressures of modern engines, if a slot were to become unstable and warp, the cooling slot could ingest hot gases rather than eject coolant.

In his 2002 paper, Bunker [30], tested two holes-in-slot configurations and compared the results to an array of standard cooling holes ejecting fluid directly to the surface rather than into a trench, see Figure 2.14. The holes-in-slot geometry appear to gain several benefits similar to slot cooling while not degrading the structural integrity of the component like a standard slot.

Bunker found that a narrow slot, just slightly larger than the inlet holes, achieved the best results. Combining this geometry with a shallow trench, less than half the hole diameter, achieved increases in film cooling effectiveness of 50 - 75% compared to a discrete hole scheme. The shallow trench results are shown in Figure 2.15. He also found that there was virtually no variation in the results over the blow-

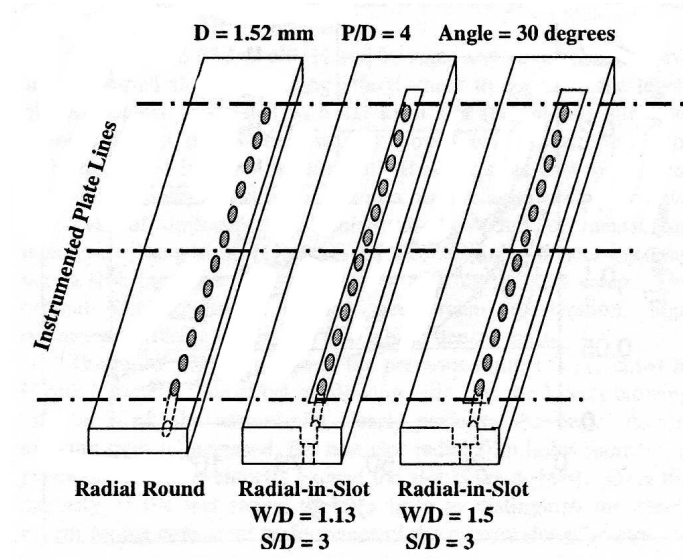


Figure 2.14: Radial Film Hole Geometries [30]

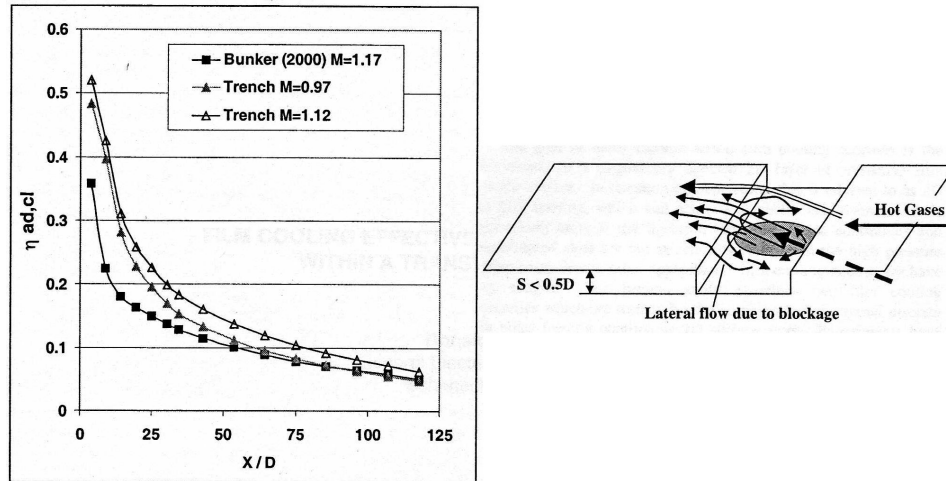


Figure 2.15: Shallow Trench Geometry and Results [30]

ing ratio range 1 - 4. Using this scheme could offer the possibility for coolant savings compared to a discrete hole scheme and significant savings compared to a standard slot scheme.

The current film cooling analysis discussed in this report included a standard slot cooling scheme. Due to manufacturing times and availability of experimental test resources, the holes-in-slot geometry could not be tested.

2.5 Heat Transfer and Surface Temperature Calculations

In the experimental testing conducted by Evans [8], the surface temperature of the test rig flat plate and the heat flux to the flat plate surface were determined using temperature measurements from two thermocouples embedded at different depths in a heat transfer gauge that mounts flush with the flat plate. Applying Fourier's Law and assuming one-dimensional heat transfer, the heat transfer between the thermocouples can be found. Equation 2.16 shows Fourier's Law where k is the thermal conductivity of the conducting medium, T is the temperature at known locations and x is the distance from a reference location [31].

$$q_x'' = -k \frac{dT}{dx} \quad (2.16)$$

For steady-state conditions the value of q_x'' is constant allowing Equation 2.16 to be rearranged and integrated as shown in Equation 2.17.

$$\int q_x'' dx = - \int k dT \quad (2.17)$$

The heat transfer gauges are made from Hastelloy-X[®]. From the experiments of Evans [8], the temperatures in the gauge material range from 450K at the deeply embedded thermocouple, 1.9 cm from the surface of the flat plate, to 850K near the surface. Within this range the thermal conductivity of the Hastelloy-X[®] varies significantly. The manufacturer, Haynes International, provided the thermal conductivity in a product data sheet summarized in Table 2.1. Using the provided data a linear least squares fit can be found for the variation of thermal conductivity over the given temperature range as shown in Figure 2.16.

From the linear least squares fit, the value of k can be written as show in Equation 2.18 where a_0 and a_1 are constants from the least squares analysis of the thermal conductivity of Hastelloy-X[®].

Table 2.1: Summary of Thermal Conductivity of Hastelloy-X[®] [32]

Temperature (K)	k (W/m-K)
366.5	11.0
533.2	14.1
866.5	20.8
977.6	22.9

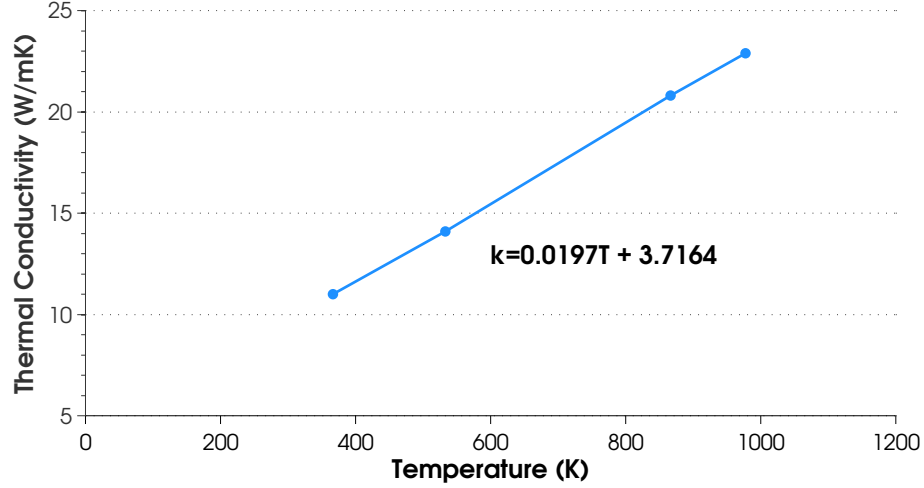


Figure 2.16: Least squares linear fit of thermal conductivity of Hastelloy-X[®]

$$k(T) = a_0 + a_1T \quad (2.18)$$

Following the derivation in [8], Equation 2.18 can be substituted into (2.17) and integrated.

$$\int q_x'' dx = - \int (a_0 + a_1T) dT \quad (2.19)$$

$$q_x''x - C = - \left(a_0T + a_1 \frac{T^2}{2} \right) \quad (2.20)$$

$$\frac{a_1T^2}{2} + a_0T + q_x''x - C = 0 \quad (2.21)$$

In the above equations C is the constant of integration. Since there are two thermocouples in the heat transfer gauge, two temperatures are known and two equations can be written to solve for C .

$$\frac{a_1 T_1^2}{2} + a_0 T_1 + q_x'' x_1 - C = 0 \quad (2.22)$$

$$\frac{a_1 T_2^2}{2} + a_0 T_2 + q_x'' x_2 - C = 0 \quad (2.23)$$

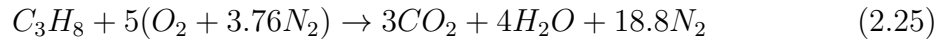
By setting (2.22) equal to (2.23) the value of q_x'' can be solved. Equation 2.24 shows the value of the heat flux per unit area.

$$q_x'' = \frac{\frac{a_1}{2}(T_1^2 - T_2^2) + a_0(T_1 - T_2)}{(x_2 - x_1)} \quad (2.24)$$

The value of C can be found by substituting the value of q_x'' back into Equation 2.22 or 2.23. When the values of q_x'' and C are known, the surface temperature can be calculated using equation 2.21 by setting $x=0$ and solving for T .

2.6 Calculation of Stoichiometric Fuel-to-Air and Equivalence Ratios

In the test rig used by Evans [8], propane was used as fuel in a well stirred reactor, WSR, to test the performance of film cooling schemes in a fuel rich environment. Turns [33], provides the global reaction for propane-air combustion presented as Equation 2.25.



The equivalence ratio, Φ , is used to determine quantitatively whether a combustion condition is rich ($\Phi > 1$), lean ($\Phi < 1$) or stoichiometric ($\Phi = 1$). The equivalence ratio is defined as the ratio of the fuel-to-air ratio at a given condition relative to the stoichiometric fuel-to-air ratio. This relationship is better shown in equation form as

Equation 2.26

$$\Phi = \frac{\left(\frac{\dot{m}_{fuel}}{\dot{m}_{air}}\right)}{\left(\frac{\dot{m}_{fuel}}{\dot{m}_{air}}\right)_{stoic}} \quad (2.26)$$

In Equation 2.26, \dot{m}_{fuel} is the mass flow rate of propane (fuel) and \dot{m}_{air} is the mass flow rate of air (oxidizer). The stoichiometric fuel-to-air ratio can be found using the number of moles of fuel and oxidizer on the left-hand side of Equation 2.25 since the global reaction is written to stoichiometric conditions. The stoichiometric values are shown in Equation 2.27 where MW is the molecular weight.

$$\left(\frac{\dot{m}_{fuel}}{\dot{m}_{air}}\right)_{stoic} = \frac{1 \times MW_{C_3H_8}}{5 \times (4.76 \times MW_{air})} = 0.06395 \quad (2.27)$$

2.7 *Experimental Analysis of Film Cooling*

The effect of heat release in cooling films due to secondary combustion was studied experimentally in [8], [34] and [35] all using the same test rig. The test rig, described in detail by Evans [8], used a WSR whose exhaust flowed over an instrumented flat plate. The flat plate contained two ports for interchangeable film cooling inserts where each insert featured a different cooling hole shape. The previous studies tested several cooling hole shapes for a number of blowing ratios, equivalence ratios and using nitrogen and air for the coolant gases. Figure 2.17 shows the test rig and an enlarged view of the film cooling inserts.

The three previous studies report that the magnitude of the heat release due to combustion in the cooling film was controlled by the amount of fuel in the exhaust, the blowing ratio of the cooling scheme and the geometry of the cooling hole. These studies also found that there was no heat release in the cooling film for main stream fuel-to-air ratios less than stoichiometric [34]. Polanka et al [34] also reported that the fanshaped hole provided the expected adiabatic effectiveness for all non-reacting flows, however, when fuel streaks were present in the exhaust stream this cooling hole

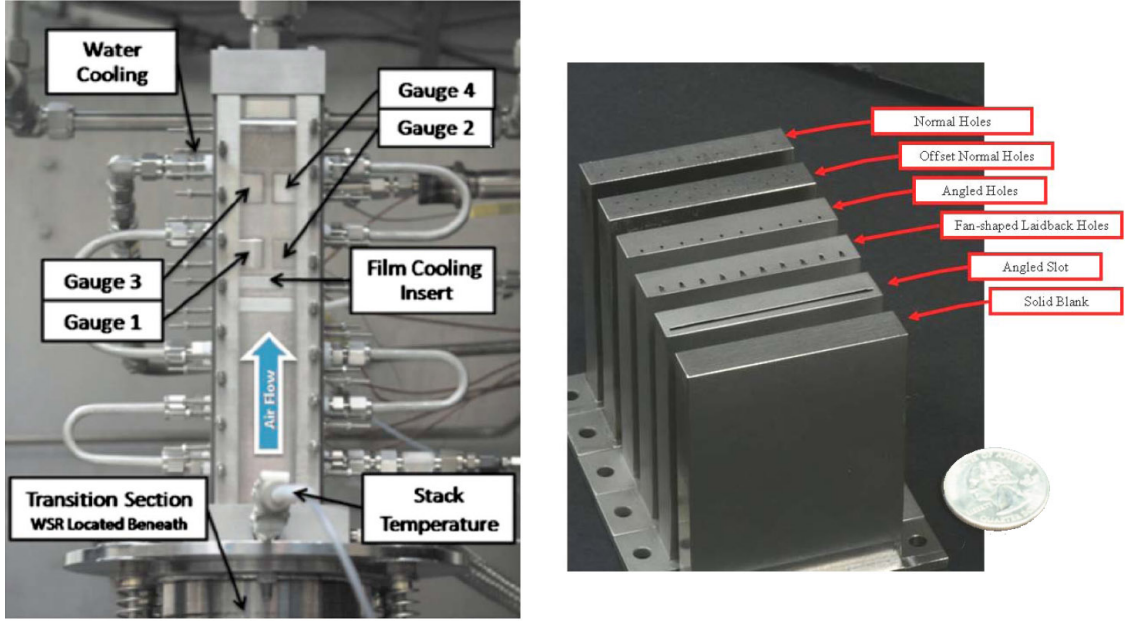


Figure 2.17: Previous research test rig (left) [35] and film cooling inserts (right) [8]

shape had the largest area of negative effectiveness of all the shapes tested for the same blowing ratios. The negative effectiveness was due to a secondary combustion of the exhaust fuel streaks reacting with the cooling air resulting in an increased heat transfer rate to the surface. Figure 2.18 shows a secondary combustion for an equivalence ratio of 1.5 using an angled cooling hole and blowing ratios of 0.5, 1.0 and 1.5. As expected the secondary combustion only occurred when air was used as the cooling gas since nitrogen is inert. As the blowing ratio was increased, the length of the flame caused by secondary combustion was also increased.

The plots in Figure 2.19 confirm that there was no heat release in the cooling film for equivalence ratios less than 1.0 as the nitrogen and air coolants produced seemingly identical heat flux results. For an equivalence ratio of 1.5, the nitrogen and air coolants produced very different results with the air coolant yielding a higher heat flux for all blowing ratios and all hole shapes. The difference in heat flux between the nitrogen and air coolants was a minimum for the normal coolant holes meaning that there was less of an impact on the surface due to the secondary combustion.

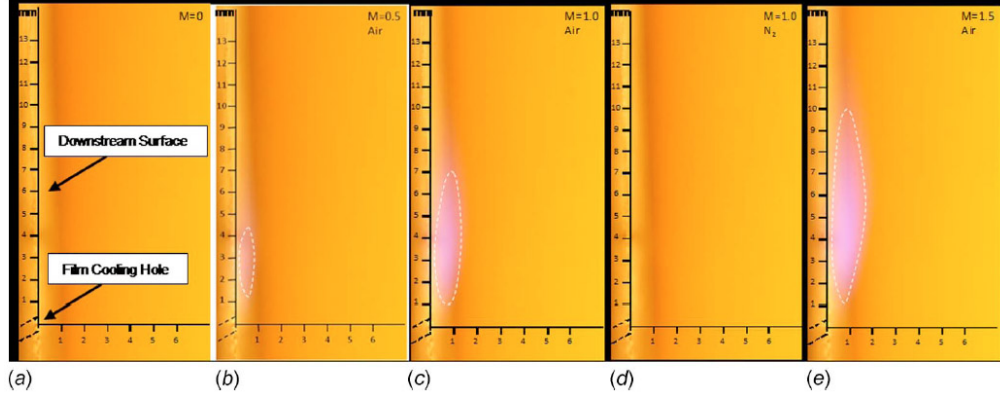


Figure 2.18: Angled hole visible burning for (a) $M=0$, (b) $M=0.5$, air, (c) $M=1.0$, air, (d) $M=1.0$, N_2 , and (e) $M=1.5$, air [35]

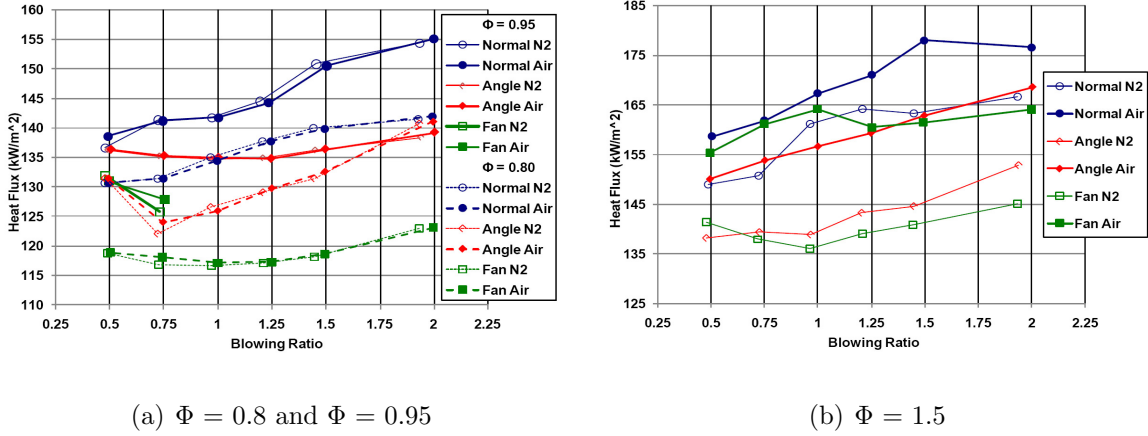


Figure 2.19: Graphical relationship of blowing ratio to heat flux for three equivalence ratios at $x/D = 20$ [34]

Polanka et al. [34] included a companion CFD study to their experimental data which examined the secondary combustion process of fuel streaks reacting with film cooling air. Lin et al. [36] was an in-depth follow-on study to [34] that was strictly CFD based. Both studies used three-dimensional geometry, $k-\omega$ SST turbulence models and a two-step propane reaction model. In these studies, no flow stagnation would occur so the $k-\omega$ SST turbulence model was a good choice since this model performs very well for wall bounded flows. The turbulence-chemistry interaction was handled through the use of the eddy-dissipation-concept, EDC, which is an extension of the

eddy-dissipation model capable of handling multi-step reactions in turbulent flows. The EDC makes the assumption that reactions occur in small turbulent structures over a given time scale where the time scale is proportional to the square root of the kinetic viscosity over the dissipation rate. Three coolant hole geometries were studied including normal holes, angled holes and fanshaped holes. Both studies found that for equivalence ratios below 1.0, no secondary combustion occurred. Lin et al. [36] presented a vector flowfield for the flow pattern above and downstream of the cooling hole for a blowing ratio of 1.0 shown in Figure 2.20. Like the results shown in Figure 2.13b, the flow pattern obtain by Lin et al. showed a pair of counter-rotating vortices originating from the fluid ejection from the hole and dissipating as they traveled downstream.

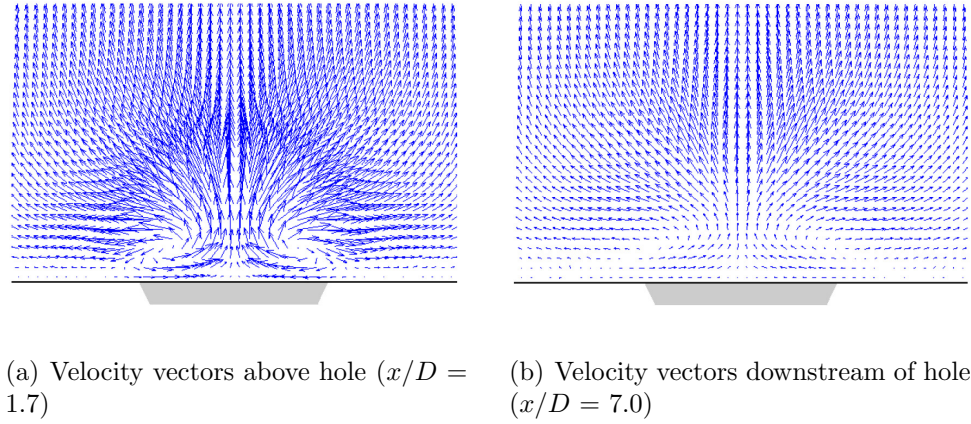


Figure 2.20: Velocity vectors above and downstream of cooling hole highlighting secondary flow structure [36]

One significant benefit to CFD is the ability to create visualizations of any parameter of interest from any angle. The images of secondary combustion from previous experimental testing like those shown in Figure 2.18 were reported to be difficult to capture and do not quantify the resulting temperatures of combustion. The CFD visualization shown in Figure 2.21 clearly shows the combustion temperatures achieved in the secondary reactions as well as the negative cooling effectiveness for the air coolant cases for a main stream equivalence ratio of 1.5 and a coolant blowing ratio

of 1.0. These CFD results from Polanka et al. [34] confirm their experimental data in that the fanshaped cooling hole did produce the largest region of high temperature combustion and negative effectiveness compared to the other two hole shapes.

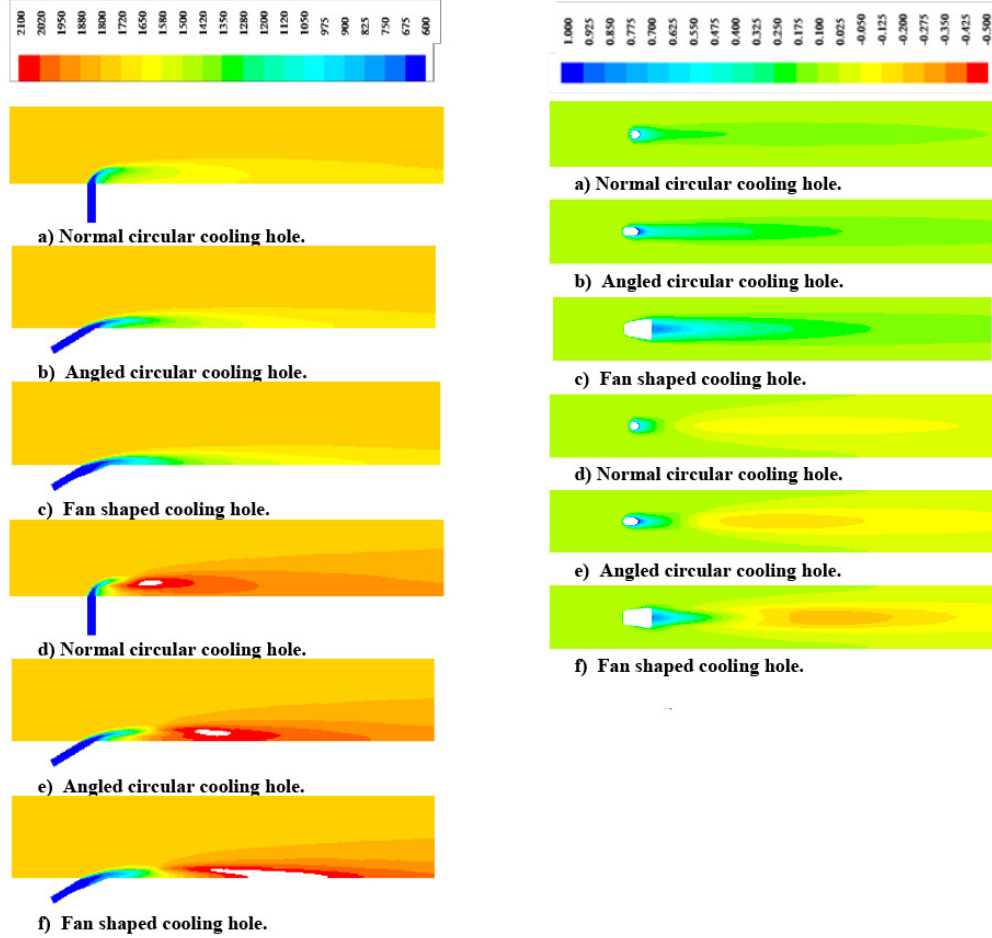


Figure 2.21: Temperature contours (left) and cooling effectiveness (right) for $\Phi = 1.5$ and $M = 1.0$. a-c) N_2 injection d-f) air injection [34]

2.8 Limitations of Previous Research

All the previously mentioned papers related to the UCC covered experimental and numerical analysis of small scale systems with a cavity radius on the order of 5.5 centimeters. To date, there are no know papers related to UCC analysis for a fighter scale engine. For this reason information related to the UCC design and g-loaded combustion were gathered from the previously mentioned sources and used as

a starting place for a fighter scale analysis. The generation of the UCC geometry used in the current study is discussed in the next chapter. While there was no information directly related to fighter scale UCC analysis, studies related to numerical analysis of turbines and reacting flows would prove useful in the numerical setup of the current study.

The previous experimental testing discussed in Section 2.7 regarding secondary reactions in cooling films did not test the slot or offset normal hole inserts. Additionally, only one cooling scheme was tested at a time using the downstream insert location with the upstream bay filled by the solid blank insert. These studies did not determine the impact combining cooling schemes could have on the formation or mitigation of secondary reactions.

III. UCC Numerical Analysis Methodology

This chapter discusses the test methodology of the numerical analysis on the UCC system. A numerical analysis was used to characterize the flow conditions in the UCC test section over a wide range of flow and geometry variations for increasing levels of computational complexity.

3.1 *UCC Geometry*

A traditional combustor section of a fighter-scale engine features a compressor exit guide vane to turn the flow axial prior to entering the combustor, and a turbine inlet guide vane at the exit of the combustor to provide fluid at the correct angle to the first turbine stage. In a UCC, the compressor exit guide vane and the turbine IGV are combined into a single vane located directly below the UCC cavity. Figure 3.1 shows the orientation and dimension of components in the ultra-compact combustor tested in this study. The combustor section inlet is on the left of Figure 3.1 with the combustion products exiting to the right. The inlet and exit dimensions were sized to nominal fighter scale engine dimensions for the compressor exit and the turbine inlet passages, respectively. The inner radius of the passage at the exit was 31.75 centimeters with an outer radius of 38.1 centimeters. The passage expansion was performed at a shallow 7° angle per wall to prevent separation due to the adverse pressure gradient resulting from the diffusion. A single test was conducted in the preliminary analysis that used a 3.81 centimeter circumferential cavity in place of the 4.83 centimeter dimensions. The results of this test are shown in Chapter 4, but no further discussion of this configuration will be made since the remaining dimensions are consistent with Figure 3.1 and only one test was conducted.

For the current study, two UCC turbine vane designs were used. The first design was a ‘typical’ turbine vane design that assumed the flow entering the combustor section exited the compressor axially. This vane turned the axial flow 70° with a Zweifel load coefficient of 0.80 to match a representative turbine inlet angle. The Zweifel load coefficient was calculated using the definition presented by Baskharone [37] shown in

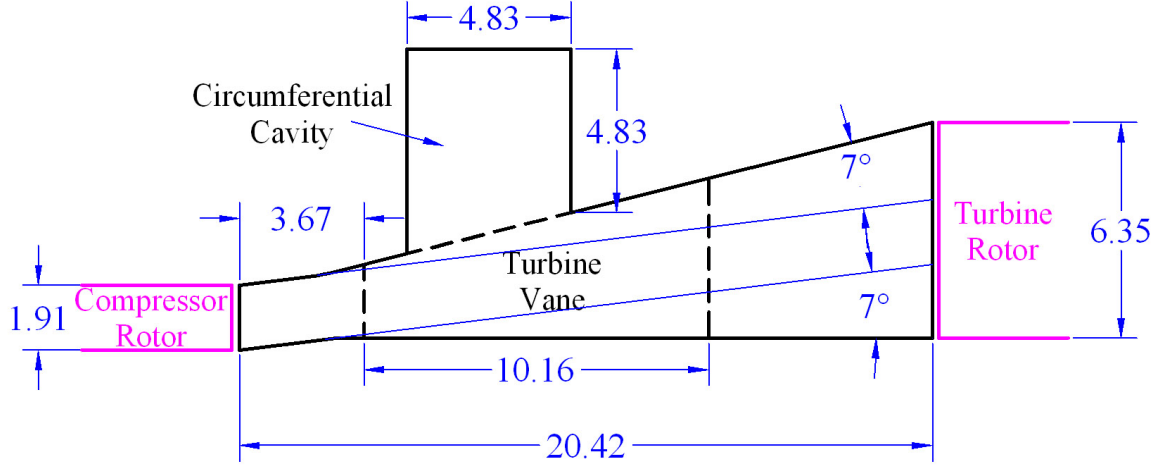


Figure 3.1: Cross-sectional view of UCC section used in the current analysis (cm)

Equation 3.1.

$$Z = 2 \frac{b}{s} \cos^2 \beta_2 (\tan \beta_1 - \tan \beta_2) \quad (3.1)$$

In Equation 3.1, s is the vane spacing, b is the vane chord, β_1 is the vane inlet angle and β_2 is the vane exit angle. A compressor exit guide vane would be required to achieve axial flow into the combustor section, however, this vane was used to compare to previous small scale UCC testing which used a similar vane design. The 10.16 centimeter axial chord of the vane was longer than a typical turbine vane to allow the vane to establish the flow turning prior to the UCC cavity. The cavity could then introduce the hot gases prior to the vane throat. Furthermore, the combination of the vane turning and flowpath expansion was anticipated to further disperse the hot gases. The resulting chord of this vane was 12.03 centimeters. To study the effects of vane solidity on the interaction of the fluid in the circumferential cavity with the core flow, the number of vanes arrayed around the annulus was varied. The orientation and thickness of this vane allowed for up to 60 vanes to fit without overlap or sonic conditions in the vane passages.

The second vane studied was a composite of a representative compressor exit guide vane and turbine IGV. With the compressor exit guide vane removed, this ‘hybrid’ vane allowed the fluid exiting the compressor to maintain its swirl as it entered

the UCC section. The fluid was then turned slightly more in the circumferential direction to match the same representative turbine inlet angle as the typical vane. The hybrid vane only required 16° of turning and had a Zweifel load coefficient of 0.70. Figure 3.2 shows the development of the hybrid vane shape. The axial chord of this vane was also set at 10.16 centimeters, however, due to the steep angle of the vane, the chord length was 21.07 centimeters. The maximum vane thickness was 2.07 centimeters to enable internal cooling passages to be added in the airfoil at a later date. Due to the orientation and thickness of the hybrid vane, metallic blockage of the core flow and overlap occurred if the number of vanes was increased beyond 30. The typical vane and the hybrid vane are shown in Figure 3.3 relative to the UCC circumferential cavity. The leading edge of both vanes was positioned upstream of the circumferential cavity to introduce the hot gases from the cavity prior to the throat of the vane passage to aid in mixing with the core flow. The circumferential cavity was positioned upstream in the diffuser to allow fluid exiting the cavity to more easily span a shorter radial distance and to provided the greatest length for mixing of the core flow with the hot cavity flow.

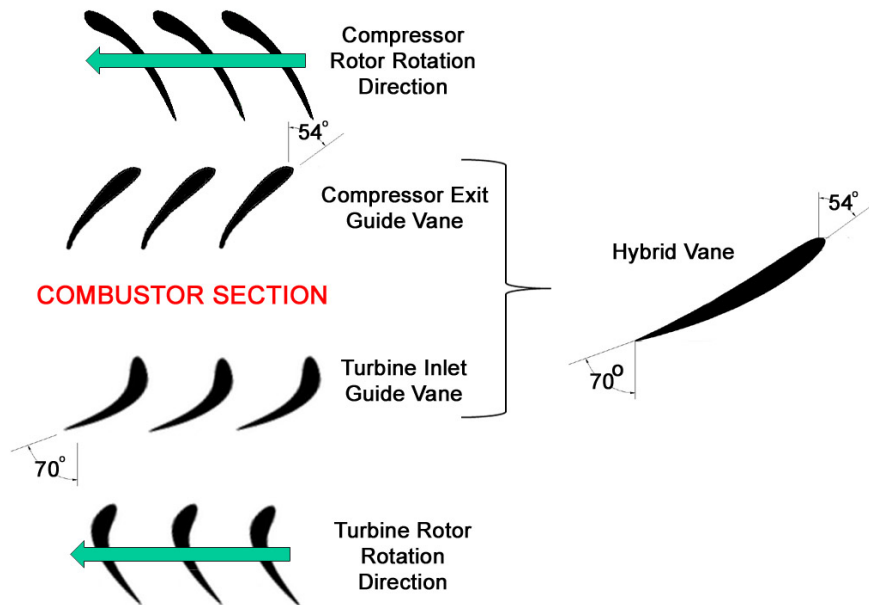


Figure 3.2: Origin of the hybrid vane design

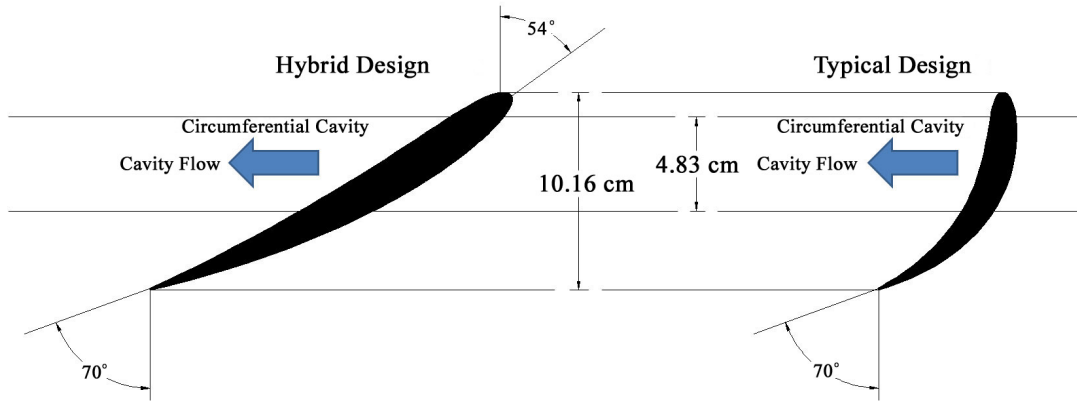


Figure 3.3: UCC turbine vane designs tested

3.2 CFD Solver Settings

There are a number of CFD codes in existence today, many of which are designed for very specific research applications or flow regimes. The current study takes advantage of the commercially available FLUENT[®] 6.3 code which is capable of parallel processing while modeling three-dimensional internal flows, combustion, turbulence, heat transfer and easily exporting data to a post-processing package such as TecPlot 360[®] or FieldView[®] for creating visualizations. All test configurations discussed later used a three-dimensional, node centered, steady-state, pressure-based solver with a RANS turbulence model. The SIMPLE algorithm was selected for pressure-velocity coupling which uses a relationship that enforces mass conservation and establishes the pressure field within the domain. All solutions presented in Chapter 4 were run with second-order accuracy for momentum, density, energy and species where applicable. Turbulent production and dissipation along with pressure were kept first-order to aid computational speed and stability. A single unstructured block resolved the domain volume. All mesh generation was performed in Gridgen[®] and exported for use in FLUENT[®]. For numerical stability, the test cases could be started at the final desired settings and order of accuracy. The starting sequence for each level of analysis discussed in this chapter is shown in Appendix A.

3.3 Secondary Flow Study (Turbulence Model Selection)

With the anticipation that secondary flows could have a substantial impact within the UCC section, specifically from horseshoe and passage vortices, a simplified study was conducted. This study ensured the computational grid resolution that would be used in the analysis was sufficient to capture the secondary flows and that the turbulence model selected was capable of capturing the desired flow structures prior to creating computational domains of the full UCC test sections. This study was performed without the presence of the circumferential cavity and strictly modeled the flow around the hybrid vane using the designed entrance length of 3.67 centimeters between the last compressor rotor (entrance to the combustor section) and the leading edge of the UCC turbine vane as shown in Figure 3.1. Following the findings of Hermanson and Thole [13], the RNG $k - \epsilon$ turbulence model was selected for the secondary flow study for the models' ability to handle stagnation flows and conditions with high streamline curvature.

The secondary flow study used the computational domain shown in Figure 3.4, which represents a simplified combustor passage section with the vane spacing based on 20 vanes arrayed around the UCC annulus. The mass flow rate through the passage was set to 2.5 kg/s which represents 1/20 of a nominal total engine core mass flow rate of 50 kg/s with an engine representative operating pressure of 4.6 MPa. This test was conducted with two grid configurations. The first used an unstructured lower

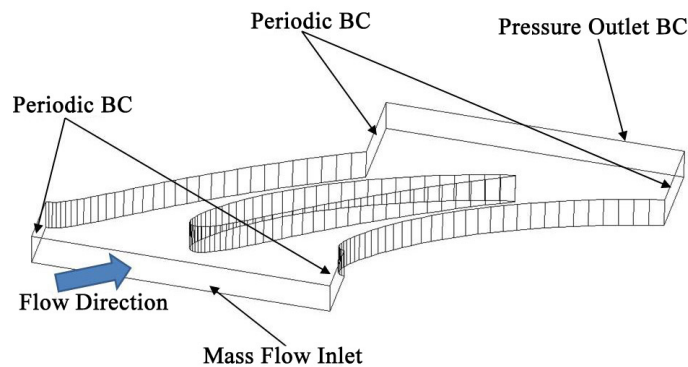


Figure 3.4: Secondary flow test domain

wall mesh that was extruded into a structured volume. The initial cell spacing was adjusted to achieve a wall y^+ value between 30 and 60. The second configuration used an unstructured volume mesh generated from the same wall meshes used in the first configuration. The volume grid boundary decay was adjusted to set the wall y^+ values in the domain between 30 and 60. The same solver settings were used as discussed in Section 3.2.

In both test cases a sufficient boundary layer was established to form a horseshoe and passage vortex around the vane as shown in Figure 3.5. However, due to the short entrance length, the vortex structures were weak and dissipated quickly rather than grow through the passage. This study did conclude that the RNG $k - \epsilon$ turbulence model combined with the tested unstructured grid resolution was capable of generating secondary flow structures identical to the results obtained using the structured volume grid. The RNG $k - \epsilon$ turbulence model was used for all remaining analysis documented in this report. Additionally, it was shown that due to the short entrance length producing weak vortex structures, the effect of the secondary flows would not be as large as originally anticipated.

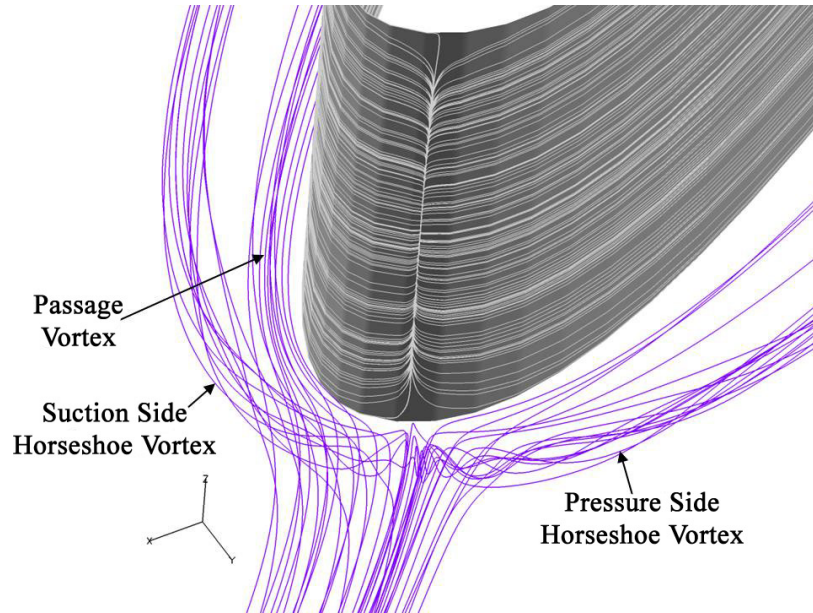


Figure 3.5: Resulting horseshoe and passage vortices with surface trace on the vane surface

3.4 Computational Domain

The UCC computational domain consisted of a single vane extracted from the complete three-dimensional UCC section. Figure 3.6 shows the domain highlighted from the full annulus, shown here for the 20 hybrid vane array. Computational domains were created for the typical vane featuring 20-vanes, 30-vanes, 45-vanes and 60-vanes arrayed around the complete UCC annulus. A 20- and 30-vane domain was also created for the hybrid vane. A 0-vane domain was created using the 30 hybrid vane domain with the vane removed, making a total of 7 domains. The 0-vane domain was used twice, once with an axial core flow input as with the typical vane and again with a 54° inlet angle comparable to the hybrid vane. As the number of turbine vanes arrayed around the complete annulus was increased, the width of the computational domain was decreased to maintain only one vane in the domain, as shown in Figure 3.7. The use of rotationally periodic boundaries allowed only a single vane section to be computed while including the effects of having the remaining vanes in the complete circular array. Figure 3.7 shows the locations of the periodic surfaces along with the other boundary conditions, all non-labeled boundaries were walls. A 3-axis reference frame is also shown in each domain with the z-axis representing the axial direction of the engine. All domains used an unstructured volume mesh with a combination of structured and unstructured meshes along the walls and inlets. The vane surface and the walls of cylindrical inlet ports were gridded with a structured mesh to reduce faceting while the remainder of the surfaces were meshed with an unstructured grid.

The specifications of the vane spacing, throat width and axial solidity (σ) as defined by Equation 3.2 [38] are shown in Table 3.1 for each of the cases represented in Figure 3.7. In Equation 3.2, c is the chord and s is the vane spacing.

$$\sigma = \frac{c}{s} \quad (3.2)$$

In both 20-vane domains and the 0-vane domain, a total of 80 pairs of air injector ports were used, this resulted in 8 ports per domain. It was anticipated that

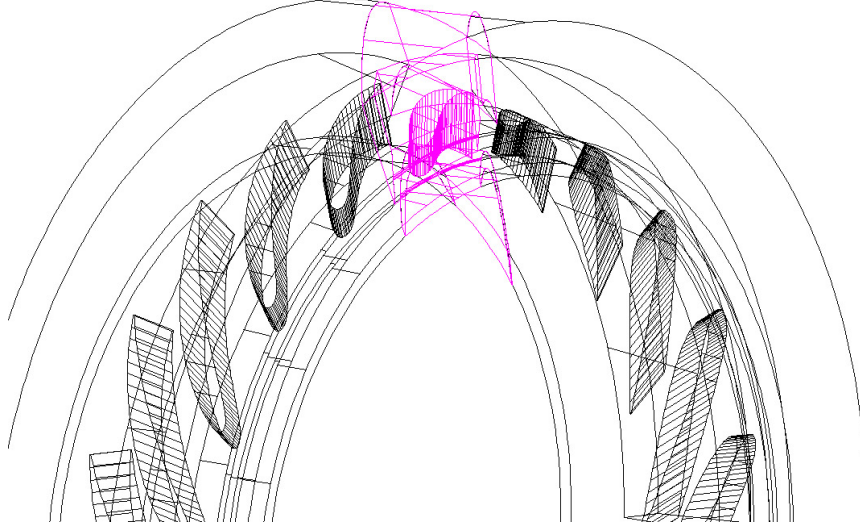
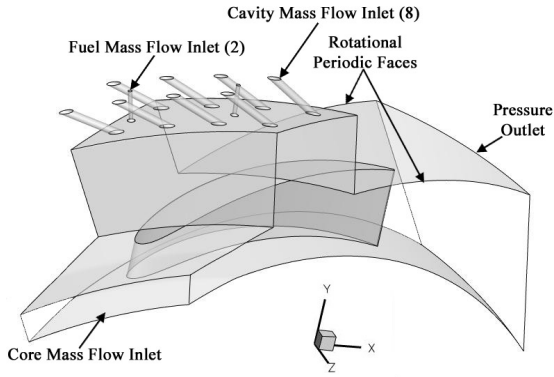


Figure 3.6: Computational domain relative to full array

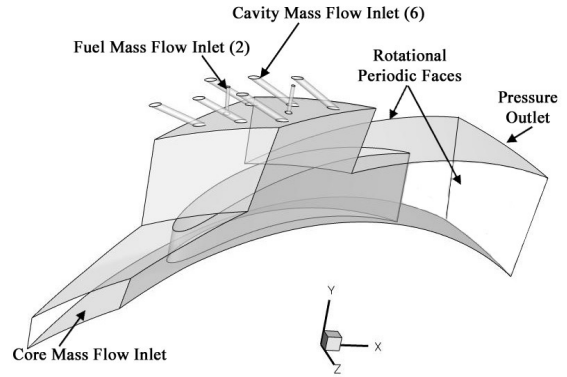
Table 3.1: Vane spacing, throat width and axial solidity for all test configurations

Vane Count	Vane Style	Vane Spacing	Throat Width	Axial Solidity
20	Hybrid	10.0 cm	2.82 cm	2.09
30	Hybrid	6.65 cm	1.34 cm	3.11
20	Typical	10.0 cm	5.50 cm	1.19
30	Typical	6.65 cm	3.10 cm	1.78
45	Typical	4.43 cm	1.77 cm	2.67
60	Typical	3.32 cm	1.20 cm	3.62

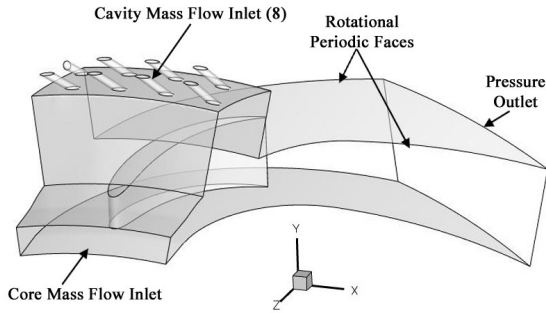
at least 40 fuel injectors would be needed for the system to meet the fuel mass flow requirements for a fighter scale engine. The fuel injectors were centered on the OD wall of the circumferential cavity to allow for a 90° spray angle while maximizing the distance to either wall. For adequate mixing of the fuel and air in the circumferential cavity, four air injectors were positioned around each fuel injector. For comparison purposes, the number of air injection ports in the remaining domains were adjusted to maintain as close to 80 pairs of air inlet ports as possible around the complete UCC annulus without having partial holes in individual domains. The 30-vane and 45-vane configurations required 90 pairs of injector ports while the 60-vane configuration could only fit 60 pairs of ports. All ports injected air into the circumferential cavity at 35°



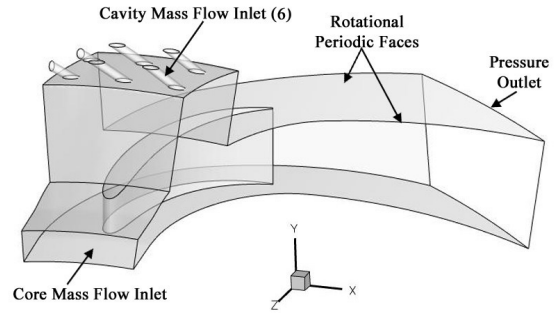
(a) 20 hybrid vane domain



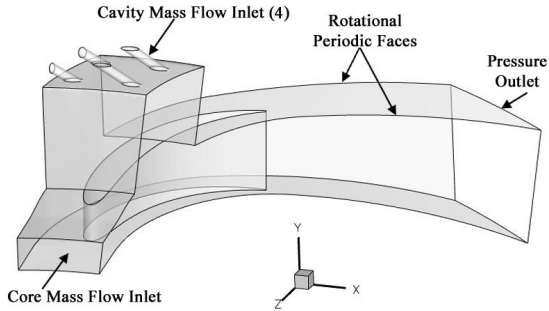
(b) 30 hybrid vane domain



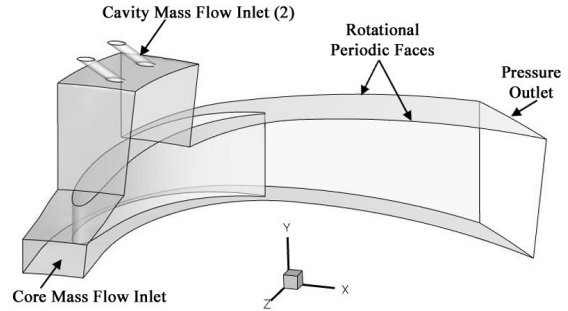
(c) 20 typical vane domain



(d) 30 typical vane domain



(e) 45 typical vane domain



(f) 60 typical vane domain

Figure 3.7: Computational domains

relative to the tangent of the cavity. Table 3.2 shows the port spacings and total number of ports for each domain tested. Simple math proves that it is not possible to have 80 inlet ports and 90 inlet ports arrayed around the same diameter engine

and achieve the same spacing as Table 3.2 shows for the 20 and 45-vane domains. The 20-vane domain maintained constant spacing around the full annulus while the 45-vane domain maintained uniform spacing of the inlet ports within the domain but required a smaller spacing between domains. The 30 and 60-vane configurations were able to maintain uniform spacing around the full annulus. In addition to the 20 hybrid vane domain, only the 30 hybrid-vane domain was used in reacting flow simulations where the fuel injectors would be used. As with the 20-vane configuration, two fuel injectors were used per domain and spaced such that equal spacing would be maintained around the complete array. This spacing pattern did not result in the uniform pattern obtained with the 20-vane domain. The position of the fuel injectors relative to the air inlet ports for the 20 hybrid vane and 30 hybrid vane domains is shown in Figure 3.8.

Table 3.2: Circumferential cavity fuel and air inlet specifications per test section

Parameter	0-Vane	20-Vane	30-Vane	45-Vane	60-Vane
Number of Air Ports	6	8	6	4	2
Air Inlet Port Spacing*(cm)	2.81	3.16	2.81	3.16	4.21 [†]
Air Inlet Port Spacing (deg)	4	4.5	4	4.5	6
Number of Fuel Injectors	N/A	2	2	N/A	N/A
Fuel Injector Spacing*(cm)	N/A	6.34	4.23	N/A	N/A
Fuel Injector Spacing*(deg)	N/A	9	6	N/A	N/A

* Linear distance between hole centers

[†] Equivalent spacing measured to adjacent domain

For the reacting flow tests which are discussed later, two types of fuel injectors were used to test a liquid and a gaseous fuel. For the liquid fuel, the particle injection function in FLUENT[®] was used to allow a 90° hollow cone liquid fuel spray to be injected at the specified locations without requiring any grid modifications to the domains to create nozzles. For the gaseous fuel testing, the grids in the original domains were modified to incorporate nozzles. Figure 3.9 shows the nozzle which was designed to spray the gaseous fuel in a 90° hollow cone.

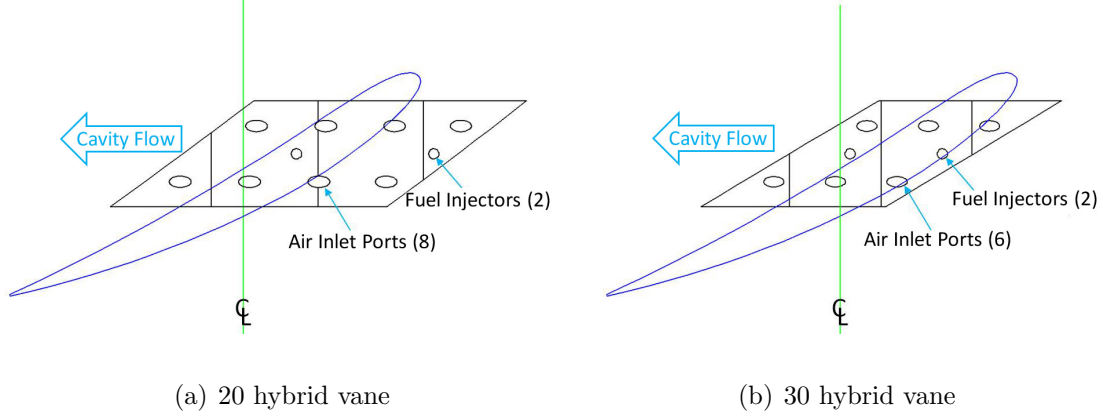


Figure 3.8: Fuel injector positioning relative to air inlet ports

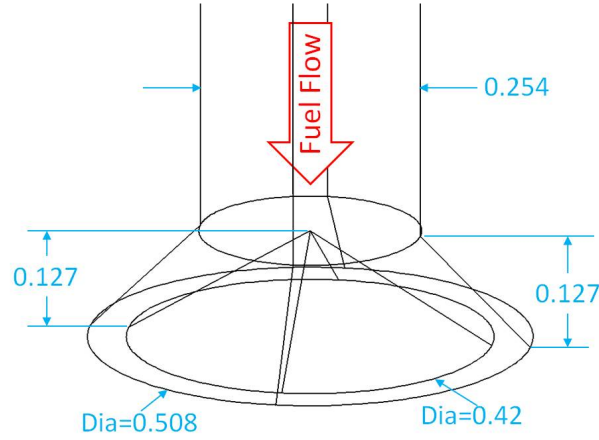


Figure 3.9: Gaseous fuel nozzle specifications (cm)

In addition to a baseline UCC air injector size which had a diameter of 0.54 centimeters, additional domains were created for the 20 hybrid-vane and 30 hybrid-vane test cases which increased the diameter of the air injector ports to 2 times and 3 times the baseline diameter. A final increase in inlet area was created by converting the upper wall of the baseline geometry circumferential cavity to a mass flow inlet with the inlet ports converted to walls. The 30 hybrid-vane test cases were not tested with a 3x air injector diameter because there was not sufficient room for 6 ports of that size. In fact, the 2x air injector ports for this domain were not fully 2 times the baseline diameter due to insufficient space. Using the full 2x dimension resulted in

the ports ending so close to the domain boundary that only highly skewed, irregular cells could be generated for the circumferential cavity upper wall surface mesh and no volume mesh could be produced. The actual 30 hybrid vane 2x air inlet port diameter was 0.99 centimeters rather than the full 1.08 centimeters used in the 20 hybrid vane domain. Figure 3.10 shows the three air inlet port variations. While the diameter of the ports were increased, the on-center spacing for each configuration was held constant.

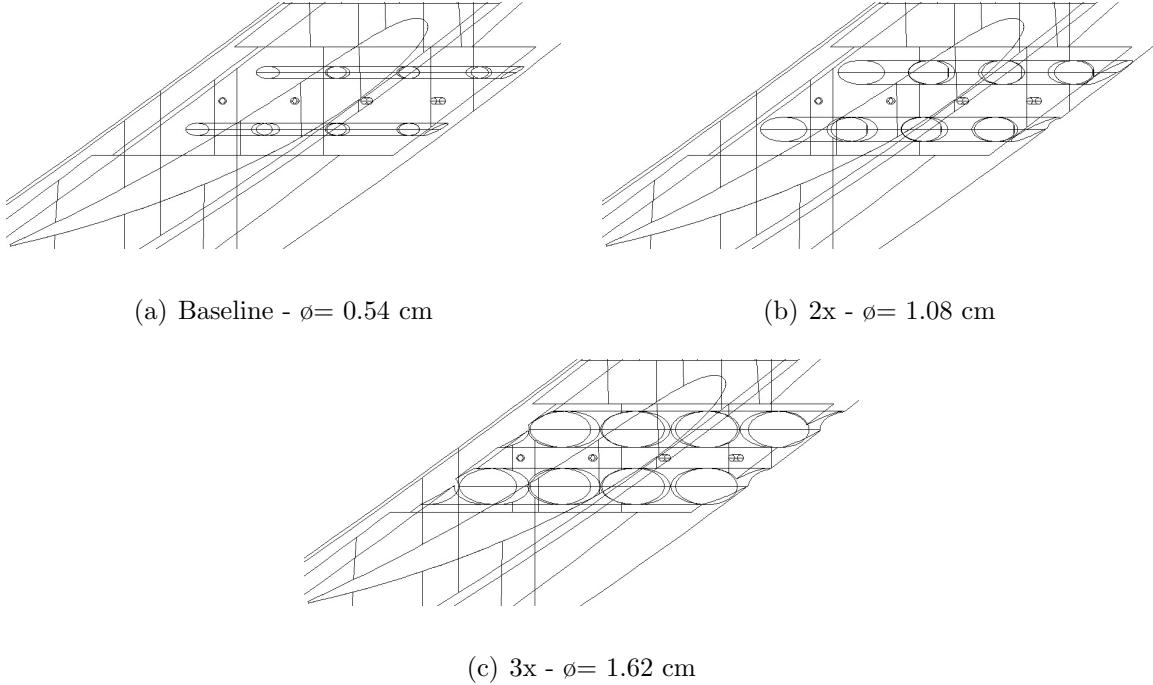


Figure 3.10: Air inlet port size variations (Shown for 20 vane configuration)

Since all air inlet ports were drilled at an angle relative to the tangent of the circumferential cavity, the inlet and exit area of the ports were elliptical. An equation for the area of an ellipse was derived such that the area could be found relative to the hole diameter and the inlet port injection angle. The area relationship is shown in Equation 3.3, where $A_{ellipse}$ is the elliptic area, ϕ is the diameter and λ is the injection angle.

$$A_{ellipse} = \frac{\pi \phi^2}{4 \sin(\lambda)} \quad (3.3)$$

Table 3.3 shows the port diameters and total inlet area for each domain section for the 20 hybrid vane and 30 hybrid vane configurations.

Table 3.3: Hybrid-vane domain air inlet port variations

Inlet Name	20-vane		30-vane	
	Port Diameter	Total Inlet Area	Port Diameter	Total Inlet Area
Baseline	0.54 cm	3.19 cm ²	0.54 cm	2.40 cm ²
2x	1.08 cm	12.87 cm ²	0.99 cm	8.05 cm ²
3x	1.62 cm	28.75 cm ²	N/A	N/A
Upper Wall	N/A	57.29 cm ²	N/A	37.89 cm ²

3.5 Preliminary Analysis

A preliminary, non-reacting flow analysis was conducted to observe bulk flow patterns in the UCC system and determine what geometric parameters were most influential in effecting changes in tangential velocity of fluid in the circumferential cavity, radial migration of hot fluid out of the circumferential cavity and temperature distribution at the domain exit. In place of numerically reacting fuel, air was injected into the circumferential cavity at an estimated combustion temperature.

3.5.1 Grid Independence Check. Prior to the analysis, a grid independence check was performed on the two 20-vane domains and the 30-vane domain with the hybrid vane to ensure the resolution of the computational domain was not influencing the test results. The independence with resolution of the above mentioned domains were checked directly, however, the resolution of the remaining domains were determined from the findings of the grid independence check and scaled according to the domain width. While the width of each domain varied for each vane count around the complete annulus, the vane and circumferential cavity cross-sectional dimensions remained the same across all domains for each vane style and thus were gridded with the same node spacing as the domains that were shown to be independent. Figure 3.11 shows the results of the variation of tangential velocity with increasing grid resolution.

The variation in tangential velocity across all resolutions was less than 2.4%. A variation of less than 5% within the CFD solution is considered independent and thus any resolutions could have been used. The computational time for each grid resolution was acceptable so larger cell volumes were selected for each case to ensure sufficient resolution of the secondary flows. The average wall y^+ value for each domain selected was approximately 42, which falls within the required range of 30 to 60 for the $k-\varepsilon$ RNG turbulence model. Table 3.4 shows the resolution of each test domain.

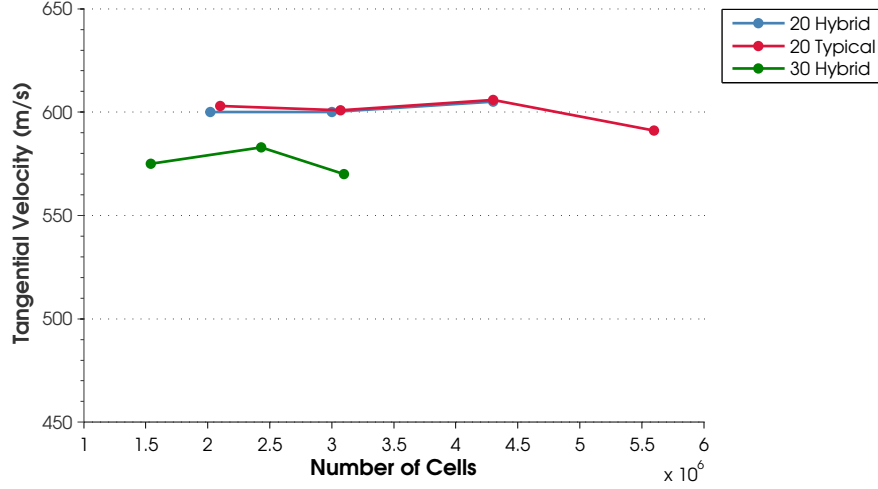


Figure 3.11: Grid independence check - Variation of circumferential cavity tangential velocity with grid resolution

Table 3.4: Mesh volume for each test domain

Vane Style	Total # Vanes	Number of Cells
Hybrid	20	4.4×10^6
Hybrid	30	3.1×10^6
Typical	20	4.4×10^6
Typical	30	3.6×10^6
Typical	45	2.8×10^6
Typical	60	2.3×10^6
No Vane	0	1.1×10^6

3.5.2 Test Conditions. For ground takeoff, the total fuel burn for a fighter-scale engine was approximated at 2 kg/s. The compressor was estimated to

provide air at a total flow rate of 72 kg/s. Removing flow for turbine cooling left 66 kg/s usable mass flow. The remaining core flow was split such that the mass flow rate into the circumferential cavity was approximately 30% that of the core flow rate. The resulting core mass flow rate was 50.5 kg/s and 15.5 kg/s was fed into the circumferential cavity along with the 2 kg/s of fuel. For a 30% split, an equivalence ratio of 2 in the circumferential cavity was achieved. In the preliminary analysis, 17.5 kg/s of air was injected into the circumferential cavity at an estimated combustion temperature of 2200 K to account for the fuel and air mass flow rates and eliminate the need for combustion modeling at this stage of the analysis. This simplification drastically reduced computational time for each test case. Any density differences due to modeling the fuel as air or energy losses that would occur to heat or vaporize incoming fuel were neglected. The tests conducted in this analysis were performed for an engine representative condition and a condition that could be run in an atmospheric pressure laboratory test rig. The rig conditions were scaled to be comparable to the engine conditions when operating at standard atmospheric pressure. Table 3.5 shows various operating parameters for both the engine condition and the rig condition. The mass flow rate values shown represent the mass flow rate through the complete annulus.

Table 3.5: Operating parameters used in preliminary analysis for engine condition and rig condition for complete annulus

Parameter	Engine Condition	Rig Condition
Operating Pressure (Static)	4,626,377 Pa	101,325 Pa
Core Mass Flow Rate	50.5 kg/s	1.47 kg/s
Core Flow Inlet Angle	54°	54°
Core Flow Temperature	960 K	530 K
Core Flow Turbulence Intensity	5 %	5 %
Cavity Inlet Mass Flow	17.5 kg/s	0.58 kg/s
Cavity Inlet Flow Temperature	2200 K	1000 K
Cavity Inlet Turbulence Intensity	2 %	2 %

To ensure that all configurations of the computational domains maintained the same total mass flow rates for the full annulus, the total mass flow rate was divided

by the corresponding number of vanes since each domain contained only a single vane. Table 3.6 shows the resulting core mass flow rate through the UCC test section and the mass flow rate injected into the circumferential cavity (which included the fuel flow rate) for the engine representative condition.

Table 3.6: Core and circumferential cavity inlet mass flow rates for engine conditions, per section

Parameter	0-Vane	20-Vane	30-Vane	45-Vane	60-Vane
Core Inlet (kg/s)	1.683	2.525	1.683	1.122	0.8417
Cavity Inlet [*] (kg/s)	0.583	0.875	0.583	0.389	0.292

^{*} Includes mass flow rate of fuel

Fluid density in this series of tests was modeled as an ideal gas. The constant pressure specific heat, C_p , of the fluid was set as a constant at the default value for air. The solution was run adiabatic with the effects of heat transfer to the metallic structures of the UCC ignored. The solutions were run to 8,250 iterations, with convergence monitored by residual plots and a force monitor.

A series of tests were conducted to characterize the flow properties in the circumferential cavity based on variations in the cavity inlet mass flow rate as well as variations in the UCC test section geometry. The mass flow rate of air into the circumferential cavity was tested at the values shown in Table 3.6 for the engine condition as well as 75%, 50% and 25% of these values for each of the vane count variation domains using both vane styles. The rig condition was tested at the same percentages of cavity inlet mass flow rate but for the 20 hybrid vane domain only. The values in Table 3.5 represent a full throttle flight condition. The cavity inlet mass flow rate variation tests simulated throttled conditions while testing the benefits and drawbacks of having more or less vanes below the circumferential cavity. To determine the impact of variations in core flow on the fluid properties in the circumferential cavity, the core mass flow rate was varied at 125%, 100%, 75%, 50% and 25% of the core flow rate listed in Table 3.6 using the 20-vane, hybrid vane style domain while maintaining a 100% cavity inlet mass flow rate.

The final series of tests conducted in the preliminary analysis was to observe the changes in flow properties as a result of variations in the cavity air inlet diameter. For a constant cavity inlet mass flow rate, variations in inlet diameter effectively change the inlet velocity. This series tested the impact of the injection velocity on the flow properties, specifically the tangential velocity, in the circumferential cavity. All four air inlet variations outlined in Table 3.3 were tested at 100%, 75%, 50% and 25% cavity inlet mass flow rates while maintaining 100% core mass flow rate. Additionally, the rig condition was run for 100% cavity inlet mass flow rate for each of the four air inlet variations.

For each test case, the area-weighted average of tangential velocity, velocity magnitude and density in the circumferential cavity were recorded. The difference between the tangential velocity and the velocity magnitude allows the flow angle to be calculated. The density was combined with the tangential velocity of the fluid and the known cross-sectional area of the cavity to calculate the mass flow rate in the circumferential cavity. Additionally, the area-weighted averaged total temperature was recorded for the exit face of the domain and plots of the circumferentially-averaged total temperature on the exit plane were created.

3.6 5-Species Reacting Flow Analysis

Following the preliminary analysis, the next level of analysis was to remove the previous simplifications and include a 5-species reacting flow model. The 5-species model used only stoichiometric products including the fuel, O_2 , N_2 , CO_2 and H_2O . This analysis was performed using the 20- and 30-vane domains with the hybrid style vane only.

3.6.1 Reacting Flow Grid Independence Check. Prior to completing the reacting flow analysis, a grid independence check was performed to ensure that the grid resolution was not influencing the test results. While it was found that the grid resolution used in the preliminary analysis was also sufficient for the reacting

flow analysis, this outcome should not be assumed. The variations in grid resolution were performed on the 20 hybrid vane domain using the grid adaptation function in FLUENT®. The grid was adapted two times from the original domain consisting of 4.4×10^6 cells to form domains with 7.1×10^6 and 10×10^6 cells. Figure 3.12 shows the variation of tangential velocity in the circumferential cavity with grid resolution. A maximum variation of only 1.8% was observed with the lowest and the highest grid resolutions producing seemingly identical results. For this analysis, unlike the preliminary analysis, the lowest grid resolution case was selected for use. With the addition of the combustion modeling, the computational time was significantly increased and any savings that could be obtained using a smaller grid was appreciated. Depending on the machine processing the solution, the reacting flow cases took anywhere from 24-72 hours per case to reach convergence, using a maximum of 12 processing cores.

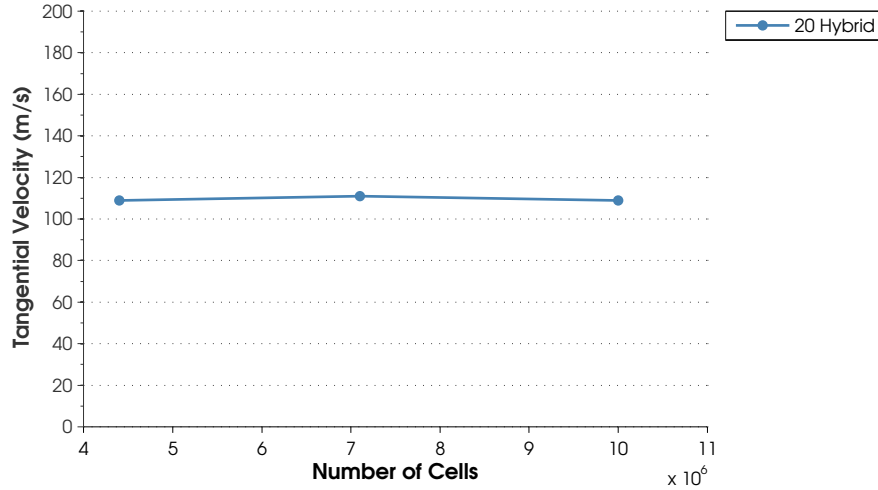


Figure 3.12: Reacting flow grid independence check - Variation of circumferential cavity tangential velocity with grid resolution

3.6.2 Test Conditions. With the removal of the previous simplifications, fuel and air needed to be injected separately into the circumferential cavity with the fuel being injected using one of the methods discussed in Section 3.4. For engine condition test cases, liquid kerosene was used as the fuel and for the rig condition test cases, gaseous propane was used. Additionally, the inlet temperature of the

cavity air was set to the same temperature as the core air inlet temperature since in an engine application both inlets would be fed from the compressor. Table 3.7 shows the operating parameters for the engine and rig conditions calculated using the same estimations for the compressor mass flow rate, film cooling requirements, circumferential cavity split and fuel mass flow rate outlined in Section 3.5.2. Maintaining a mass flow rate of 2 kg/s of fuel and 15.5 kg/s of air, an equivalence ratio of 2 was achieved in the circumferential cavity. The inlet temperature for the rig condition was reduced to more closely match an obtainable temperature using the air heaters in the AFIT COAL Lab. Additionally, the rig core mass flow rate, cavity inlet mass flow rate and fuel flow rate were recalculated from the previous values to more closely scale to the engine values.

Table 3.7: Operating parameters used in 5-species reacting flow analysis for engine condition and rig condition for complete annulus

Parameter	Engine Condition	Rig Condition
Operating Pressure (Static)	4,626,377 Pa	101,325 Pa
Core Mass Flow Rate	50.5 kg/s	1.94 kg/s
Core Flow Inlet Angle	54°	54°
Core Flow Temperature	960 K	366 K
Core Flow Turbulence Intensity	5 %	5 %
Cavity Inlet Mass Flow	15.5 kg/s	0.45 kg/s
Cavity Inlet Flow Temperature	960 K	366 K
Cavity Inlet Turbulence Intensity	2 %	2 %
Fuel Mass Flow Rate	2 kg/s	0.064 kg/s
Fuel Inlet Temperature	300 K	300 K

To include combustion modeling in FLUENT[®], species transport with volumetric reactions was activated. Species transport allows the code to calculate the transport of each species and with the addition of volumetric reactions the code allows for reacting flow using a finite-rate formulation. The effects of inlet diffusion were also considered. Regardless of the fuel used, a single-step, 5-species model was selected. The effects of turbulence and chemistry interactions were modeled using the Eddy-Dissipation model. This model computes the mixing rate within a turbulent

flow under the assumption that chemical kinetics occur quickly compared to the rate that reactants are mixed by turbulent eddies. For inlet boundary conditions, the gas species that are entering the domain need to be specified. The fraction of O_2 entering at each air inlet boundary was set to 0.23. With no other gases specified, FLUENT® then assumes that the remainder of the gas composition is N_2 .

For the engine condition test cases, two liquid kerosene particle injections were created in FLUENT® using the injections function. The coordinates of the injection source matched the locations shown in Figure 3.8. The vertical coordinate was reduced slightly to insure that the injection was taking place fully inside the domain and not on the surface of the cavity wall. The injectors were modeled as hollow cones with 300 particle streams each. The nozzle radius was 0.127 centimeters with a spray angle of 90° . A total of 10 diameter sizes of injected particles was used with a Rosin-Rammler size distribution. The Rosin-Rammler distribution is an application of the Weibull probability distribution as applied to the size of particles. The fuel mass flow rate into each injector was $1/40$ or $1/60$ of the total fuel mass flow rate shown in Table 3.7 depending on whether the 20-vane or 30-vane domain was used, respectively.

Along with the particle injections, discrete phase modeling, DPM, was also included in the simulation. DPM allows the code to model discrete liquid particles that interact with the continuous bulk flow. The heat transfer into the liquid particles was calculated and the particles were allowed to evaporate and combust. The interaction of the discrete phase with the continuous phase occurred every 5 iterations.

For the rig condition test cases, two gaseous propane inlets were added to the domain and the block mesh was regenerated. Using gaseous fuel did not require the use of particle injections or DPM. A mass flow inlet boundary condition was added to the inlet of the gas injector ports with the inlet species defined as 100% propane with a 2% turbulent intensity.

For this series of tests, density was modeled as an ideal gas for both air and the air-fuel mixture. The constant pressure specific heat for the mixture was set to

‘mixing law’ which takes the properties of the individual species and the concentration of the species into account. The C_p values for each individual fluid species was set at the default constant values. The solution was run non-adiabatic with respect to the fluids which allowed for heating of the fuels and/or evaporation of the liquid fuel. The solution was run adiabatic with respect to the walls in that heat transfer to the metal surfaces in the UCC section were not considered. The solutions were run to a minimum of 7,000 iterations with convergence monitored by residual plots and a force monitor.

A series of tests were conducted using the 20 and 30 hybrid vane domains with varying cavity air inlet diameters to characterize the relationship between cavity air inlet velocity and cavity tangential velocity for both the engine and rig conditions. The engine condition was tested with the air inlet diameter variations shown previously, while the rig was tested with these same diameters plus a diameter smaller than the baseline to have the engine and rig results cover roughly the same inlet velocity range. A plot was generated that showed the relationship between the cavity air inlet diameter, the cavity air inlet velocity and the tangential velocity for both vane configurations at both test conditions. To show the accuracy of the plot, four additional tests were run for the ‘ideal’ cavity tangential velocity of 114 m/s. The air inlet diameter needed to achieve this velocity in each case was determined from the plotted relationships. For the current engine diameter, a velocity of 114 m/s represented a g-load of 3,500 g’s which according to Lewis [3] has the highest benefit from g-loaded combustion. Based on the findings of Zelina et al. [2], this g-load also represents the largest load possible at an equivalence ratio of 2 before blowout occurred, as shown in Figure 2.4.

For each test case, the area-weighted average of the cavity air inlet velocity magnitude along with the tangential velocity, velocity magnitude and density in the circumferential cavity were recorded. Using the density and tangential velocity of the fluid and the known cross-sectional area of the cavity, the mass flow rate in the circumferential cavity was calculated. Additionally, the area-weighted aver-

aged total temperature was recorded for the exit face of the domain and plots of the circumferentially-averaged total temperature on the exit plane were created.

3.7 12-Species Reacting Flow Analysis

With the UCC operating fuel rich at an equivalence ratio of 2, four additional tests were run using a 12-species combustion model to determine if fuel was exiting the circumferential cavity or if the fuel was broken down and intermediate species were exiting the cavity. Additionally, the concentrations of the specific species exiting the cavity were of interest. The 12-species model included the fuel, O_2 , N_2 , CO_2 , H_2O , CH_4 , CO , OH , H_2 , O , H and HO_2 which represents stoichiometric products, less complex fuel species and unstable intermediate combustion species. Since this analysis was only a minor variation of the 5-species reacting flow analysis, an additional grid independence check was not performed.

The FLUENT[®] settings used in this analysis differed from the 5-species reacting flow analysis. In place of species transport with volumetric reactions, the non-premixed combustion setting was activated. With this setting the code calculates the mixture fraction, which is the local mass fraction of fuel elements in all species for each cell. Since all atomic elements are conserved in chemical reactions, tracking burned and unburned fuel elements in each cell allows the combustion to be modeled as a mixing problem rather than a complex non-linear combustion problem. The chemistry was modeled as being in chemical equilibrium through the use of the equilibrium model. The system was modeled as non-adiabatic to account for heat transfer to the incoming fuel, and in the case of the liquid fuel allow for evaporation. The effects of inlet mixture fraction diffusion were also included in the simulation.

The fuel inlet conditions were setup in the same way as the 5-species model. Two discrete particle injections were created in the domains operating at the engine condition using liquid kerosene and two gaseous propane inlets were added to the domains for the rig condition tests. At domain boundaries, the mixture fraction needed to be defined to tell the code what species were entering the domain. At the

air inlet boundaries, a mixture fraction of 0.0 was used which stated that no fuel species were entering. For the gaseous propane mass flow inlets, a mixture fraction of 1.0 was used which means that only fuel species were entering.

The density of the mixture and individual fluid species in this analysis were specified by a probability density function, PDF. A series of PDF's were created as look-up tables for values of temperature, density and mixture fractions of species at a number of flow conditions. It was also at this point that the number of species desired was entered. Under equilibrium conditions FLUENT[®] allows as many as 500 species to be tracked. For this analysis only the primary 12 species were used. The C_p value for the mixture was again specified by the 'mixing law', but the C_p values of the individual species were modeled as piecewise-polynomials. According to the FLUENT[®] manual [39], the C_p settings used in the preliminary and 5-species analysis tend to over-predict temperature. Using the current settings, the combustion temperatures should be more accurate.

The 12-species analysis was performed using the 'ideal' inlet diameters found in the previous 5-species analysis for the engine and rig conditions using the hybrid style vane with both the 20 and 30-vane configurations. These four tests used the same operating parameters from the previous study as outlined in Table 3.7. For each test case, the area-weighted average of tangential velocity, velocity magnitude and density in the circumferential cavity were recorded. Using the density and tangential velocity of the fluid and the known cross-sectional area of the cavity, the mass flow rate in the circumferential cavity was calculated. The area-weighted averaged total temperature was recorded for the exit face of the domain and plots of the circumferentially-averaged total temperature on the exit plane were created. Additionally, the area-weighted average of the mass fractions of each species were recorded in the cavity, at the exit plane of the cavity and at the domain exit.

3.8 Domain Modification Analysis

In an effort to improve the temperature distribution at the domain exit and reduce the endwall heating on both the OD and ID endwalls, a modification to the domain was considered. A 0.159 centimeter thick flat plate was positioned 0.32 centimeters above the ID endwall beginning 0.32 centimeters upstream of the vanes array and ending 0.32 centimeters downstream of the vanes as shown in Figure 3.13. The plate allowed cool core flow to travel below the circumferential cavity region without mixing with the fluid exiting the cavity. When the plate ended downstream of the vanes, the fluid exited the passage buffering the ID endwall from the hot gases in a similar manner as a film cooling slot.

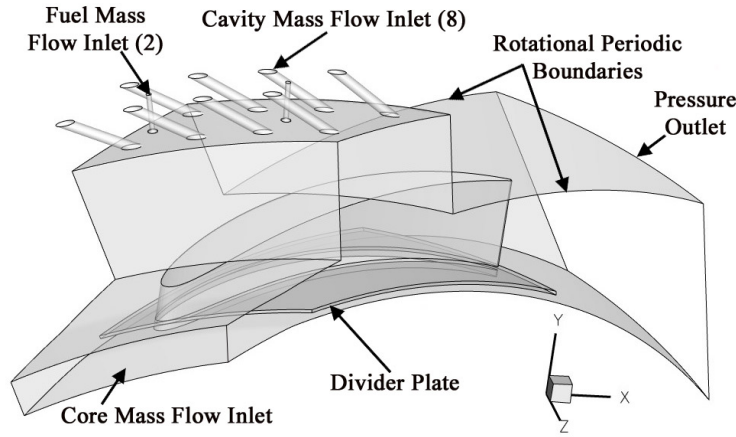


Figure 3.13: 20 hybrid vane domain with core flow divider plate

This domain was tested under rig conditions with both the 5-species and 12-species combustion models. The 12-species combustion model was used as described in Section 3.7. The 5-species analysis differed slightly from the description given in Section 4.2. Rather than use a constant C_p value for the individual species, variable piecewise-polynomial values for C_p of each fluid species were used in an attempt to obtain a more accurate combustion temperature. As with the previous analysis, the area-weighted average of tangential velocity, velocity magnitude and density in the circumferential cavity were recorded and used to find the mass flow rate in the circumferential cavity. The area-weighted averaged total temperature was recorded for the

exit face of the domain and plots of the circumferentially-averaged total temperature on the exit plane were created. Additionally, for the 12-species analysis, the area-weighted average of the mass fractions of each species were recorded in the cavity, at the exit plane of the cavity and at the domain exit.

3.9 Engine Condition Domain Modification

It was noted during testing, and presented in Chapter 4, that a variation in static pressure existed between the domain inlet and the cavity inlet. Running the rig condition in a laboratory setting would allow each inlet to be fed from separate air sources with different pressures if necessary. In an operational engine condition, this variation would not be present because both inlets would be fed from the same compressor. A modified 20-vane domain was created to allow the cavity inlet holes to be fed from a bypass off the core flow as shown in Figure 3.14. The splitter duct is 1/3 the height of the core flow inlet attempting to capture 1/3 of the core flow to maintain the 30% cavity to core air ratio. Three cavity inlet port diameters were tested including the baseline and 2x diameters discusses previously and 0.864 centimeters (1.6x) which is shown in Section 4.2 to be the ideal air inlet diameter for the 20-vane engine condition.

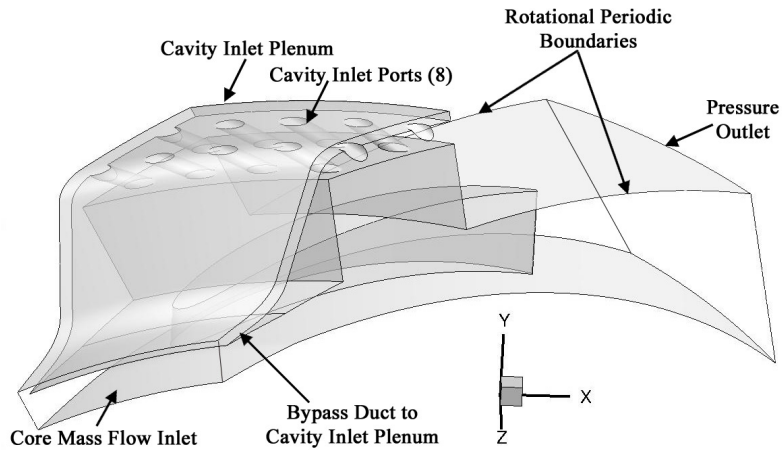


Figure 3.14: 20 hybrid vane domain with cavity inlet splitter duct

This domain was tested under engine conditions using liquid fuel with the 5-species combustion model discussed in Section 4.2. The core mass flow inlet was increased from 2.525 kg/s to 3.3 kg/s to include the cavity inlet mass flow requirement. All remaining parameters were maintained from those outlined in the ‘engine condition’ column of Table 3.7.

3.10 Uncertainty

The uncertainty within the CFD solution is dependent on the accuracy of the CFD solver, turbulence model, reaction mixing models, chemical kinetics models and specific heat values. Most of these properties are internal to FLUENT[®] and not directly visible to the user. The repeatability of the solution and variation of results within a converged solution were very good. A repeat test, using the same operating conditions, showed a difference of less than 1 m/s in average tangential velocity and less than 10 degrees in the average temperature at the domain exit plane. The variation within a converged solution with additional iterations showed oscillations of approximately ± 1.5 m/s tangential velocity from an average value and oscillations of approximately ± 10 degrees from an average total temperature on the domain exit face. The values of tangential velocity reported in Chapter 4 was the peak value obtained within a solution oscillation and the exit temperature listed was the total temperature associated with that tangential velocity. The uncertainty due to the grid resolution was previously shown to be 2.4% for the non-reacting cases and 1.8% for the reacting flow cases.

IV. UCC Numerical Analysis Results

The results of the series of numerical studies outlined in Chapter 3 is presented in this chapter in order of increasing complexity beginning with the preliminary analysis and ending with the 12-species analysis. Each level of complexity offered a deeper level of understanding into the flow structures and behavior of fluid in the UCC section.

4.1 Preliminary Analysis

The preliminary analysis provided bulk flow results and a comparison of the hybrid vane with the typical vane currently used in the small-scale studies. The two vane designs represent two very different inlet conditions into the combustor section yet the exit angle for both vanes was identical. The difference in circumferential cavity tangential velocity between the two vane designs was minimal for the higher mass flow rates but did reach a maximum of 45% for the 25% cavity inlet mass flow rate in the 30-vane domains. It was also found that there was a 20% variation in tangential velocity as the number of vanes below the circumferential cavity was changed. This result can be seen in Figure 4.1 which shows the variation of tangential velocity as a function of vane count for each cavity inlet mass flow rate tested.

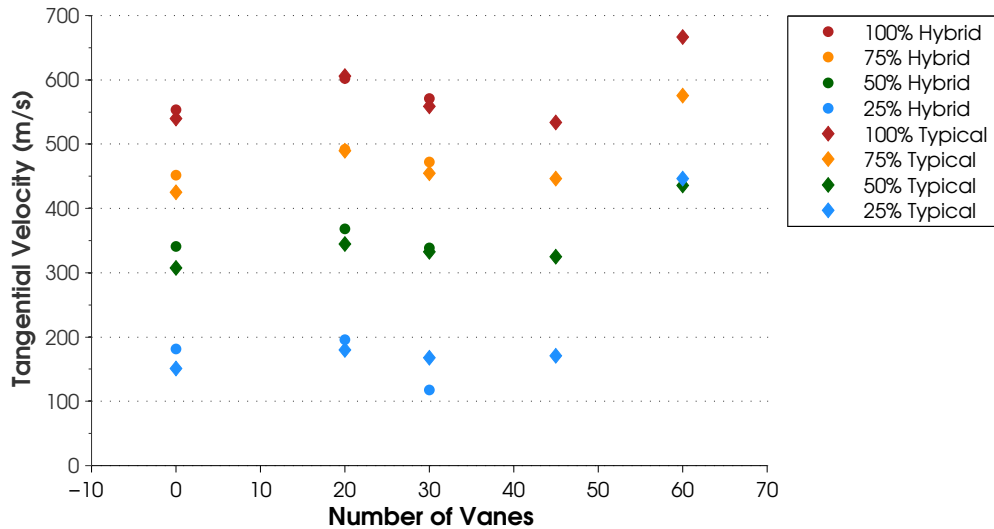


Figure 4.1: Tangential velocity as a function of vane count and cavity mass flow inlet percentage (engine conditions)

At the time these results were obtained, the cause of the fluctuation in tangential velocity relative to the number of vanes was not known. However, after completing the air inlet port diameter study at the end of the preliminary analysis, the cause of the variations became more apparent. There were two factors that were combined to produce the variations; one related to the cavity inlet condition and the other related to the flow pattern of fluid through the vane passages. For the 0-vane, 30-vane and 45-vane domains, 90 pairs of air inlet ports were used. This number represents the most inlet ports used around the complete annulus and thus the largest total inlet area. All vane count variations used the same inlet mass flow rate and applying Equation 2.12 shows that the larger the area the slower the inlet velocity. It will be shown later that there is a direct correlation between cavity inlet velocity and tangential velocity. The 60-vane domain had the least number of air inlet ports for the complete array and thus had the largest cavity inlet velocity for the same inlet mass flow rate. Allowing the cavity inlet mass flow rate to decrease while fixing the inlet area shows the trend of increased tangential velocity for increased cavity inlet mass flow rate (increased inlet velocity) as shown in Figure 4.2. If this relationship was the only factor contributing to the tangential velocity, the 0-vane, 30-vane and 45-vane domains would all have the same tangential velocity. For low tangential velocities, however, such as the 25% cavity inlet mass flow rate shown in Figure 4.1, the variation between the 0-vane, 30-vane and 45-vane for the typical vane type was minimal.

The second cause for the velocity variation was a balance between metallic blockage and benefits obtained by accelerated core flow through smaller vane passages for increased numbers of vanes. Additional vanes below the circumferential cavity reduced the area that the fluid could exit the cavity. This restriction caused an increase in the mass flow rate in the cavity which resulted in a slightly increased velocity. However, additional vanes also caused a greater pressure reduction between the smaller vane passages. This reduction in pressure helped to draw fluid out of the circumferential cavity which reduced the mass flow rate and ultimately caused a slight decrease in tangential velocity. It is not possible to quantify the individual impact on

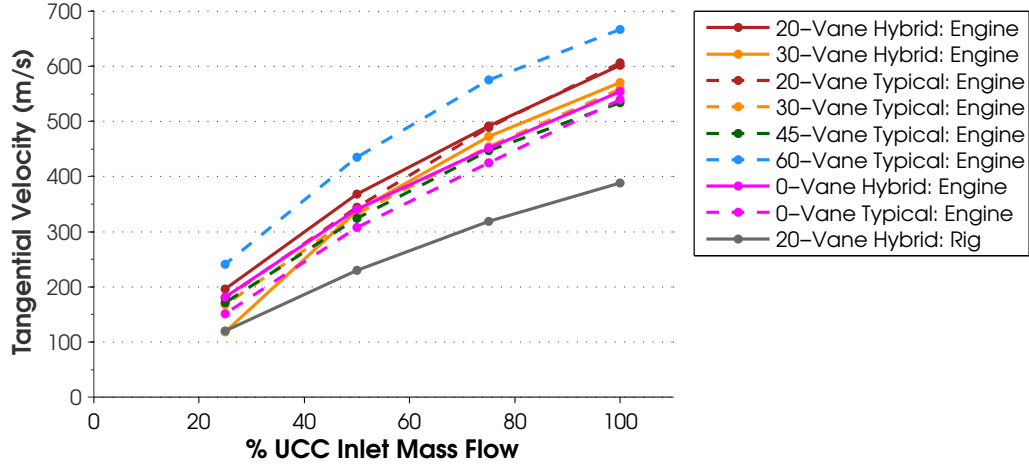


Figure 4.2: Tangential velocity as a function of cavity mass flow inlet percentage

the mass flow rate resulting from metallic blockage or the pressure reduction between the vanes since both variations occur as a pair. The combined effect can be quantified and is shown in Figure 4.3 as the resulting cross-sectional mass flow rate in the cavity for each vane count. For both vane types the 0-vane case serves as a baseline.

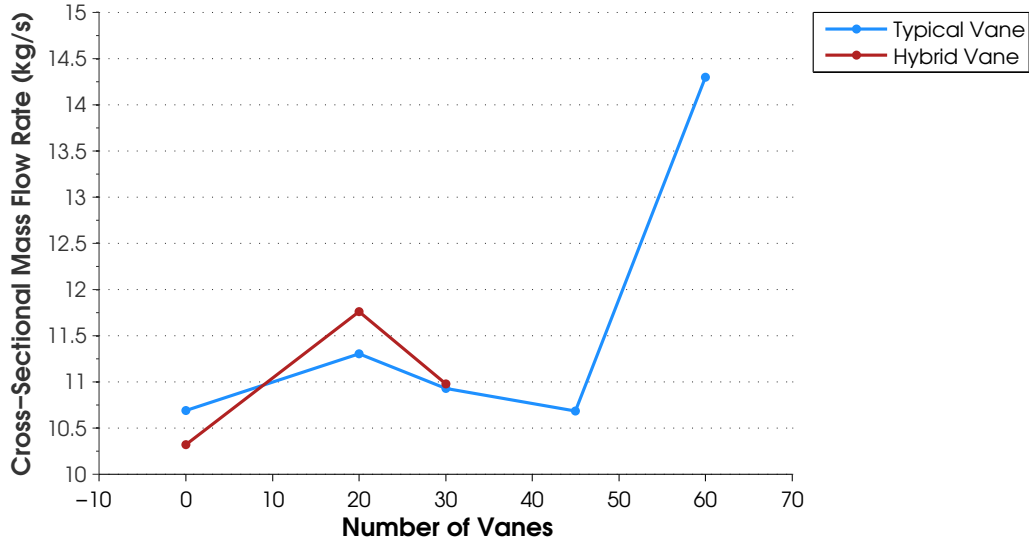
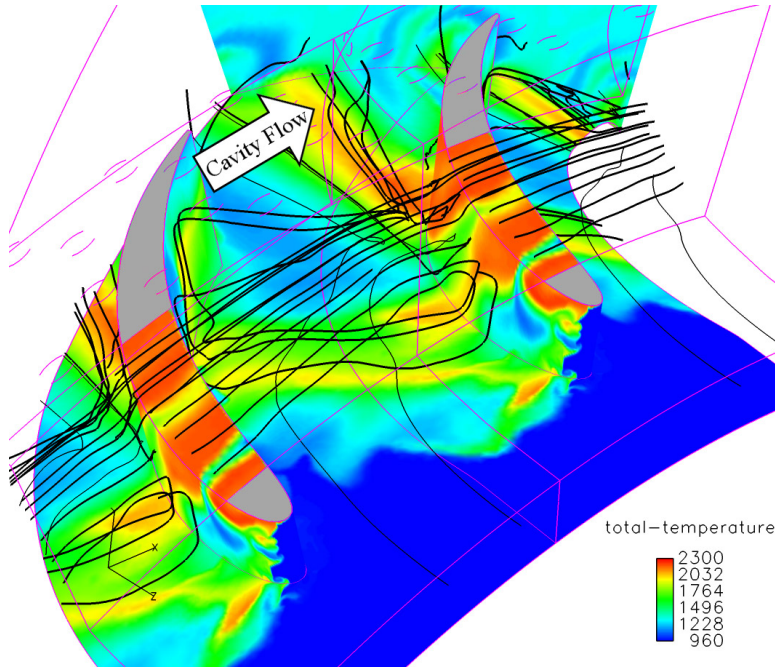


Figure 4.3: Cavity cross-sectional mass flow rate as a function of vane count (100% cavity inlet mass flow rate)

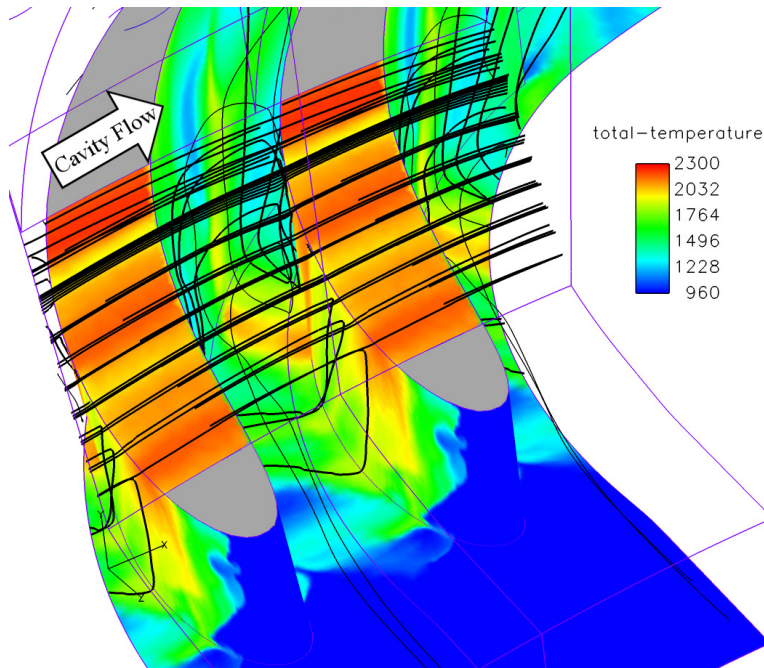
From Figure 4.3 it can be seen that the addition of 20 vanes below the circumferential cavity resulted in a mass flow rate increase, meaning that the effects from

metallic blockage dominated. For increased vane count beyond 20 vanes, the mass flow rate in the cavity was reduced, indicating that the pressure reduction between the vanes had enough of an impact to counter the effects from blockage. For both vane types the mass flow rate in the cavity was never reduced below the 0-vane values. An explanation of the large increase in mass flow rate for the 60-vane case is given below.

Adding additional vanes had a negative effect at very high tangential velocities. The fluid exiting the circumferential cavity hit the suction surface of the turbine vane and flowed down the face of the airfoil to the ID endwall. Since the passage was short, the fluid maintained enough momentum to roll up the pressure surface of the neighbor vane. If the distance between vanes was decreased sufficiently, such as the 60-vane case, the high-velocity fluid exiting the cavity could roll up the neighbor vane faster than it could be convected downstream by the core flow and could actually re-enter the cavity or at a minimum block a large amount of fluid from exiting the downstream section of the cavity. This flow pattern resulted in a much larger mass flow rate in the cavity for the 60-vane domain than any other test case. Figure 4.4 shows streamlines of the exiting flow for the 20- and 60-vane domains with contours of total temperature to show how the flow pattern affects the exit of hot gases from the cavity. The negative effect of this flow pattern was removed by controlling the tangential velocity in the cavity as shown later in this section. In Figure 4.4, the thick black lines are streamlines of fluid exiting the cavity (streamlines are not shown in the cavity for figure clarity) and the thin black lines are streamlines of the core flow. In both test cases shown, the core flow near the OD endwall became entrained by the cavity flow and was redirected into the vane, reducing the surface temperature drastically.



(a) 20-vane



(b) 60-vane

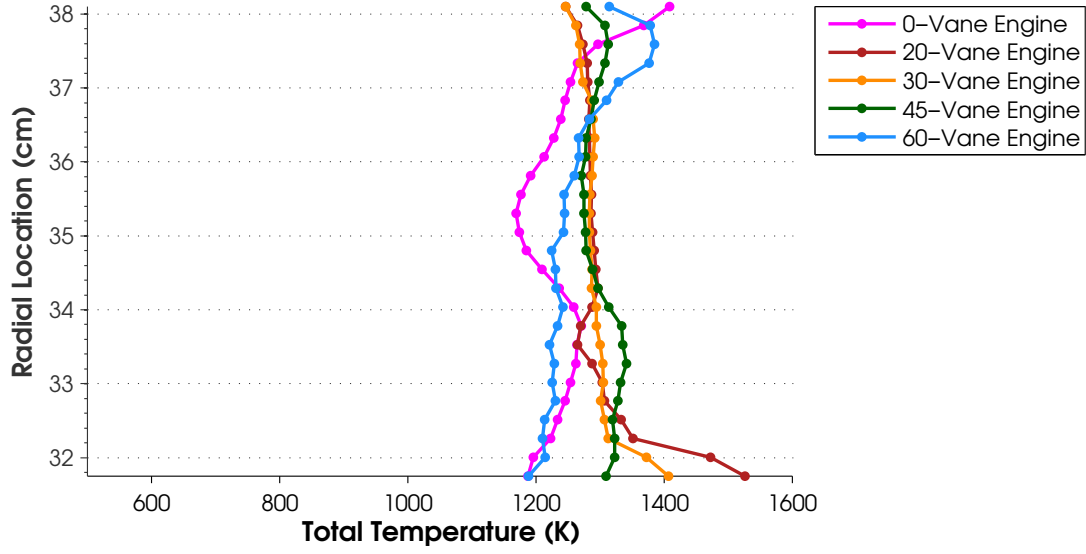
Figure 4.4: Streamlines and contours of total temperature for typical style vane domains (Thick black lines are streamlines exiting the circumferential cavity, thin black lines are core flow streamlines)

The combustor section exit temperature profile is of critical importance to the turbine blade durability. The temperature profile, or pattern factor, establishes the work potential of the turbine rotor along with setting the cooling flow requirements to the airfoil. Ideally, the temperature in the middle third of the blade would be the hottest with the temperature decreasing toward the endwalls. Because endwalls are difficult to cool, and there are other complications with hot gas ingestion in the engine seams along the ID endwall, it is important to keep these surfaces as cool as possible. The temperature at the domain exit plane is presented using a pattern factor as defined by Mattingly et al. [1] and shown in Equation 4.1. All station 4 temperatures in this equation were taken as total temperatures on the exit plane.

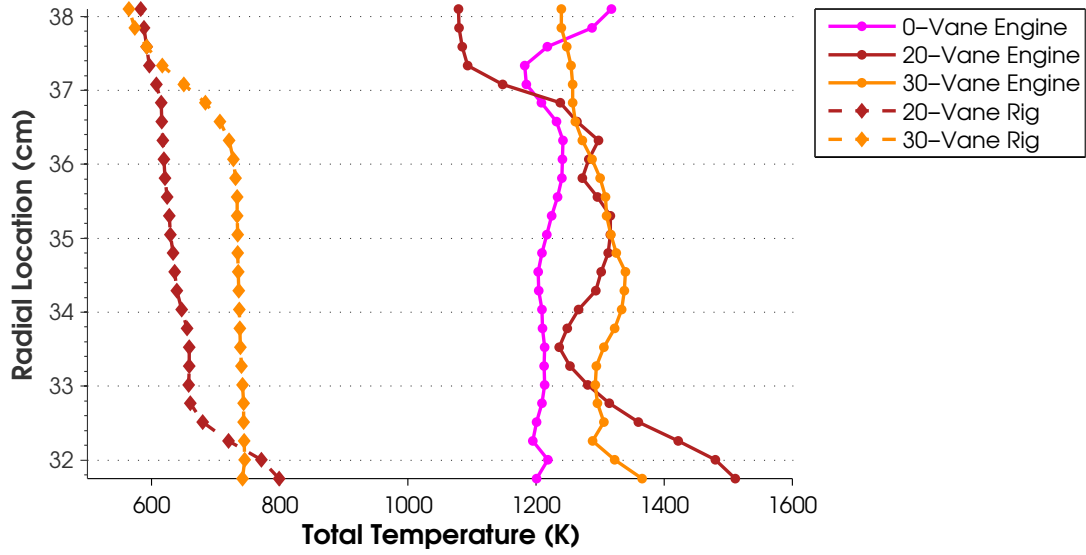
$$PF = \frac{T_{t4max} - T_{t4avg}}{T_{t4avg} - T_{t3}} \quad (4.1)$$

Figure 4.5 shows the circumferentially-averaged temperatures at the combustor section exit for 100% cavity inlet mass flow rate in all tested domains. Of the cases shown, the 45-vane, typical vane style, resulted in the most uniform temperature distribution with no excess heating of either endwall. Of the remaining cases, at least one endwall was heated above the average temperature. Reductions of cavity inlet mass flow rate in general resulted in a more uniform temperature distribution as the mass flow rate into the cavity was reduced. Additionally, because of the way the test cases were set up using injection of hot gas into the cavity rather than combustion modeling, lower mass flow rates into the circumferential cavity resulted in less available energy and lower average temperatures at the exit to the combustor section. These results are shown in Appendix D.

For the 20 hybrid vane case shown in Figure 4.5, the fluid exiting the circumferential cavity was able to maintain more momentum due to the larger angle of the vane. The high momentum resulted in the fluid exiting out of the cavity further in the radial direction, leaving a cooler upper endwall. The cooler OD endwall resulted in a lower average temperature which caused an increase in the pattern factor compared



(a) Typical Style Vane



(b) Hybrid Style Vane

Figure 4.5: Circumferentially-averaged total temperatures at combustor section exit (100% cavity inlet \dot{m})

to the typical vane. The tabulated properties of tangential velocity, cavity mass flow rate, pattern factor and g-load for the 100% cavity inlet mass flow rates are shown

in Table 4.1. With the more perpendicular typical vane, the momentum of the fluid exiting the cavity was reduced and the fluid stayed closer to the OD endwall resulting in a higher average temperature. Both vanes produced approximately the same maximum temperature at the ID endwall. The rig condition using the 20 hybrid vane domain, which was shown in Figure 4.2 to have a lower tangential velocity, produced a more uniform result similar to the 30-vane domains. The tabulated properties of the rig condition tangential velocity, cavity mass flow rate, pattern factor and g-load for 100% cavity inlet mass flow rate is shown in Table 4.2.

Table 4.1: 100% mass flow rate into the circumferential cavity test results for varied geometry (engine conditions)

Vane Style	Vane Count	Tangential Velocity	Mass Flow Rate¹	Pattern Factor	g-Load
No-Vane ²	0	540 m/s	10.70 kg/s	0.62	78,000
No-Vane ³	0	554 m/s	10.32 kg/s	0.38	82,100
Typical	20	606 m/s	11.31 kg/s	0.66	98,250
Hybrid	20	602 m/s	11.76 kg/s	0.79	97,000
Typical	30	558 m/s	10.93 kg/s	0.34	83,300
Hybrid	30	571 m/s	10.98 kg/s	0.21	87,200
Typical	45	534 m/s	10.69 kg/s	0.12	82,100
Typical	60	667 m/s	14.3 kg/s	0.42	119,000

¹ Cross-sectional mass flow rate through circumferential cavity

² Axial core flow representative of typical vane configuration

³ 54° angled core flow representative of hybrid vane configuration

Table 4.2: Result for 100% mass flow rate into the cavity using the 20 and 30 hybrid vane domains (rig conditions)

Vane Style	Vane Count	Tangential Velocity	Mass Flow Rate¹	Pattern Factor	g-Load
Hybrid	20	388 m/s	0.36 kg/s	1.4	40,250
Hybrid	30	334 m/s	0.44 kg/s	0.22	30,000

¹ Cross-sectional mass flow rate through circumferential cavity

Variation of the core flow percentage had virtually no effect on the velocity of the fluid in the circumferential cavity or the mass flow rate through the cavity.

Table 4.3 shows the results of the five core flow percentage variations. The area-weighted averaged total temperature at the exit to the domain, however, increased as the core mass flow rate was decreased, which resulted in a corresponding decrease in the pattern factor. This pattern is the expected result. Since the mass flow rate into the circumferential cavity was unchanged for all core flow variations, the same energy was released from the cavity. For reduced core mass flow rates, the hot cavity air was mixed with less cooler core air, allowing the fluid at the exit of the domain to remain hotter. For the higher core flow rates, the ID endwall temperature was elevated but had a lower average temperature at the exit plane. Additionally, as the core mass flow rate was reduced, the temperature distribution at the exit plane became more linear. Figure 4.6 shows the circumferentially-averaged total temperature at the exit of the domain for each variation of the core mass flow rate.

Table 4.3: Results for core mass flow rate variations. 20-vane, hybrid style vane domain, engine conditions

Core Flow Percentage	Tangential Velocity	Mass Flow Rate¹	Pattern Factor²	g-Load
125%	594 m/s	11.52 kg/s	1.83	94,400
100%	602 m/s	11.97 kg/s	0.79	97,000
75%	594 m/s	11.40 kg/s	0.53	94,400
50%	592 m/s	11.37 kg/s	0.42	93,800
25%	591 m/s	11.07 kg/s	0.53	93,450

¹ Cross-sectional mass flow rate through circumferential cavity

The one major problem with the results presented thus far is the g-loading on the fluid in the circumferential cavity. For all test cases, with the exception of one of the 25% mass flow rate test cases, the g-load on the fluid well exceeded 7,500 g's, which both Lewis [3] and Zelina et al. [2] reported to be the blow out limit for stoichiometric combustion. From Figure 2.4 it can be seen that at an equivalence ratio of 2, on which the mass flow rate values were based, any g-loading value above 3,500 g's would result in blowout. Even if a reduced equivalence ratio was used, the g-loading cutoff for blowout would be exceeded. While the variations in mass flow rate

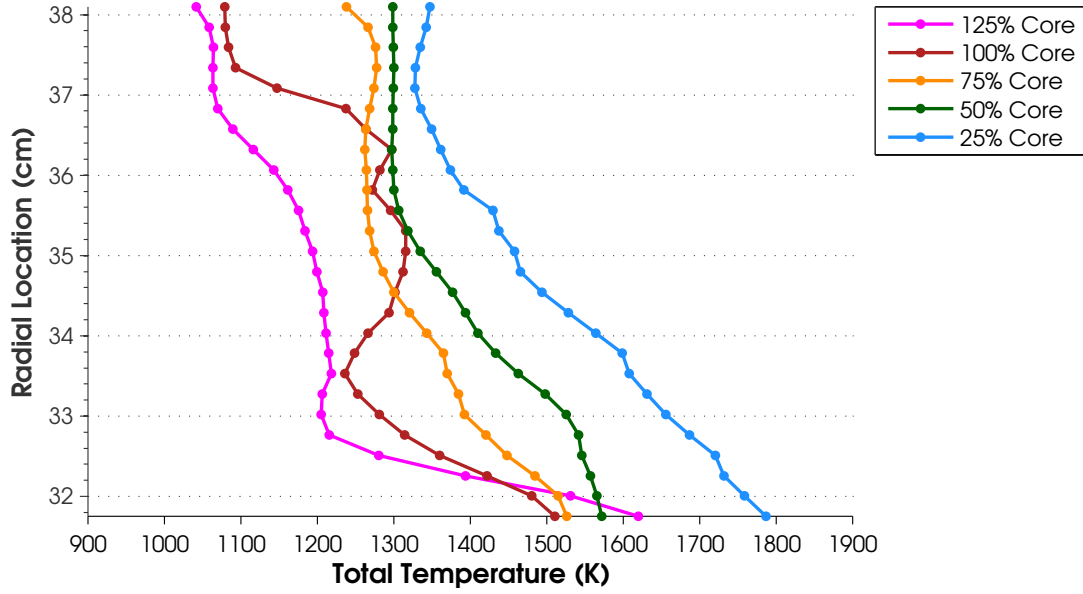


Figure 4.6: Circumferentially-averaged total temperatures at combustor section exit with core mass flow rate variations using 20-vane, hybrid vane style domain (engine conditions)

into the circumferential cavity helped to understand the flow physics, the 100% test cases represent takeoff conditions and other full throttle maneuvers. The engine must be able to operate at the full range of mass flow rates, meaning that simply reducing the mass flow rate into the cavity is not an option to limit the g-load. G-loadings upwards of 80,000 g's, as seen in the previously presented results, would immediately result in a blowout and an unusable engine as the throttle setting was increased. The tangential velocity of the fluid in the cavity must be reduced to reduce the g-load to no more than 3,500 g's at the takeoff condition to ensure the engine could operate at the desired equivalence ratio and necessary mass flow rates.

Since variations in the number or geometry of the vanes and core flow percentages did not cause any appreciable reduction in tangential velocity, another alternative was sought to reduce the g-load. Reduction of the injection velocity was investigated by changing the cavity air inlet area. Using the 20 and 30 hybrid vane domains, the diameter of the air injection ports were enlarged, as discussed in Section 3.4. For constant mass flow rates, as the inlet area increased, the injection velocity decreased.

As shown in Tables 4.4 and 4.5 for 100% cavity inlet mass flow rate for engine and rig conditions, the tangential velocity within the cavity was extremely dependent on the inlet velocity. Figures 4.7 and 4.8 show that this dependence is linear. These figures also reveal that this relationship was maintained at lower cavity inlet mass flow rates, making the relationship mass flow rate independent.

Table 4.4: Results for air inlet area variations, 100% cavity inlet mass flow rate, 20-vane, hybrid style vane domain

Op Con	Inlet Name	Inlet Area ¹	Tangential Velocity	Mass Flow Rate ²	Pattern Factor	g-Load
Engine	Baseline	3.19 cm ²	602 m/s	11.76 kg/s	0.79	97,000
Engine	2x	12.87 cm ²	213 m/s	3.79 kg/s	0.41	12,100
Engine	3x	28.75 cm ²	89 m/s	1.67 kg/s	0.35	2,100
Engine	Top Wall	57.29 cm ²	61 m/s	1.20 kg/s	0.34	1,000
Rig	Baseline	3.19 cm ²	388 m/s	0.36 kg/s	1.66	40,300
Rig	2x	12.87 cm ²	141 m/s	0.12 kg/s	0.37	5,300
Rig	3x	28.75 cm ²	60 m/s	0.05 kg/s	0.55	1,000
Rig	Top Wall	57.29 cm ²	40 m/s	0.04 kg/s	0.64	400

¹ Total inlet area for the domain section

² Cross-sectional mass flow rate through circumferential cavity

Table 4.5: Results for air inlet area variations, 100% cavity inlet mass flow rate, 30-vane, hybrid style vane domain

Op Con	Inlet Name	Inlet Area ¹	Tangential Velocity	Mass Flow Rate ²	Pattern Factor	g-Load
Engine	Baseline	2.40 cm ²	571 m/s	10.98 kg/s	0.21	87,000
Engine	2x	8.05 cm ²	210 m/s	4.08 kg/s	0.43	11,800
Engine	Top Wall	37.89 cm ²	67 m/s	1.15 kg/s	0.32	1,200
Rig	Baseline	2.40 cm ²	334 m/s	0.44 kg/s	0.22	30,000
Rig	2x	8.05 cm ²	136 m/s	0.13 kg/s	0.19	5,000
Rig	Top Wall	37.89 cm ²	41 m/s	0.04 kg/s	0.23	450

¹ Total inlet area for the domain section

² Cross-sectional mass flow rate through circumferential cavity

The results for the 20-vane and 30-vane analysis were presented on separate plots for clarity, but as shown in Figure 4.9, the relationship is the same for both

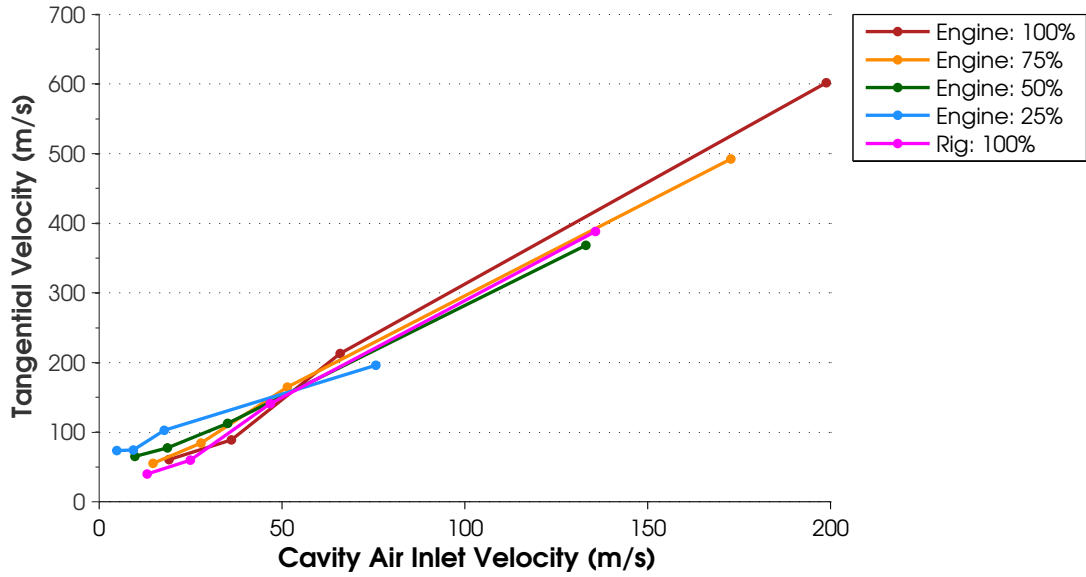


Figure 4.7: Plot of tangential velocity vs. cavity air inlet velocity for the 20 hybrid vane domain

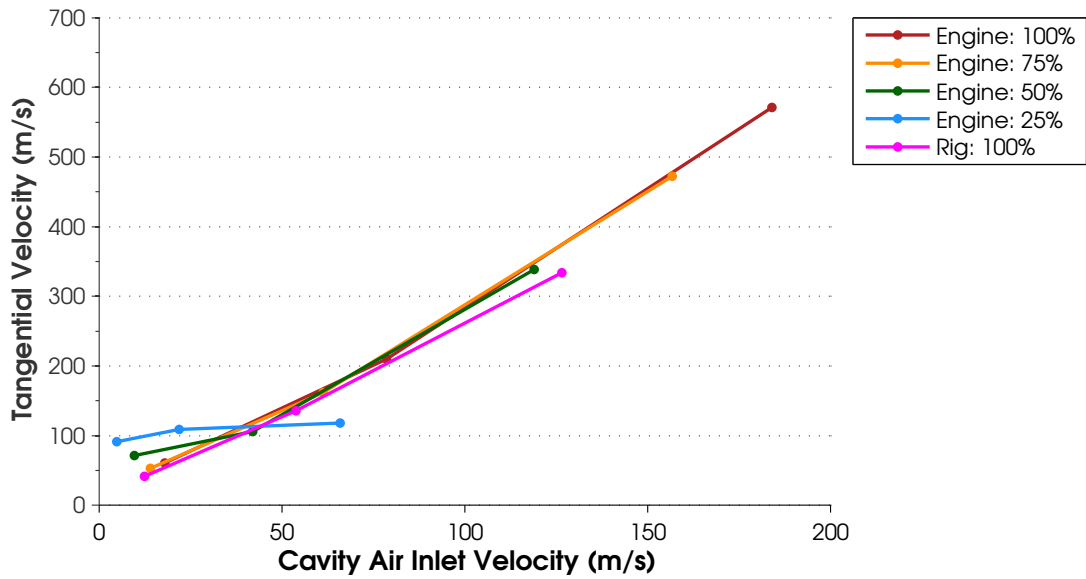


Figure 4.8: Plot of tangential velocity vs. cavity air inlet velocity for the 30 hybrid vane domain

geometries. Figure 4.10 shows the resulting relationship between the inlet area and the tangential velocity.

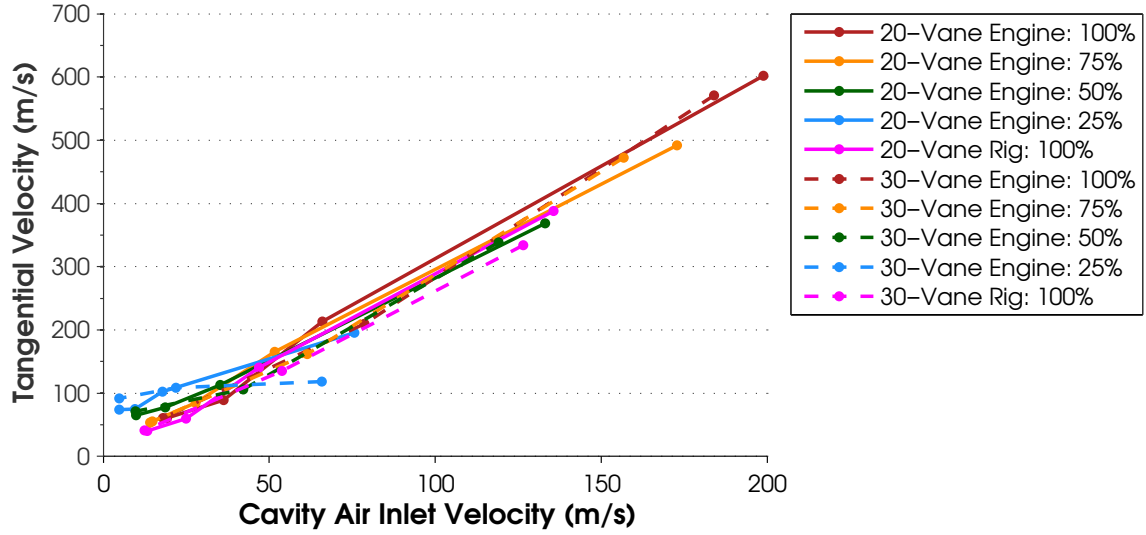


Figure 4.9: Plot of tangential velocity vs. cavity air inlet velocity for both hybrid vane domains

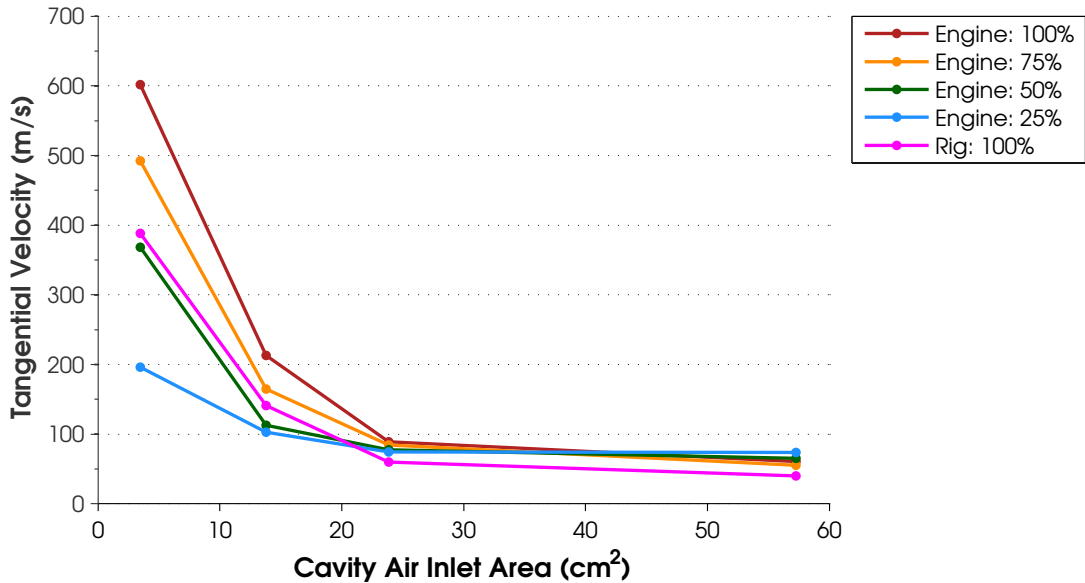


Figure 4.10: Plot of tangential velocity vs. cavity air inlet area for the 20 hybrid vane engine condition

In Figures 4.7, 4.8 and 4.10 it can be seen that the rig condition tangential velocity results were closely matched to the 50% mass flow rate engine condition despite a large difference in operating pressure, mass flow rate and inlet temperature. The results are similar because the resultant inlet velocities were very closely matched,

confirming that the inlet velocity is the driving parameter in controlling tangential velocity regardless of the remaining parameters.

In Figure 4.7 it can be seen that the lower cavity mass flow rates (50% and 25%) operating with the larger diameter inlets (slower velocity inlets) achieved faster cavity tangential velocities than the higher mass flow rate cases using the same inlets. This anomaly was the result of the lower mass flow rates entraining core flow fluid into the cavity. Another effect of the entrained core flow in the circumferential cavity was a greatly reduced cavity temperature. The flow pattern in the cavity for the lower mass flow rates revealed a bulk flow in the circumferential direction in conjunction with a swirl component. This pattern was not observed in the higher flow rate cases which only had a circumferential flow component.

The exit temperature profile was impacted by the variation of the air inlet area as well. Figures 4.11 and 4.12 show the circumferentially-averaged total temperatures for each inlet area variation using 100% cavity inlet mass flow rate for the 20 and 30 hybrid vane domains at engine conditions, respectively. Figures 4.13 and 4.14 show the same parameters for the 20 and 30 hybrid vane domains at rig conditions, respectively. In all four cases the OD endwall temperature was fairly constant with the largest variation at 13%. The ID endwall, however, was the region most impacted by the air inlet area variation and the change in tangential velocity. In general, higher inlet velocities resulted in higher ID endwall temperatures. There was not a direct linear relationship that applied to the results since the 20-vane, 3x diameter case resulted in a lower ID endwall temperature than the top wall injection case. This relationship does show, however, that slower tangential velocities do not allow the fluid exiting the circumferential cavity to completely penetrate the core flow and heat the endwall as it is convected downstream.

To understand why the exit temperature changes, contour plots of the total temperature on the vane, ID endwall and domain exit are shown in Figure 4.15 for 100% cavity inlet mass flow rate for each inlet diameter test case using the 20 hybrid

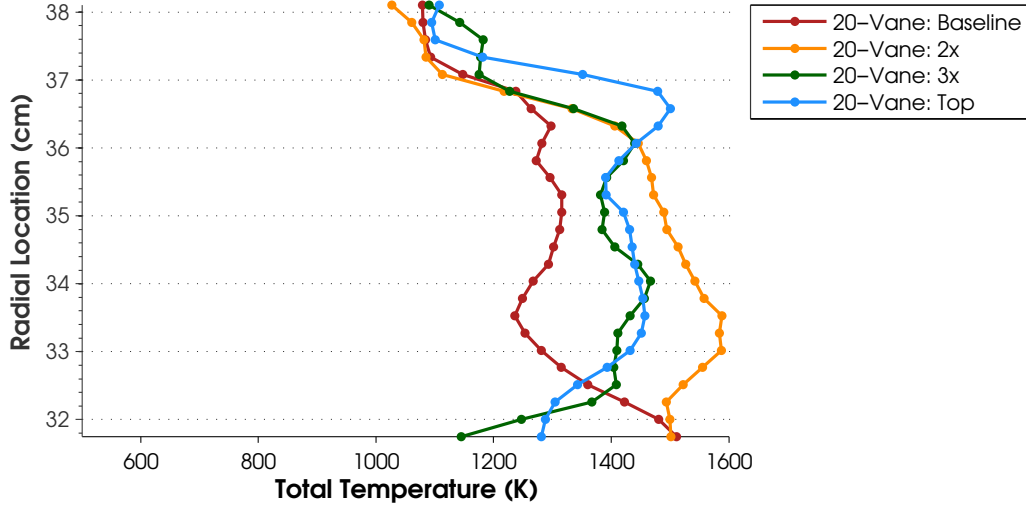


Figure 4.11: Circumferentially-averaged total temperatures at combustor section exit with air inlet variations using the 20 hybrid vane domain (engine conditions)

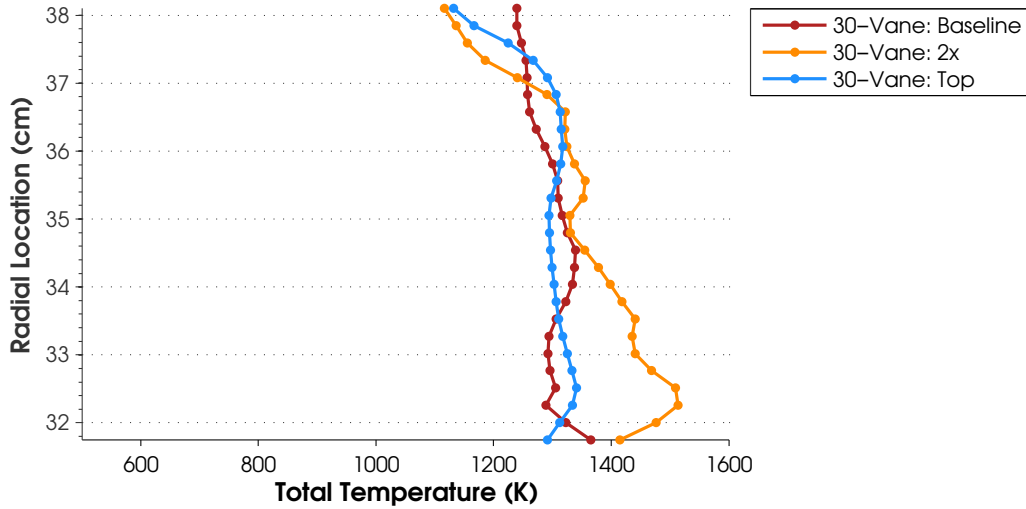


Figure 4.12: Circumferentially-averaged total temperatures at combustor section exit with air inlet variations using the 30 hybrid vane domain (engine conditions)

vane domain. In the baseline and 2x diameter inlet test cases, region 1 highlights the areas on the suction surface that were cooled by OD core flow that was entrained by the high-velocity cavity flow and swirled into the vane. The profile of the hot fluid on the vane surface after exiting the cavity was directly proportional to the velocity of the fluid in the circumferential cavity. Faster cavity flows had little or no

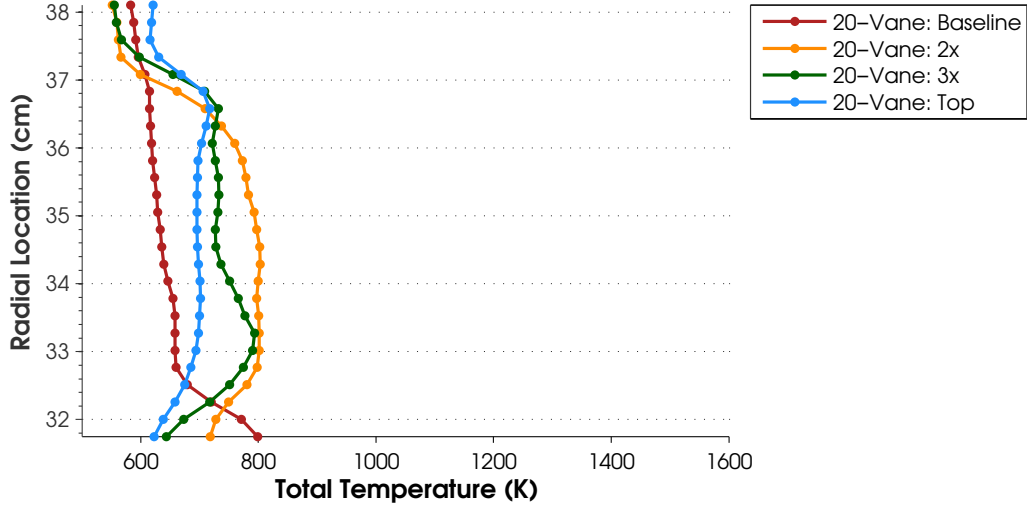


Figure 4.13: Circumferentially-averaged total temperatures at combustor section exit with air inlet variations using the 20 hybrid vane domain (rig conditions)

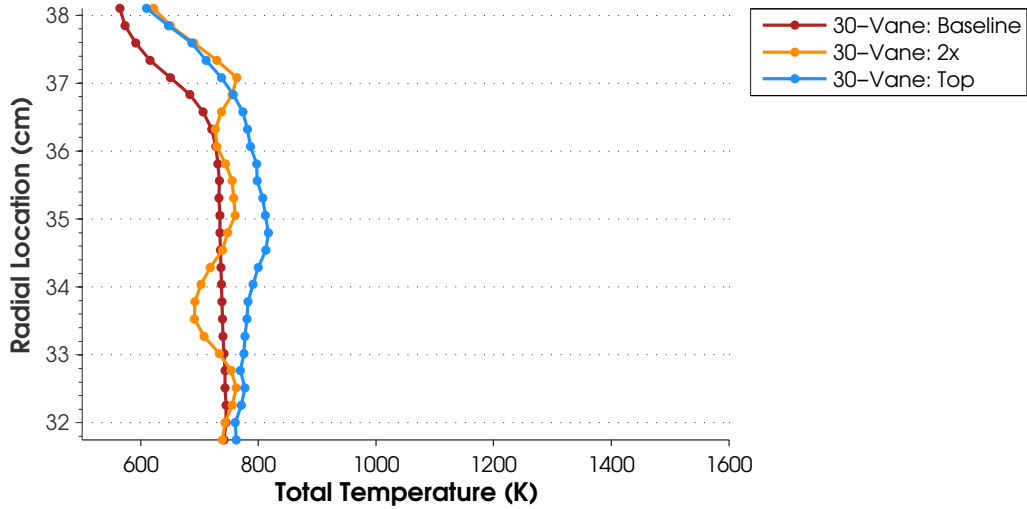


Figure 4.14: Circumferentially-averaged total temperatures at combustor section exit with air inlet variations using the 30 hybrid vane domain (rig conditions)

curvature at location 2, but due to the momentum of the fluid exiting the cavity, the profile at location 3 was almost linear. The 3x and top wall inlet domains showed more curvature at location 2, to the extent that the fluid on the vane surface did not reach the endwall. There was still fluid downstream, however, that swirled off the vane surface and caused ID endwall heating. Additionally, the fluid at location 3 did

not have the same linear profile observed in the baseline case resulting in a reduced heated footprint. A smaller heated area on the vane surface means that there will be less area to cool in future iterations of the analysis. Because the endwall surface is difficult to cool and ingestion of hot gases into the ID engine seams could result in catastrophic failure, the ideal situation would have no excess heating of either endwall. The contour plots for the 30 hybrid vane domain under engine conditions and the rig condition tests using the 20 and 30 hybrid vane domains are shown in Appendix D.

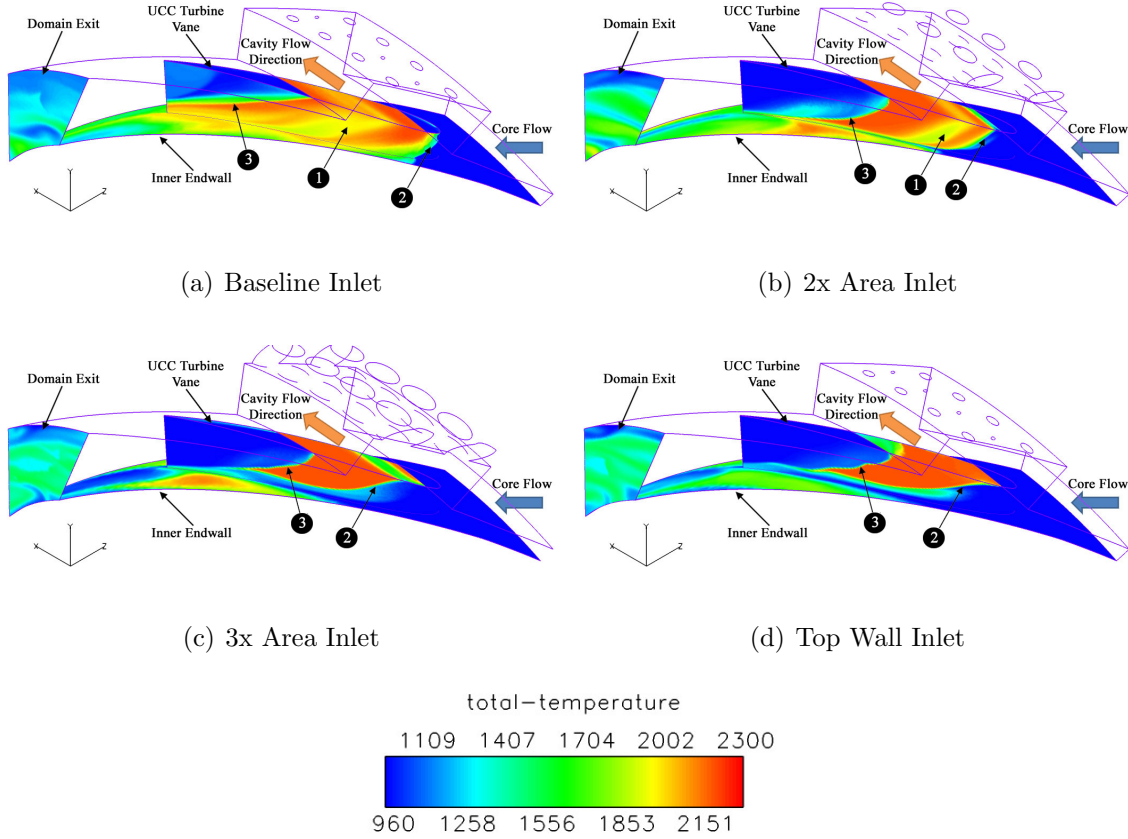


Figure 4.15: Total temperature contours on UCC components using 100% cavity inlet mass flow, 20 hybrid vane domain under engine conditions

Figure 4.16 shows streamlines from the 3x air inlet test case of the flow exiting the circumferential cavity interacting with the core flow and convecting downstream. Reducing the tangential velocity in the cavity allowed greater control over the exit pattern of the cavity fluid. The slower cavity flow did not have the same swirl pattern

between the vanes that was shown in Figure 4.4 and thus did not heat the pressure surface of the neighbor vane or the ID endwall below the cavity. There was, however, some localized heating of the ID endwall downstream. Additionally, the cavity fluid was able to exit across the entire width of the cavity uninhibited by fluid that exited from the upstream edge of the cavity and swirled around to block the fluid at the downstream edge of the cavity.

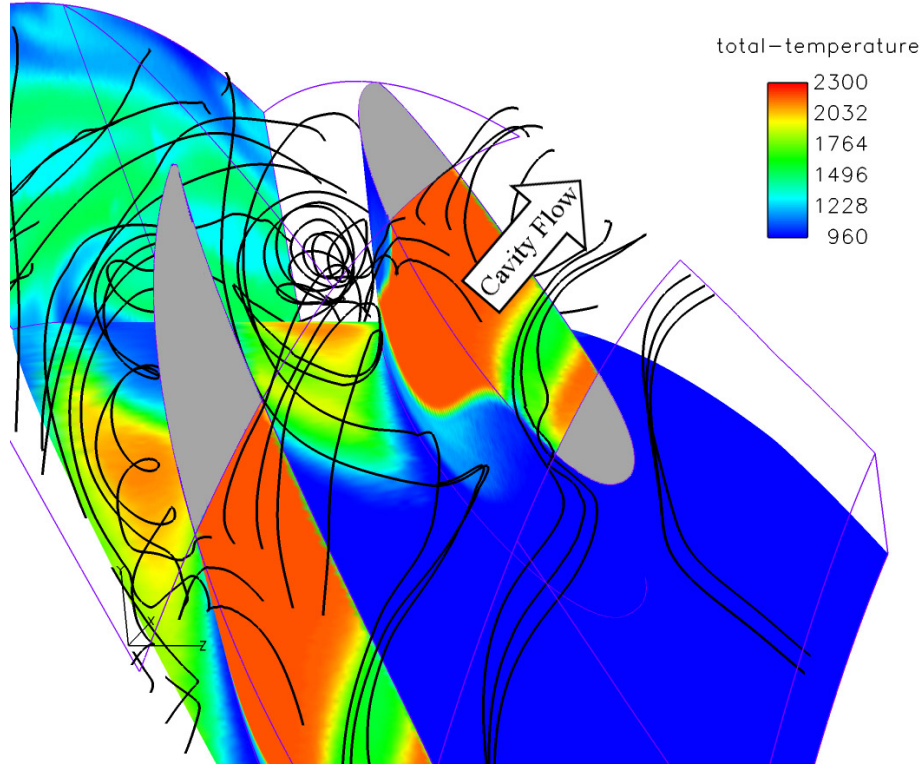


Figure 4.16: Streamlines from the 3x area air inlet, 20 hybrid vane domain under engine conditions

While no fighter-scale UCC experimental studies have been conducted to support the current CFD results, a recent experimental study by LeBay et al. [40] conducted on a small-scale UCC section showed the flow pattern of hot gases exiting the circumferential cavity. The geometry and flow conditions in the study by LeBay et al. were not exactly matched to the current fighter-scale numerical analysis, however, the pattern of fluid exiting the circumferential cavity provided some confidence that the CFD results from the current analysis were reasonable. Figure 4.17 shows a time

lapsed sequence of pictures from the LeBay et al. study using a circumferential cavity velocity to core flow velocity ratio of 3.456 operating at atmospheric pressures. The test rig used in the study featured a constant core flow channel (and vane) height of 2.8 centimeters with a circumferential cavity width of 3.8 centimeters. The radius of curvature of the cavity was 5.5 centimeters.

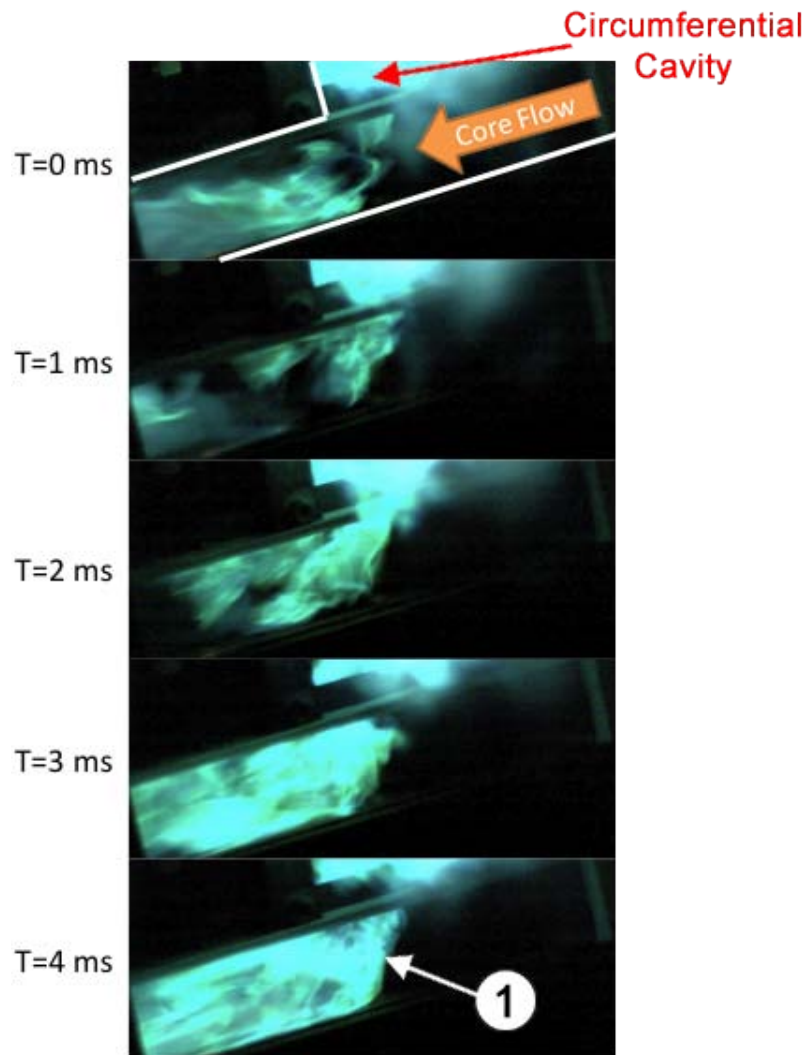


Figure 4.17: Time lapse sequence of fluid exiting the circumferential cavity during small-scale UCC experimental testing [40]

The velocity ratio in the current CFD analysis that was most closely matched to the experimental conditions used by LeBay et al. was 4.45 and was found using

the 30 hybrid vane domain with a baseline air inlet diameter under rig conditions. The contours of total temperature on the vane surface for this test case are shown in Figure 4.18.

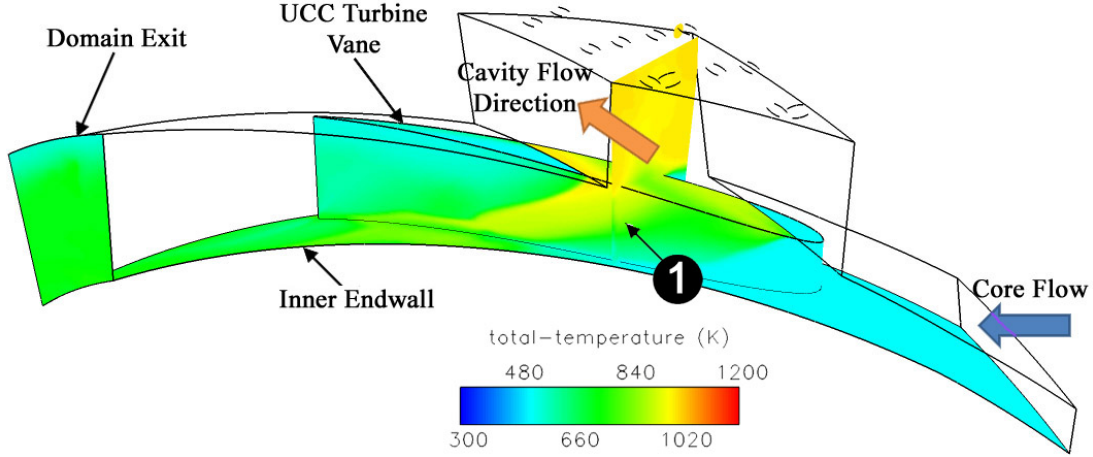


Figure 4.18: Contours of total temperature in the 30 hybrid vane domain with baseline air inlet diameters under rig conditions. Velocity ratio = 4.45

Comparing the CFD results from the current numerical study shown in Figure 4.18 to the experimental results from LeBay et al. shown in Figure 4.17 produced several similarities. In both figures the majority of the hot gases exited the circumferential cavity from approximately the downstream third of the cavity. Additionally, the profile of the hot gases at location 1 in both figures is fairly linear and spanned the radial distance of the vane. While it is not clearly visible in the still images of Figure 4.17, a fluid swirl pattern between the UCC turbine vanes similar to that shown in Figure 4.16 can be seen in a corresponding video taken by LeBay et al. (not shown).

The mass flow rate in the circumferential cavity is an indicator of how far the fluid travels in the cavity from the injection hole to its exit into the core flow. Using the 20-vane domain as an example, the value of the mass flow rate into and out of the circumferential cavity was 0.875 kg/s per section. The cross-sectional mass flow rate in the circumferential cavity, however, was much higher. This value was larger than the section inlet mass flow rate but less than the total inlet mass flow rate for the engine. The cavity cross-sectional mass flow rate was a result of the fact that the fluid

does not enter the cavity and immediately exit the cavity at the next vane, resulting in a build-up of fluid. The amount of fluid transported in the cavity was proportional to the number of inlets upstream from a reference location whose fluid has not exited the cavity. Larger mass flow rates mean that fluid is staying in the cavity longer and thus traveling farther before exiting. Dividing the cavity mass flow rate from Table 4.4 by the inlet mass flow rate per vane section (0.875 kg/s), the number of vanes and the physical distance between the inlet and exit position were determined. These measurements were verified by interrogating the streamlines in the CFD solutions. Figure 4.19 shows the streamlines in the circumferential cavity for the 20 hybrid vane domain at engine conditions for the baseline and 3x air inlets.

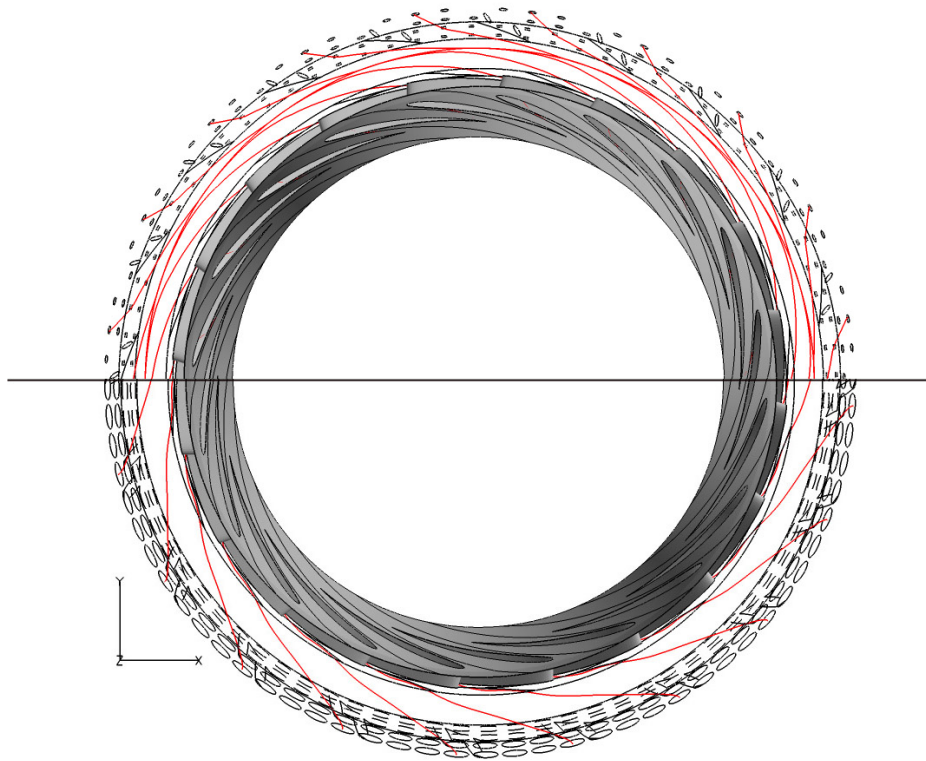


Figure 4.19: Streamlines in the circumferential cavity for the 20 vane domain using baseline air inlets (above) and 3x air inlets (below)

Using the tangential velocity from Tables 4.4 and 4.5 and the arc length traveled between the fluid inlet and exit, the residence time was computed. The resulting

residence times are shown in Table 4.6 for engine and rig conditions for 20 and 30 vane domains. The range of residence times shows the lowest and highest time calculated for all air inlet variations. Between the two vane types there was virtually no difference in residence time further supporting that for low vane counts, the number of vanes has little to no effect on the properties in the circumferential cavity.

Table 4.6: Residence time for 20 and 30-vane domains

Vane Count	Test Condition	Residence Time
20	Engine	0.0024-0.0027 sec
20	Rig	0.0034-0.0038 sec
30	Engine	0.0026 sec
30	Rig	0.0039-0.0043 sec

Despite the fact that the 3.81 centimeter circumferential cavity test case was the first case run in the preliminary analysis, it is the last geometry variation discussed in this section. The reason the results are presented out of order is because the previous analysis and discussion helped to explain the results obtained in the 3.81 centimeter case. This test was run only once and used the engine conditions in a 20 hybrid vane domain with baseline diameter air inlet ports. The result from this test is shown in Table 4.7 with the results of the same test conducted with the 4.83 centimeter cavity used in all other analysis in this report.

Table 4.7: Circumferential cavity flow properties using different cavity sizes

Cavity Size	Vane Count	Tangential Velocity	Mass Flow Rate ¹	g-Load
3.81 cm	20	610 m/s	6.77 kg/s	99,500
4.83 cm	20	606 m/s	11.31 kg/s	98,250

¹ Cross-sectional mass flow rate through circumferential cavity

When the results of the 3.81 centimeter cavity test case were obtained, it was hypothesized that the cavity was too small to hold the desired cavity inlet mass flow rate which resulted in a large cross-sectional mass flow rate through the cavity and the extremely high tangential velocity. Based on this result, a larger cavity measuring 4.83

centimeters, was tested. From Table 4.7, it can be seen that the tangential velocity in the circumferential cavity was only reduced 0.7% with the new cavity size; not the reduction in velocity that was expected. The mass flow rate through the cross-section of the circumferential cavity was increased for the larger cavity while maintaining a similar tangential velocity and fluid density. The only reason the larger cavity resulted in a larger cross-sectional mass flow rate was due to the larger cross-sectional area. It was not until the preliminary analysis was completed that these results made sense. Both domains used the same size and number of cavity inlet ports with the same cavity inlet mass flow rate. From the previous analysis it was shown that the inlet velocity had the largest control over the tangential velocity and that the seemingly linear relationship of cavity inlet velocity to tangential velocity was independent of the inlet mass flow rate. From the comparison between the different cavity sizes, it was determined that this relationship extends beyond a correlation that only applied to a specific cavity dimension. For a steady-state solution, the amount of fluid in the circumferential cavity was adjusted to maintain the flow properties dictated by the cavity inlet conditions.

While the relationships of inlet velocity to tangential velocity and bulk flow patterns were validated by the complex analysis of the reacting flow models, the pressures on the cavity inlets obtained in the preliminary analysis were not feasible. In FLUENT[®], only the domain exit pressure and mass flow rates into the domain could be set. Due to the extremely high cavity inlet temperature resulting from injecting air at combustion temperatures, the pressure required to maintain the desired mass flow rate into the cavity was 55% larger than the domain inlet pressure. This resulted in a cavity inlet pressure in excess of 7,227,000 Pa. The large cavity inlet pressure resulted in an increase in total pressure across the combustor section in approximately 50% of the test cases. In an engine, both the domain inlet and the cavity inlet would be fed from the same compressor. The huge pressure demand for the cavity inlet ports could not be supported. The cavity inlet pressure was reduced in the advanced analysis using realistic inlet temperatures with combustion models.

4.2 5-Species Reacting Flow Analysis

The primary focus of the 5-species analysis was to quantify the relationship of cavity inlet velocity to tangential velocity using a 5-species reacting flow model that included stoichiometric reactants and products. This model allowed fuel and air to be injected into the cavity separately and the cavity inlet temperature to be reduced from the preliminary analysis value. Using the air inlet variations and solver settings discussed in Section 4.2, the 20 and 30 hybrid vane domains were run with engine and rig conditions. Each domain was run at each operating condition using several cavity inlet diameters. The results for each test case series are shown in Figure 4.20 as the solid lines. These lines use the common x-axis and the y-axis on the left side of the plot to display the relationship between cavity inlet velocity and tangential velocity. From these results it can be seen that the engine conditions produced a slightly higher tangential velocity for the same inlet velocity. The engine condition also had a higher combustion temperature which could be contributing to a lower cavity density and slightly higher tangential velocity. The tangential velocity data range in the figure goes from 350 g's to 7,000 g's.

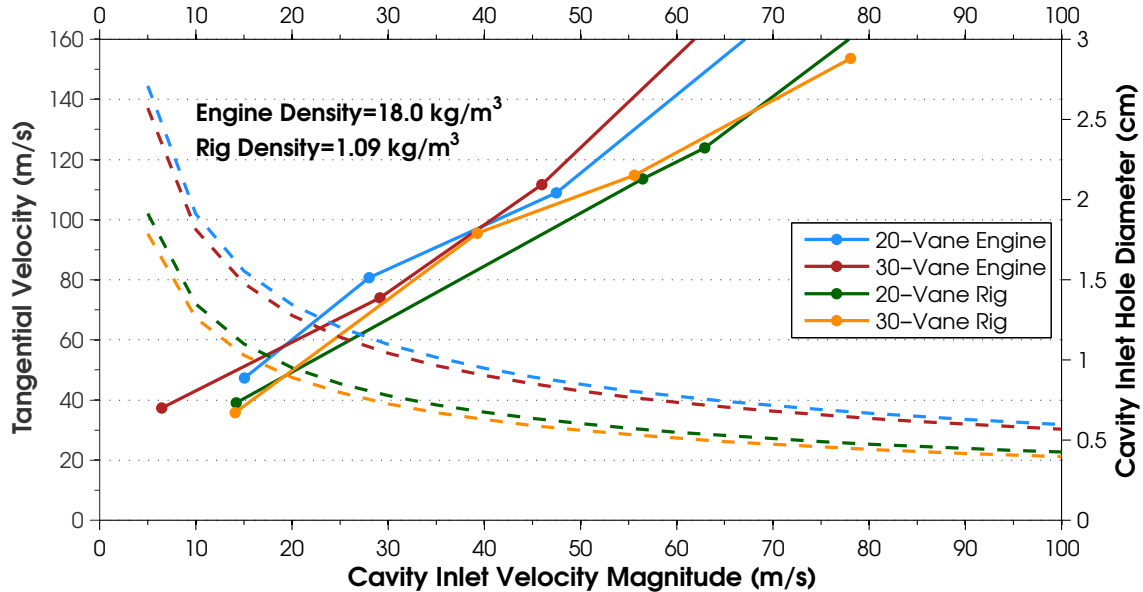


Figure 4.20: Relationship of cavity inlet velocity to cavity tangential velocity and hole diameter for the 5-species analysis

The dashed lines shown in Figure 4.20 represent the diameter of the inlet ports relative to the cavity inlet velocity. These lines use the common x-axis with the y-axis on the right side of the figure. These lines are color coded to specific test configurations and are based on the mass flow rate into the domain section and also the number of air inlet ports in each domain. There is a variation in these relationships based on the density at the inlet of the cavity inlet port and are shown for generic inlet densities. The specific mathematical relationship derived to produce the dashed lines is given in Equation 4.2. In this equation, the resulting cavity inlet port diameter (ϕ) is given in centimeters. The equation was derived using the ideal gas relationships, the area of an ellipse as determined by the injection angle, and accounts for the specified mass flow rate through all of the inlet ports in each domain section.

$$\phi = \left(\frac{4\dot{m}_{section}\sin(\lambda)}{I\rho_{inlet}V_{inlet}\pi} \right)^Q \times 100 \quad (4.2)$$

In Equation 4.2, $\dot{m}_{section}$ is the mass flow rate into the domain section, λ is the inlet port injection angle, I is the number of inlet ports per domain section and ρ_{inlet} and V_{inlet} are the density and velocity at the entrance to the cavity inlet port (boundary surface). The values of the exponent, Q , was tailored to best fit the CFD results for each test configuration and are given in Table 4.8.

Table 4.8: Values of the exponent, Q , for each test configuration

Test Configuration	Value of Q
20-Vane Engine	0.5045
20-Vane Rig	0.502
30-Vane Engine	0.5035
30-Vane Rig	0.503

The idea of an ‘ideal’ tangential velocity was introduced and discussed in Section 4.2 as relating to the maximum g-load in the circumferential cavity for a given equivalence ratio without resulting in blowout. This situation allows for the largest benefit from g-loaded combustion while maintaining a stable flame. For the current

study the ideal tangential velocity was 114 m/s resulting in a g-load of approximately 3,500 g's. Using the correlations presented in Figure 4.20, the cavity inlet velocity was found for the ideal tangential velocity for each test configuration. The cavity inlet port diameters were then determined based on these inlet velocities through the use of Equation 4.2. The cavity inlet mass flow rates were still the same as those outlined in Table 3.7. The results of the ideal tangential velocity analysis are shown in Table 4.9.

Table 4.9: Inlet port diameters and fluid properties for 5-species, 'ideal' tangential velocity analysis

Test Configuration	Inlet Port Diameter	Inlet Velocity	Tangential Velocity	Pattern Factor	g-Load
20-Vane Engine	0.8641 cm	46.9 m/s	113.5 m/s	0.45	3,446
20-Vane Rig	0.5208 cm	56.6 m/s	113.5 m/s	0.47	3,446
30-Vane Engine	0.7931 cm	46.3 m/s	111.6 m/s	0.44	3,329
30-Vane Rig	0.4789 cm	55.6 m/s	114.7 m/s	0.55	3,516

With identical cavity and core inlet mass flow rates and the inlet port diameters tuned to achieve the same tangential velocity in the circumferential cavity, the exit temperature profiles for the engine and rig conditions appear to follow similar trends. The trends are especially noticeable for the 20-vane domains, as shown in Figure 4.21. The combustion temperatures were lower for the rig conditions which resulted in a lower temperature at the domain exit plane as well.

While the 30-vane domains produced a more uniform temperature, the 20-vane domains produced a pattern closer to the desirable temperature profile with cool endwalls and a hot central section of the passage. The 20-vane domains did not produce the full desired profile due to the ID endwall remaining hot, but the profile above 33 centimeters was desirable.

Figures 4.22-4.25 are provided to help illustrate how the exit temperature profiles were formed and identify the engine surfaces impacted by the hot gases exiting the cavity. The contour plane in the circumferential cavity in Figures 4.22-4.25 shows

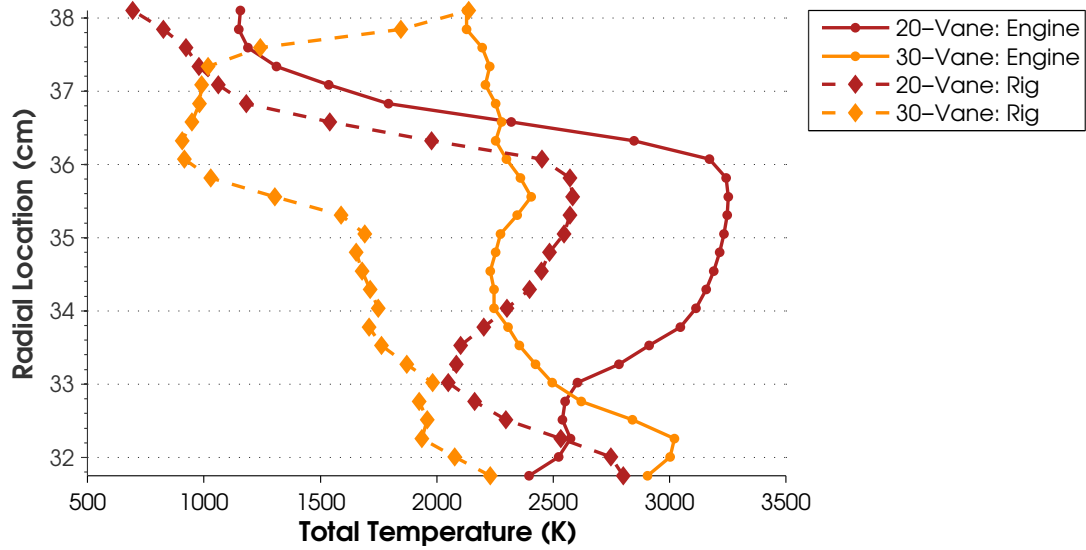


Figure 4.21: Circumferentially-averaged total temperatures at combustor section exit using the 5-species model and ideal air inlet diameters for each test configuration

a variation in cavity temperature resulting from the use of a combustion model. These contour planes also help illustrate the mixing properties and primary combustion regions within the cavity. The variation in temperature throughout the circumferential cavity was not seen in the preliminary analysis due to the simplifications used.

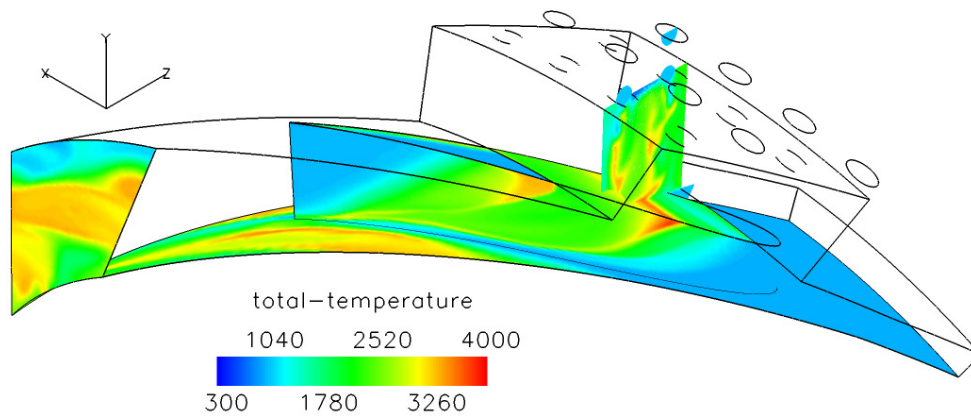


Figure 4.22: Total temperature contours on UCC components for ideal tangential velocity in the 20 hybrid vane domain under engine conditions

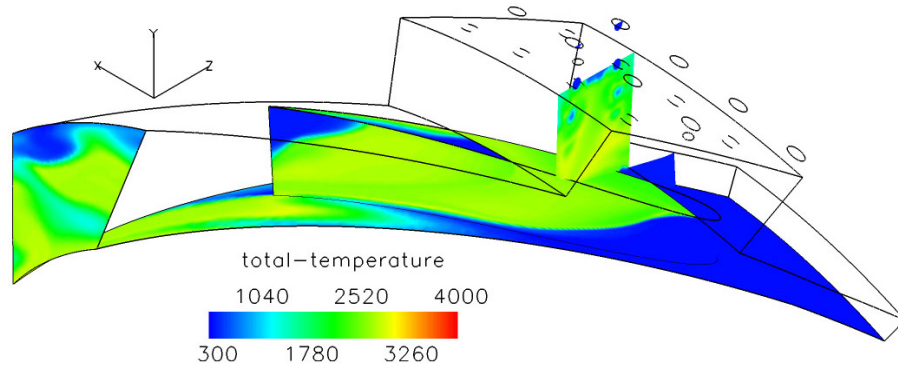


Figure 4.23: Total temperature contours on UCC components for ideal tangential velocity in the 20 hybrid vane domain under rig conditions

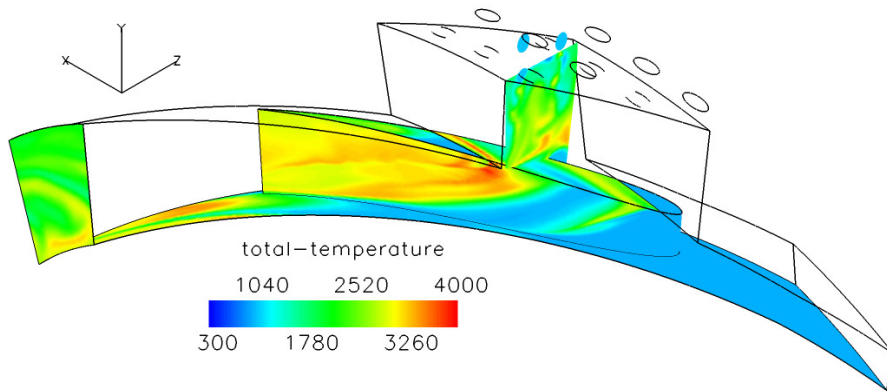


Figure 4.24: Total temperature contours on UCC components for ideal tangential velocity in the 30 hybrid vane domain under engine conditions

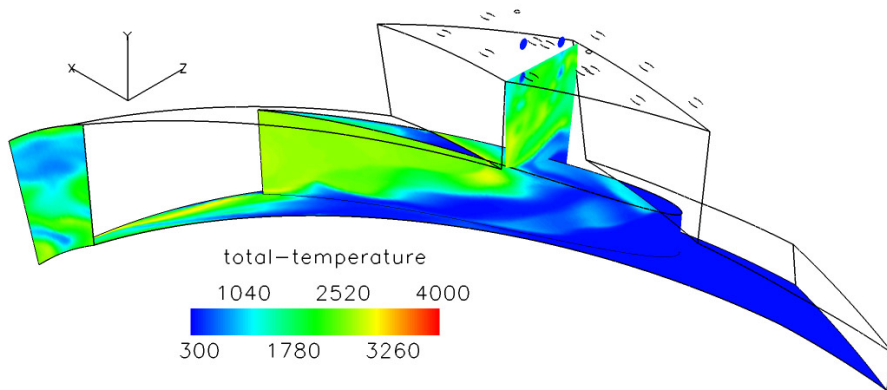


Figure 4.25: Total temperature contours on UCC components for ideal tangential velocity in the 30 hybrid vane domain under rig conditions

The static and total pressures were calculated at the domain inlet, circumferential cavity inlet and domain exit for each ideal test configuration. The results are reported in Table 4.10 along with the pressure difference from the domain inlet to the domain exit. A negative percent difference indicates a pressure drop across the combustor.

Table 4.10: Calculated pressures for ‘ideal’ test configurations using a 5-species combustion model

Test Configuration	Pressure Type	Domain Inlet (Pa)	Cavity Inlet (Pa)	Domain Exit (Pa)	% Difference
20-Vane Engine	Static	4,975,743	5,112,463	4,626,353	-7.02
	Total	5,113,571	5,139,236	4,834,597	-5.45
20-Vane Rig	Static	115,951	131,303	101,325	-12.61
	Total	119,212	133,820	108,022	-9.39
30-Vane Engine	Static	5,459,956	5,579,885	4,625,999	-15.27
	Total	5,584,357	5,606,926	4,923,104	-11.84
30-Vane Rig	Static	126,864	141,146	101,314	-20.14
	Total	129,817	143,723	110,730	-14.7

Any pressure drop within the combustor section reduces the drop that could be obtained across the turbine rotors and therefore reduces the work potential of the turbine. The UCC is being designed to replace a traditional can-type combustor which currently has an average pressure drop of 6%. For an accurate comparison of the complete pressure drop across the same set of components, the pressure drop across the turbine inlet guide vane must also be considered for the traditional combustor since the UCC includes that component. With the turbine inlet guide vane included, the complete pressure drop across a traditional combustor from the exit of the last compressor rotor to the inlet of the first turbine rotor is approximately 8%. The 20-vane domain offered the lowest pressure drop in static and total pressure for both the engine and rig conditions for the conditions tested and reduced the pressure losses compared to the traditional combustor. One item to note, however, is that using the current test setup with a domain inlet and a separate cavity inlet each operating

at slightly different pressures allowed additional pressure to be added to the system through the cavity inlets. This configuration could be artificially reducing the pressure drop across the UCC section due to the addition of pressure. In an engine where the core flow and cavity inlet flow would both be fed from the same compressor and have the same static pressure, the pressure loss across the combustor system could potentially be increased.

To show the primary regions of pressure loss within the domains Figures 4.26 through 4.29 are provided. These figures show contours of absolute and total pressure on the walls of the 20-vane domain under engine and rig conditions. Due to the relatively small difference in pressure from the domain inlet to the exit, the contours in Figures 4.26 - 4.29 are shown in gray scale because this color scheme more clearly shows subtle variations in value. The absolute pressure shown in the figures is the actual static pressure at each location. As a result of the way FLUENT® outputs pressure data, the total pressure values are referenced to the operating pressures shown in Table 3.7 for each condition. From the contours of Figures 4.26 - 4.29 it can be seen that the bulk of the pressure drop (darker contours) occurred immediately downstream of the circumferential cavity. The pressure drop in this location was the result of a large shear interaction between the UCC and core flows.

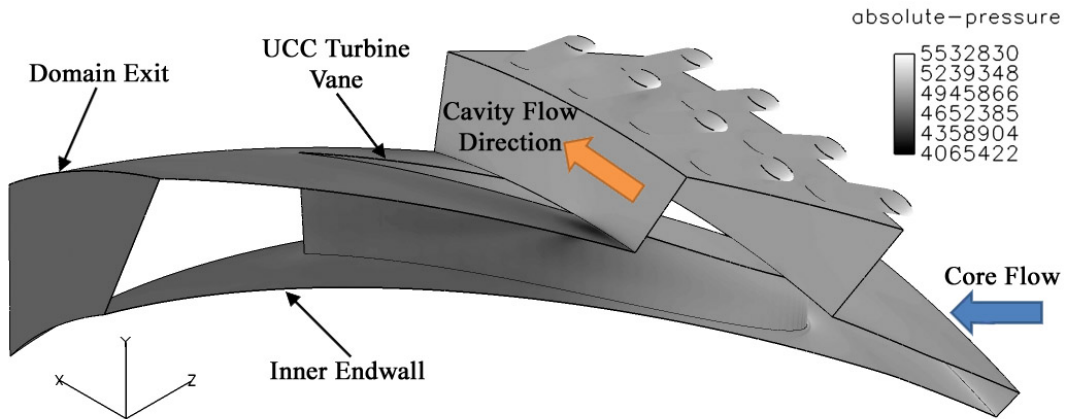


Figure 4.26: Absolute (static) pressure contours on UCC components in the 20 hybrid vane domain under engine conditions

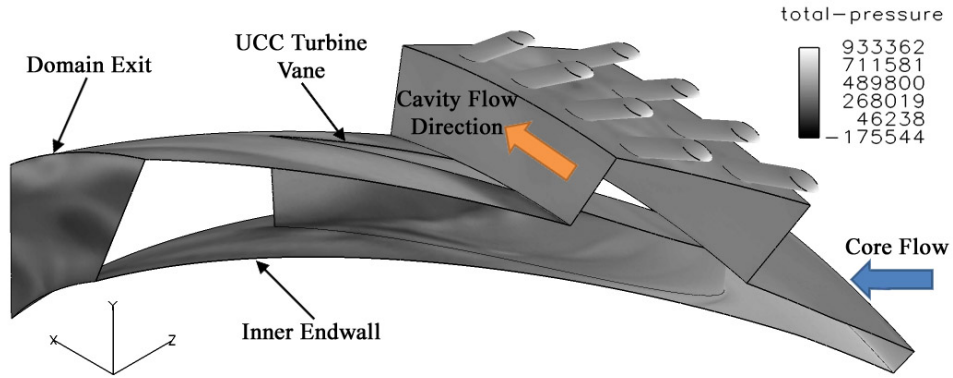


Figure 4.27: Total pressure contours on UCC components in the 20 hybrid vane domain under engine conditions

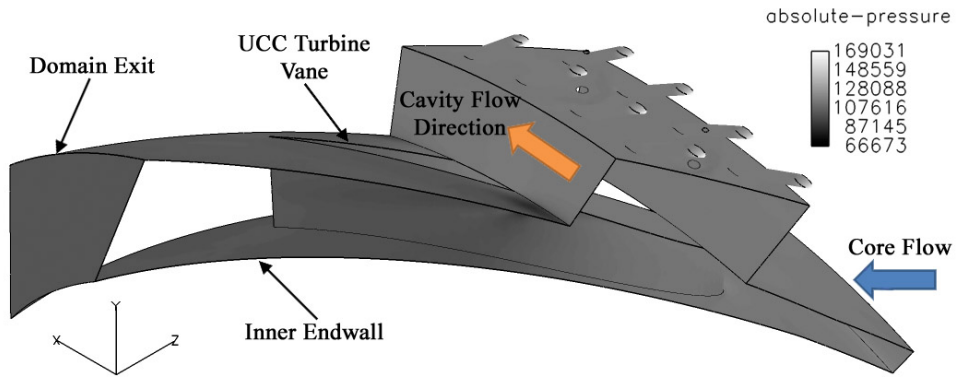


Figure 4.28: Absolute (static) pressure contours on UCC components in the 20 hybrid vane domain under rig conditions

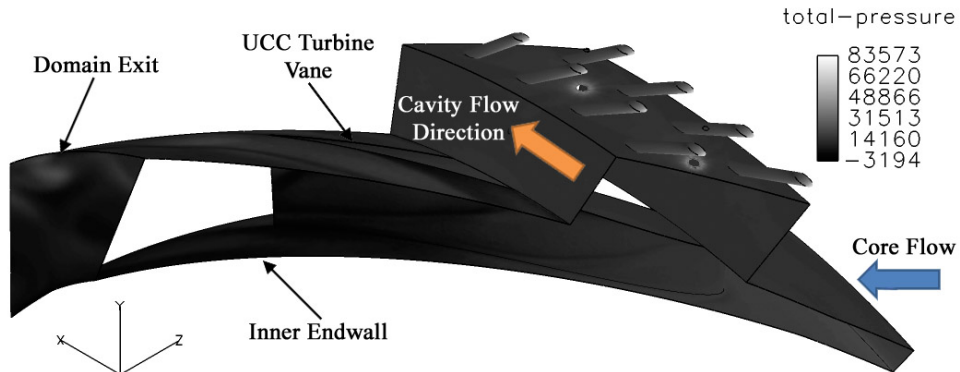


Figure 4.29: Total pressure contours on UCC components in the 20 hybrid vane domain under rig conditions

The previous 5-species results were all obtained using a constant value of C_p for each fluid species as discussed in Section 4.2. Based on the FLUENT[®] documentation [39], a variable value of C_p for each fluid species using a piecewise-polynomial relationship as a function of temperature more accurately predicts combustion temperatures. A constant value of C_p tends to over predict temperature. The 20-vane ideal rig configuration was re-run using the 5-species model and piecewise-polynomial relationships of C_p to determine the impact on the combustion temperatures and tangential velocity in the circumferential cavity. Figure 4.30 shows the circumferentially-averaged total temperatures on the domain exit for the 20-vane ideal rig configuration with constant C_p values and again with piecewise-polynomial values of C_p . From Figure 4.30 it can be seen that the variable C_p reduced the maximum temperature and produced a more uniform profile while leaving the upper endwall temperature the same. The average temperature in the cavity was reduced 19% and the average temperature at the domain exit was reduced 13%. The temperature variation caused a 2.9% increase in tangential velocity resulting from a 1.2% increase in inlet velocity. A negligible difference in pressure at the domain inlet and the cavity inlet was observed. Table 4.11 shows the differences in the fluid properties resulting from the two C_p definitions.

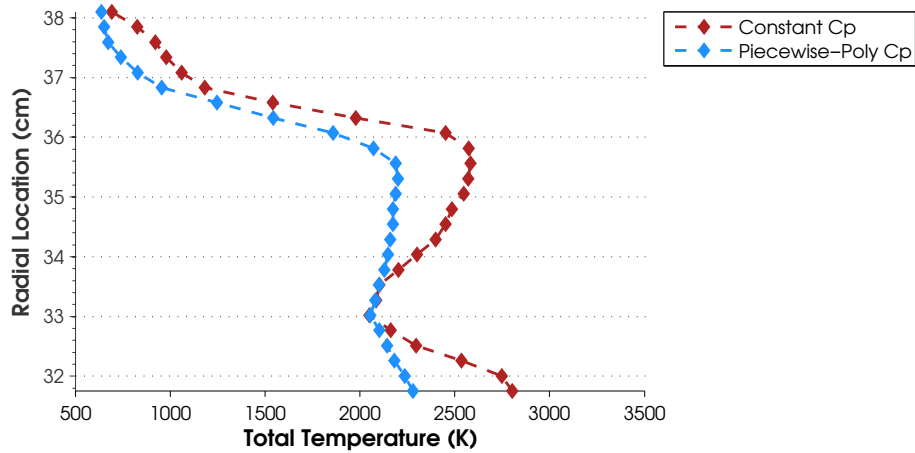
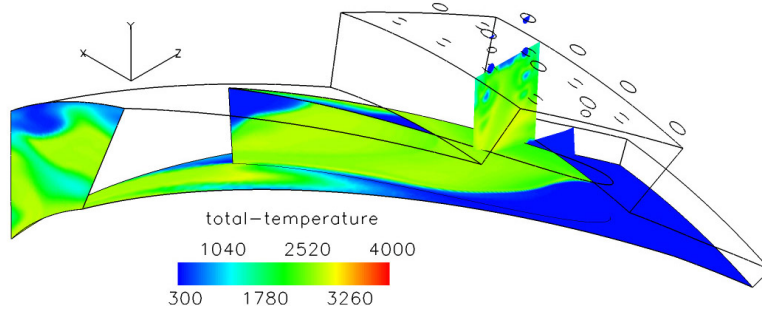


Figure 4.30: Comparison of circumferentially-averaged total temperatures at combustor section exit using the 5-Species model and ideal air inlet diameter for the 20 vane domain under rig conditions with and without variable C_p values

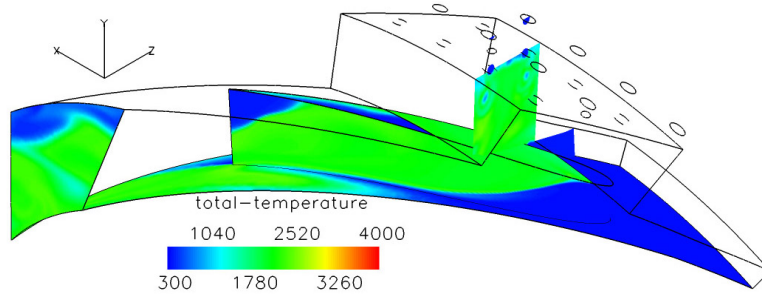
Table 4.11: Fluid properties for 5-species ‘ideal’ tangential velocity analysis for constant and variable C_p values using the rig condition

C_p Model	Tangential Velocity	Inlet Velocity	Average Cavity Temperature	Average Exit Temperature
Constant	113.5 m/s	56.6 m/s	2,346 K	2,018 K
Piecewise-Poly	116.8 m/s	57.2 m/s	1,906 K	1,755 K

Figure 4.31 shows the difference in temperatures calculated using the two definitions of C_p using contour plots which show more of the domain than the exit plane temperature profiles. The differences between the contours is subtle with both solutions displaying almost identical flow and temperature patterns, but the temperatures calculated using the variable C_p were slightly lower.



(a) Constant C_p



(b) Piecewise-Polynomial C_p

Figure 4.31: Total temperature contours on UCC components for ideal tangential velocity in the 20 hybrid vane domain under rig conditions using different definitions of C_p

4.3 12-Species Reacting Flow Analysis

The purpose of the 12-species analysis was to determine the concentrations of species throughout the combustor section and also characterize the species entering the turbine section. The 12-species analysis was performed for the 20 and 30 hybrid vane domains using engine and rig conditions for the ideal cavity inlet diameters determined during the 5-species analysis. The tangential velocity in the circumferential cavity and the corresponding inlet velocity for each case is shown in Table 4.12.

Table 4.12: Inlet port diameters and fluid properties for 12-species analysis using ‘ideal’ inlet diameters determined from 5-species analysis

Test Configuration	Inlet Port Diameter	Inlet Velocity	Tangential Velocity	g-Load
20-Vane Engine	0.8641 cm	51.87 m/s	115 m/s	3,500
20-Vane Rig	0.5208 cm	72.9 m/s	142 m/s	5,400
30-Vane Engine	0.7931 cm	55.7 m/s	133.1 m/s	4,700
30-Vane Rig	0.4789 cm	77.2 m/s	151.2 m/s	6,100

From Table 4.12 it can be seen that the tangential velocities obtained using the 12-species analysis did not result in the ideal velocity of 114 m/s with the exception of the 20-vane engine configuration. The reason for the difference is due to the fluid in the 12-species analysis being treated as an incompressible fluid. The solution was run incompressible due to stability requirements of the CFD simulations. For incompressible solutions, the CFD code determines the operating density based on the operating pressure. The operating pressure in each test configuration was only matched at the domain exit with all other upstream locations operating at higher pressures. This meant that the density at the domain and cavity inlets was too low in each test configuration. A lower density fluid at the cavity inlet resulted in a higher inlet velocity as shown in Equation 2.12. Based on the relationship of inlet velocity to tangential velocity shown in Figure 4.20, the higher inlet velocity resulted in higher tangential velocity. The 20-vane, engine configuration, was least effected by the change to an incompressible fluid because this solution had the lowest cavity

inlet pressure relative to the operating pressure and thus had the smallest change in density at the cavity inlet. Figure 4.32 shows the original tangential velocity to cavity inlet velocity relationship obtained during the 5-species analysis with the locations of the 12-species solutions plotted as well.

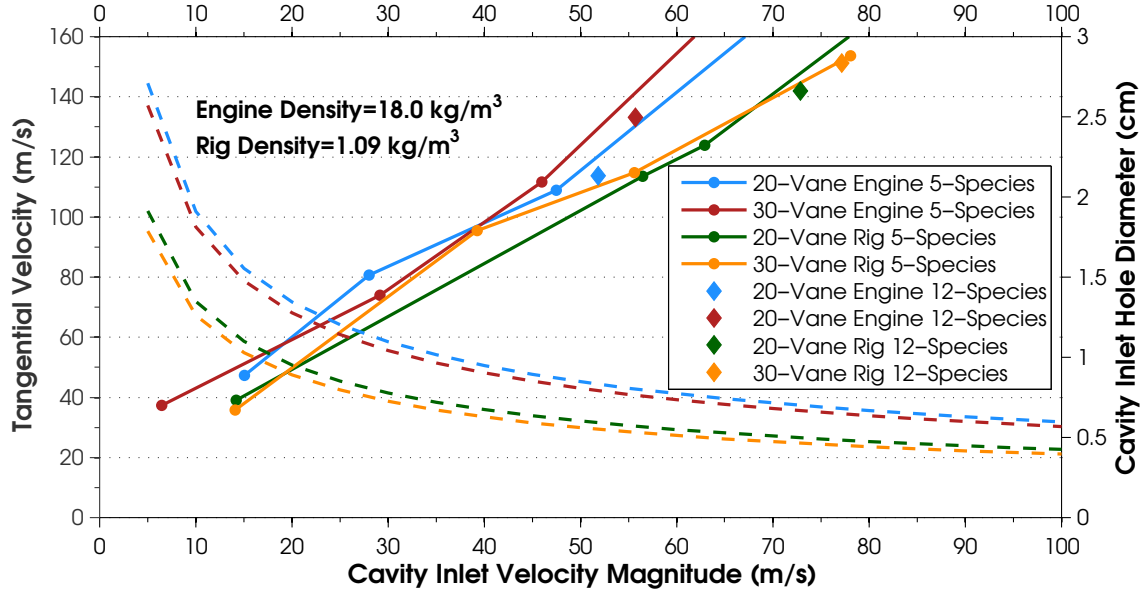


Figure 4.32: Relationship of cavity inlet velocity to cavity tangential velocity and hole diameter

From Figure 4.32 it can be seen that with the exception of the 30-vane rig configuration, the data points collected during the 12-species analysis do not lie directly on the corresponding lines obtained during the 5-species analysis. It can also be seen, however, that the data points from the 12-species analysis lie between data points from the 5-species analysis that were connected linearly. If the slope of each line was continued from the slower velocities to the faster velocities and gradually turned to connect to the higher velocity data point rather than connecting the points linearly, the lines would all cross the corresponding 12-species data points.

While the temperature profiles within the domain and at the domain exit plane were not the focus of the 12-species studies, the circumferentially-averaged total temperatures on the domain exit plane were calculated and are shown in Figure 4.33. Comparing Figure 4.33 to the exit plane results calculated during the 5-species anal-

ysis shown in Figure 4.21, shows that the general profiles produced a similar pattern with the relative magnitudes between the test configurations remaining the same. The 12-species model did, however, predict decreased temperatures in each test. The temperature reduction with the 12-species model was the result of using the piecewise-polynomial values of C_p and the ability to store energy in dissociated intermediate species, neither of which was accounted for in the 5-species analysis.

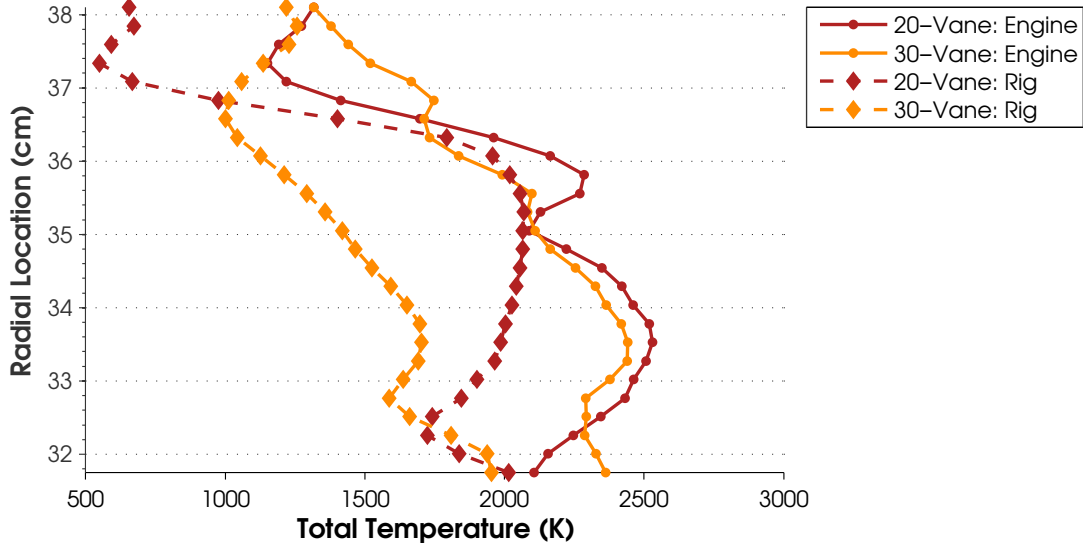


Figure 4.33: Circumferentially-averaged total temperatures at combustor section exit using the 12-Species model and ideal air inlet diameters with piecewise-polynomial C_p values

Again in this study, the static and total pressures were calculated at the domain inlet, circumferential cavity inlet and domain exit for each ideal test configuration. The results are reported in Table 4.13 along with the pressure difference from the domain inlet to the domain exit. A negative percent difference indicates a pressure drop across the combustor. For all test configurations in this series with the exception of the 30-vane rig configuration, the 12-species model predicted lower pressure losses compared to the 5-species model. Again, the 20-vane domain offered the lowest pressure drops in static and total pressure for both the engine and rig conditions with only a 5.2% loss in static pressure and a 4.4% loss in total pressure for the engine condition.

Table 4.13: Calculated pressures and losses for ‘ideal’ cavity inlet diameters using a 12-species combustion model

Test Configuration	Pressure Type	Domain Inlet (Pa)	Cavity Inlet (Pa)	Domain Exit (Pa)	% Difference
20-Vane Engine	Static	4,876,523	5,047,109	4,625,225	-5.15
	Total	5,024,492	5,076,711	4,801,645	-4.44
20-Vane Rig	Static	114,402	132,340	101,324	-11.43
	Total	118,133	135,582	106,797	-9.59
30-Vane Engine	Static	5,322,815	5,471,457	4,626,383	-13.08
	Total	5,469,196	5,504,071	4,885,918	-10.66
30-Vane Rig	Static	131,520	149,348	101,325	-22.95
	Total	135,217	152,915	108,466	-19.78

Based on the results of the 5-species analysis and the results presented above from the 12-species study, the 20 hybrid vane domain is the better UCC configuration offering the lowest pressure losses and a temperature distribution on the domain exit plane closest to the desirable temperature profile. For the remainder of this chapter the results are focused on the 20 hybrid vane domain.

Using the 12-species combustion model allowed iso-surfaces of specific species to be displayed within the domain. Figures 4.34 through 4.41 show iso-surfaces of mass fractions of fuel, CO, OH and H₂ for the 20 hybrid vane domain using the engine and rig conditions, respectively. Since iso-surfaces can only be shown for one specific quantity at a time, a mass fraction of 1/3 of the maximum mass fraction within the domain was displayed for each species. The decimal number located in the legend of each image indicates the mass fraction shown in the iso-surface. If a mass fraction near the maximum was used, only iso-surfaces within the circumferential cavity would be shown since that was the location of maximum combustion and thus resulted in the highest concentrations of the species listed above. Using a mass fraction value closer to the minimum level within the domain allowed the locations of the species outside the cavity to be seen as well. The species that are shown in Figures 4.34

through 4.41 are the compounds that can be used as fuels (fuel, H_2), produce the largest heat release (CO) and indicate combustion (OH).

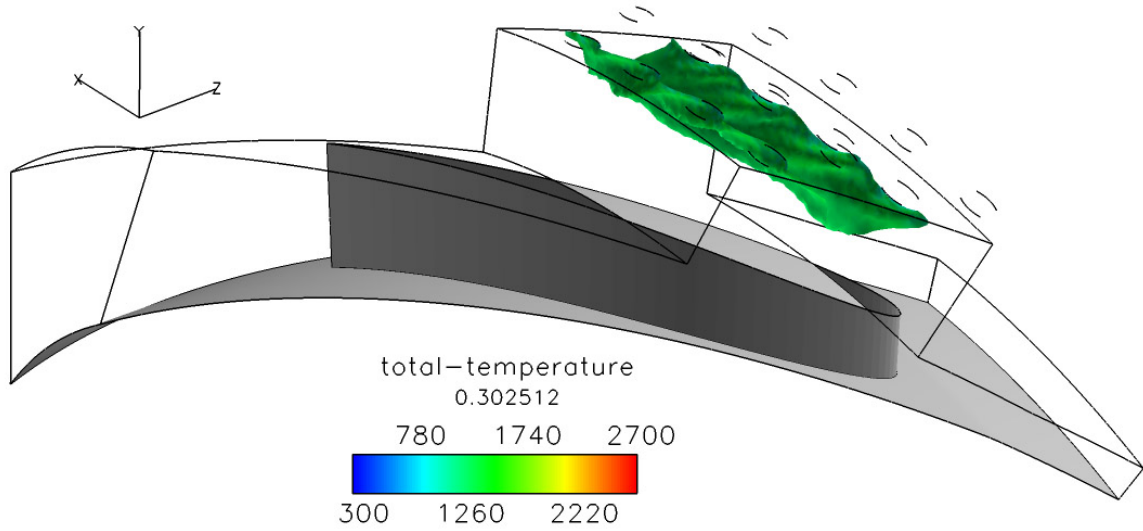


Figure 4.34: Iso-surface of $C_{12}H_{23}$ colored by total temperature using the 12-species combustion model and ideal air inlet diameters with a 20 hybrid vane engine configuration

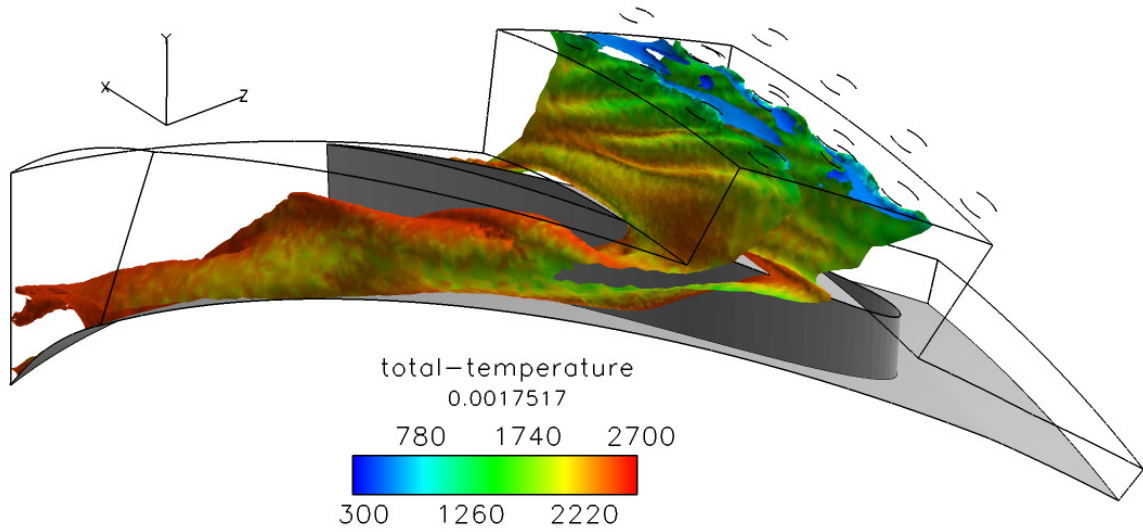


Figure 4.35: Iso-surface of H_2 colored by total temperature using the 12-species combustion model and ideal air inlet diameters with a 20 hybrid vane engine configuration

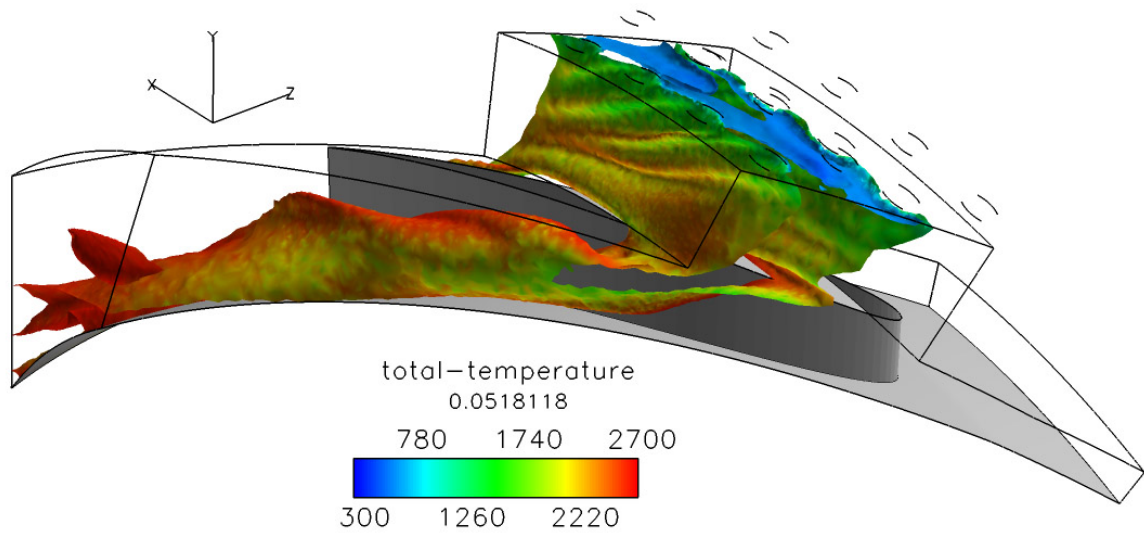


Figure 4.36: Iso-surface of CO colored by total temperature using the 12-species combustion model and ideal air inlet diameters with a 20 hybrid vane engine configuration

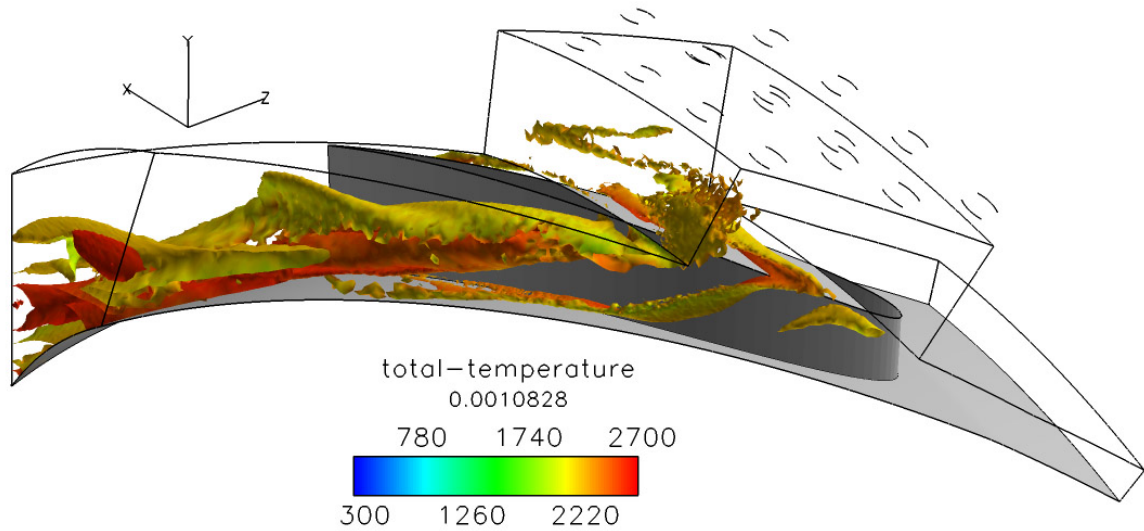


Figure 4.37: Iso-surface of OH colored by total temperature using the 12-species combustion model and ideal air inlet diameters with a 20 hybrid vane engine configuration

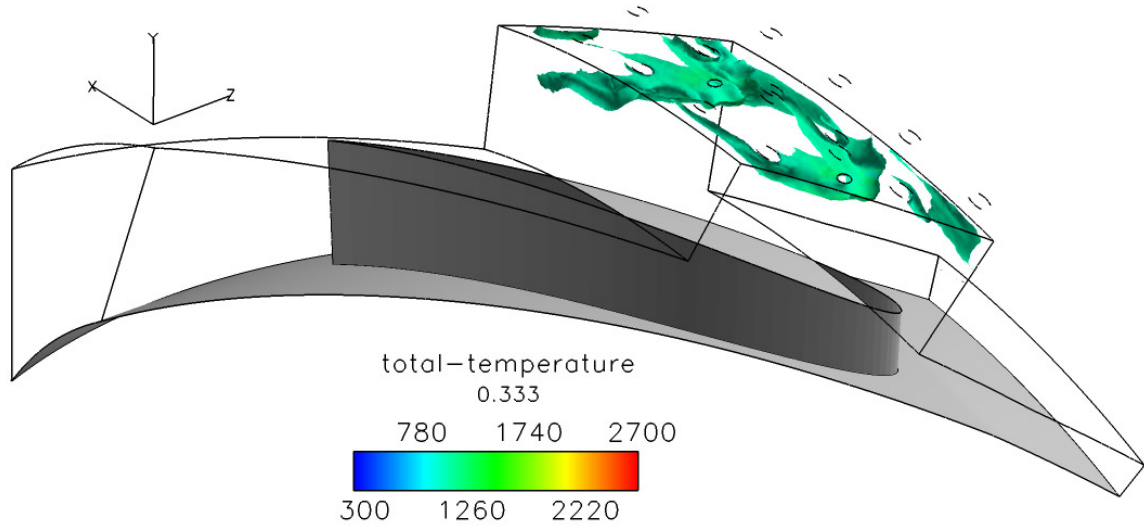


Figure 4.38: Iso-surface of C_3H_8 colored by total temperature using the 12-species combustion model and ideal air inlet diameters with a 20 hybrid vane rig configuration

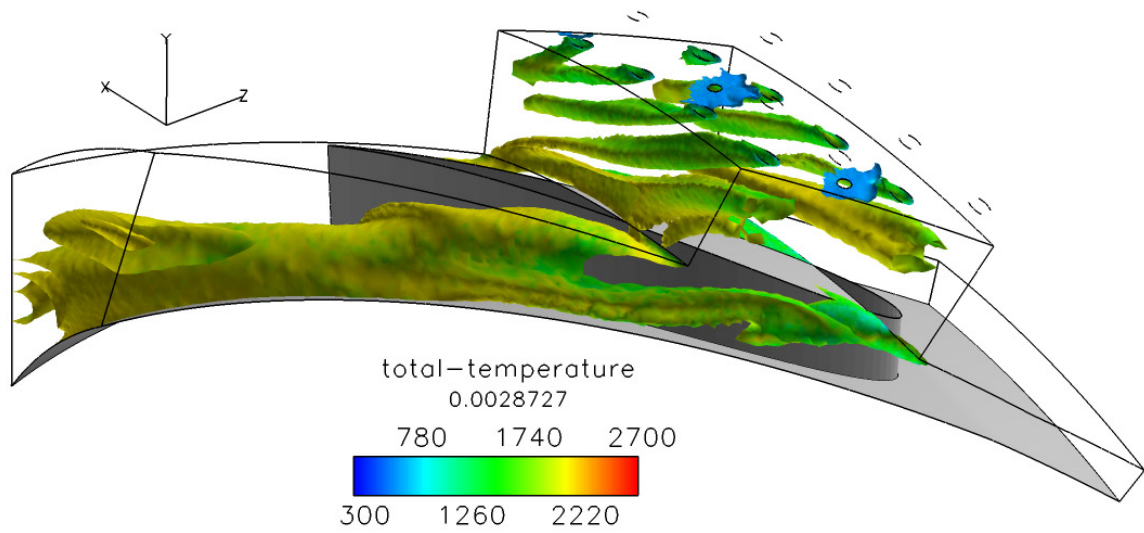


Figure 4.39: Iso-surface of H_2 colored by total temperature using the 12-species combustion model and ideal air inlet diameters with a 20 hybrid vane rig configuration

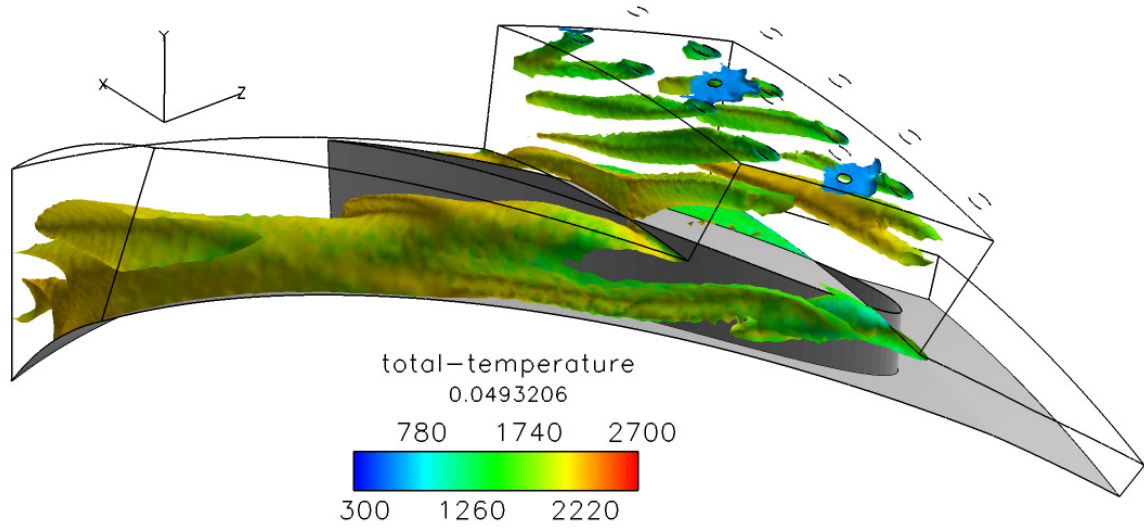


Figure 4.40: Iso-surface of CO colored by total temperature using the 12-species combustion model and ideal air inlet diameters with a 20 hybrid vane rig configuration

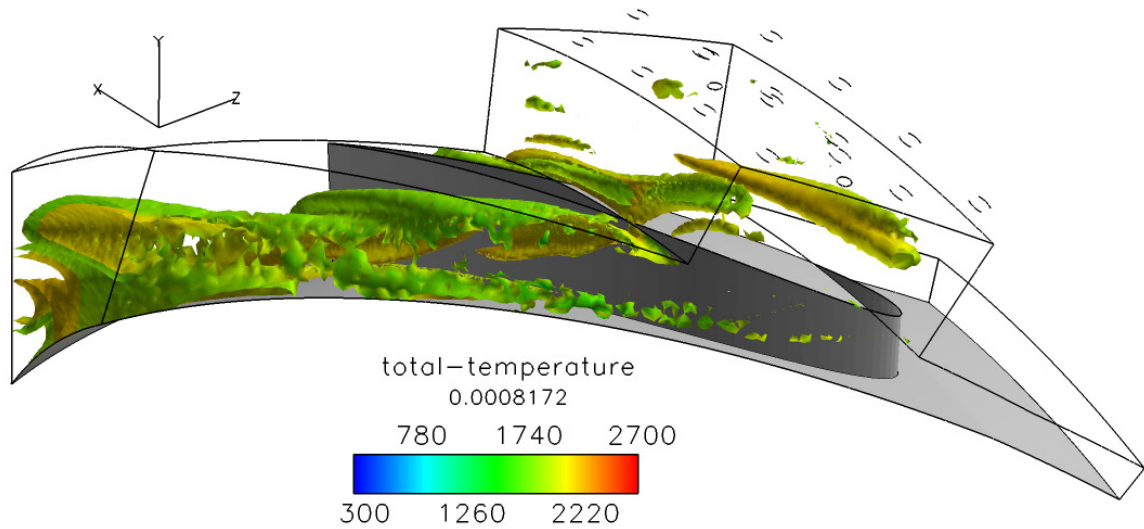


Figure 4.41: Iso-surface of OH colored by total temperature using the 12-species combustion model and ideal air inlet diameters with a 20 hybrid vane rig configuration

At the mass fractions shown, the fuels are located in a relatively cool region of the cavity. The CO and H_2 , which produce nearly identical surfaces, are the products of the fuel breakdown and are located within the hottest regions of the domain where combustion is taking place. As an indicator of combustion, OH is also located within

the hottest regions of the domain. The iso-surfaces of CO and H₂ show the flow pattern of the cavity inlet air by the formation of ripples and tubes around the air jets.

From a burning in the turbine perspective, it is important to know the species that are exiting the UCC section into the high-pressure turbine. The radial position of the species is also important. The specific species of interest are those species that contribute to secondary combustion in film cooling jets such as fuel, CO, H, H₂ and OH. CO is the primary source for heat release but the concentration of OH is also of value since it indicates the presence of combustion. Figures 4.42 and 4.43 show the circumferentially-averaged mass fractions of species at the 20 hybrid vane domain exit for high and low mass fractions, respectively. The circumferentially-averaged mass fractions of species at the domain exit for high and low mass fractions in the 20 hybrid vane rig configuration are shown in Figures 4.44 and 4.45, respectively. The species plots for the 30 hybrid vane engine and rig configurations can be found in Appendix D.

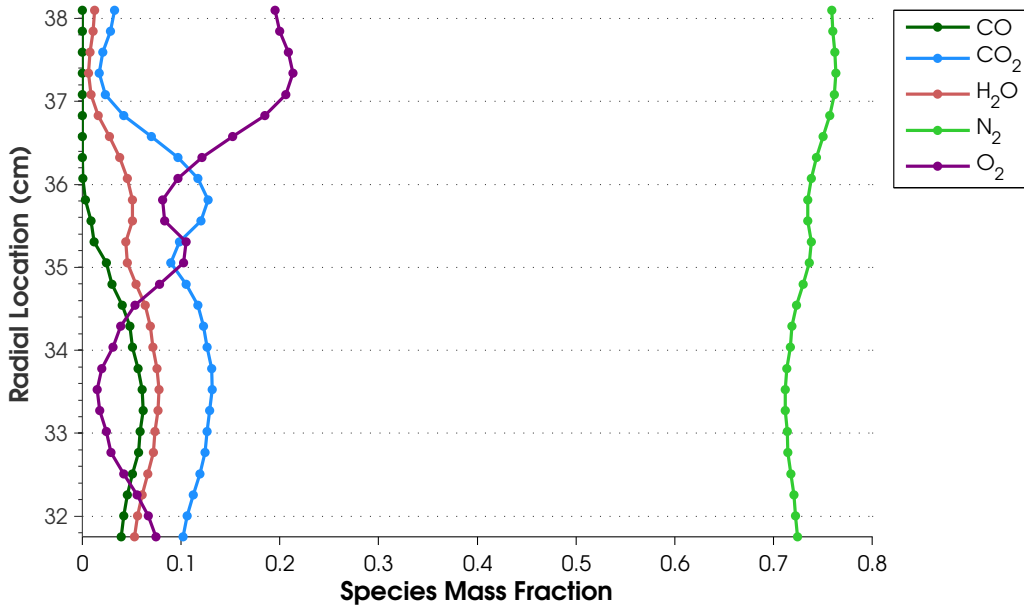


Figure 4.42: Circumferentially-averaged mass fractions of species at combustor section exit using the 12-species combustion model and ideal air inlet diameters with a 20 hybrid vane engine configuration

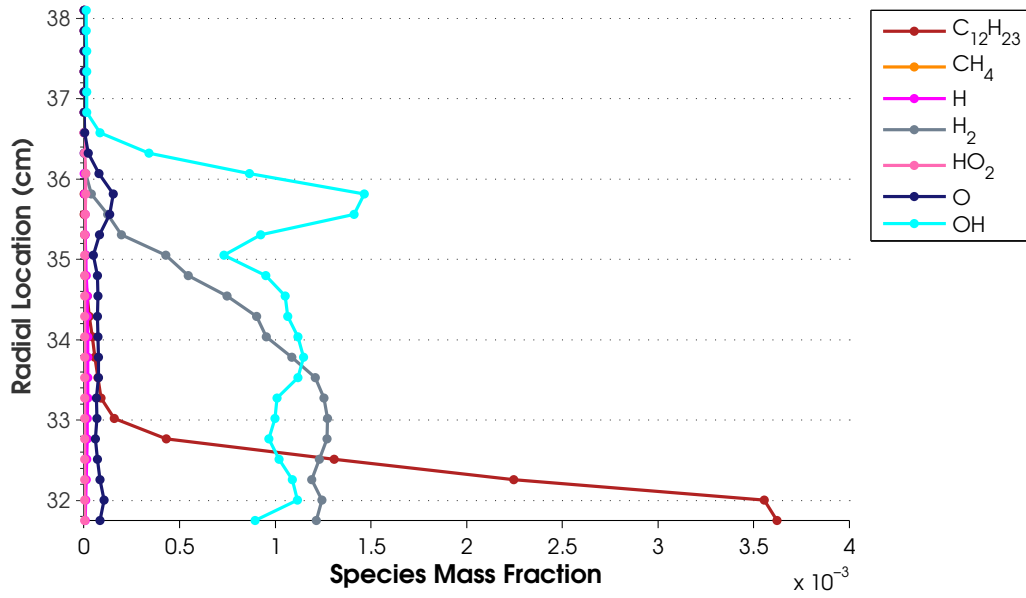


Figure 4.43: Circumferentially-averaged mass fractions of species at combustor section exit using the 12-species combustion model and ideal air inlet diameters with a 20 hybrid vane engine configuration

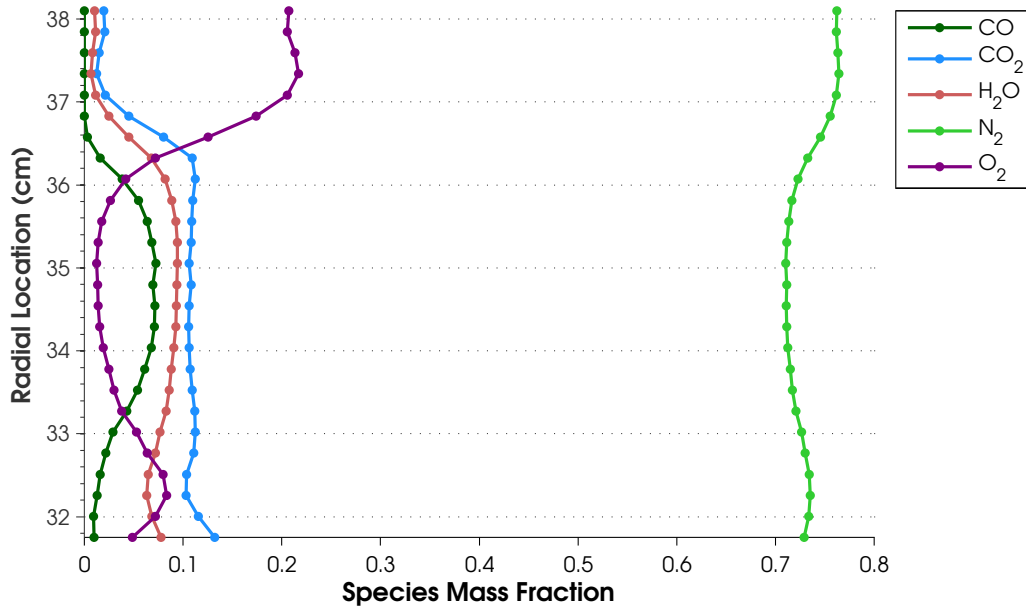


Figure 4.44: Circumferentially-averaged mass fractions of species at combustor section exit using the 12-species combustion model and ideal air inlet diameters with a 20 hybrid vane rig configuration

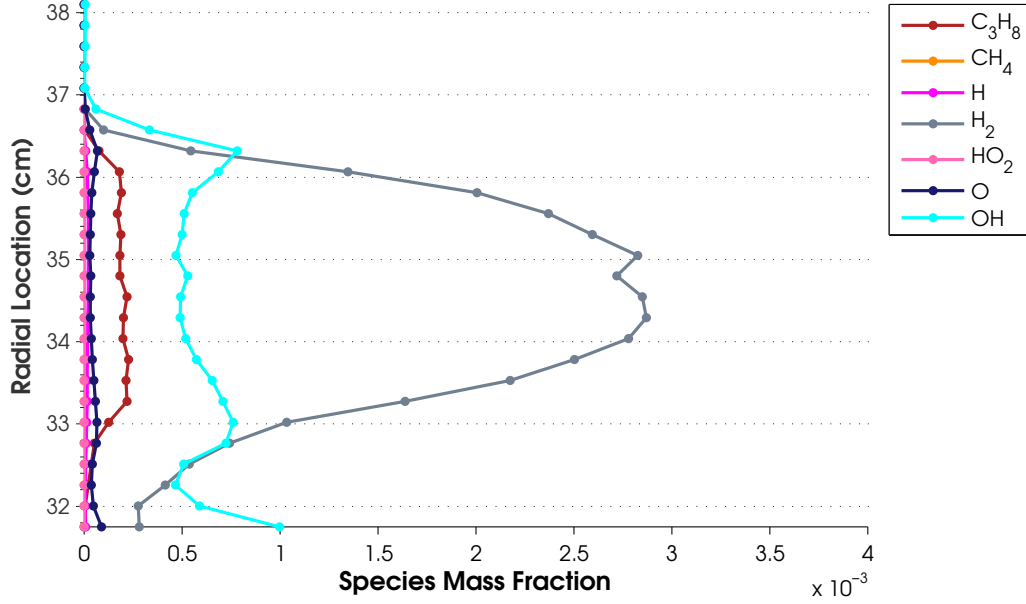


Figure 4.45: Circumferentially-averaged mass fractions of species at combustor section exit using the 12-species combustion model and ideal air inlet diameters with a 20 hybrid vane rig configuration

A comparison of the exit temperature profiles from Figure 4.33 to the species mass fraction plots show a correlation between higher temperature regions at the exit plane and higher mass fractions of CO , OH and H_2 . The profiles of these species and CO_2 have very similar shapes to the temperature profiles indicating that CO , OH and H_2 are the primary sources and indicators of heat release and combustion while CO_2 is the primary combustion product. As expected, the profile of O_2 had an inverse shape from the temperature and combusting species profiles since O_2 is used in the reactions.

4.4 Domain Modification Analysis

From Figures 4.30 and 4.33 it can be seen that the 20 hybrid vane domain only produced half of the desired temperature profile at the exit of the UCC section by leaving the ID endwall extremely hot. Additionally, from Figures 4.22 and 4.23 it can be seen that the ID endwall was excessively heated in the region between the

circumferential cavity and the domain exit. To solve the problem of the ID endwall heating, a divider plate was added to the domain as discussed in Section 3.8. The addition of the divider plate allowed cool air to bypass the circumferential cavity region and exhaust along the ID endwall just beyond the trailing edge of the vanes. By doing this, the bypassed air remained cool and produced a film cooling like effect on the ID endwall buffering the hot gases off the wall. The plate not only allowed the ID endwall to remain cool, but the temperature profile at the domain exit was also effected, producing the desired heating profile. Since the temperature profiles of the engine and rig condition have been shown to produced similar trends, this test was conducted using the rig condition only. The exit temperature profiles are shown in Figure 4.46 for the 5-species and 12-species models with and without the divider plate. All models used in this comparison used piecewise-polynomial values of C_p . The temperature at the ID endwall was reduced to match the OD endwall temperature, however, the change in temperature with increased radial position was not as large. This result is an indication that the height of the slot created by the splitter plate was too large. Figure 4.47 shows the total temperature contours on the domain exit plane for each combustion model with and without the divider plate. Figure 4.42 was provided to show contours of total temperature throughout the remainder of the domain. This figure shows contours on the domain exit, ID endwall, divider plate and vane surface compared to the original 20 hybrid vane rig configuration without the divider plate. The temperature scale in Figure 4.42 was set to match the scale used in the previous domain plots from Section 4.2 while the temperature scale in Figure 4.47 was set to a more refined range based on the local maximum.

In Figure 4.42 it can be seen that the heating on the upper surface of the divider plate was not nearly as severe as the heating on the ID endwall in the domain without the plate. It seems logical that the ID endwall downstream of the plate would remain cool due to the film cooling effect produced by the divider plate, but it would also be expected that the upper surface of the divider plate would have the same heating pattern as the ID endwall from the domain without the plate. The difference is the

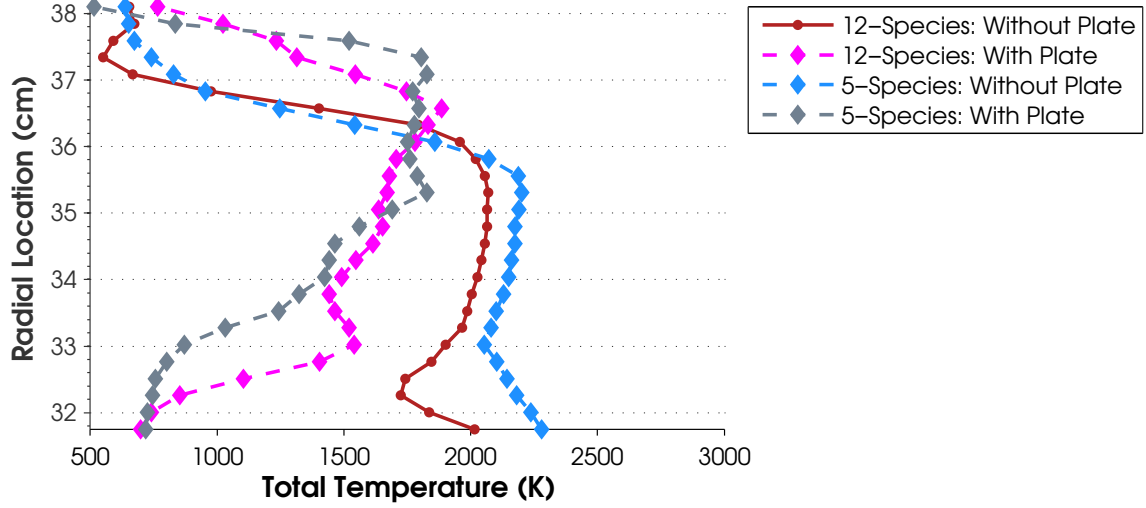
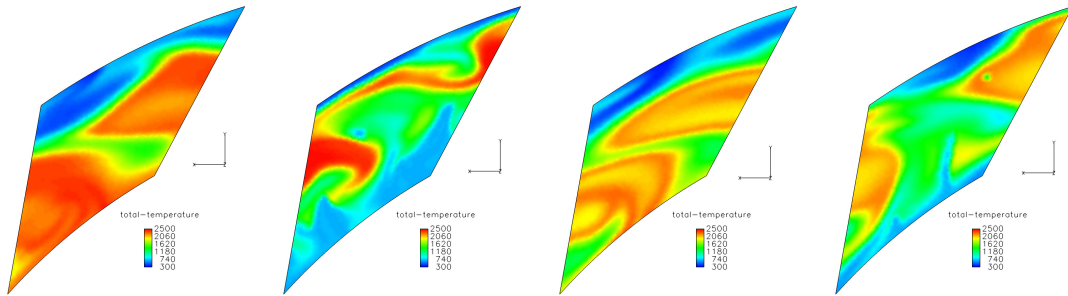


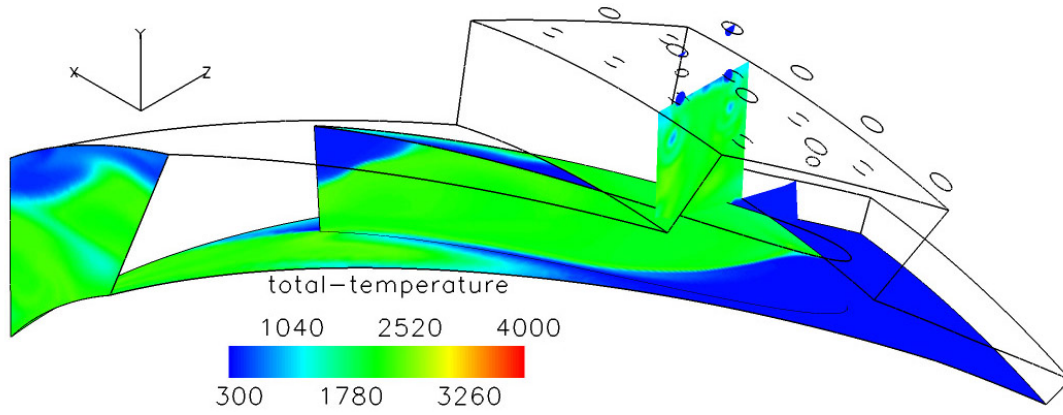
Figure 4.46: Circumferentially-averaged total temperatures at combustor section exit using the 5- and 12-species combustion model and ideal air inlet diameters with piecewise-polynomial C_p values for a domain with and without the divider plate



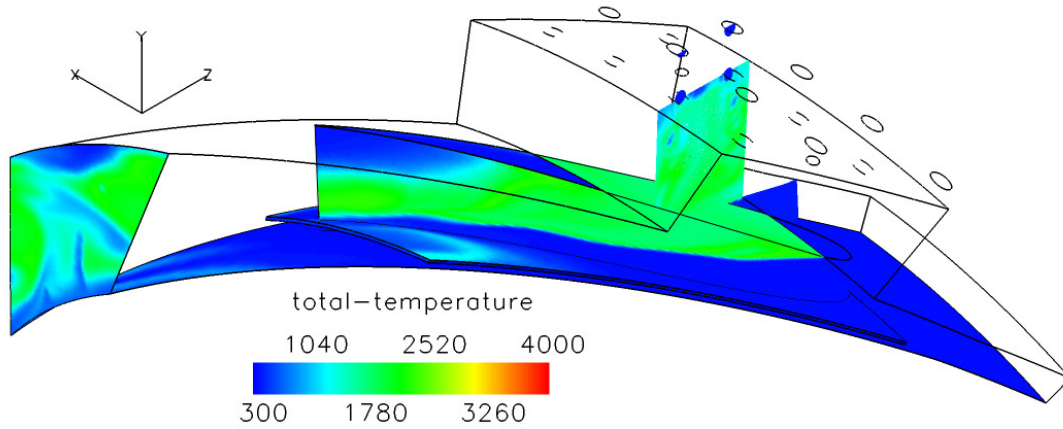
(a) 5-Species no plate (b) 5-Species w/ plate (c) 12-Species no plate (d) 12-Species w/ plate

Figure 4.47: Total temperature contours on domain exit plane for 5- and 12-species combustion models with and without the divider plate

result of a vortex created on the upper surface at the leading edge of the divider plate. To help prevent separation through the diffused combustor section, the walls of the diffuser were each tapered at a shallow 7° angle. In order to achieve a constant radius ID endwall that produced a 7° taper angle, the inlet to the combustor section was also angled at a 7° angle as shown in Figure 3.1 and also in Figure 4.49 which includes the divider plate. Due to the 7° inlet angle, the fluid entering the combustor section



(a) Without Divider Plate



(b) With Divider Plate

Figure 4.48: Total temperature contours on UCC components for ideal tangential velocity in the 20 hybrid vane domain under rig conditions with and without the divider plate

hit the lower surface of the divider plate and produced a separation and recirculation region on the leading edge upper surface. This recirculation formed a vortex that was convected into and along the suction surface of the UCC turbine vanes as shown in Figure 4.50. In contrast, the streamlines shown in Figure 4.51 pass through the same points in the domain, but these streamlines originated in the circumferential cavity thus directing hot gases directly to the endwall. With the addition of the plate induced vortex, the fluid exiting the circumferential cavity was buffered off the divider

plate. This interaction of fluid exiting the cavity and the plate induced vortex is better shown in Figure 4.52 which shows a vector plane downstream of the circumferential cavity. In this figure it can be seen that the upper cavity exit vortex caused by the shear interaction of circumferential flow and core flow is countered by the divider plate induced vortex which forced the hot gases off the vane surface and into the free stream. There was some heating of the upper surface of the divider plate near the trailing edge of the vane caused by the plate induced vortex entraining some hot gas from the cavity exit vortex and directing it down into the plate surface. Additionally, the plate induced vortex was significantly weakened as it convected downstream due to the interaction with the cavity exit vortex. The weakened vortex allowed some hot gases to reach the divider plate surface. The temperatures in Figures 4.50 and 4.51 appear hotter than those in Figure 4.48 because a more refined scale was used in Figures 4.50 and 4.51.

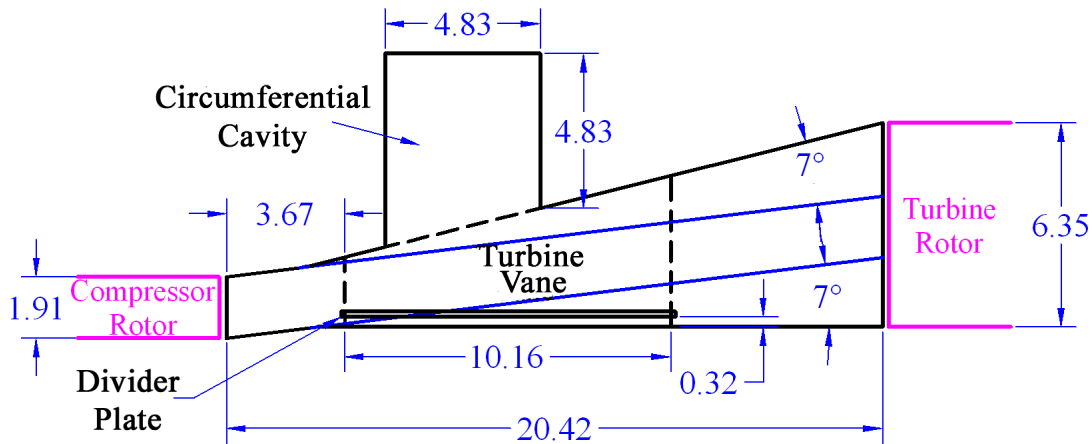


Figure 4.49: Cross-sectional view of UCC section with the divider plate (Dimensions are in centimeters)

The addition of the divider plate had a minimal impact on the fluid properties within the circumferential cavity. Table 4.14 shows a comparison of the previously presented 5- and 12-species, 20 hybrid vane rig condition data without the divider plate along with the results using the divider plate.

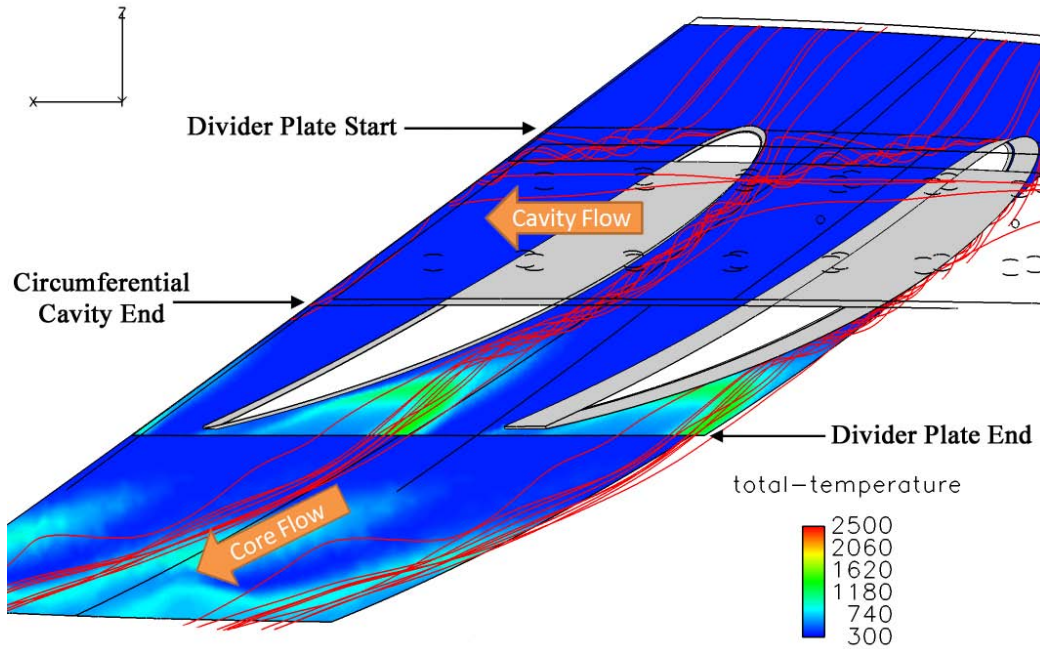


Figure 4.50: Plan view of domain showing streamlines of the vortex formed from the divider plate, contours are colored by total temperature

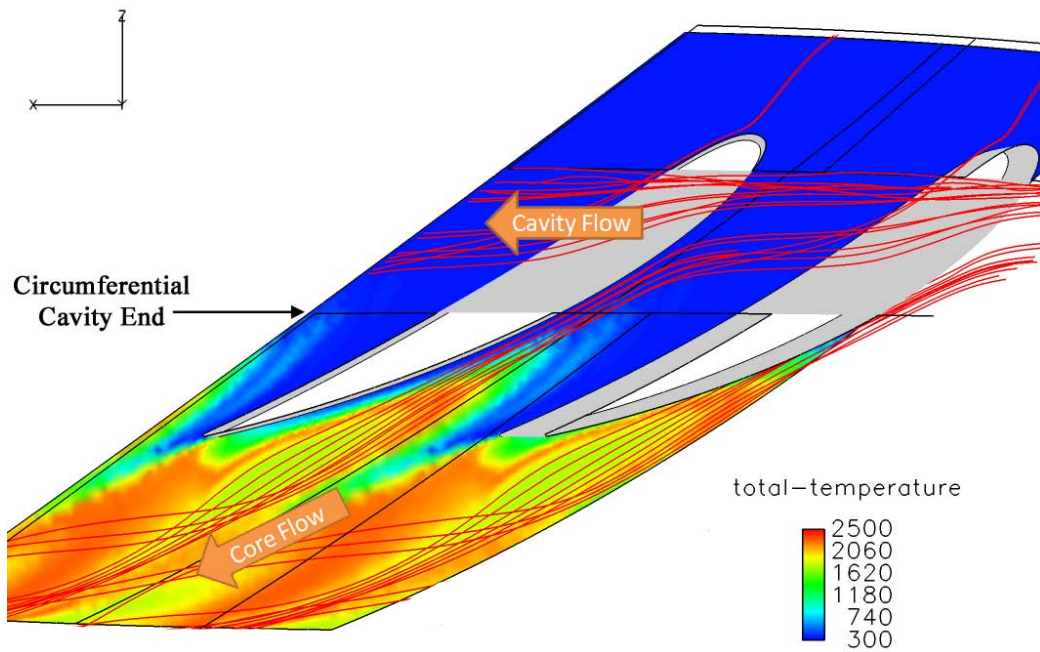


Figure 4.51: Plan view of domain without the divider plate showing streamlines through the same points in the domain as Figure 4.50, contours are colored by total temperature

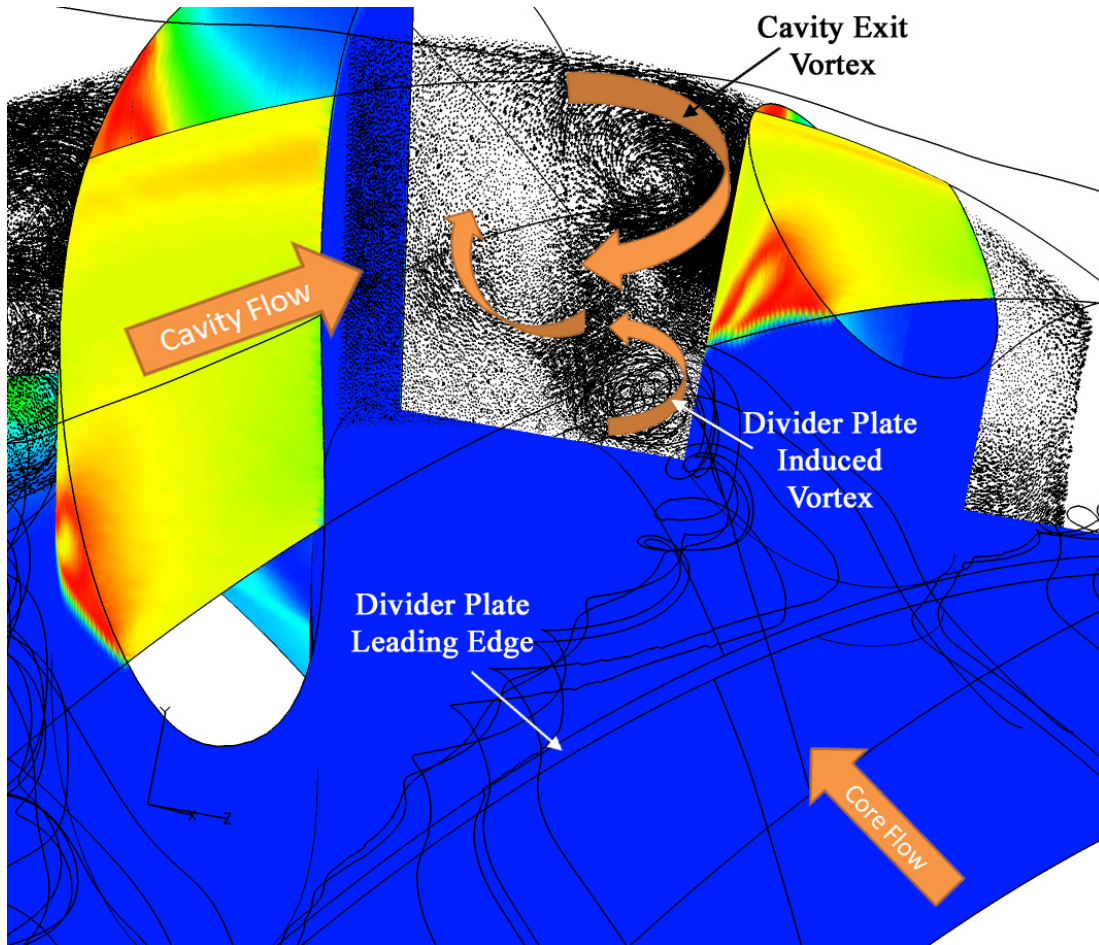


Figure 4.52: Upstream view of UCC turbine vanes with divider plate showing streamlines and a vector plane positioned downstream of the circumferential cavity

Table 4.14: Comparison of fluid properties within the circumferential cavity for 5- and 12-species combustion models with ‘ideal’ inlet diameters with and without the divider plate

Combustion Model	Test Config.	Inlet Port Diameter	Inlet Velocity	Tangential Velocity	Pattern Factor	g-Load
5-Species	w/o Plate	0.5208 cm	57.2 m/s	116.8 m/s	0.37	3,646
5-Species	w/ Plate	0.5208 cm	58.0 m/s	117.8 m/s	0.51	3,709
12-Species	w/o Plate	0.5208 cm	72.9 m/s	142 m/s	0.34	5,400
12-Species	w/ Plate	0.5208 cm	72.8 m/s	142 m/s	0.44	5,389

From Table 4.14 it can be seen that the cavity inlet velocity and tangential velocity was only increased approximately 1 m/s for the 5-species case while there was virtually no change in the velocities in the 12-species case. Using both combustion models, the pattern factor was increased using the divider plate. Both endwalls remained cool using the divider plate which made the temperature profile less uniform and resulted in an increased pattern factor.

Using the results from the 12-species analysis, iso-surfaces of C_3H_8 , CO , H_2 and OH were created within the domain to show the change in the locations of the reactions as a result of the addition of the endwall plate. The iso-surfaces are shown in Figures 4.53 through 4.56. Comparing each of these figures to the corresponding species in Figures 4.38-4.41 shows that the species, and therefore the reactions that took place outside of the cavity, were moved in the positive Y direction off the ID endwall. The upward shift can also be seen in Figure 4.46 where the upper boundary of the region of hot temperatures was moved upward from the 36 centimeter to 37 centimeter radial position. Also using the 12-species model, the circumferentially-averaged species mass fractions at the domain exit were calculated and plotted for the domain with the addition of the endwall plate. These plots are shown in Figures 4.57 and 4.58. Compared to the previous circumferentially-averaged species mass fraction plots which skewed the species toward the ID endwall, the plots for the domain with the divider plate are nearly symmetric about the center line of the passage.

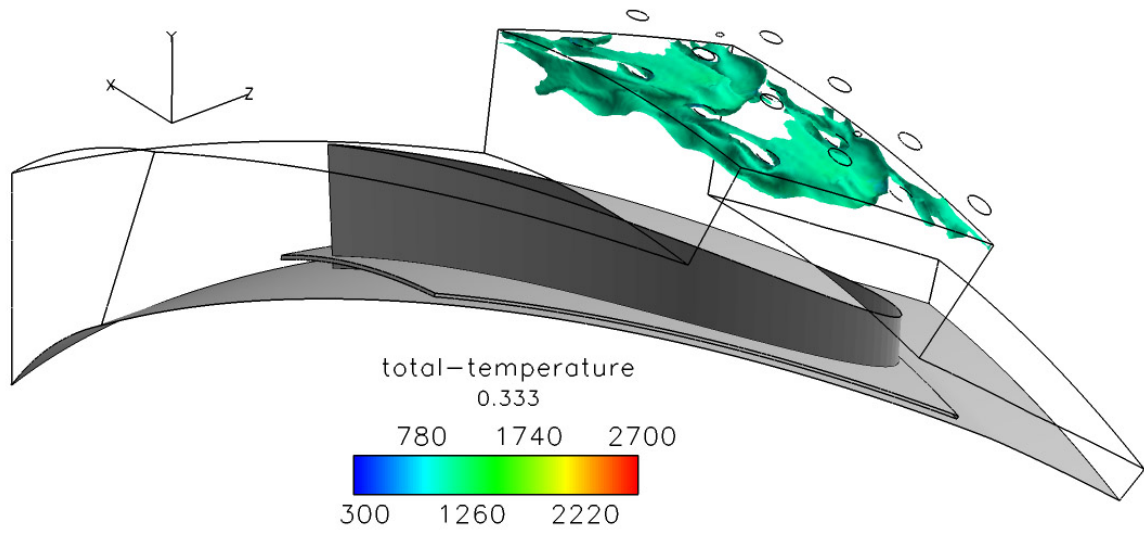


Figure 4.53: Iso-surface of C_3H_8 colored by total temperature using the 12-species combustion model and ideal air inlet diameters with a 20 hybrid vane rig configuration with divider plate

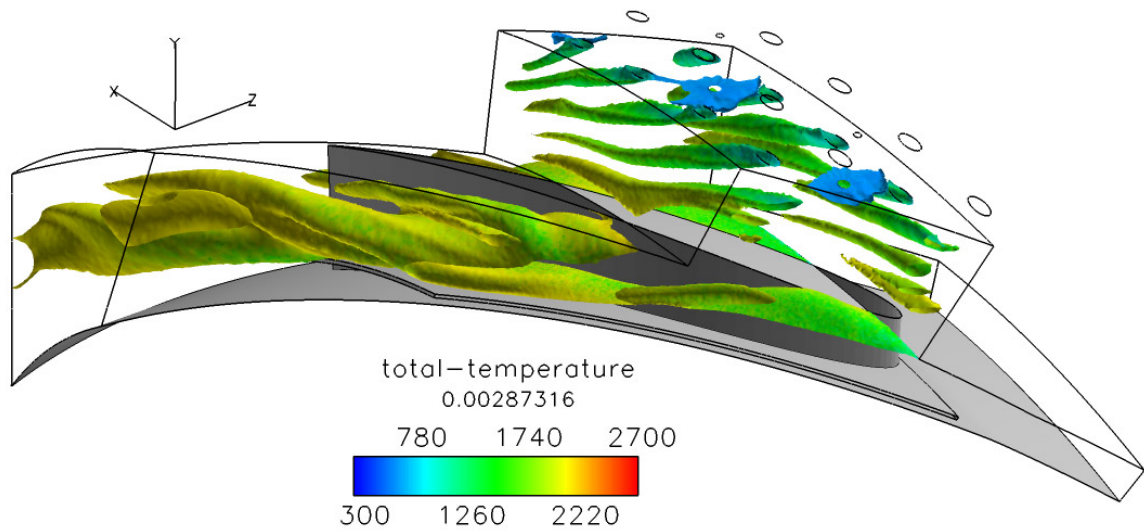


Figure 4.54: Iso-surface of H_2 colored by total temperature using the 12-species combustion model and ideal air inlet diameters with a 20 hybrid vane rig configuration with divider plate

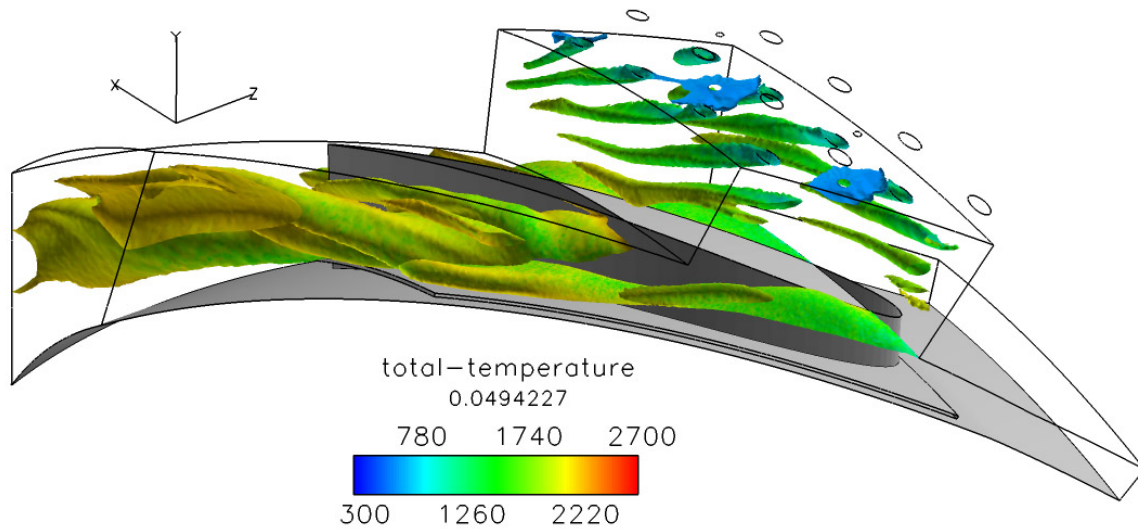


Figure 4.55: Iso-surface of CO colored by total temperature using the 12-species combustion model and ideal air inlet diameters with a 20 hybrid vane rig configuration with divider plate

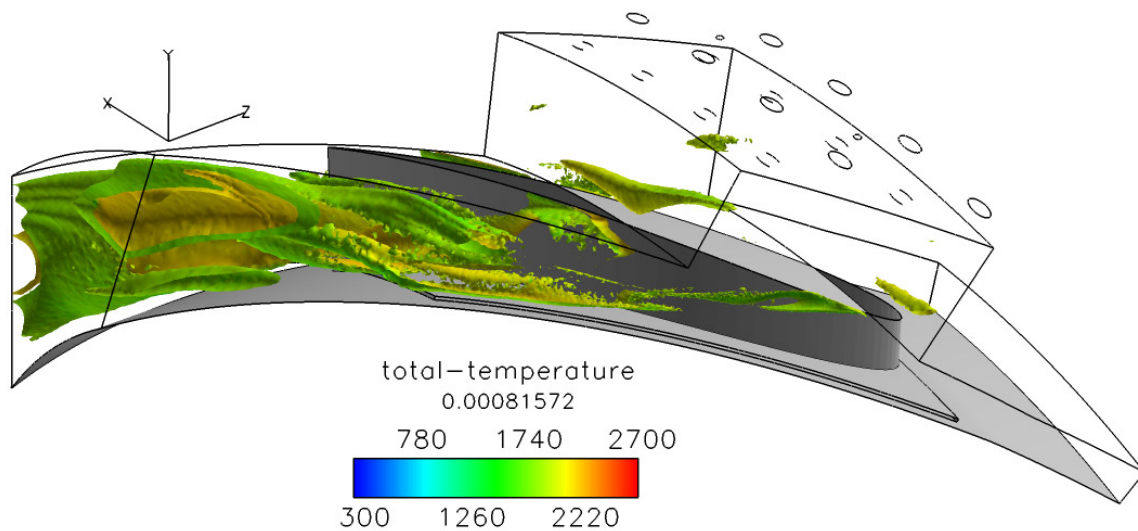


Figure 4.56: Iso-surface of OH colored by total temperature using the 12-species combustion model and ideal air inlet diameters with a 20 hybrid vane rig configuration with divider plate

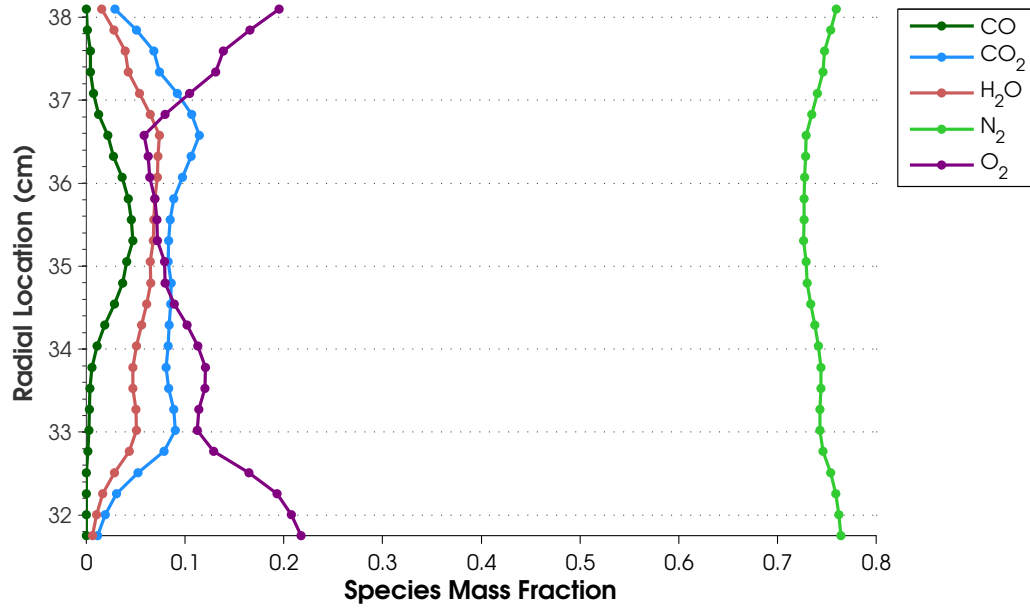


Figure 4.57: Circumferentially-averaged mass fractions of species at combustor section exit using the 12-species combustion model and ideal air inlet diameters with a 20 hybrid vane rig configuration

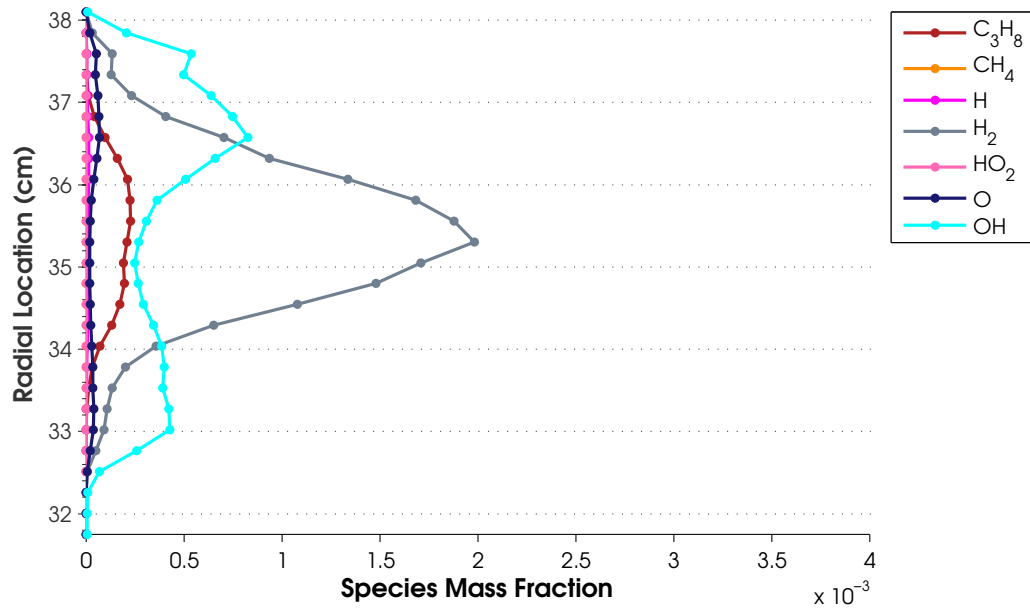
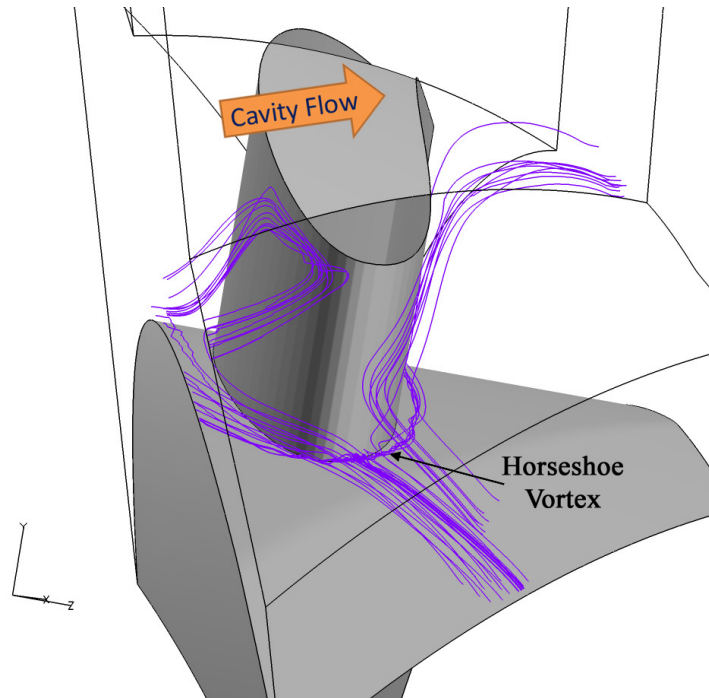


Figure 4.58: Circumferentially-averaged mass fractions of species at combustor section exit using the 12-species combustion model and ideal air inlet diameters with a 20 hybrid vane rig configuration

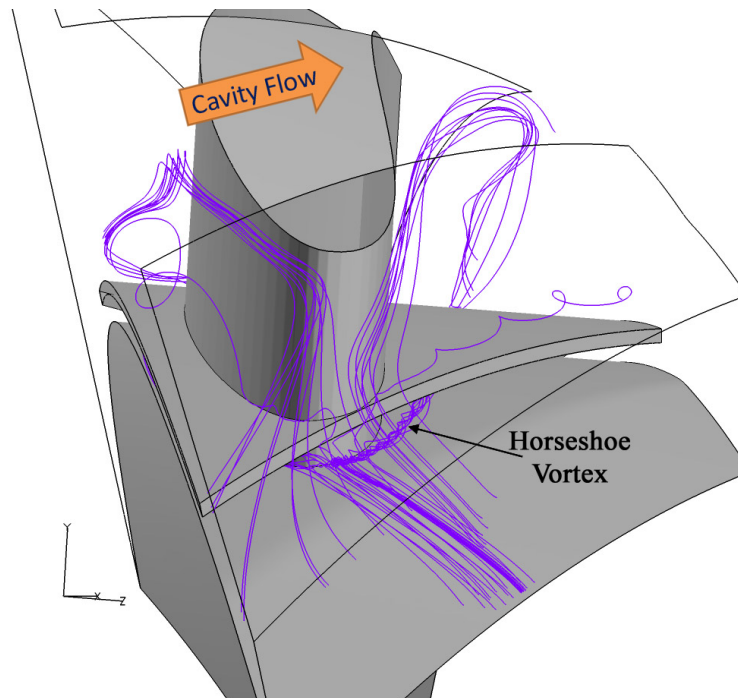
In addition to the thermal management provided by the divider plate, the pressure losses across the combustor were reduced approximately 2% in static pressure and about 1% in total pressure. The pressures calculated using both combustion models along with the corresponding results without the divider plate are shown in Table 4.15. The reduced pressure losses can possibly be attributed to the divider plate reducing the impact of secondary flow structures. While the horseshoe and passage vortices were still present around the leading edge of the UCC turbine vane, the vortices were trapped below the divider plate. Figure 4.59 shows the streamlines around the leading edge of the UCC turbine vane with and without the divider plate. While the divider plate was only tested for the rig condition, the pressure losses for the engine condition could be expected to be reduced a similar amount. If the same reduction in pressure loss is applied to the 20-vane engine condition, a static pressure loss of 3.2% and a total pressure loss of 3.4% would be obtained across the combustor.

Table 4.15: Calculated pressures and losses for ‘ideal’ cavity inlet diameters using a 5- and 12-species combustion model with and without the divider plate

Combustion Model	Test Configuration	Pressure Type	Domain Inlet (Pa)	Domain Exit (Pa)	% Difference
5-Species	w/o Plate	Static	115,951	101,325	-12.61
		Total	119,212	108,022	-9.39
5-Species	w/ Plate	Static	113,263	101,248	-10.61
		Total	116,613	106,384	-8.77
12-Species	w/o Plate	Static	114,402	101,324	-11.43
		Total	118,133	106,797	-9.59
12-Species	w/ Plate	Static	112,081	101,299	-9.62
		Total	115,814	106,219	-8.28



(a) Without Divider Plate



(b) With Divider Plate

Figure 4.59: Streamlines around UCC turbine vane for the 20 hybrid vane domain under rig conditions with and without the divider plate

4.5 Engine Condition Domain Modification

In Tables 4.10 and 4.13 a static pressure difference between the domain inlet and the cavity inlet ports was observed on the order of 2.6% for the engine condition and 11.7% for the rig condition. For rig testing, the cavity inlet ports and the domain inlet will be fed from separate air sources. For each of these inlets, the mass flow rate can be set and the resulting pressures needed to maintain that flow rate are free to vary until a steady-state solution is achieved. In an engine, however, the cavity and the domain inlet will both be fed from the same compressor. As such a pressure differential between the inlets cannot occur. To show that the a solution could still be achieved and that the relationships of tangential velocity and cavity inlet velocity are still valid for this case, an additional series of tests was conducted using the domain shown in Figure 3.14. This domain used a bypass duct off the domain inlet to redirect air to the circumferential cavity. Having a direct linkage between the two inlet locations ensured the static pressures would match. Three tests were conducted with this domain under engine conditions only with the air inlet port diameters as the only variation between the test cases. The 2x and baseline inlets discussed in Section 3.4 were used along with the ideal diameter inlet (0.8641 cm) found in Section 4.2. The static pressures at the domain inlet, entrance to the cavity inlet ports and domain exit are shown in Table 4.16 for each of the ducted test configurations.

Table 4.16: Calculated static pressures at the domain inlet, cavity inlet port and domain exit for the ducted domain

Test Configuration	Cavity Inlet Diameter	Domain Inlet	Cavity Inlet Port	Domain Exit
2x Inlet	1.08 cm	4,872,379 Pa	4,863,176 Pa	4,620,780 Pa
Ideal Diameter Inlet	0.864 cm	5,000,664 Pa	5,002,625 Pa	4,621,007 Pa
Baseline Inlet	0.54 cm	4,700,694 Pa	4,705,004 Pa	4,625,829 Pa

From Table 4.16 it can be seen that the static pressure difference described above was reduced to approximately 0.1%. This slight variation in pressures is due to noise

within the CFD solution. Figure 4.60 shows the relationship of cavity inlet velocity to tangential velocity and the corresponding inlet port diameter. While the layout of this plot is the same as Figures 4.20 and 4.32, the location measured for the cavity inlet velocity was different. In the previous plots, the cavity inlet velocity was measured at the entrance to the cavity inlet port. This location was convenient because the surface was a boundary condition making the calculation of the area weighted velocity easy. Additionally, with this location being a boundary condition, the fluid entered the cavity inlet ports with a uniform velocity and direction. With the current ducted domain, the entrance to the cavity inlet ports had fluid entering in a non-uniform manor with the inlet velocity influenced by the free stream velocity in the plenum. Streamlines through the cavity inlet are shown in Figure 4.61 for the original domain and the ducted cavity inlet domain. To get a more accurate velocity measurement, the location where the measurement was taken was moved from the cavity inlet port entrance to the cavity inlet port exit. This move allowed the fluid in the inlet ports to stabilize in both direction and velocity before the measurement was taken. The 20-vane engine condition relationship shown in Figure 4.20 was adjusted to represent the relationship with respect to the cavity inlet port exit velocity and is shown in Figure 4.60 as the solid blue line. The dashed blue line represents the relationship between cavity inlet velocity and inlet port diameter based on a representative cavity inlet density of 18.0 kg/m^3 . This line was generated using the relationship shown in Equation 4.3 discussed at the end of this section.

The three diamond markers in Figure 4.60 represent the three ducted inlet test cases. It can be seen that there was a slight variation in tangential velocity of approximately 5-7 m/s for the ducted cases compared to the previous relationship, though the same general trend was followed. It can also be noted that unlike the previous cases with a fixed mass flow rate into the cavity, the cavity inlet velocities with the ducted test cases were not necessarily larger for smaller diameter inlets. Using a fixed bypass duct did not allow for variations in the bypass ratio to be made to achieve the desired cavity mass flow rate for each case. The reduced mass flow rate

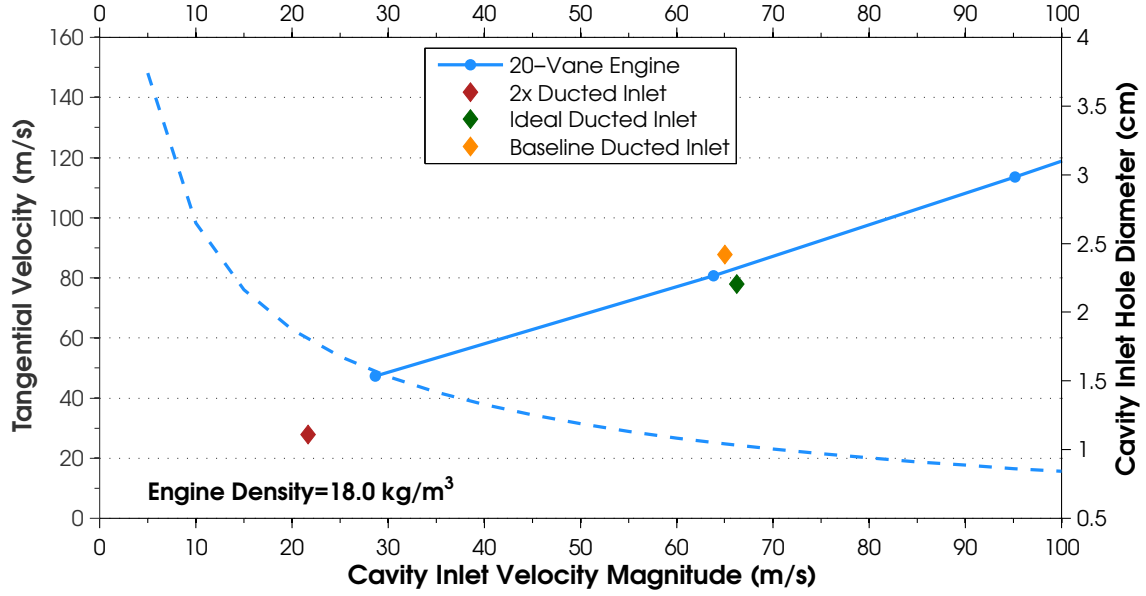


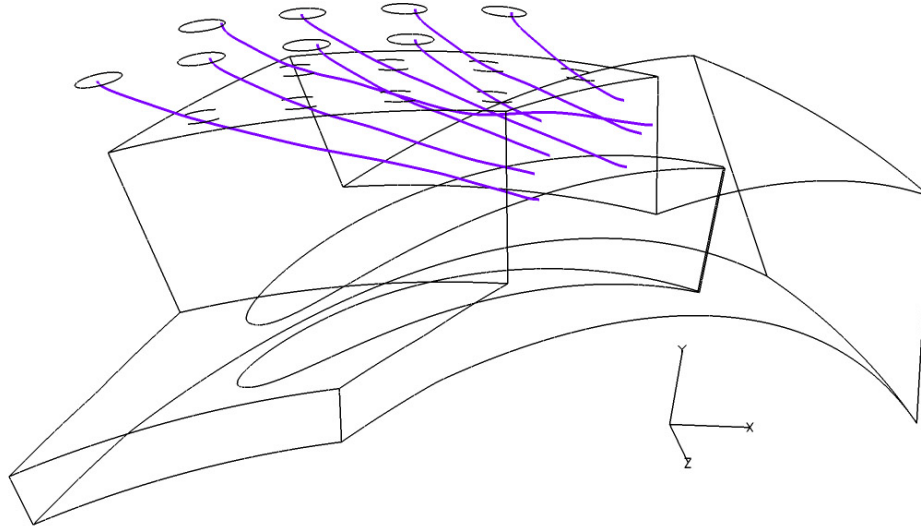
Figure 4.60: Relationship of cavity inlet velocity to cavity tangential velocity and hole diameter for the ducted cavity inlets

into the cavity using the bypass duct drastically impacted the cavity inlet velocity, and thus the tangential velocity. Table 4.17 shows the magnitude of the reduction in mass flow rate into the cavity summed for all 8 inlet ports in the domain section as well as the resulting tangential velocity, cavity inlet velocity and cavity inlet density. As a reference, the previous test cases used a fixed cavity inlet mass flow rate of 0.775 kg/s.

Table 4.17: Fluid properties in the ducted domain

Test Configuration	Cavity Inlet Velocity	Tangential Velocity	Cavity Inlet Density	Inlet Mass Flow Rate
2x Inlet	21.7 m/s	27.87 m/s	17.4 kg/m ³	0.278 kg/s
Ideal Inlet	66.28 m/s	78.0 m/s	18.0 kg/m ³	0.560 kg/s
Baseline Inlet	65.4 m/s	87.7 m/s	44 kg/m ³	0.526 kg/s

In Figures 4.20, 4.32 and 4.60 the value of the inlet velocity does not actually matter. This value is simply an intermediate value used to correlate the tangential velocity and the cavity inlet port diameter. In the previous analysis which used the cavity inlet velocity at the entrance of the cavity inlet port, the inlet port diameter



(a) Original Domain



(b) Ducted Domain

Figure 4.61: Streamlines into the circumferential cavity for the 20 hybrid vane domain under engine conditions with and without a ducted cavity inlet

was calculated based on the elliptical area of the port as shown in Equation 4.2. With the cavity inlet port exit used as the reference velocity for the ducted domains, the area used in the calculation of the inlet port diameter was the circular area of the port.

Equation 4.3 shows the derived relationship of cavity inlet velocity to the diameter of the cavity inlet ports, measured in centimeters, for all cases with the cavity inlet velocity measured at the inlet port exit.

$$\phi = \left(\frac{4\dot{m}_{section}}{I\rho_{exit}V_{exit}\pi} \right)^{0.4981} \times 100 \quad (4.3)$$

In Equation 4.3, I is the number of cavity inlet ports used in the mass flow rate measurements, ρ_{exit} is the density at the exit of the inlet port and V_{exit} is the velocity at the exit of the inlet port. The exponent was adjusted slightly from 0.5 to more accurately represent the CFD results. For the previous test cases that used the controlled boundary condition inlet, Equations 4.2 and 4.3 will produce the same inlet diameter result provided the correct velocity is used in each equation. The same cannot be said for the ducted inlet test cases which require the length of the inlet port to stabilize the fluid. These cases can only use the relationship shown in Equation 4.3. To show the validity of this relationship, cavity inlet diameters calculated using Equation 4.3 are shown in Table 4.18 for each test case compared to the actual inlet diameter specified in the domain geometry.

Table 4.18: Calculated versus actual cavity inlet diameters

Test Configuration	Calculated Inlet Diameter	Actual Inlet Diameter
2x Inlet	1.10 cm	1.082 cm
Ideal Inlet	0.864 cm	0.88 cm
Baseline Inlet	0.54 cm	0.55 cm

This series of tests was performed as a proof of concept to show that the engine condition could be run at matched pressures between the domain inlet and the cavity inlet. Additionally, these tests further confirmed that the relationship of tangential velocity to cavity inlet velocity was independent of mass flow rate. Additional tests will be required to optimize the bypass ratio and cavity inlet port configuration to obtain the desired mass flow rate for a given cavity inlet port diameter.

V. Experimental Film Cooling Test Methodology

With the UCC and many modern production turbine engines operating at fuel rich conditions, the likelihood of secondary combustion reactions occurring in the film cooling streams of these engines increases drastically. An experimental film cooling study was performed to try and mitigate the negative impact of reacting coolant films by using combinations of cooling films in series. By putting the coolant streams in series it was thought that the reactions would occur in the first coolant stream enabling the second coolant stream to buffer the hot gases from the surface the way typical film cooling was designed to work.

5.1 Test Setup

The test setup consisted of an instrumented flat plate test rig that channeled the exhaust from a well stirred reactor (WSR) over a flat plate. Figure 5.1 shows the orientation of the test rig with the WSR. The flat plate test section was the same as outlined in great detail by Evans [8], but the test setup included several changes.

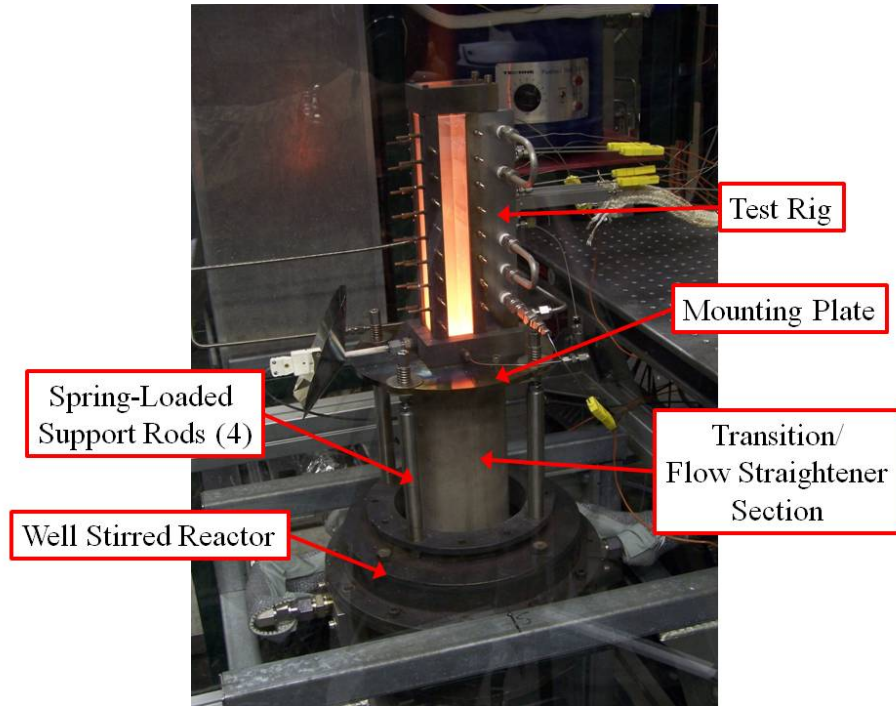


Figure 5.1: Experimental test setup

5.1.1 Well Stirred Reactor. The well stirred reactor developed by Nenniger et al. [41], and modified by AFRL after several years of design iterations was used to replicate the flow conditions at the exit of the circumferential cavity of a UCC or the turbine inlet conditions downstream of a conventional burner. The WSR is aptly named since the combustion products are mixed at a very high rate resulting in a nearly uniform distribution of temperature and reactant species in the exhaust stream.

The AFRL WSR was formed from two toroidal half sections made of cast zirconia-oxide separated by an Inconel[®] jet ring and placed inside a metal housing. The internal reactor volume formed by the two toroidal sections was 250 cm³. In contrast to the toroidal components used by Evans [8] which featured discrete exhaust holes, the toroid design used in the current study featured a continuous exhaust port. The thermal and aerodynamic stresses exerted on the ceramic surrounding the discrete exhaust holes of the previous reactor often resulted in oblation, cracks and breakage. The current design minimized the stresses in the ceramic by allowing the exhaust products to freely exit the reactor through a continuous exhaust port. Figure 5.2 shows the lower half of the WSR toroid with the jet ring and several additional features used to start and monitor the reactions. Figure 5.3 shows the complete toroidal assembly with the continuous exhaust port. Premixed fuel and air were fed into the jet ring manifold through two inlet ports. The fuel-air mixture then exited the jet ring into the reactor toroid through 48 discrete jets. Thermocouples located in four positions around the jet ring monitored the ring temperature to ensure warping or material failure temperatures were never reached. Additionally, large variations in temperature from one part of the ring to another could indicate a crack in the reactor. The jet ring and reactor ceramic components were cooled by nitrogen which continuously flowed through the metal housing. In addition to cooling the reactor components, the nitrogen filled the housing with an inert gas which minimized the risk of explosion if a fuel leak occurred as the result of cracks in the reactor.

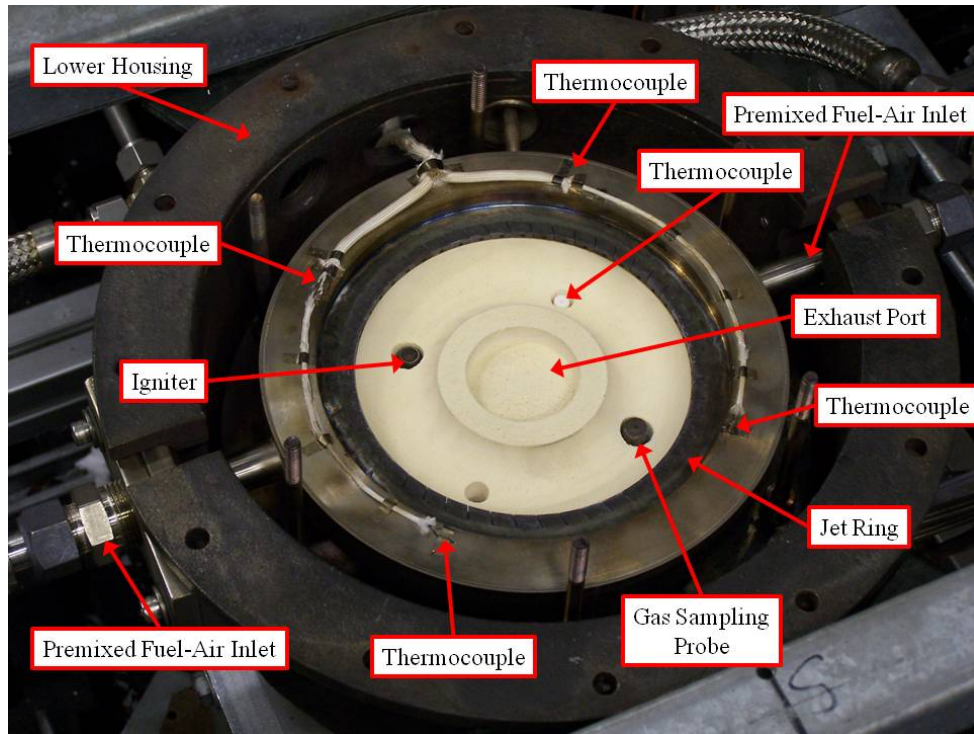


Figure 5.2: Lower half of the toroid with the jet ring in the WSR housing

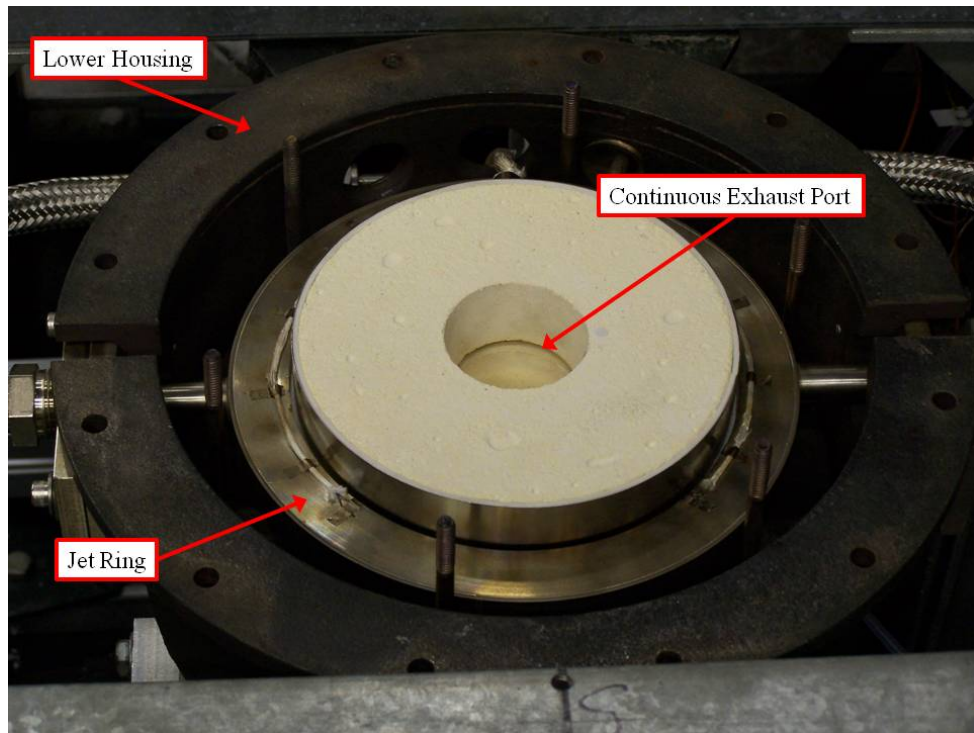


Figure 5.3: Complete toroidal setup with the jet ring in the WSR housing

5.1.2 Test Rig. With the exception of the Hastelloy-X[®] pipe that contained the transition section, the remainder of the test rig was identical to the rig described by Evans in Section 3.2 of [8]. The Hastelloy-X[®] pipe was replaced by a longer stainless steel pipe to house the transition section and a new flow straightener section designed for this study. With the details about the test rig provided by Evans, only an overview of the test rig and the modifications used in the current study are described in this report. The test rig was a turbulent flat plate modified to accept film cooling inserts and water cooling while providing temperature and pressure measurements in strategic locations around the rig. The rig as designed by Evans included a test section, two film cooling assemblies, four heat transfer gauge assemblies, a transition section, a window assembly and an aft plate. Figure 5.4 shows the arrangement of the components within the test rig.

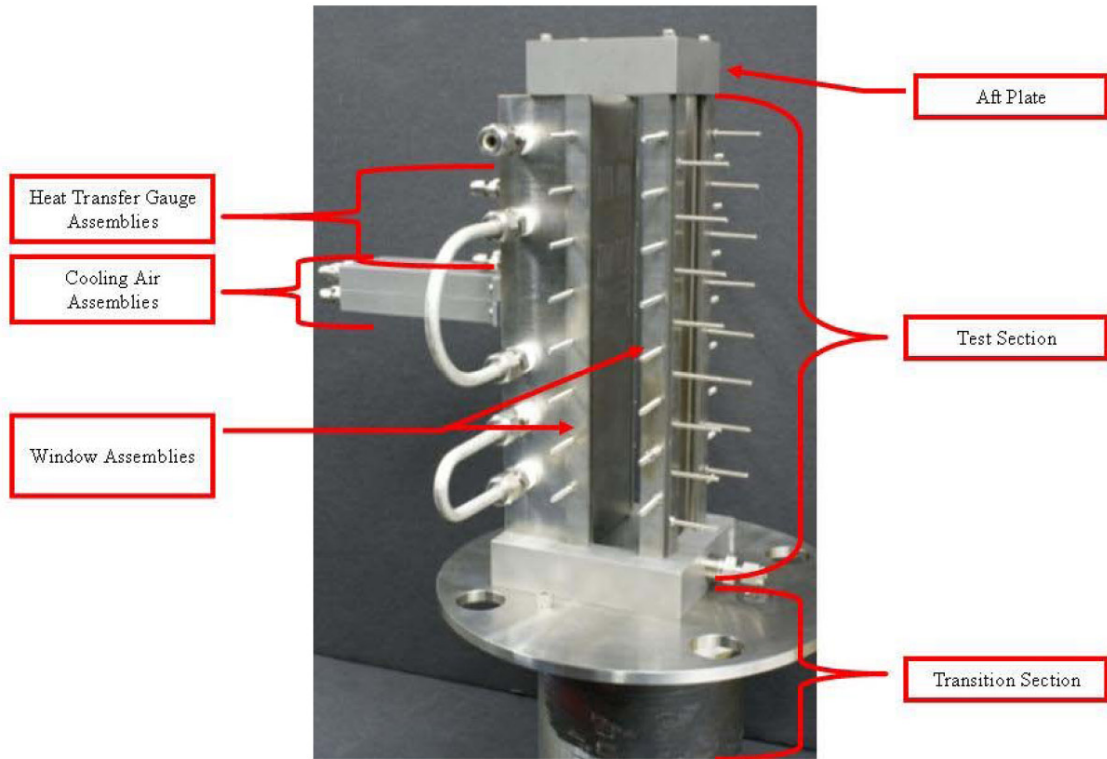


Figure 5.4: Test rig with sections and assemblies labeled [8]

5.1.2.1 Test Section. The test section was comprised of two separate pieces; a flat plate and an instrument block. The flat plate was machined from a solid piece of Hastelloy-X[®] measuring 22.9 cm by 5.1 cm by 5.1 cm. Slots were cut into the material as shown in Figure 5.5 to allow two film cooling assemblies and four heat transfer gauge assemblies to be inserted through the back of the plate. The inserts were sized such that all surfaces were flush with the surface of the flat plate. Water cooling holes were drilled through the side of the plate near the back surface to allow a continuous flow of water to cool the material to prevent warping or failure. The water entered the flat plate in the channel closest to the instrument block and exited at the top of the plate. This flow direction is opposite from the direction used by Evans. The grooves machined along the length of the plate were sized to accept the glass for the window assembly.

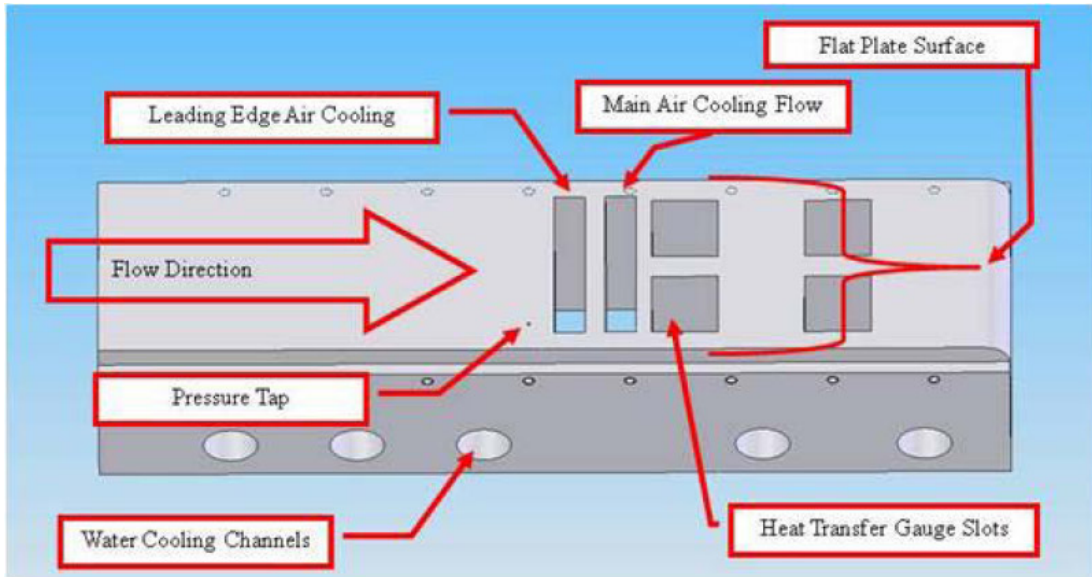


Figure 5.5: Test section, flat plate design [8]

The instrument block was fitted with a pressure tap and thermocouple port, as shown in Figure 5.6, to measure the properties of the fluid as it entered the test section. The flat plate was connected to the instrument block in such a way as to create a 2.5 mm forward facing step as shown in Figure 5.7. The step was intended to

trip the boundary layer to the turbulent regime for a wide range of Reynolds numbers and ensure the boundary layer was fully turbulent at the film cooling air inlets.

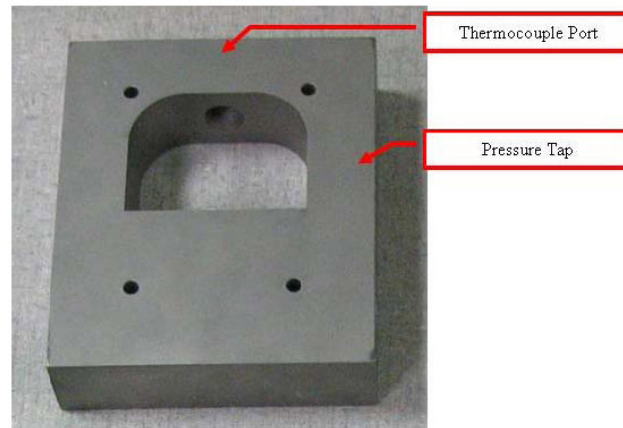


Figure 5.6: Test section, instrument block [8]

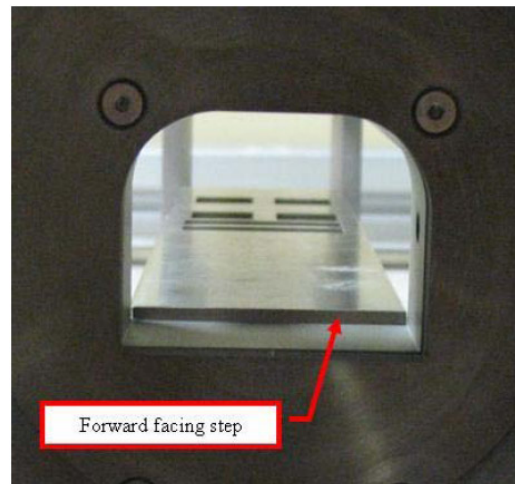


Figure 5.7: Test section, forward facing step [8]

5.1.2.2 Film Cooling Assemblies. The film cooling assemblies are comprised of a cooling hole insert and a plenum. The cooling hole insert is the portion of the assembly that is inserted through the flat plate of the test section to eject the film cooling fluid. Six cooling hole inserts were created, as shown in Figure 5.8, including normal holes, offset normal holes, angled holes, fan-shaped laidback holes, an angled slot and a solid blank. For the current study the fan-shaped laidback

holes, the angled slot, offset normal holes and the solid blank were used in varying combinations.

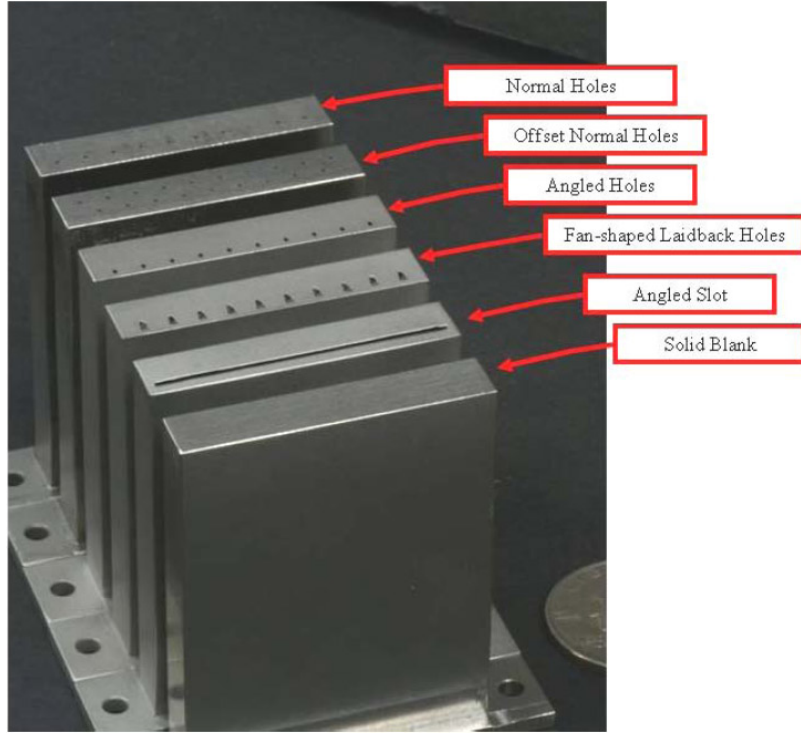


Figure 5.8: Film cooling inserts [8]

The normal hole and the offset normal hole inserts featured cylindrical holes with a 0.51 mm diameter drilled perpendicularly through the 2.54 mm thick end of the cooling insert. At this ratio of hole diameter to material thickness an (L/D) of 5 was achieved. The holes were spaced 3.81 mm apart. The offset normal holes included an additional row of holes, offset from the first row but with the same diameter and spacing. The fan-shaped laidback holes started with a 0.51 mm cylindrical hole drilled at 30° to the surface. An (L/D) of 5 was attained in this insert by reducing the wall thickness to 1.27 mm. At the exit, the hole was flared 10° and a layback of 10° was added. Figure 5.9 shows a schematic of the fan-shaped laidback cooling holes. The angled slot was 0.51 mm by 3.81 cm cut through the 1.27 mm thick end of the cooling insert at 30° . Appendix B shows detailed schematic drawings of the cooling inserts used in this study.

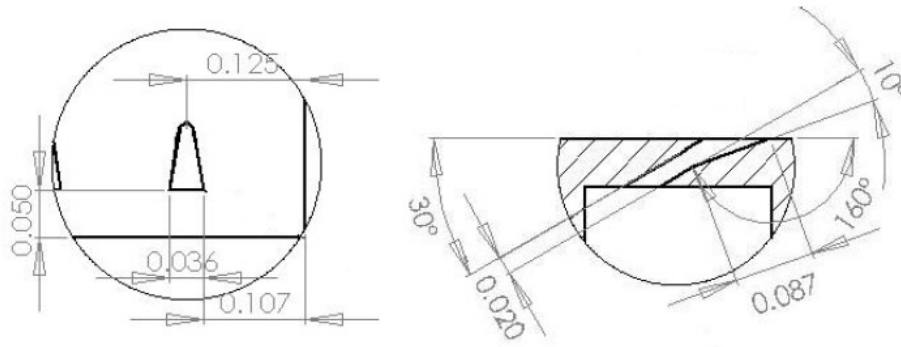


Figure 5.9: Schematic of the fan-shaped laidback holes (in inches) [8]

The cooling hole insert was connected to the plenum with a high-temperature gasket adhesive. Each assembly was secured to the back of the test section with two machine screws. Air or nitrogen was fed into the plenum from the AFRL facility supply. Thermocouples located inside the plenum measured the temperature of the cooling fluid at a distance of 5.1 mm from the outside surface of the cooling insert. The thermocouples were shielded by ceramic sleeves to ensure that no contact occurred between the thermocouple and the walls of the cooling insert. Figure 5.10 shows the components of the film cooling assemblies.

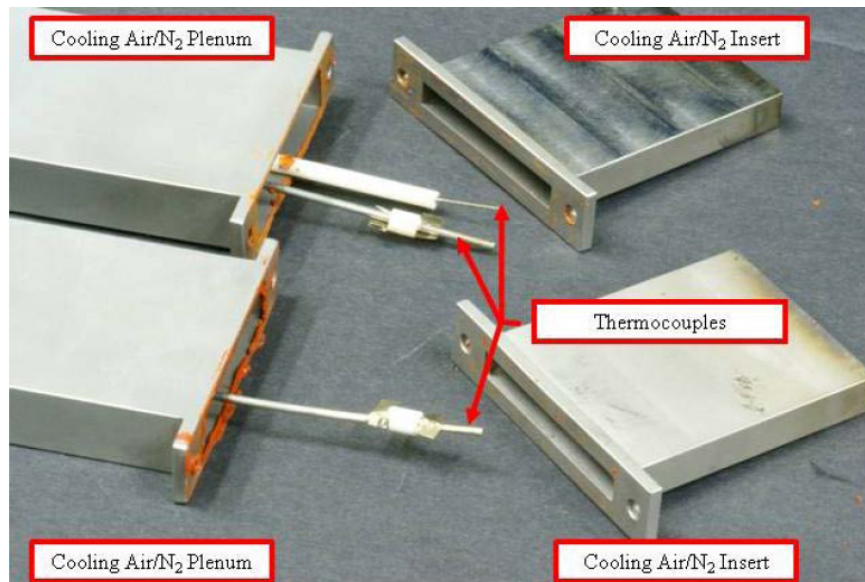


Figure 5.10: Film cooling assemblies [8]

5.1.2.3 Heat Transfer Gauge Assembly.

The heat transfer gauge assembly is composed of a solid machined Hastelloy-X[®] block and a mounting plate as shown in Figure 5.11. Similar to the cooling inserts, the heat transfer block is designed to be inserted through the back of the flat plate of the test section with the gauge surface flush with the flat plate. The mounting plate is used to secure the heat transfer block to the flat plate while allowing two thermocouples to pass through it into the block.

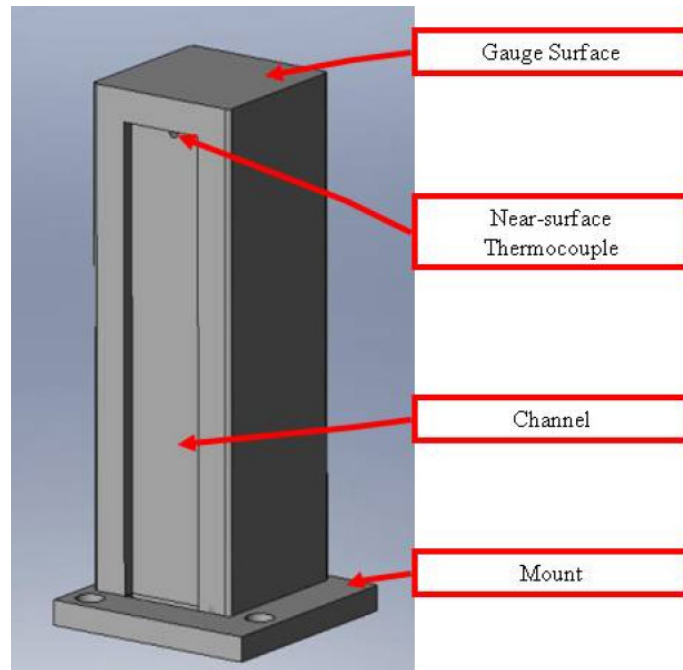


Figure 5.11: Heat transfer gauge assembly [8]

The two thermocouples embedded in the heat transfer block were installed at two separate depths from the surface but in-line relative to the gauge surface. The near-surface thermocouple was inserted to a depth of 11.7 mm into the block at a distance of 3.8 mm from the gauge surface. The channel machined into the block allowed access for the thermocouple wire to reach the front of the block without interacting with the second thermocouple. The second thermocouple was installed through the back of the block and inserted to a location 19.1 mm from the gauge surface.

The thermocouples in the two upstream gauges labeled ‘C’ and ‘D’ in Figure 5.12 were 10.4 mm downstream from the downstream cooling hole insert (approximately 20 cooling hole diameters). The thermocouples in the downstream gauges labeled ‘A’ and ‘B’ were 38.4 mm downstream of the downstream cooling hole insert (approximately 75 cooling hole diameters). The on-center spacing between the film cooling inserts was 12.7 mm (approximately 25 cooling hole diameters). Figure 5.12 shows the labeled heat transfer gauges and the relative position with respect to the cooling hole inserts.

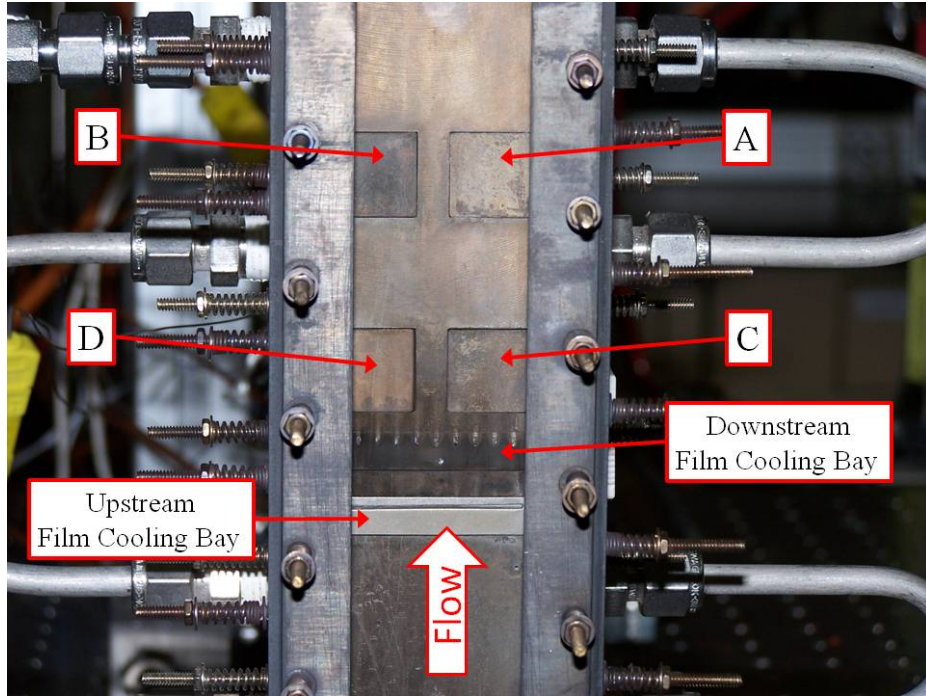


Figure 5.12: Heat transfer gauge labels and positions

5.1.2.4 Transition & Flow Straightener Section. The high-density ceramic components in the transition section designed by Evans [8] were unchanged in the current experiment, however, a flow straightener was introduced upstream of the transition section. The transition section was designed to smoothly connect the circular exhaust port of the WSR with the modified rectangular shape of the test section inlet. Six discs of high-density zirconia-oxide measuring 8.9 cm in diameter and 2.5 cm thick were used to build up the transition. Zirconia has a

very high heat tolerance, is an excellent insulator and is easily machined into the desired shape. The transition stack was pinned together with ceramic alignment rods and inserted into a sleeve of lower density zirconia-oxide. The entire assembly was inserted into the test rig end of a 19.5 cm long stainless steel flanged pipe as shown in Figure 5.13. The flange allowed the pipe to be connected to a spring supported mounting plate bolted to the bottom of the test rig. The mounting plate supported the weight of the test rig and was spring supported to allow for thermal expansion. In addition to the transition stack, a stack of three machined 8.9 cm diameter by 2.5 cm thick high-density zirconia-oxide discs which served as a flow straightener (see Figure 5.14) were inserted into the WSR end of the stainless steel pipe. This stack also used two ceramic alignment pins to maintain orientation. The ceramic discs of the flow straightener sat directly on the upper toroid of the WSR and funneled the exhaust into the circular end of the transition section. In the previous work by Evans [8], a difference in temperature and heat flux was noticed between the left heat transfer gauges and the right heat transfer gauges. This difference was believed to be the result of exhaust that maintained a swirl through the test section after exiting the WSR. The flow straightener was implemented to eliminate or reduce the swirl in the exhaust.

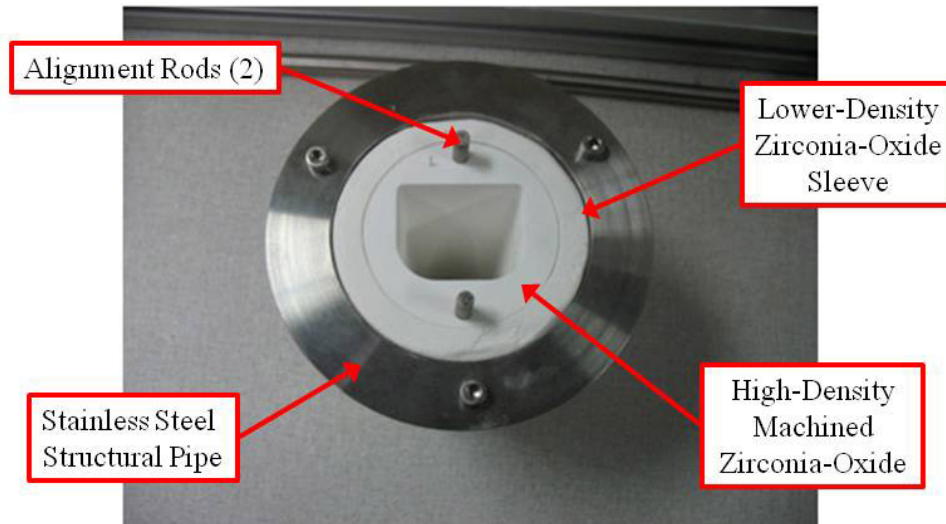


Figure 5.13: Transition section assembly

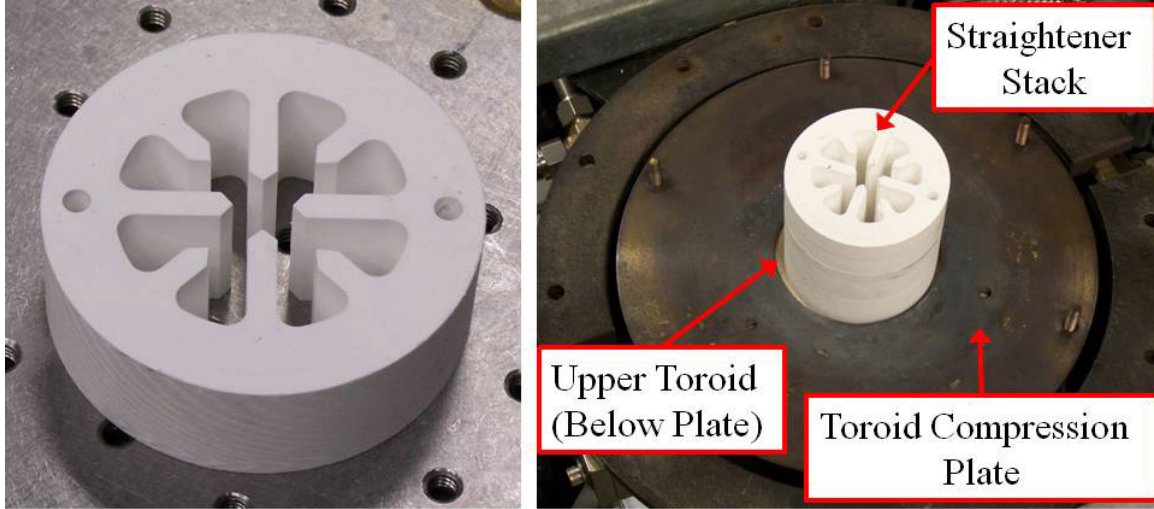


Figure 5.14: Single machined flow straightener disc (left), flow straightener stack sitting on WSR exhaust port (right)

Several flow straightener designs were considered and a CFD analysis was performed to determine the extent to which the final design could remove the swirl in the flow. Figure 5.15 shows the five flow straightener designs that were considered and Table 5.1 outlines several parameters including the hole diameter, material blockage of the flow and (L/D) or equivalent (L/D) for each design. All variations are designed to match the 5.08 cm diameter dimension of the exhaust port on the WSR and the inlet to the transition section.

Table 5.1: Flow straightener design specifications for all designs considered

Design	Hole Diameter	Blockage Area	Percent Blocked	L/D
Design 1	0.635 cm	11.88 cm ²	59 %	12
Design 2	0.508 cm	12.77 cm ²	63 %	15
Design 3	N/A	7.57 cm ²	37 %	5.7
Design 4	N/A	5.5 cm ²	27 %	5.5
Design 5	N/A	6.73 cm ²	33 %	6.0

Despite having the highest (L/D) values, Designs 1 and 2 were not used due to the large percentage of blockage they produced. Design 3 offered a reduced blockage while maintaining a respectable (L/D) value. This design was not used because it

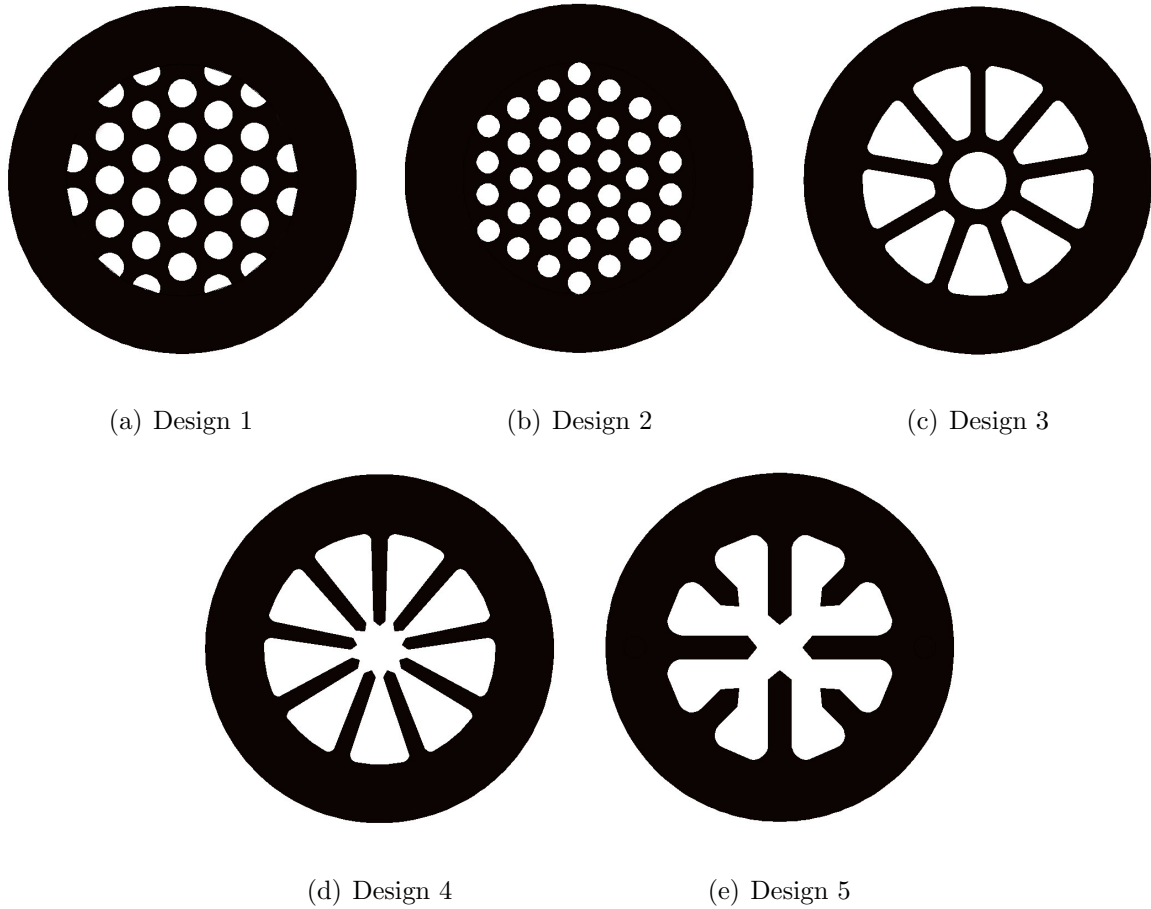


Figure 5.15: Flow straightener designs considered

was predicted that thermal expansion of the inner ring would result in compression fractures and ultimately breakage of the arms. Design 4 offered similar benefits to Design 3, but allowed the arms to freely expand. This design was not used due to manufacturing issues and the thin dimension of the arms. The 0.25 inch diameter tool required for use in the CNC machine that was planned to cut the ceramic discs could not fit between the tips of the arms of Design 4. Design 5 was selected for use because it offered a respectable (L/D) while meeting manufacturing requirements with an increased arm thickness. A detailed manufacturing drawing of the Design 5 flow straightener is shown in Appendix C.

Design 5 was tested numerically using FLUENT[®] to determine the extent that it could remove swirl from a test flow. A numerical ‘test rig’ was created as shown in

Figure 5.16 that injected hot air into a lower circular chamber below the straightener section to impart a swirl. The total mass flow rate of air entering the chamber from all four inlet ports was 0.0085 kg/s which is roughly 450 SLPM. The fluid was allowed to pass through the straightener section and exit from the pressure outlet at the top of the rig.

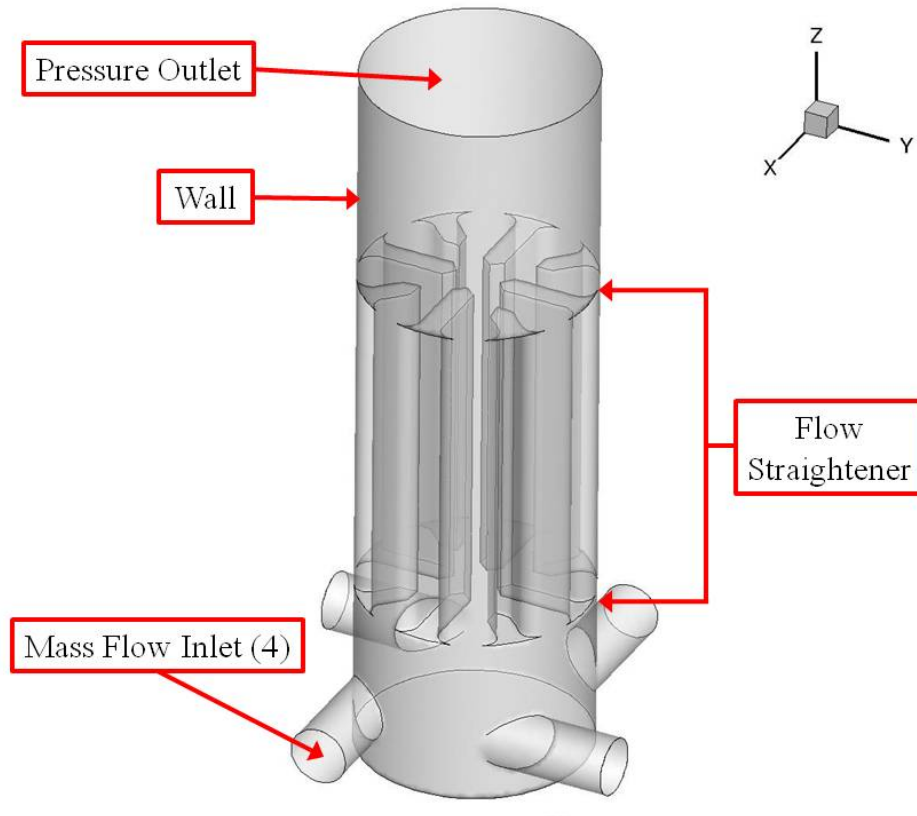
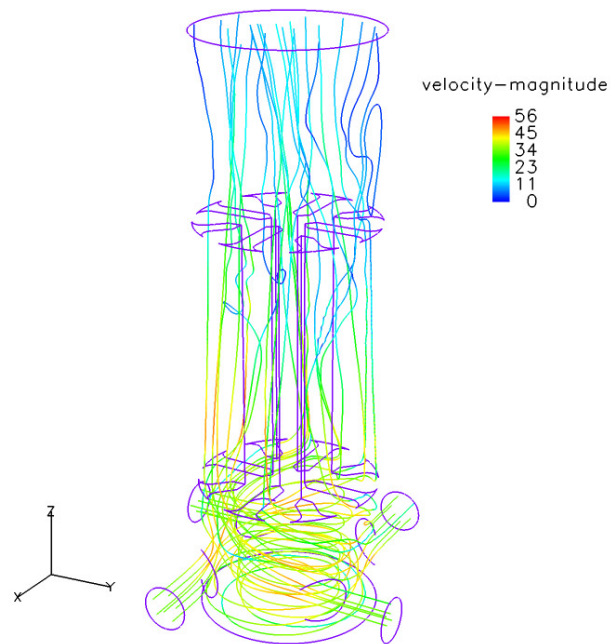
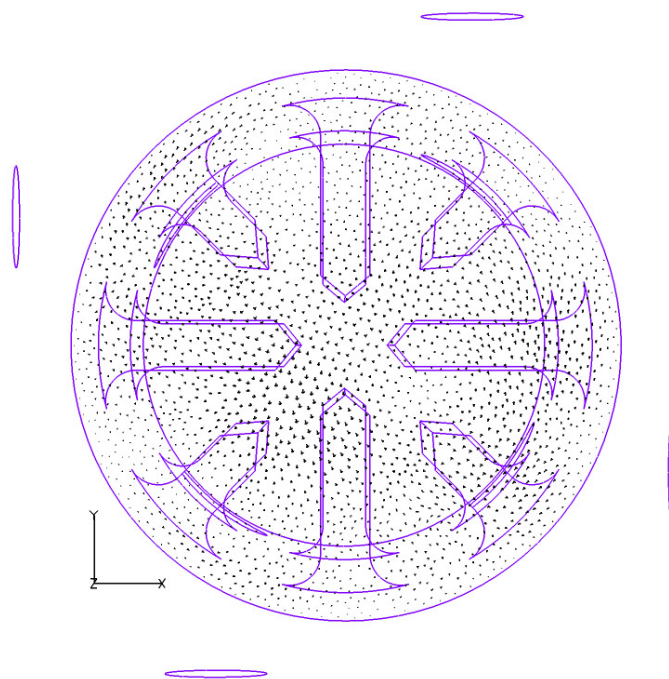


Figure 5.16: Numerical ‘test rig’ for flow straightener testing

The streamline results of the numerical analysis shown in Figure 5.17a show that the swirl was removed from the fluid after the flow straightener section. A review of the vectors at the test rig exit plane shown in Figure 5.17b show that there was no bulk flow swirl as evidenced by the fact that only the arrowheads are visible.



(a) Design 5 Streamlines



(b) Design 5 Exit Plane Vectors

Figure 5.17: Design 5 flow straightener numerical test results

5.2 Air, Nitrogen and Fuel Supply

Air and Nitrogen were both supplied under pressure by the AFRL facility supply. Air was used as the oxidizer in the WSR and as a cooling gas in the majority of the film cooling experiments. Nitrogen was used to cool the WSR jet ring as discussed in Section 5.1.1 and as a cooling gas in some film cooling experiments. The plumbing to the test rig was configured to allow the independent manual selection of either nitrogen or air to either of the film cooling assemblies. This setup allowed one film cooling assembly to use one coolant gas while the other assembly used the other gas. Having this ability allowed for greater flexibility in the test matrix and a wider range of test configurations to be performed. All fluids that were provided to the WSR and test rig were heated. For consistency, the temperature of the combustion air that fed the WSR was heated to 310° K for all testing. The temperature of the cooling gases was not easily controlled and the fluid temperature varied based on the flow rate.

The propane used to fuel the WSR was provided from a 100 lb (45.4 kg) tank located outside the test cell. To ensure a sufficient supply of gaseous propane to meet the flow rate demand, the tank was heated with a belt heater. The propane supply lines located just inside the facility were also heated to prevent condensation of propane inside the pipe. The flow rate of propane was regulated by a mass flow controller located along the supply line after the heaters. The propane and heated combustion air were combined just upstream of the premixed fuel-air inlet to the WSR.

The mass flow rates (measured in SLPM) of the majority of the fluids used in this experiment were managed by the mass flow controllers located on the blue panel shown in Figure 5.18. This panel has controls for combustion air, fuel vaporizer air, afterburner air, combustion dilution nitrogen, and fuel. The combustion air and fuel controls were used as intended, but the fuel vaporizer air and dilution nitrogen control were used to manage the flow rate of coolant gases into the upstream film cooling assembly plenum. Both coolant gases supplied to the downstream film cooling

assembly were managed by the Brooks Instruments controller shown in Figure 5.18, external to the panel.

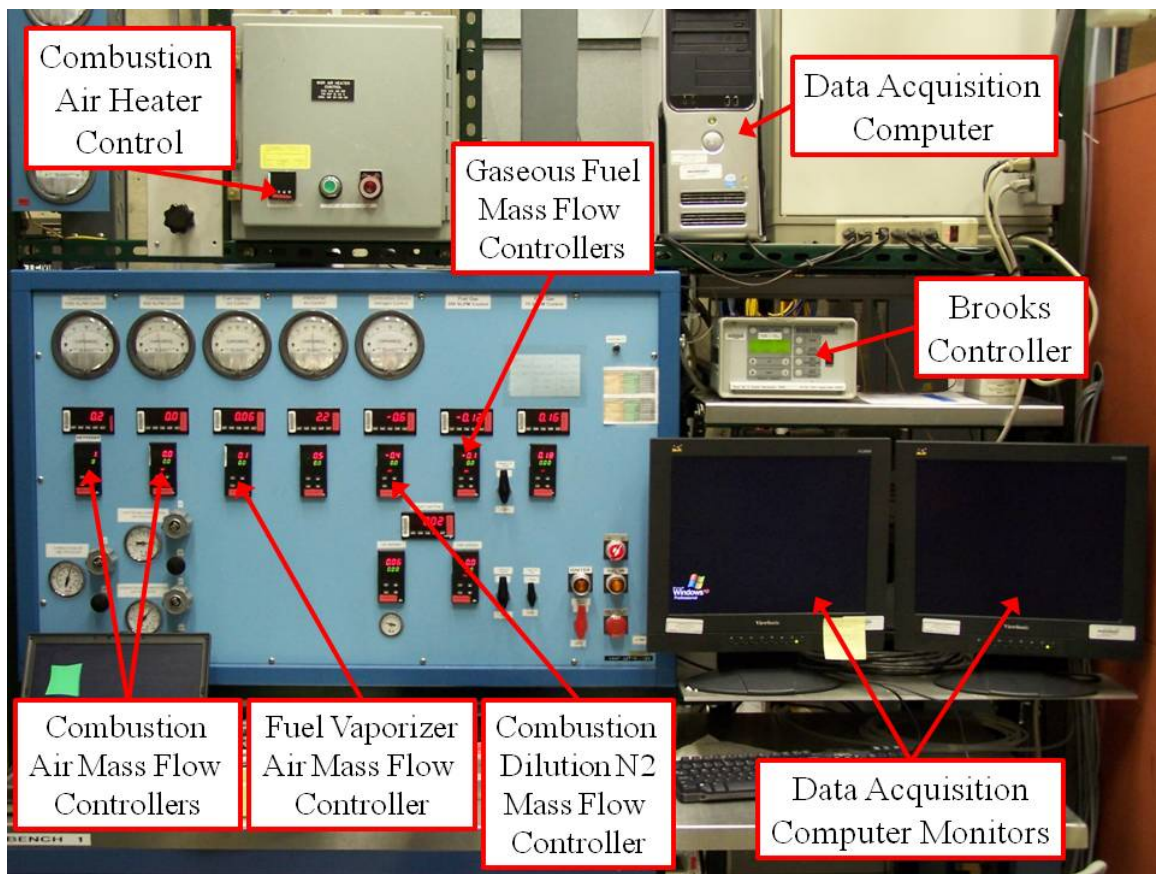


Figure 5.18: Flow controls for air, nitrogen and fuel supplied to the WSR and test rig film cooling plena

5.3 Data Acquisition

All thermocouple, pressure and chemical sampling measurements from the test rig and the WSR were recorded automatically every 2 seconds using a LabView interface running on the data acquisition computer shown in Figure 5.18. All of the mass flow controller settings with the exception of the Brooks Instruments controller were also recorded using LabView. The Brooks Instruments controller settings were manually logged during testing. Figure 5.19 shows a screen shot of the LabView software used for system monitoring and data logging.

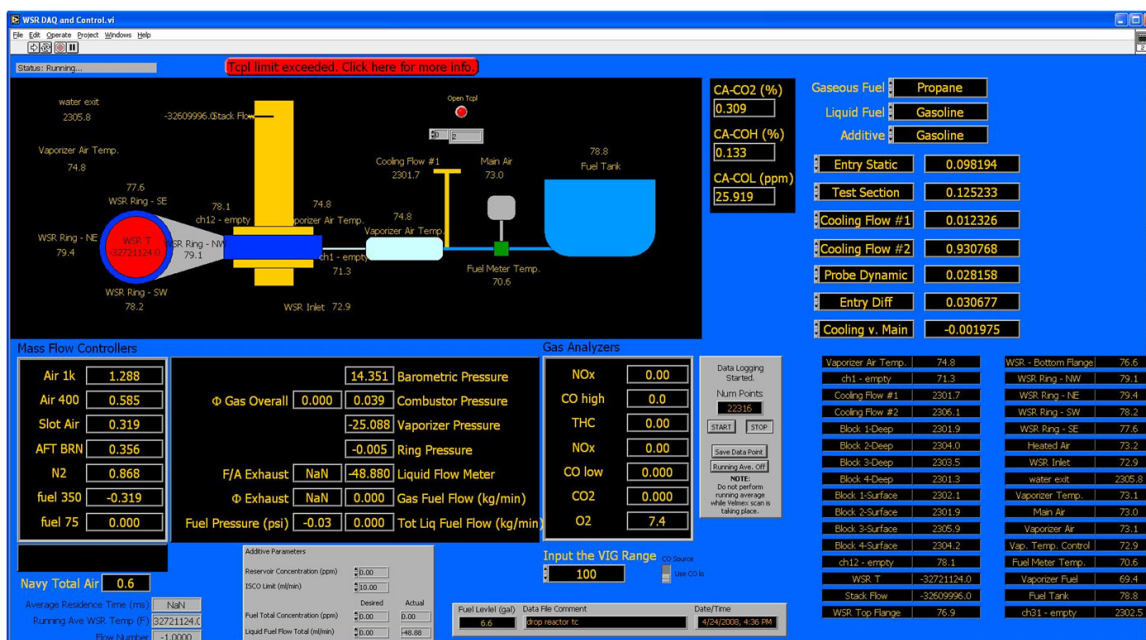


Figure 5.19: Screen shot of LabView system monitor and data logging interface

The manual log not only recorded the Brooks Instruments controller settings for each test case, it also recorded the data point window and blowing and equivalence ratios for each test case. The manual log was created in Microsoft Excel and included calculations of the required flow rates in each film cooling assembly to achieve the desired blowing ratios. The upstream blowing ratio calculation included the free stream contributions of the flow rates of combustion air and fuel while the downstream blowing ratio calculations included the free stream contributions of the flow rates of the combustion air, fuel and upstream cooling fluid. An example of the manual log is shown in Figure 5.20

Data Point	Φ (desired)	Upstream Bay (slot)		Downstream Bay (Fan)		Total Air (SLPM 70)	Propane (SLPM 70)	Calcd Φ	Req'd Air (SLPM 70)	Upstream Bay (Slot)		Downstream Bay (Fan)		Water Cooling Flow (GPM)			
		M (des.) (air)	Air(0) or N2(1)	M (des.) (air)	Air(0) or N2(1)					Vaporizer set	M for Air	M for N2	Req'd Air (SLPM 0)		Brooks Entered	M for Air	M for N2
755	785	0.6	0.5	0	0	426.1	10.75	0.60044046	2.31252287	2.35	0.5081031	0.4913267	0.97381	1.01	2.07432	2.00583	0.5
960	990	0.6	1	0	0	426.1	10.75	0.60044046	4.62504575	4.6	0.9945848	0.961746	0.97874	1.015	2.0741	2.00562	0.5
1155	1185	0.6	2	1	1	426.1	10.75	0.60044046	9.25009149	9.3	2.0107909	1.9443994	0.98903	1.025	2.07275	2.00431	0.5
1355	1385	0.6	0.5	0	0	426.1	10.75	0.60044046	2.31252287	2.35	0.5081031	0.4913267	0.97381	0.975	2.00244	1.93633	0.5
1545	1575	0.6	1	0	2	426.1	10.75	0.60044046	4.62504575	4.6	0.9945848	0.961746	0.97874	0.98	2.00258	1.93646	0.5
1750	1780	0.6	2	0	2	426.1	10.75	0.60044046	9.25009149	9.3	2.0107909	1.9443994	0.98903	0.99	2.00197	1.93587	0.5
2130	2160	1.3	4	0	2	426.1	23.3	1.30141978	19.2988943	19.3	4.0002292	3.8661512	1.05274	1.09	2.07079	2.00241	0.5
2325	2355	1.3	3	0	2	426.1	23.3	1.30141978	14.4741707	14.5	3.0053535	2.906124	1.04223	1.08	2.07248	2.00405	0.5
2540	2570	1.3	2	0	2	426.1	23.3	1.30141978	9.6494715	9.6	1.9897513	1.9240545	1.0315	1.07	2.07464	2.00614	0.5
2750	2780	1.3	1	0	2	426.1	23.3	1.30141978	4.82472357	4.8	0.9948756	0.9620272	1.021	1.06	2.07641	2.00785	0.5
2945	2975	1.3	0.5	0	2	426.1	23.3	1.30141978	2.41236179	2.4	0.4974378	0.4810136	1.01574	1.055	2.0773	2.00871	0.5
3145	3175	1.3	4	0	2	426.1	23.3	1.30141978	19.2988943	19.3	4.0002292	3.8661512	1.05274	1.055	2.00429	1.93812	0.5
3345	3375	1.3	3	0	2	426.1	23.3	1.30141978	14.4741707	14.5	3.0053535	2.906124	1.04223	1.045	2.00631	1.9391	0.5
3535	3565	1.3	2	0	2	426.1	23.3	1.30141978	9.6494715	9.6	1.9897513	1.9240545	1.0315	1.035	2.00678	1.94052	0.5
3725	3755	1.3	1	0	2	426.1	23.3	1.30141978	4.82472357	4.8	0.9948756	0.9620272	1.021	1.025	2.00784	1.94155	0.5
3920	3950	1.3	0.5	0	2	426.1	23.3	1.30141978	2.41236179	2.4	0.4974378	0.4810136	1.01574	1.02	2.00839	1.94207	0.5
4120	4150	1.3	4	1	2	426.2	23.3	1.30111443	19.3030755	20	4.1444173	4.0075786	1.05449	1.055	2.00097	1.9349	0.5
4340	4370	1.3	3	1	2	426.2	23.3	1.30111443	14.4773066	15	3.103313	3.0056839	1.04354	1.045	2.00279	1.93666	0.5
4555	4585	1.3	2	1	2	426.2	23.3	1.30111443	9.65153774	10	2.0722087	2.0037893	1.0326	1.035	2.00465	1.93846	0.5
4760	4790	1.3	4	1	2	426.2	23.3	1.30111443	19.3030755	20	4.1444173	4.0075786	1.05449	1.095	2.07683	2.00826	0.5
4975	5005	1.3	3	1	2	426.2	23.3	1.30111443	14.4773066	15	3.103313	3.0056839	1.04354	1.08	2.06987	2.00153	0.5
5165	5195	1.3	2	1	2	426.2	23.3	1.30111443	9.65153774	10	2.0722087	2.0037893	1.0326	1.07	2.07244	2.00401	0.5
5560	5590	1.5	4	0	2	426.2	26.9	1.50214498	19.5321879	19.5	3.9934082	3.8615555	1.06539	1.105	2.07435	2.00586	0.5
5841	5871	1.5	3	0	2	426.2	26.9	1.50214498	14.6491409	14.65	3.0001759	2.9011173	1.05477	1.095	2.07627	2.00772	0.5
6052	6082	1.5	2	0	2	426.2	26.9	1.50214498	9.76609395	9.8	2.069436	1.9407392	1.04416	1.085	2.07823	2.00961	0.5
6250	6280	1.5	1	0	2	426.2	26.9	1.50214498	4.88304697	4.9	1.034718	0.9703396	1.03343	1.07	2.07078	2.0024	0.5
6450	6480	1.5	0.5	0	2	426.2	26.9	1.50214498	2.44152349	2.5	0.5119754	0.4950712	1.02818	1.065	2.07163	2.00323	0.5
6655	6685	1.5	4	0	2	426.2	26.9	1.50214498	19.5321879	19.5	3.9934082	3.8615555	1.06539	1.07	2.00865	1.94233	0.5
6860	6890	1.5	3	0	2	426.2	26.9	1.50214498	14.6491409	14.7	3.0104154	2.9110187	1.05488	1.055	2.00022	1.93418	0.5
7065	7095	1.5	2	0	2	426.2	26.9	1.50214498	9.76609395	9.8	2.069436	1.9406792	1.04416	1.045	2.00161	1.93553	0.5
7260	7290	1.5	1	0	2	426.2	26.9	1.50214498	4.88304697	4.9	1.034718	0.9703396	1.03343	1.035	2.00304	1.9369	0.5
7465	7495	1.5	0.5	0	2	426.2	26.9	1.50214498	2.44152349	2.5	0.5119754	0.4950712	1.02818	1.03	2.00355	1.9374	0.5
7675	7705	1.5	4	1	2	426.2	26.9	1.50214498	19.5321879	20.2	4.1367614	4.0001754	1.06693	1.07	2.00576	1.93954	0.5
8060	8090	1.5	3	1	2	426.2	26.9	1.50214498	14.6491409	15.2	3.1128105	3.010033	1.05598	1.06	2.00762	1.94133	0.5
8280	8310	1.5	2	1	2	426.2	26.9	1.50214498	9.76609395	10.1	2.0683807	2.0008877	1.04481	1.05	2.00993	1.94356	0.5
9470	9500	1.5	4	1	2	426.2	26.9	1.50214498	19.5321879	20.2	4.1367614	4.0001754	1.06693	1.105	2.07137	2.00298	0.5
9225	9255	1.5	3	1	2	426.2	26.9	1.50214498	14.6491409	15.2	3.1128105	3.010033	1.05598	1.095	2.07391	2.00543	0.5
9030	9060	1.5	2	1	2	426.2	26.9	1.50214498	9.76609395	10.1	2.0683807	2.0008877	1.04481	1.085	2.07693	2.00835	0.5

Figure 5.20: Sample of manual log and blowing ratio calculation spreadsheet

5.4 Test Plan

Testing included analysis of the fan-shaped laidback holes with the solid blank upstream, the angled slot upstream with the fan-shaped laidback holes downstream and the offset normal holes upstream with the fan-shaped laidback holes downstream. Both air and nitrogen were tested as the cooling fluid to determine the performance of the film cooling schemes with and without secondary reactions. With the exception of a baseline case running at fuel lean conditions for each configuration, the remainder of the testing was conducted at fuel rich conditions. All testing was conducted with a water cooling flow rate of 0.5 GPM. Data was taken for 60 seconds for each test point with a 5 minute delay after changes in cooling scheme parameters and a 10 minute delay after equivalence ratio changes to allow temperatures in the rig to stabilize before the next data point was taken.

5.4.1 Single Cooling Scheme. Testing with a single cooling scheme allowed for a baseline result of the surface temperature, heat flux and convective heat transfer coefficient in the presence of secondary combustion to be measured. The fan-shaped laidback holes were tested with a blowing ratio of 0.5, 1 and 2 with a WSR equivalence ratio of 0.6, 1.1, 1.3 and 1.5 with air and nitrogen used as the film cooling fluid. The total combustion air flow rate into the WSR was 425 SLPM, half of the value used by Evans [8]. The flow rate was reduced to reduce the thermal and aerodynamic stresses on the WSR and test rig since testing was conducted at hotter conditions near stoichiometric. A reduced data set was conducted at an equivalence ratio of 0.6 and 1.5 at a combustion air flow rate of 850 SLPM for comparison to the results obtained by Evans [8].

5.4.2 Cooling Schemes in Series. The study of film cooling with two cooling schemes in series was conducted to observe the variation in surface temperature, heat flux and convective heat transfer coefficient in the presence of secondary combustion compared to the baseline result. The angled slot and offset normal holes were tested upstream of fan-shaped laidback holes at blowing ratios of 0.5, 1, 2, 3

and 4 for the upstream scheme and a constant blowing ratio of 2 for the fan-shaped laidback holes. Equivalence ratios of 0.6, 1.1, 1.3 and 1.5 were run in the WSR with multiple combinations of air and nitrogen used in the upstream and downstream film cooling assemblies. All testing was completed at a combustion air flow rate of 425 SLPM.

VI. Experimental Film-Cooling Test Results

For each of the test configurations described in Chapter 5, the values of the heat flux, temperature at the surface of the heat flux gauges and the convective heat transfer coefficient were calculated. These values were found using the heat transfer equations and thermal conductivity of Hastelloy-X[®] presented in Section 2.4. The calculations were performed using the experimentally collected free stream exhaust temperature and both temperatures from each heat transfer gauge. The differences between air and nitrogen as the cooling gas were also calculated for the heat flux and heat transfer coefficient. The film cooling effectiveness was computed but will not be presented in this report. The use of water cooling artificially increased the film cooling effectiveness to levels near, and in some cases above, 1.

Figure 6.1 shows the exhaust exiting the test rig for several WSR equivalence ratios. For $\Phi < 1$, there was no fuel in the exhaust to react with the ambient air as the exhaust stream exited the test rig, however, for $\Phi > 1$ the amount of the fuel in the exhaust stream is clearly shown by the intensity of the reaction caused by the interaction of the fuel in the exhaust with the ambient air. The intensity of the reactions caused by fuel in the exhaust interacting with oxygen in the film coolant followed the same pattern.

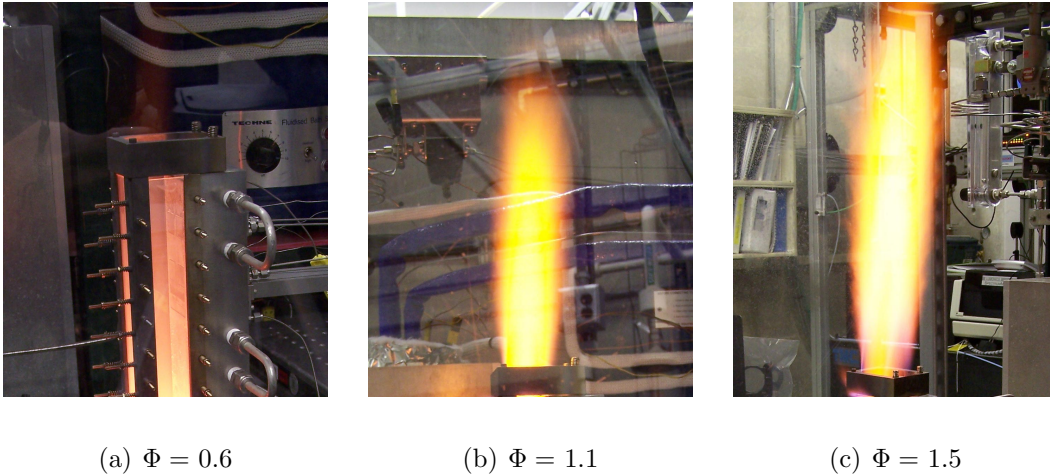


Figure 6.1: Fluid exiting the test rig for various WSR equivalence ratios ($\dot{m}_{air} = 425$ SLPM)

As expected, the temperature of the exhaust from the WSR was directly related to the equivalence ratio of combustion within the reactor. The solid blue markers and polyfit line in Figure 6.2 shows the relationship of equivalence ratio and reactor exhaust temperature as measured at the inlet of the test rig, under current test conditions. This figure also shows data obtained by Evans [8] at a higher flow rate and comparison data collected at the same flow rate at the start of the current study. The largest measured temperature occurred during slightly fuel rich combustion at an equivalence ratio of 1.1.

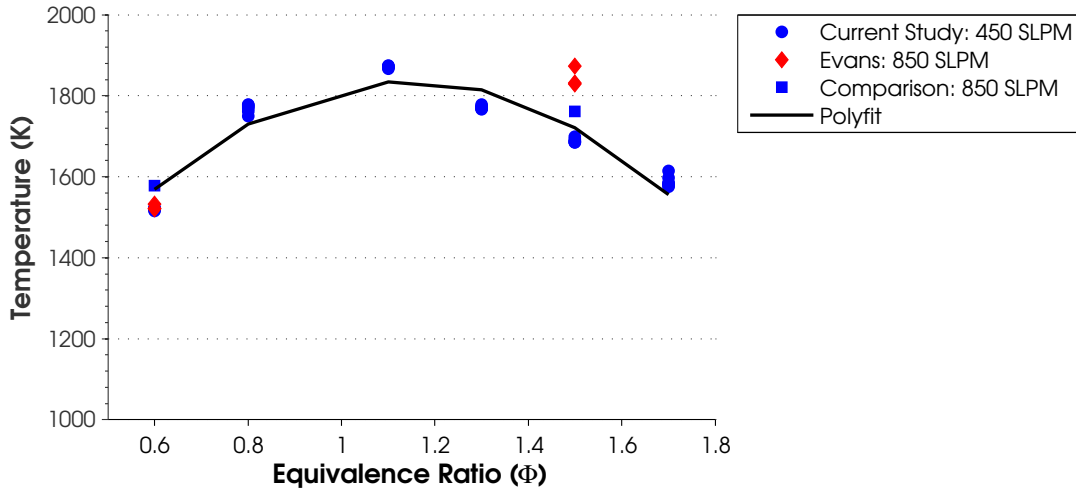


Figure 6.2: Reactor exhaust temperature at the entrance to the test rig as a function of equivalence ratio. Current study ($\dot{m}_{air}=425$ SLPM) with polyfit line. Evans [8] data and comparison data ($\dot{m}_{air}= 850$ SLPM)

The results shown in the remainder of this chapter are presented by film cooling hole configuration followed by comparisons made between the different configurations.

6.1 Single Film Cooling Scheme

The single film cooling scheme was tested to provide a baseline for the results obtained using two film cooling schemes in series. For this series of tests, the fan-shaped laidback holes were tested in the downstream position with a solid blank filling the upstream position.

In addition to comparing the WSR exhaust temperature at the entrance of the test rig to results obtained by Evans [8] at two equivalence ratios, comparisons of the heat flux and convective heat transfer coefficients were also made. This comparison ensured the WSR, instrumentation and data acquisition system were operating correctly to produce repeatable results. For an equivalence ratio of 0.6, the comparison of the heat flux is shown in Figure 6.3 with the comparison of the convective heat transfer coefficient shown in Figure 6.4. For $\Phi = 1.5$, the comparison plots are shown in Figures 6.5 and 6.6 for the heat flux and convective heat transfer coefficient, respectively. The difference in the magnitude of the results obtained by Evans and those collected in the current study were due to slight differences in the WSR exhaust temperature shown in Figure 6.2 and a 0.25 GPM difference in the water cooling flow rate. The fact that the trends in the data were maintained, however, showed that the current setup was correct and the instrumentation and data acquisition system was functional.

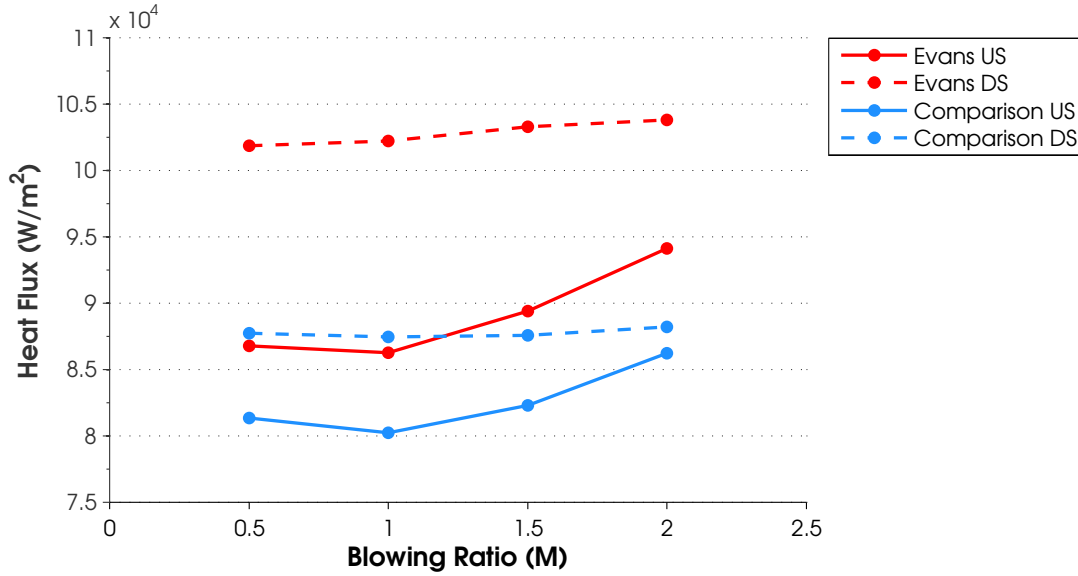


Figure 6.3: Heat flux comparison to Evans [8], $\Phi = 0.6$, $\dot{m}_{air}=850$ SLPM, Fan-shaped holes, Coolant=Air, M=Variable

Based on the results obtained by Evans [8], any condition run at $\Phi < 1$ did not show any significant differences in surface temperature, heat flux or convective

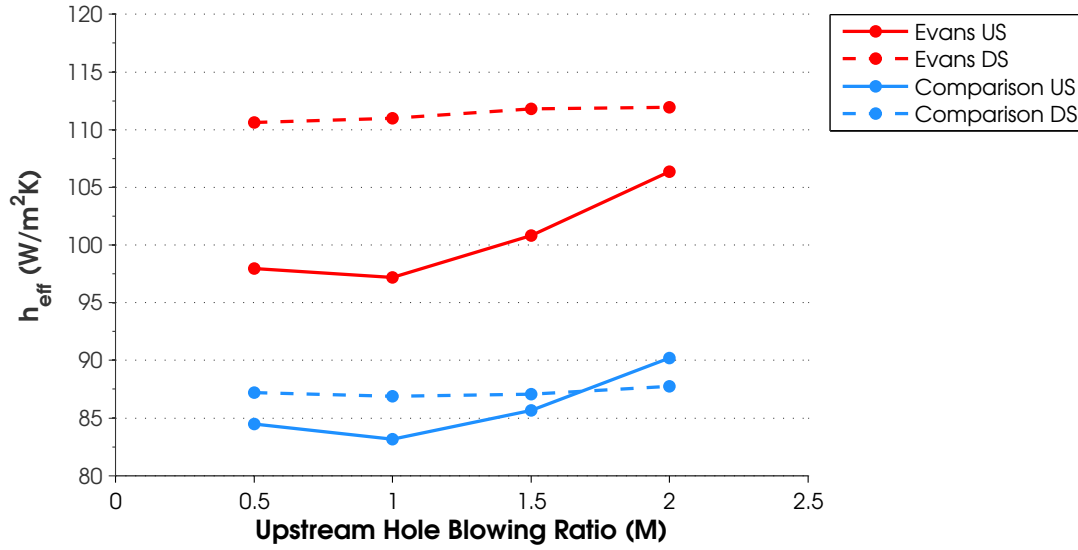


Figure 6.4: Convective heat transfer coefficient comparison to Evans [8], $\Phi = 0.6$, $\dot{m}_{air}=850$ SLPM, Fan-shaped holes, Coolant=Air, M=Variable

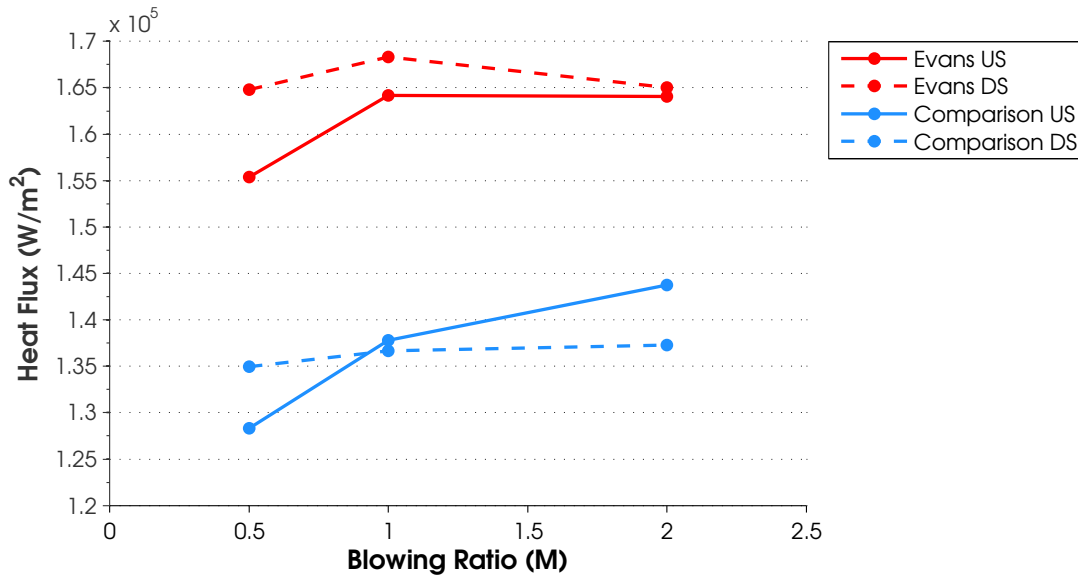


Figure 6.5: Heat flux comparison to Evans [8], $\Phi = 1.5$, $\dot{m}_{air}=850$ SLPM, Fan-shaped holes, Coolant=Air, M=Variable

heat transfer using air and nitrogen as the cooling gas. For this reason only one fuel-lean test condition was conducted at $\Phi = 0.6$. As expected, the calculated surface temperature of each heat transfer gauge was approximately equal when using air and nitrogen, as shown in Figure 6.7 where the temperature is plotted as a function

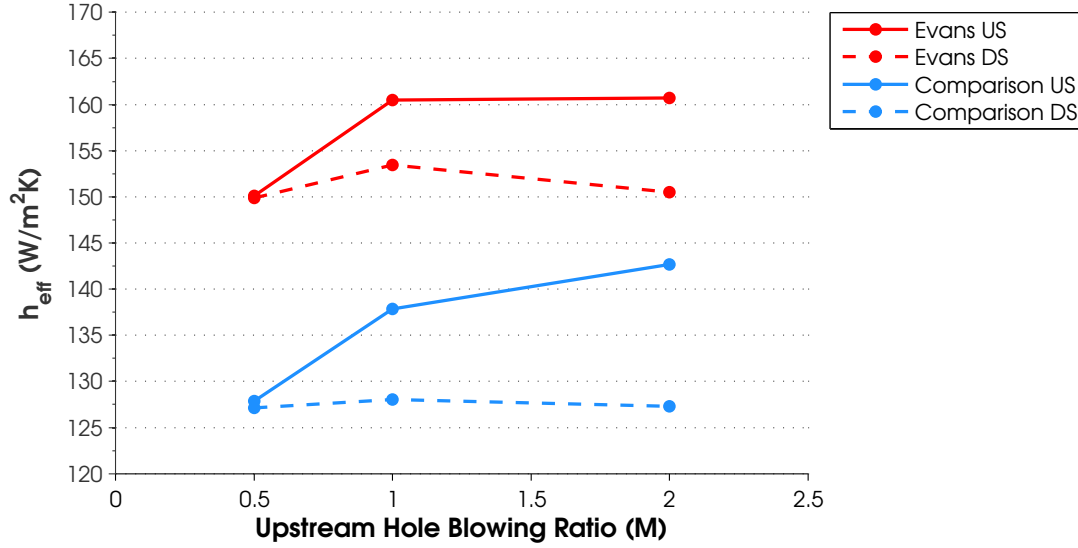


Figure 6.6: Convective heat transfer coefficient comparison to Evans [8], $\Phi = 1.5$, $\dot{m}_{air}=850$ SLPM, Fan-shaped holes, Coolant=Air, M=Variable

of blowing ratio. The heat flux and convective heat transfer coefficient were also comparable using the two coolant gases with the results shown as a function of blowing ratio in Figure 6.8 and 6.9, respectively.

In this case it is easy to see that the results using air and nitrogen as the cooling gas were almost identical, indicating that no heat release occurred in the cooling film due to secondary reactions. It can also be seen that the downstream heat flux gauges ('A' and 'B') recorded a cooler surface temperature than the upstream gauges ('C' and 'D') as shown in Figure 6.7. There was a slight difference noted between the left and right gauges for the same downstream distance. This result was also recorded in the data collected by Evans [8]. The fact that a difference in temperature was still observed even with the addition of the flow straightener shows that residual swirl in the exhaust stream was not the cause of the unbalanced temperatures reported by Evans. It was discovered during the offset normal hole testing, discussed later, that the difference was the result of improperly seated thermocouples in two heat transfer gauges in the test rig, not a flow phenomenon. The problem was easily corrected by swapping and re-seating the thermocouples between the 'B' and 'C' heat transfer

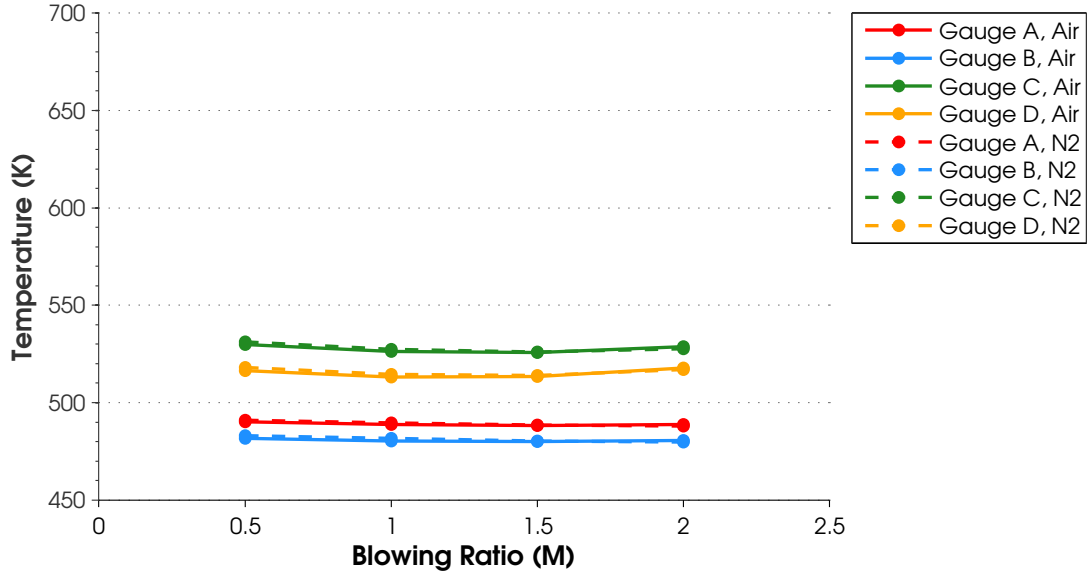


Figure 6.7: Gauge surface temperature, $\Phi = 0.6$, $\dot{m}_{air}=425$ SLPM, Fan-shaped holes, Coolant=Air/N₂, M=Variable

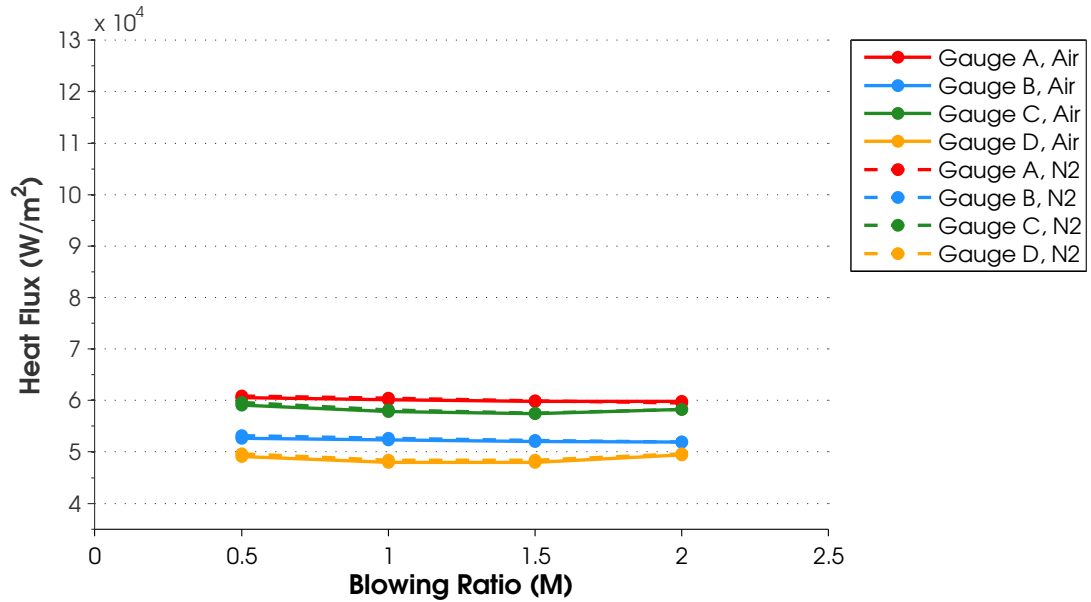


Figure 6.8: Gauge heat flux, $\Phi = 0.6$, $\dot{m}_{air}=425$ SLPM, Fan-shaped holes, Coolant=Air/N₂, M=Variable

gauges. While any residual swirl was removed from the WSR exhaust stream by the addition of the flow straightener, the flow straightener was shown to be an unnecessary addition.

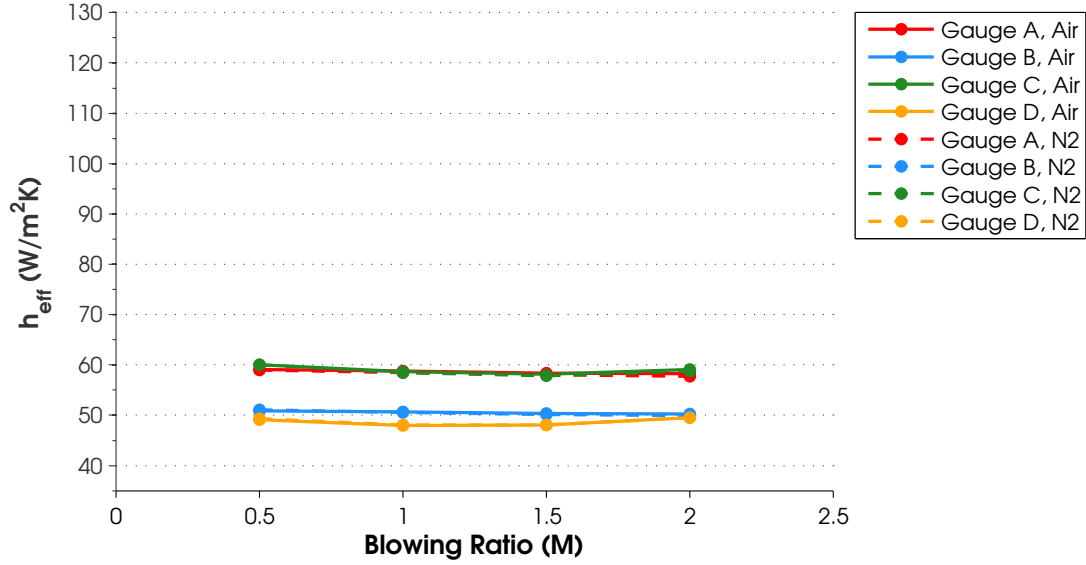


Figure 6.9: Gauge heat transfer coefficient, $\Phi = 0.6$, $\dot{m}_{air}=425$ SLPM, Fan-shaped holes, Coolant=Air/N₂, M=Variable

When the fuel-rich equivalence ratios were tested, there was a very noticeable difference in the calculated parameters between air and nitrogen. The largest differences between air and nitrogen for this film cooling configuration occurred for an equivalence ratio of 1.3. These results are shown in Figures 6.10, 6.11 and 6.12 for the surface temperature, heat flux and heat transfer coefficient, respectively. The results for the other equivalence ratios tested are shown in Appendix E.

From Figures 6.10, 6.11 and 6.12 it can be seen that the upstream gauges showed the largest difference in surface temperature, heat flux and heat transfer coefficient for the different cooling gases. The differences in these values for the downstream gauges was much less pronounced indicating that the secondary reaction in the cooling film occurred upstream or over the upstream gauges and the reactions had finished by the time the cooling air reached the downstream gauges. The temperature of the air near the wall was increased due to the secondary reaction occurring upstream of the downstream gauges and was most likely the cause of the consistent minimal difference between the cooling gases observed in the downstream position.

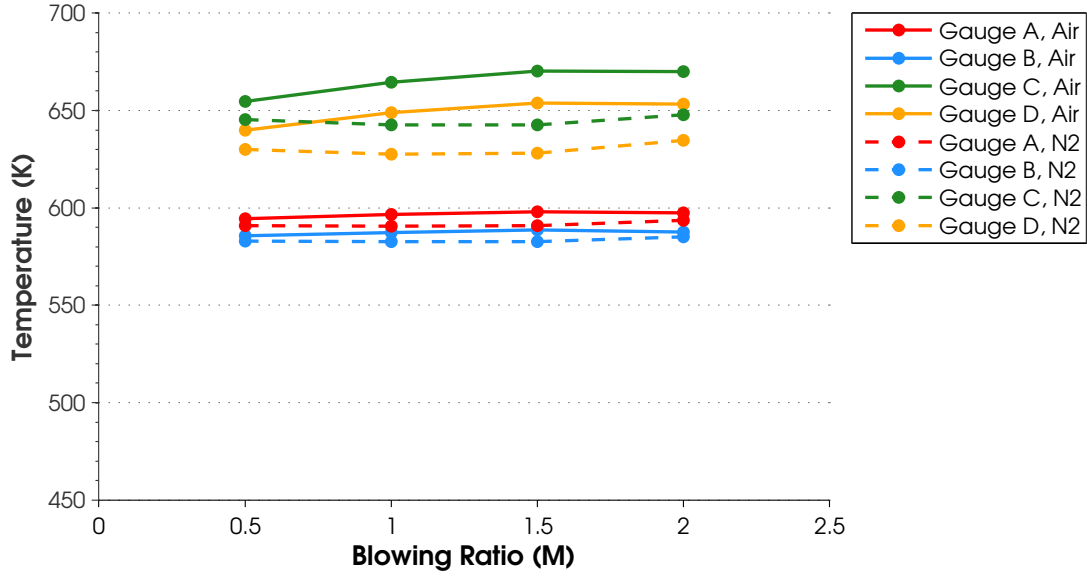


Figure 6.10: Gauge surface temperature, $\Phi = 1.3$, $\dot{m}_{air}=425$ SLPM, Fan-shaped holes, Coolant=Air/N₂, M=Variable

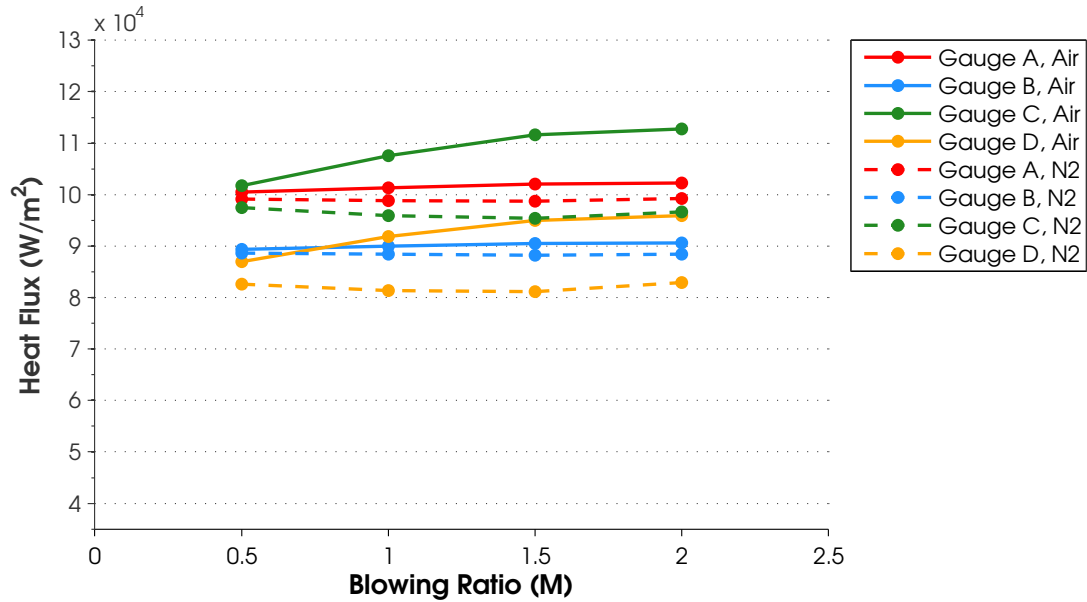


Figure 6.11: Gauge heat flux, $\Phi = 1.3$, $\dot{m}_{air}=425$ SLPM, Fan-shaped holes, Coolant=Air/N₂, M=Variable

To quantify the differences between air and nitrogen for the heat flux and the heat transfer coefficient, Figures 6.13 and 6.14 are provided. In all difference plots

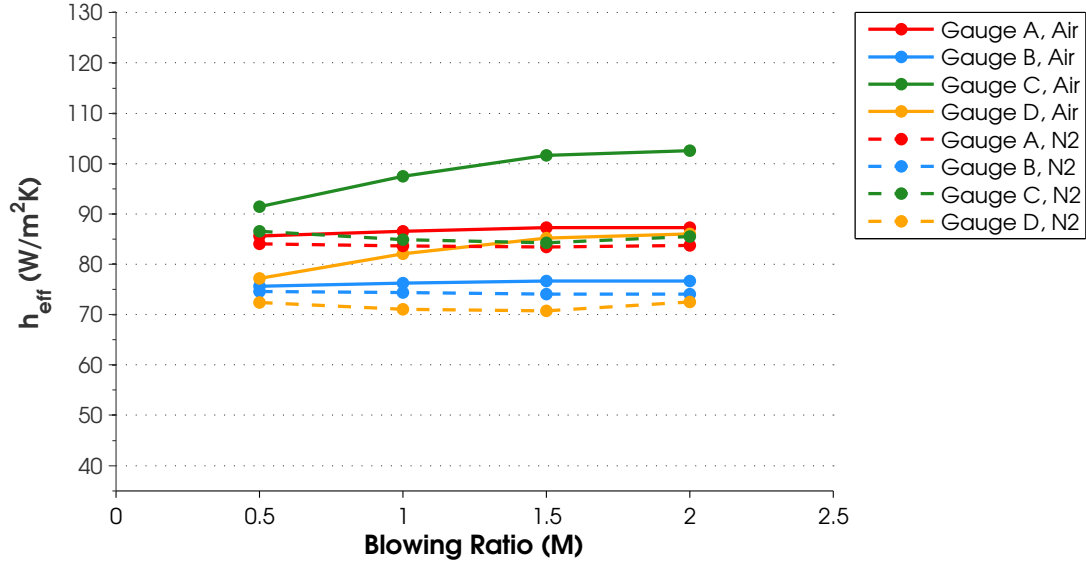


Figure 6.12: Gauge heat transfer coefficient, $\Phi = 1.3$, $\dot{m}_{air}=425$ SLPM, Fan-shaped holes, Coolant=Air/N₂, M=Variable

provided in this report, a positive value is the result of the parameter being larger with air compared to nitrogen (Difference = Air -N₂).

While the data showing an increased temperature, heat flux and heat transfer coefficient all indicate that secondary reactions occurred for all test cases with $\Phi > 1$, there was no visible reactions observed. Evans [8] reported seeing visible reactions for several test cases but no mention was made of a visible reaction occurring with the fan-shaped laidback holes despite evidence that a reaction had occurred in his analysis as well.

During this series of testing, intense localized heating of the stainless steel pipe housing the flow straightener and transition section was observed and is shown in Figure 6.15. The vertical cherry red section of the pipe was caused by a vertical crack in the low-density and high-density ceramic of the transition section which allowed heat from the exhaust to reach the stainless steel pipe. The horizontal cherry red section was caused by a horizontal crack in the low-density ceramic located between the high-density ceramic components of the flow straighter and transition section. No change in performance of the WSR or measurements in the test rig were observed as

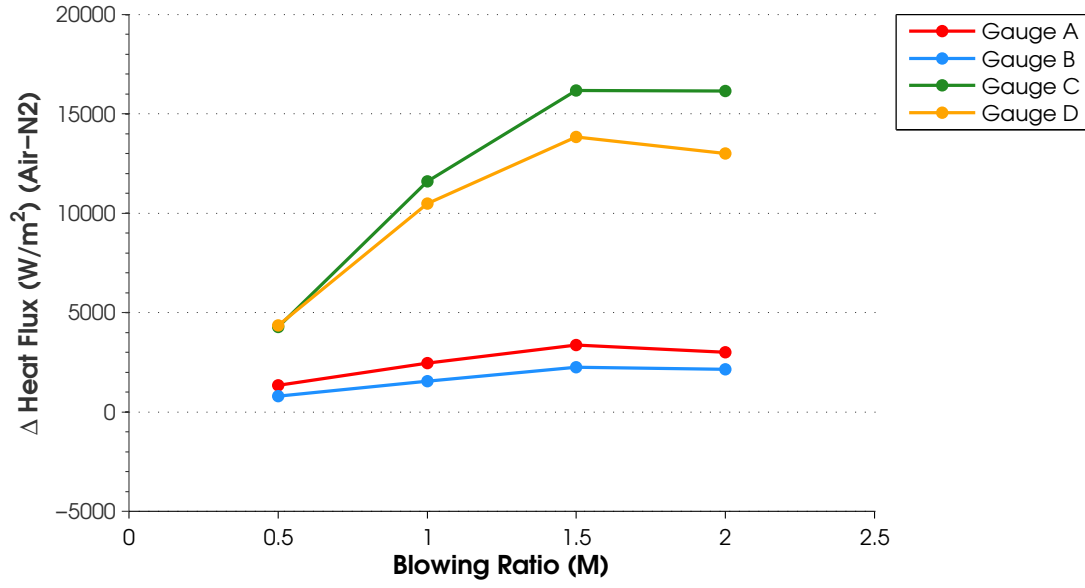


Figure 6.13: Heat flux difference, $\Phi = 1.3$, $\dot{m}_{air}=425$ SLPM, Fan-shaped holes, Coolant=Air/N₂, M=Variable

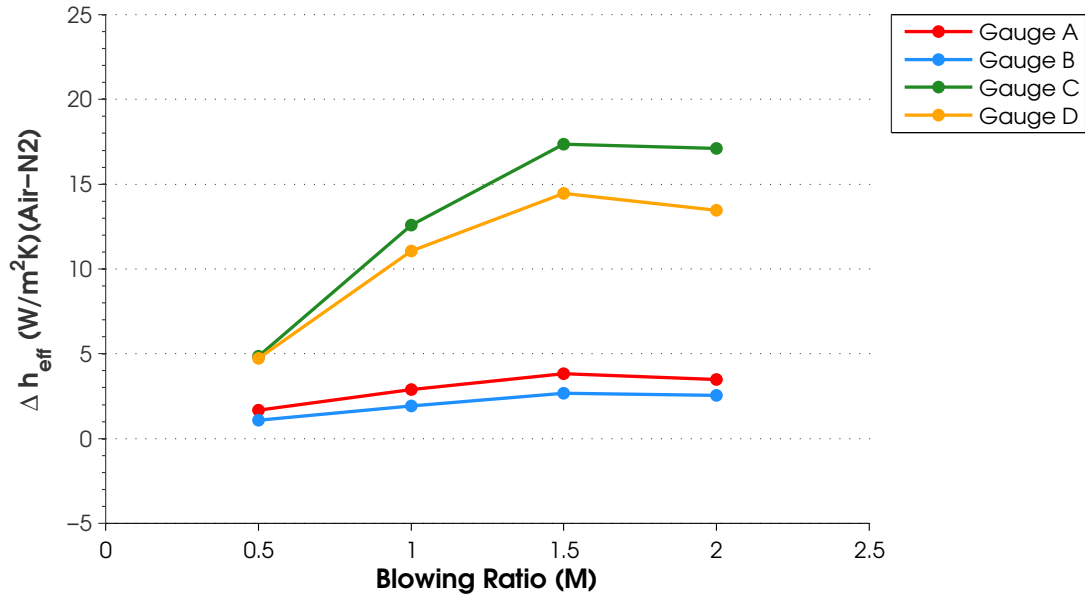


Figure 6.14: Heat transfer coefficient difference, $\Phi = 1.3$, $\dot{m}_{air}=425$ SLPM, Fan-shaped holes, Coolant=Air/N₂, M=Variable

a result of the cracks. The remaining testing was conducted without replacing the ceramic components.

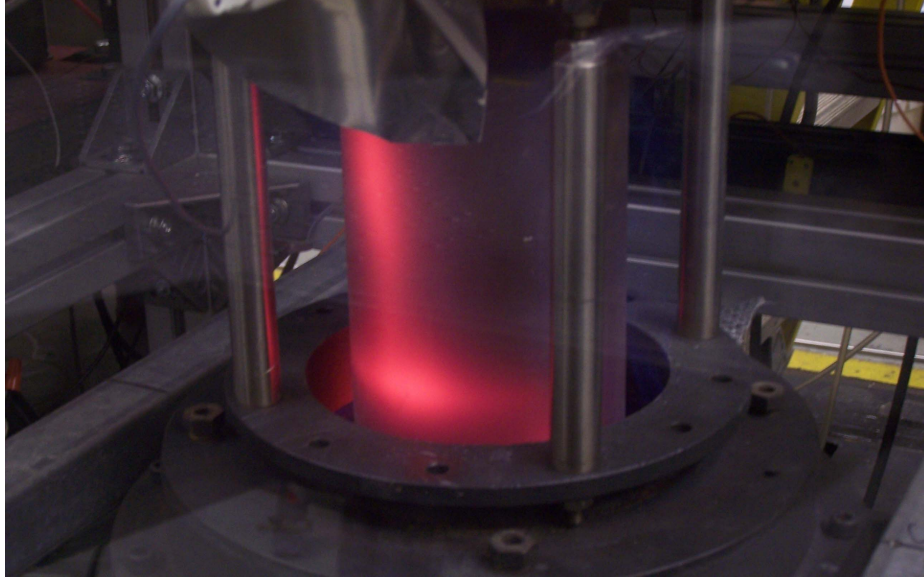


Figure 6.15: Cherry red sections of the stainless steel pipe housing the flow straightener and transition section caused by cracks in the ceramic components

6.2 *Film Cooling Schemes in Series*

Film cooling schemes in series were tested in the exhaust of fuel-rich combustion to determine if a reduction in surface temperature, heat flux and heat transfer coefficient could be achieved by controlling the location of secondary reactions. Two different configurations were tested, one with an angled slot and the other with offset normal holes upstream of the fan-shaped laidback holes. These schemes were selected for use in the upstream bay due to the volume of air that is ejected for equivalent blowing ratios compared to a single row of holes.

6.2.1 *Upstream Slot, Downstream Fan-Shaped Laidback Holes.*

This configuration was tested for a WSR equivalence ratio of 0.6 to once again verify that no secondary reactions occurred. This configuration also provides an indication of the additional cooling benefits provided by the slot. Figures 6.16, 6.17 and 6.18 show the surface temperature, heat flux and heat transfer coefficient, respectively. These figures can be compared to Figures 6.7, 6.8 and 6.9, for a blowing ratio of 2 in the fan alone. In Figures 6.7, 6.8 and 6.9 the blowing ratio variation was in the

fan-shaped holes, compared to Figures 6.16, 6.17 and 6.18 where the blowing ratio in the fan-shaped holes was fixed at 2 and the variation of blowing ratio was for the slot. For a slot blowing ratio of 0.5 the surface temperature was reduced 10 degrees and continued to decrease for higher blowing ratios compared to the fan-shaped holes alone which maintained a fairly uniform temperature across all blowing ratios.

In the remaining figures of this chapter, the figure caption outlines the test configuration for the upstream (US), and downstream (DS, cooling holes. When the plot legend indicates there are separate results for air and nitrogen, this variation occurred in the downstream fan-shaped holes that lists ‘Air/N₂’ as the coolant gas. The blowing ratio along the x-axis in all plots is for the upstream slot/holes that list the blowing ratio as ‘M=Variable’.

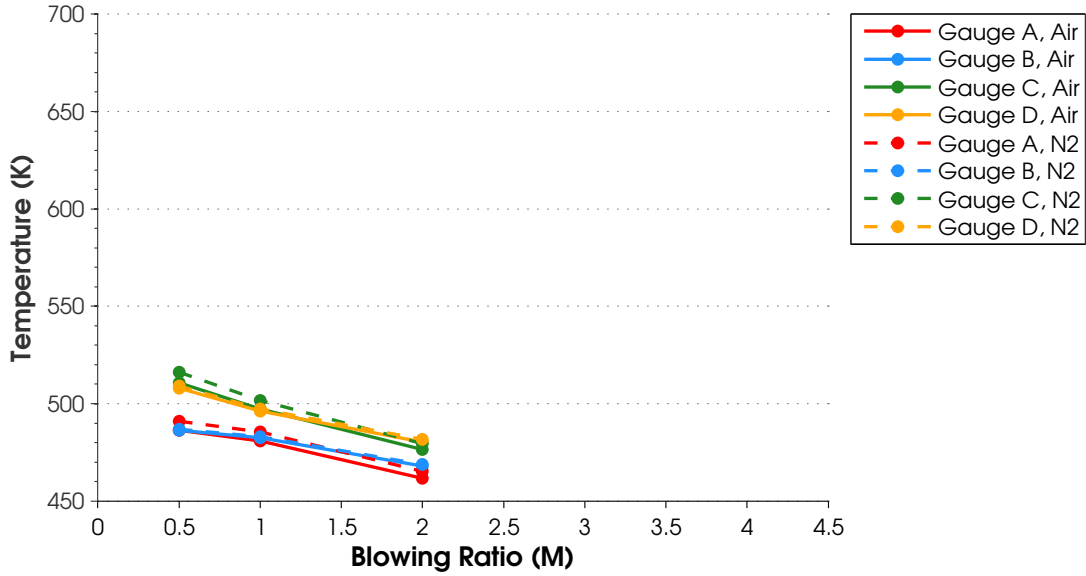


Figure 6.16: Gauge surface temperature, $\Phi = 0.6$, $\dot{m}_{air}=425$ SLPM, US: Slot, Coolant=Air, M=Variable, DS: Fan, Coolant=Air/N₂, M=2

For the slot/fan film cooling configuration, the largest surface temperature, heat flux and heat transfer coefficient occurred at $\Phi = 1.5$ with a slot blowing ratio of 0.5. These results are shown in Figures 6.19, 6.20, 6.21, 6.22 and 6.23 for the surface temperature, heat flux, delta heat flux, heat transfer coefficient and delta heat transfer coefficient, respectively. For this condition, the slot is providing sufficient oxygen, far

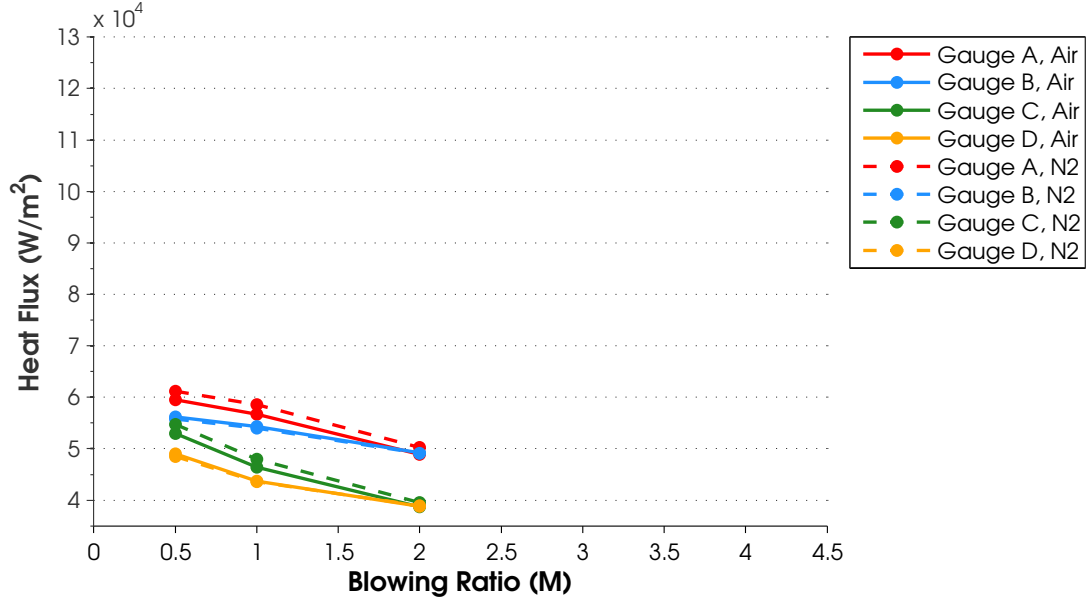


Figure 6.17: Gauge heat flux, $\Phi = 0.6$, $\dot{m}_{air}=425$ SLPM, US: Slot, Coolant=Air, M=Variable, DS: Fan, Coolant=Air/N₂, M=2

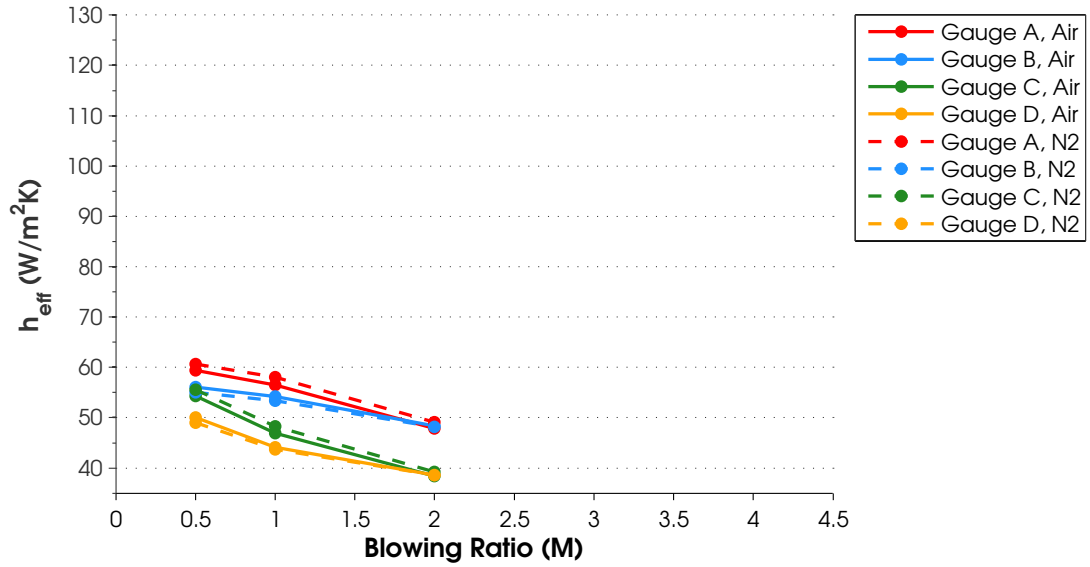


Figure 6.18: Gauge heat transfer coefficient, $\Phi = 0.6$, $\dot{m}_{air}=425$ SLPM, US: Slot, Coolant=Air, M=Variable, DS: Fan, Coolant=Air/N₂, M=2

more than the fan-shaped laidback holes alone could, with the largest amount of fuel in the exhaust tested to produce a secondary reaction. With a low blowing ratio in the slot, the reactions occurred at the exit of the slot and were quickly convected

downstream along the face of the flat plate, heating the surface. As the slot blowing ratio was increased, the secondary reactions occurred further away from the wall as the film penetrated further into the free stream which allowed the coolant from the fan-shaped laidback holes to cool the gauges.

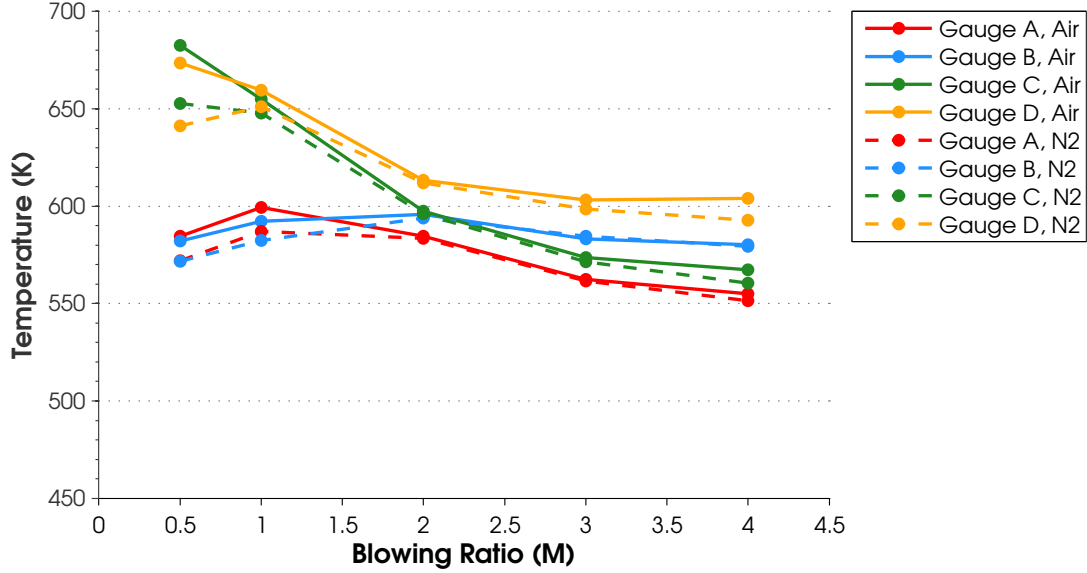


Figure 6.19: Gauge surface temperature, $\Phi = 1.5$, $\dot{m}_{air}=425$ SLPM, US: Slot, Coolant=Air, M=Variable, DS: Fan, Coolant=Air/N₂, M=2

As previously mentioned, the largest heat flux and surface temperature for this cooling configuration occurred for a slot blowing ratio of 0.5 with the upstream gauges reporting higher values than the downstream. At a slot blowing ratio of 2, the temperatures reported in all gauges were at their closest value. At a slot blowing ratio of approximately 1.5, the heat flux between the upstream and downstream gauges was approximately equal. For increased slot blowing ratios, the upstream heat flux continued to decrease while the downstream heat flux decreased slightly. This pattern supports the statement that at higher slot blowing ratios, the coolant exited the slot further into the free stream flow and caused the secondary reactions to occur away from the wall, thus resulting in less heat flux to the gauges, specifically the upstream gauges. It was also noted that with the exception of the heat transfer coefficient, beyond a slot blowing ratio of 2, there was very little difference in surface temper-

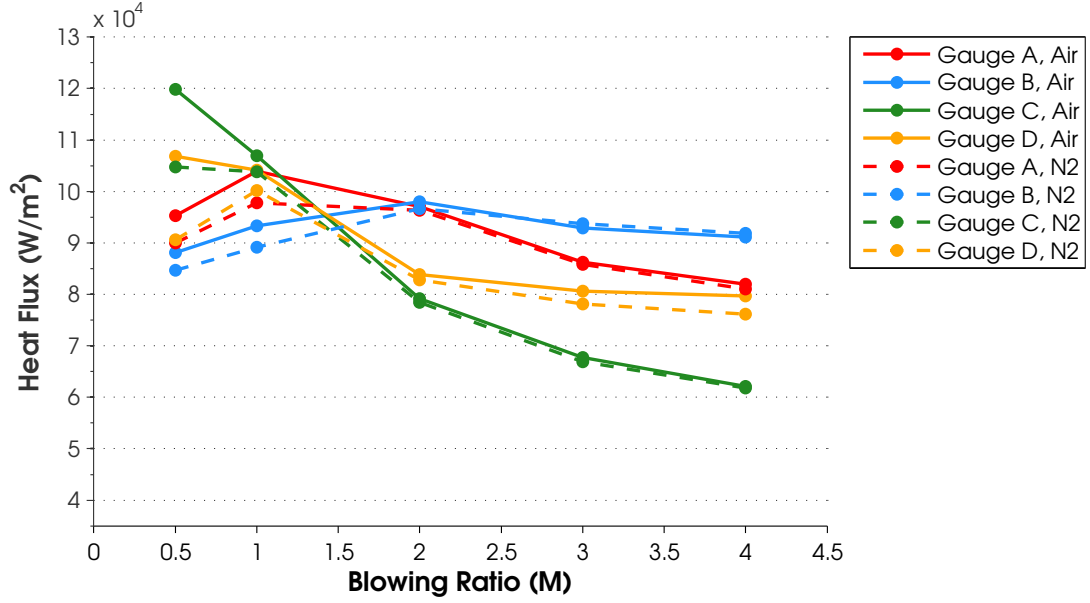


Figure 6.20: Gauge heat flux, $\Phi = 1.5$, $\dot{m}_{air}=425$ SLPM, US: Slot, Coolant=Air, M=Variable, DS: Fan, Coolant=Air/N₂, M=2

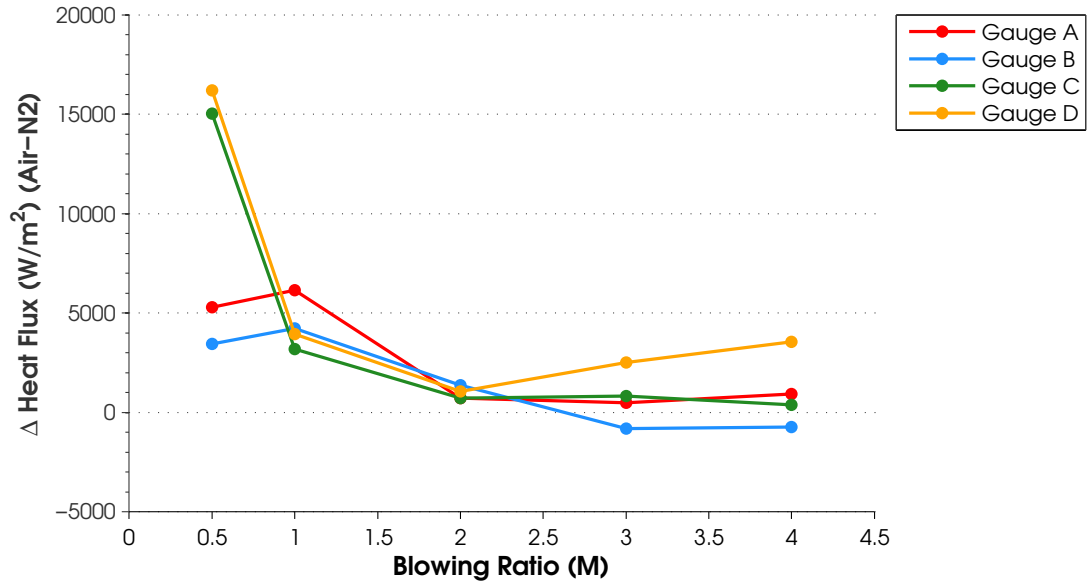


Figure 6.21: Heat flux difference, $\Phi = 1.5$, $\dot{m}_{air}=425$ SLPM, US: Slot, Coolant=Air, M=Variable, DS: Fan, Coolant=Air/N₂, M=2

ature for the downstream gauges and very little variation in heat flux on all gauges when using air or nitrogen in the fan-shaped holes. This result indicates that at a slot blowing ratio of 2, there was sufficient oxygen to burn the fuel in the exhaust near

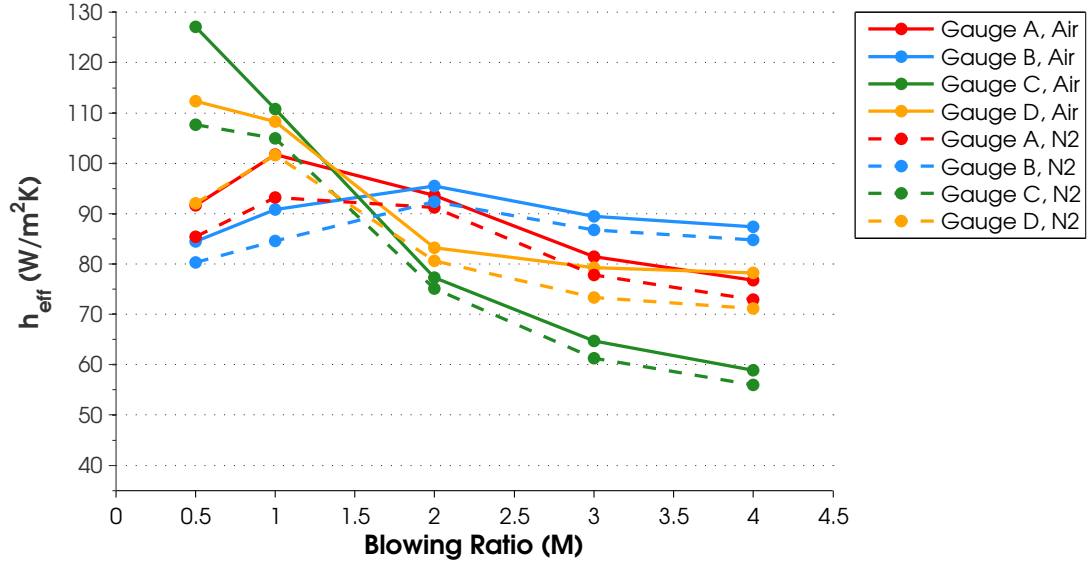


Figure 6.22: Gauge heat transfer coefficient, $\Phi = 1.5$, $\dot{m}_{air}=425$ SLPM, US: Slot, Coolant=Air, M=Variable, DS: Fan, Coolant=Air/N₂, M=2

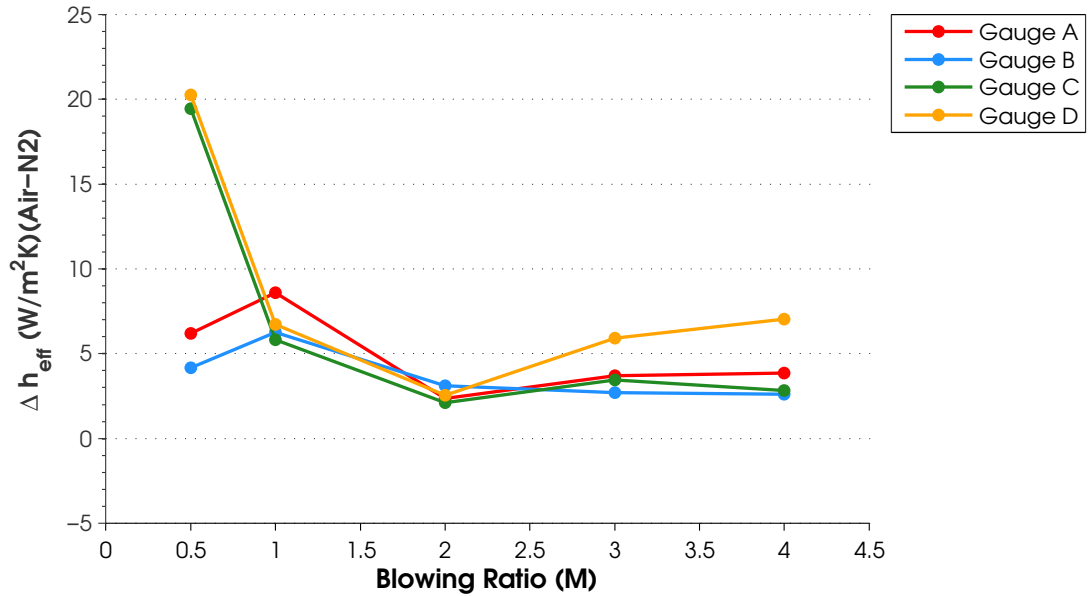


Figure 6.23: Heat transfer coefficient difference, $\Phi = 1.5$, $\dot{m}_{air}=425$ SLPM, US: Slot, Coolant=Air, M=Variable, DS: Fan, Coolant=Air/N₂, M=2

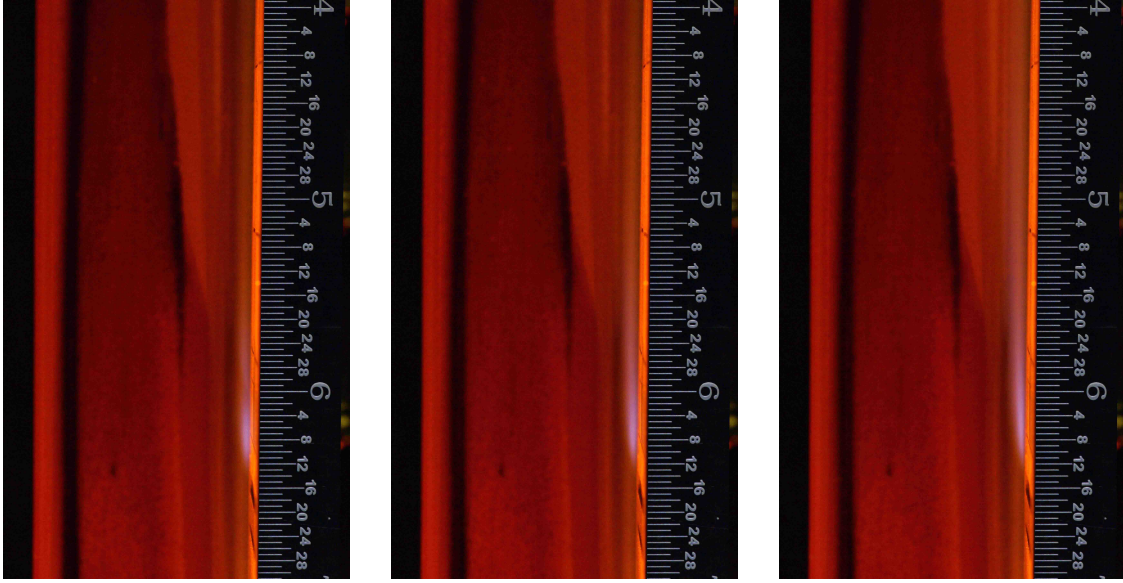
the surface of the flat plate and prevent a secondary reaction with the air exiting the fan-shaped holes. These results also show that there is a film cooling configuration that can relocate the secondary reactions away from the wall and reduce or prevent

secondary reactions near the wall from occurring downstream. Using the upstream slot, for $\Phi = 1.1$ the optimal slot blowing ratio was found to be 3, while $\Phi = 1.3$ and $\Phi = 1.5$ show a slot blowing ratio of 2 to be optimal. The results for $\Phi = 1.1$ and $\Phi = 1.3$ are shown in Appendix E.

Photos were taken during the experiments for each slot blowing ratio and equivalence ratio to capture visible burning in the slot coolant. The images associated with the plots shown in Figures 6.19, 6.20, 6.21, 6.22 and 6.23 are shown in Figure 6.24. In the figure the slot is located at approximately $6 \frac{20}{32}$ " and the fan-shaped holes are located at approximately $6 \frac{4}{32}$ ". The bottom and top edges of the upstream heat transfer gauges are located at approximately $5 \frac{27}{32}$ " and $5 \frac{6}{32}$ ", respectively. The bottom of the downstream heat transfer gauges are located at $4 \frac{9}{32}$ ". The visible reactions can be seen as a blue/white flame beginning at approximately $6 \frac{10}{32}$ " and convecting downstream (upward in the figure). The length of the flame is directly related to the blowing ratio of the slot. At a slot blowing ratio of 0.5, the flame is barely visible, but with $M=4$ in the slot, the flame is over 5.08 centimeters (2 in) long.

All the visible reactions that occurred using the upstream slot and downstream fan-shaped holes for all equivalence ratios tested occurred in the slot coolant only. Like the single cooling scheme tested using only the fan-shaped holes, no visible reactions were observed from the fan-shaped holes, even though the data showed that reactions did occur.

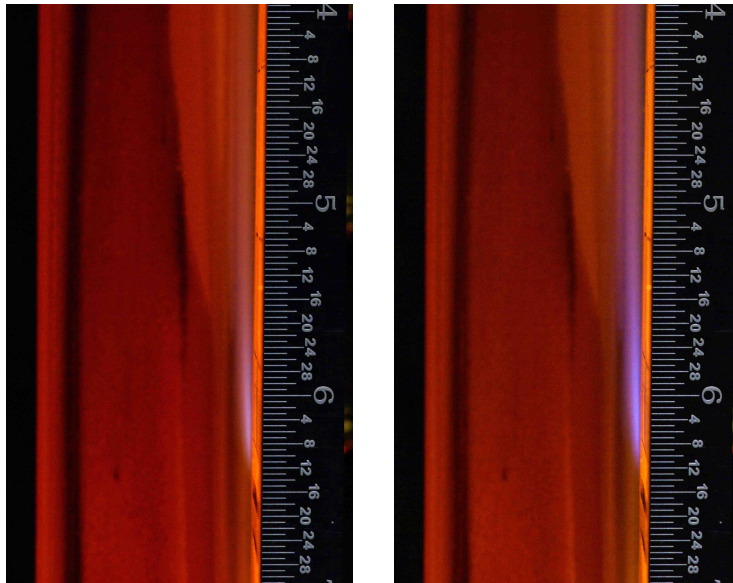
To provide a baseline for the previously presented results, the same series of tests were conducted with nitrogen as the cooling gas in the slot. The results of these tests are shown in Figures 6.25, 6.26, 6.27, 6.28, and 6.29. Due to the limitations of the nitrogen mass flow controller feeding the slot, the lowest slot blowing ratio that could be tested was 2. Using inert nitrogen in the slot helped to determine whether fuel could penetrate the slot cooling film and react with the oxygen from the fan-shaped holes. Additionally, when nitrogen was used in both cooling holes, a true non-reacting baseline for the cooling scheme could be found for each equivalence ratio. The results



(a) Slot M=0.5

(b) Slot M=1

(c) Slot M=2



(d) Slot M=3

(e) Slot M=4

Figure 6.24: Visible burning in slot film coolant ($\Phi = 1.5$), scale is in inches of the slot using nitrogen as the cooling gas with a WSR equivalence ratio of 1.1 and 1.3 are shown in Appendix E.

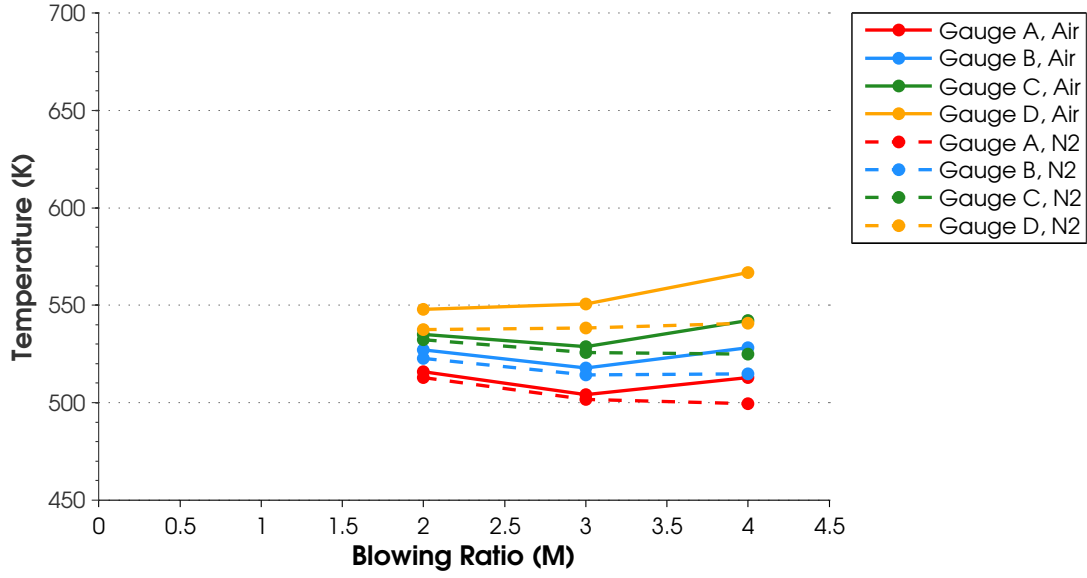


Figure 6.25: Gauge surface temperature, $\Phi = 1.5$, $\dot{m}_{air}=425$ SLPM, US: Slot, Coolant= N_2 , M=Variable, DS: Fan, Coolant=Air/ N_2 , M=2

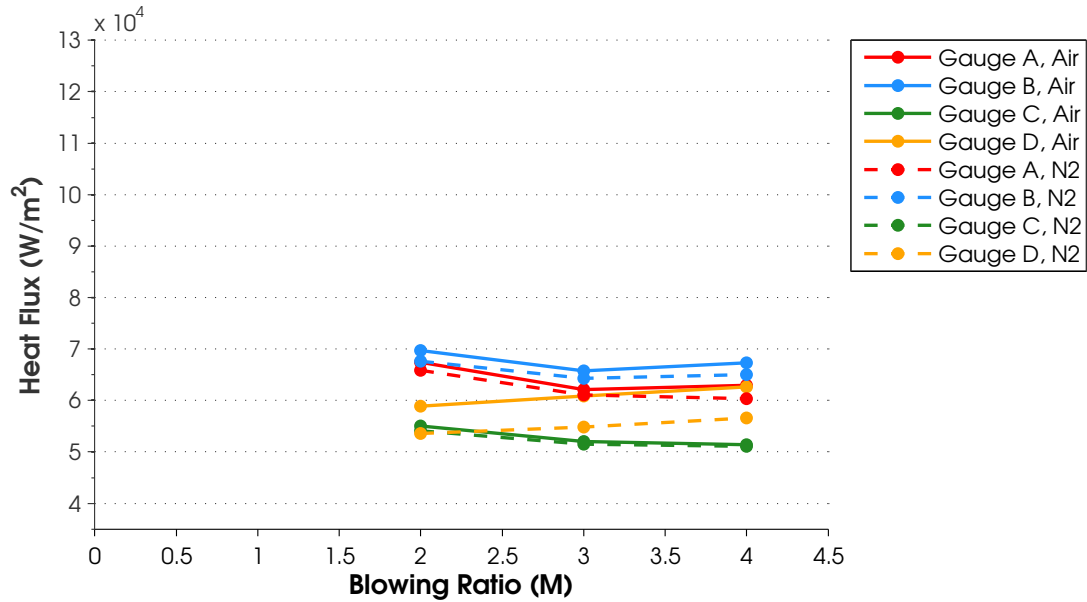


Figure 6.26: Gauge heat flux, $\Phi = 1.5$, $\dot{m}_{air}=425$ SLPM, US: Slot, Coolant= N_2 , M=Variable, DS: Fan, Coolant=Air/ N_2 , M=2

The results presented in Figures 6.25 - 6.29 show that when no oxygen was present in the slot cooling film, fuel from the exhaust was able to penetrate the film and react with the oxygen from the fan-shaped hole coolant. This result is shown

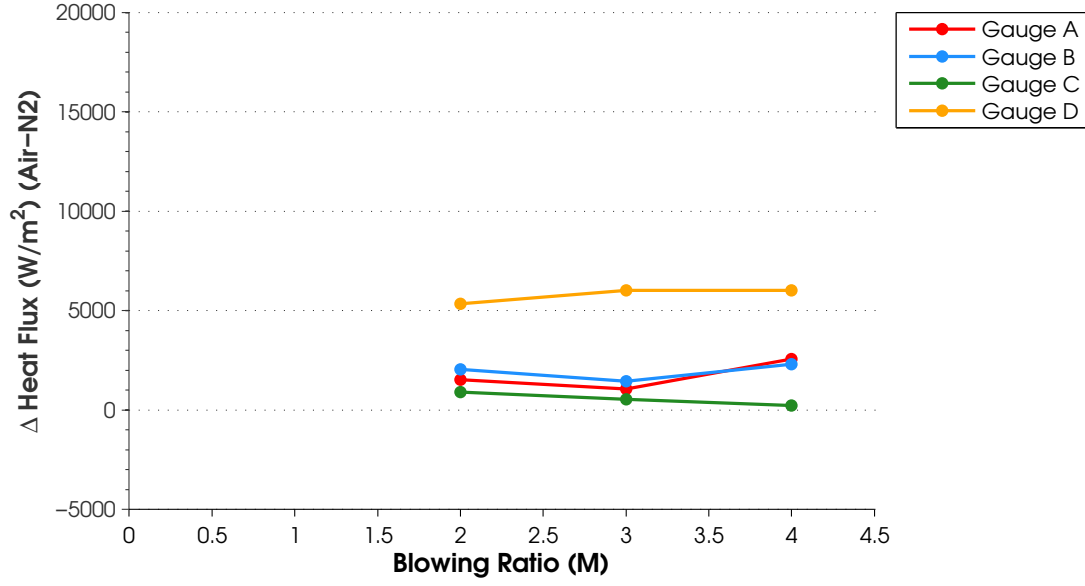


Figure 6.27: Heat flux difference, $\Phi = 1.5$, $\dot{m}_{air}=425$ SLPM, US: Slot, Coolant= N_2 , M=Variable, DS: Fan, Coolant=Air/ N_2 , M=2

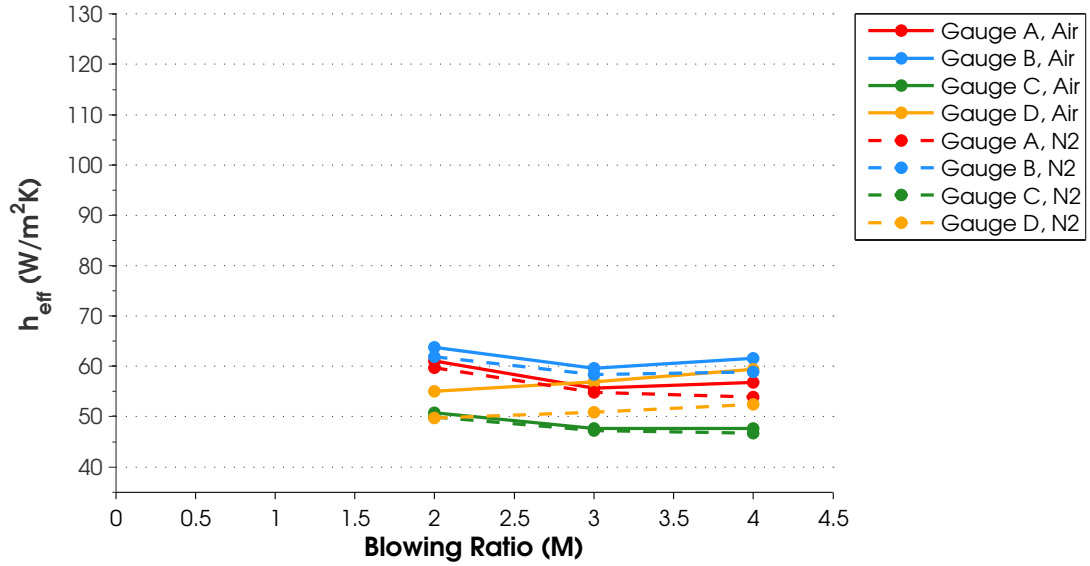


Figure 6.28: Gauge heat transfer coefficient, $\Phi = 1.5$, $\dot{m}_{air}=425$ SLPM, US: Slot, Coolant= N_2 , M=Variable, DS: Fan, Coolant=Air/ N_2 , M=2

by the difference in temperature, heat flux and heat transfer coefficient when air and nitrogen were used as the cooling gas in the downstream holes. At a slot blowing ratio of 2, even with the secondary reactions occurring in the fan-shaped hole coolant, the

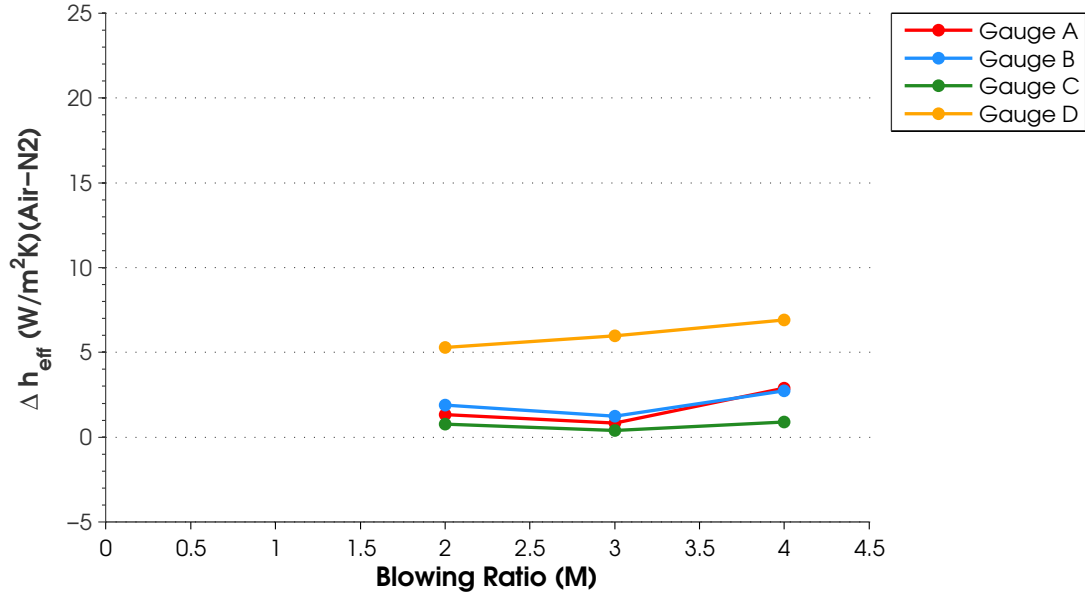


Figure 6.29: Heat transfer coefficient difference, $\Phi = 1.5$, $\dot{m}_{air}=425$ SLPM, US: Slot, Coolant= N_2 , M =Variable, DS: Fan, Coolant=Air/ N_2 , $M=2$

average surface temperature was still approximately 75 degrees cooler than when air was used as the coolant in the slot. This result indicates that the secondary reactions occurring in the slot film are still occurring close enough to the wall that the heat release effects the surface temperature.

6.2.2 US: Offset Normal Holes, DS: Fan-Shaped Laidback Holes.

Testing with an equivalence ratio of 0.6 was conducted to provide an indication of the additional cooling benefits provided by the offset normal holes. Figures 6.30, 6.31 and 6.32 show the surface temperature, heat flux and heat transfer coefficient, respectively, for the addition of offset normal holes at $\Phi = 0.6$. Once again a comparison can be made to the fan-shaped holes with the upstream blank, but for a blowing ratio of 2 in the fan alone.

The results shown in Figures 6.30, 6.31 and 6.32 indicate that there was virtually no benefit achieved by adding the offset normal holes. The heat flux and the heat transfer coefficient were actually increased slightly as a result of the additional holes.

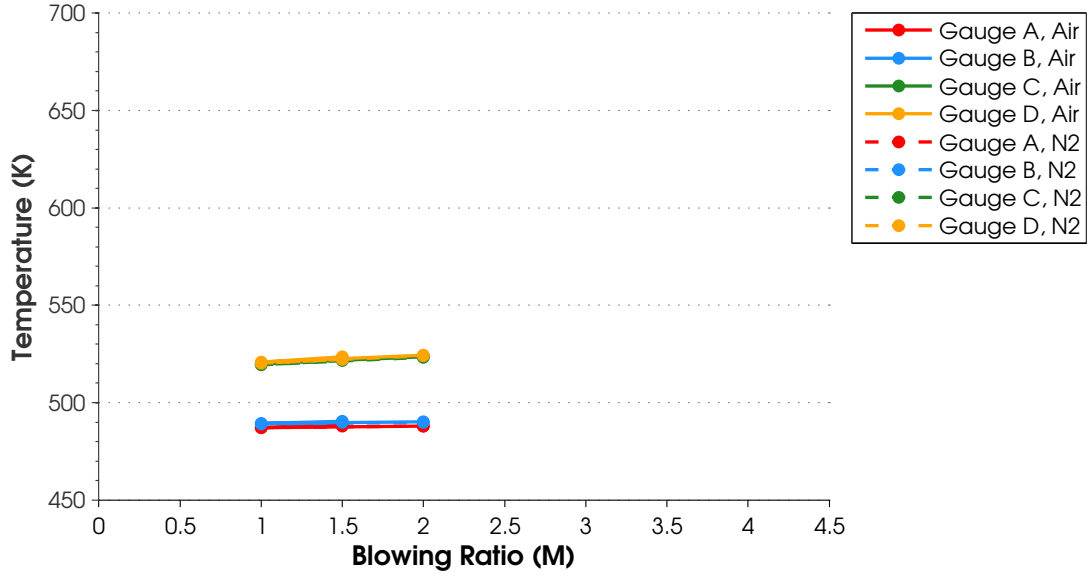


Figure 6.30: Gauge surface temperature, $\Phi = 0.6$, $\dot{m}_{air}=425$ SLPM, US: Offset normal, Coolant=Air, M=Variable, DS: Fan, Coolant=Air/N₂, M=2

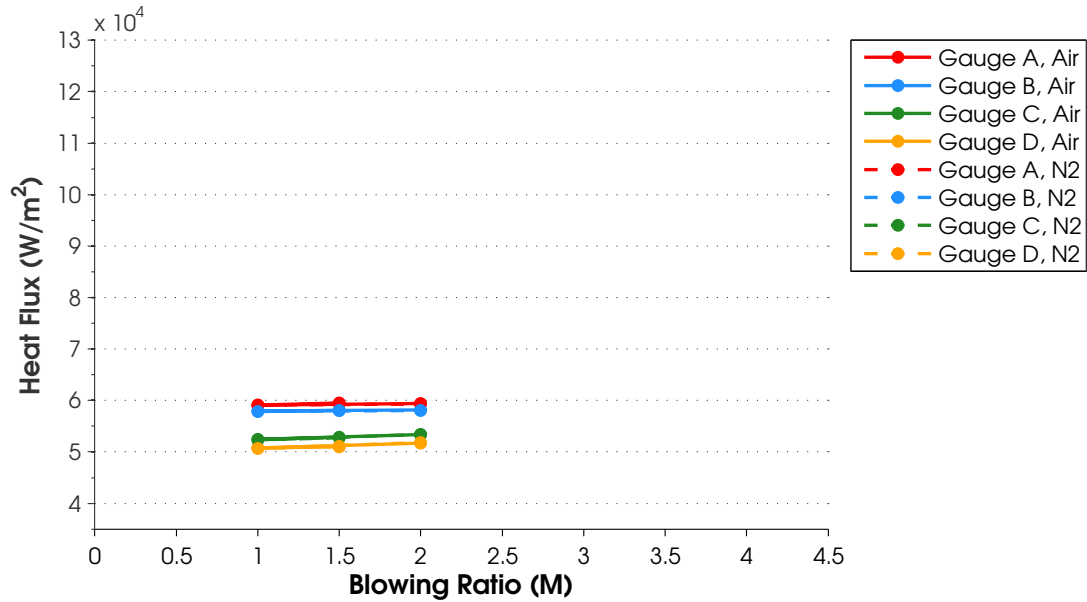


Figure 6.31: Gauge heat flux, $\Phi = 0.6$, $\dot{m}_{air}=425$ SLPM, US: Offset normal, Coolant=Air, M=Variable, DS: Fan, Coolant=Air/N₂, M=2

In the results shown above for the offset normal holes, the issue with the thermocouples in the heat transfer gauges was corrected and a difference in the results between the left and right side gauges is no longer visible.

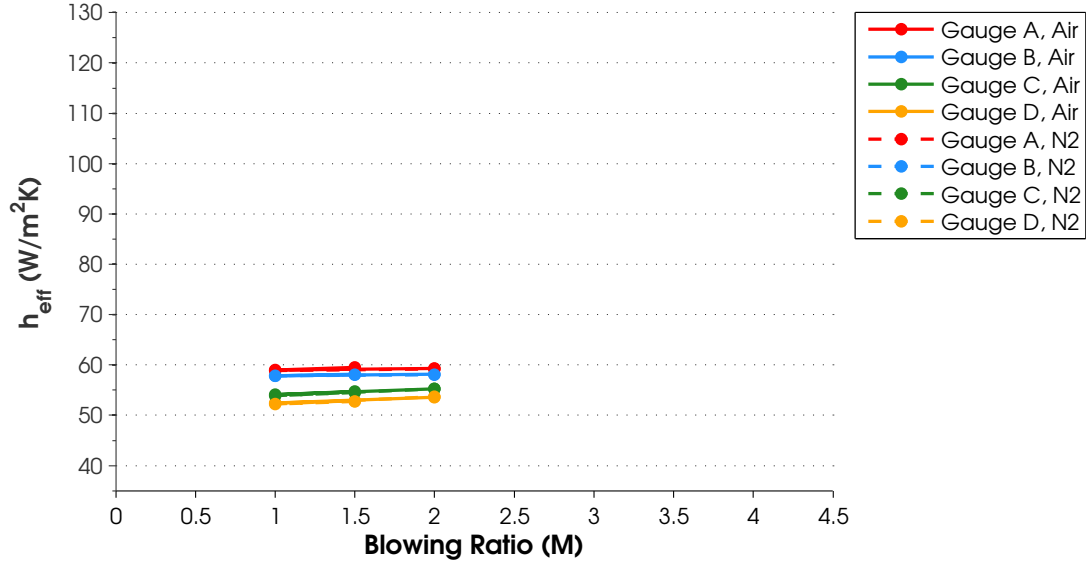


Figure 6.32: Gauge heat transfer coefficient, $\Phi = 0.6$, $\dot{m}_{air}=425$ SLPM, US: Offset normal, Coolant=Air, M=Variable, DS: Fan, Coolant=Air/N₂, M=2

For this cooling configuration, an equivalence ratio of 1.1 and 1.3 produced comparable results for the largest surface temperature and heat flux, but $\Phi = 1.1$ produced a slightly higher heat transfer coefficient. For this reason, an equivalence ratio of 1.1 is reported as the worst case condition for this cooling scheme. The results for this condition are shown in Figures 6.33, 6.34, 6.35, 6.36 and 6.37 for the surface temperature, heat flux, delta heat flux, heat transfer coefficient and delta heat transfer coefficient, respectively.

For this cooling scheme there was only a slight increase in the surface temperature using air as the cooling gas. Additionally, the temperature remained relatively constant showing only a slight increase across the range of blowing ratios. The difference in heat flux was increased slightly for higher blowing ratios as shown in Figure 6.35. Additionally, there was a sizable and steady increase in the convective heat transfer coefficient with increases in blowing ratio. These results show that for this equivalence ratio, there was no ideal blowing ratio that minimized the differences in surface temperature, heat flux and convective heat transfer coefficient.

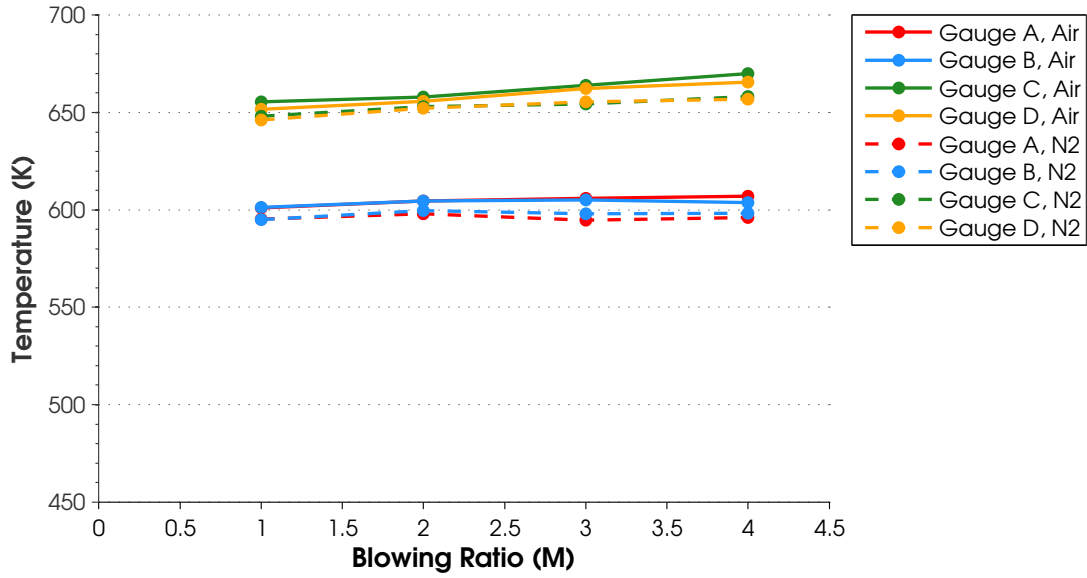


Figure 6.33: Gauge surface temperature, $\Phi = 1.1$, $\dot{m}_{air}=425$ SLPM, US: Offset Normal, Coolant=Air, M=Variable, DS: Fan, Coolant=Air/N₂, M=2

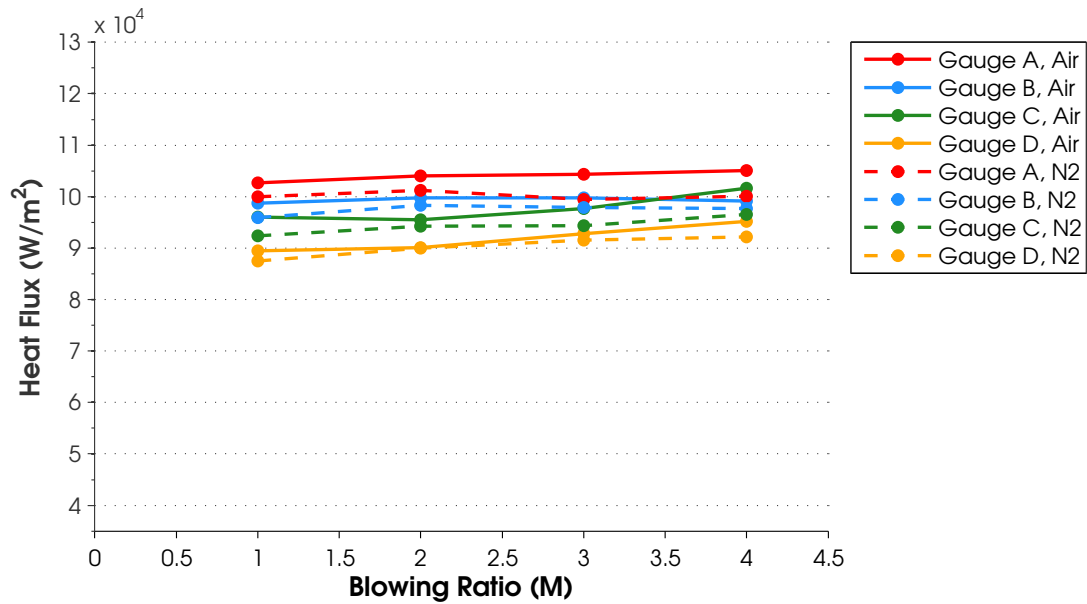


Figure 6.34: Gauge heat flux, $\Phi = 1.1$, $\dot{m}_{air}=425$ SLPM, US: Offset Normal, Coolant=Air, M=Variable, DS: Fan, Coolant=Air/N₂, M=2

Figure 6.38 shows the visible reaction images associated with the data presented in Figures 6.33 - 6.37. Unlike the previous visible reaction images that occurred with the slot, the free stream exhaust for the current condition was much brighter making

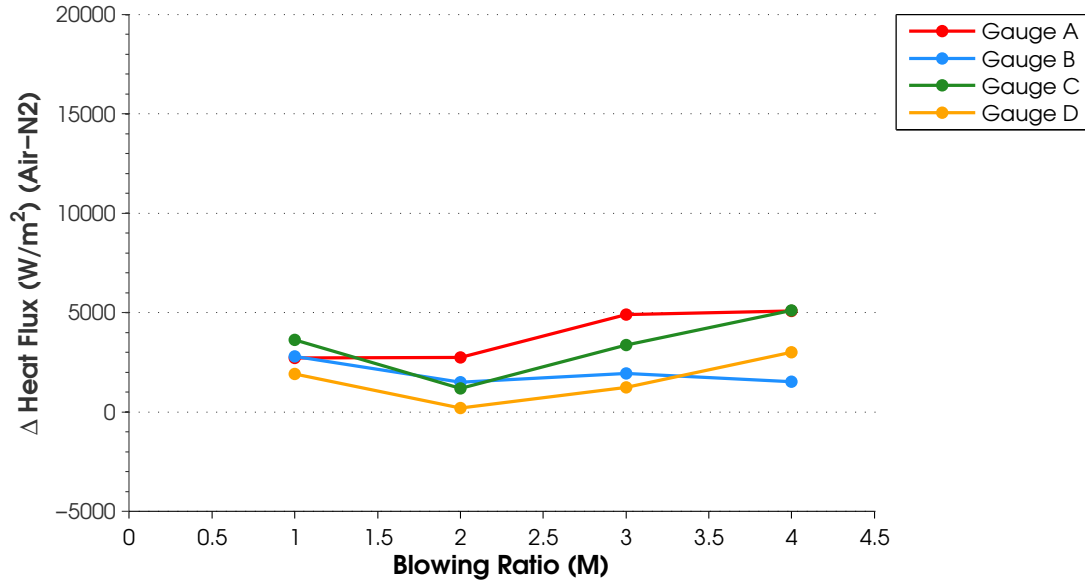


Figure 6.35: Heat flux difference, $\Phi = 1.1$, $\dot{m}_{air}=425$ SLPM, US: Offset Normal, Coolant=Air, M=Variable, DS: Fan, Coolant=Air/N₂, M=2

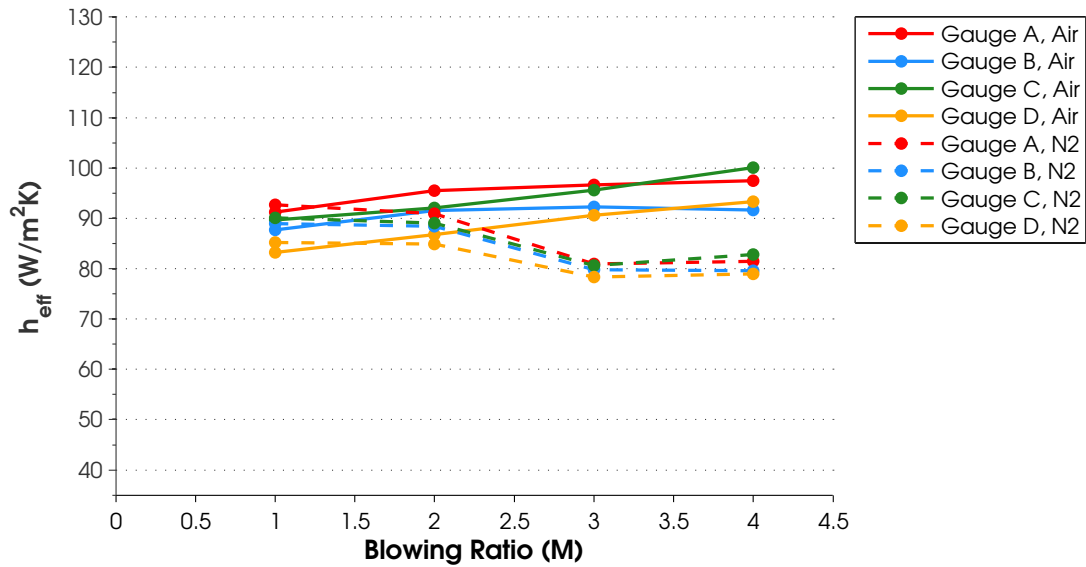


Figure 6.36: Gauge heat transfer coefficient, $\Phi = 1.1$, $\dot{m}_{air}=425$ SLPM, US: Offset Normal, Coolant=Air, M=Variable, DS: Fan, Coolant=Air/N₂, M=2

it harder to see the secondary reaction. The increased brightness was the result of hotter combustion due to an equivalence ratio closer to stoichiometric and the fact that there was no soot built up on the windows of the test rig to block some of the

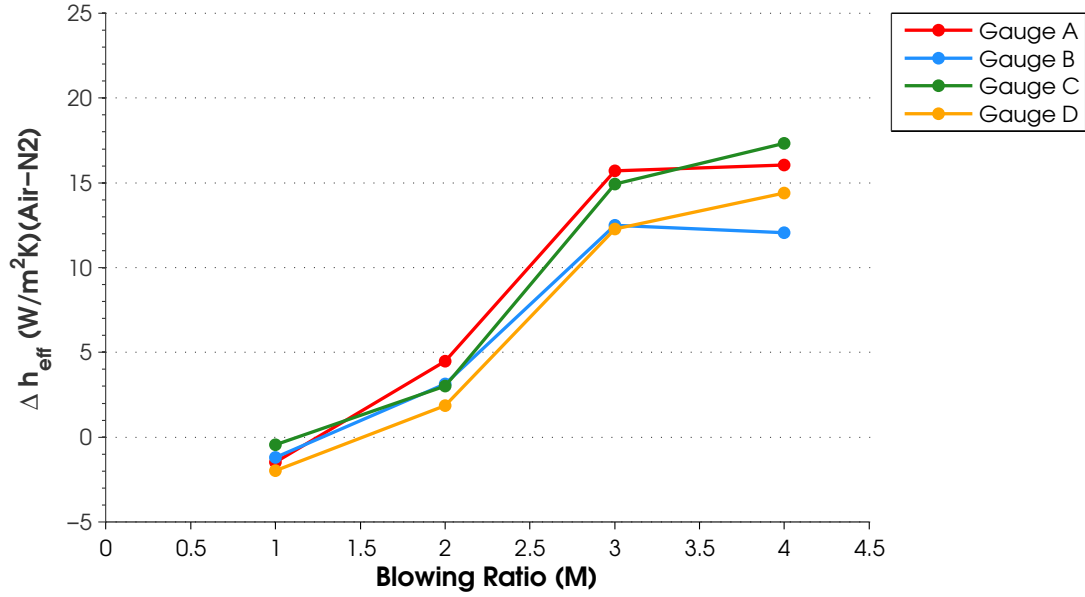
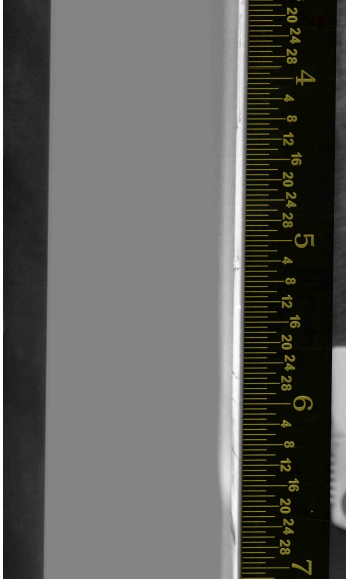


Figure 6.37: Heat transfer coefficient difference, $\Phi = 1.1$, $\dot{m}_{air}=425$ SLPM, US: Offset Normal, Coolant=Air, M=Variable, DS: Fan, Coolant=Air/N₂, M=2

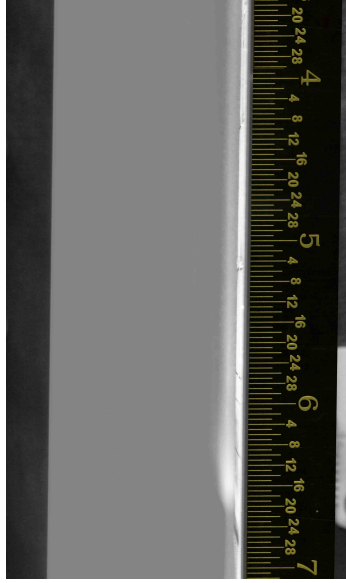
free stream light. To make the secondary reactions in the current images more visible, the images were desaturated which darkened the free stream to gray and highlighted the secondary reactions in white.

The location of the test rig components as measured by the scale in each image is the same as shown for the slot. Unlike the slot, however, which had a single exit for the coolant, the offset normal holes are located between 6 20/32" and 6 26/30". The fan-shaped holes are located at approximately 6 4/32". The bottom and top edges of the upstream heat transfer gauges are located at approximately 5 27/32" and 5 6/32", respectively. The bottom of the downstream heat transfer gauges are located at 4 9/32". The visible reactions can be seen as a white flame beginning at approximately 6 24/32" and convecting downstream (upward in the figure).

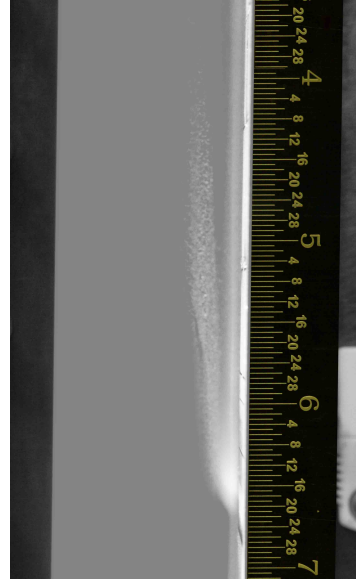
The magnitude of the secondary reaction was directly related to the blowing ratio in the offset normal holes. Low blowing ratios produced reactions near the wall which convected downstream. Higher blowing ratios produced a larger penetration of the reaction into the free stream fluid but still maintained a reaction along the wall as



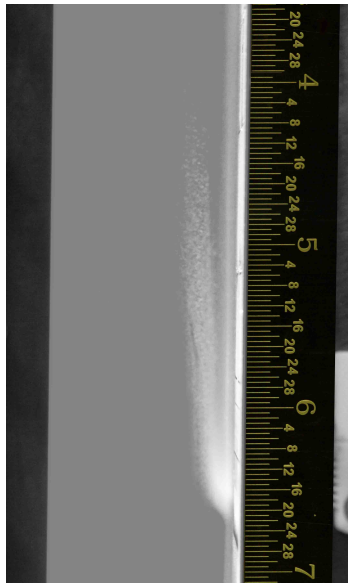
(a) Offset Normal M=1



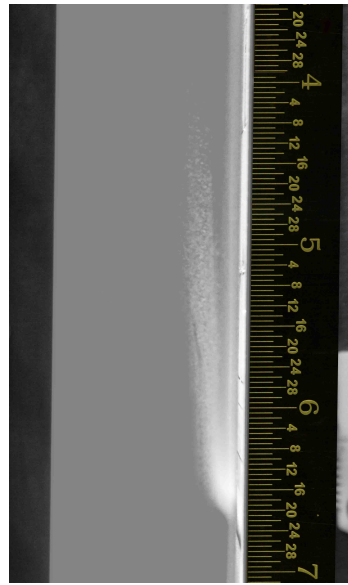
(b) Offset Normal M=2



(c) Offset Normal M=3



(d) Offset Normal M=4



(e) Offset Normal M=4

Figure 6.38: Visible burning in offset normal hole film coolant ($\Phi = 1.1$), scale is in inches

well. This result differs from the slot, where higher blowing ratios in the offset normal holes did not relocate the secondary reactions off the wall. This flow pattern explains the fairly constant surface temperature across the range of blowing ratios tested.

As a result of the decreased mass flow rate of coolant in the offset normal holes compared to the slot for the same blowing ratios, there was no baseline case conducted using nitrogen in the offset normal holes. These tests could not be conducted due to the limitation of the nitrogen mass flow controller not being able to control flow rates at the low rate required.

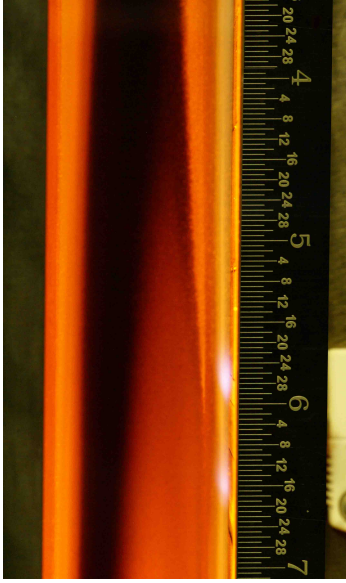
The current film cooling scheme did produce one unique result not seen in any of the other schemes or previous research conducted by Evans. At an equivalence ratio of 1.5, distinct visible reactions were observed for both the offset normal holes and the fan-shaped laidback holes. No other condition tested produced a visible reaction for the fan-shaped holes. These images can be seen in Figure 6.39. Upon close examination of the images, it is also possible to see two distinct flames resulting from the upstream and downstream rows of normal holes.

6.3 Comparisons Between Cooling Schemes

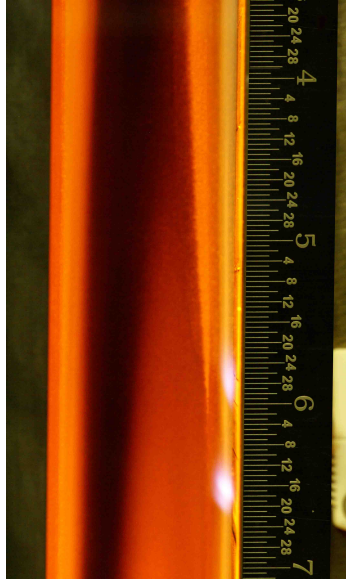
In each of the sections above, the results of a fuel-lean non-reacting condition and the worst case equivalence ratio were shown. The purpose of showing the worst case condition was to highlight the largest surface temperature, heat flux and heat transfer coefficient that could occur with each scheme. Each cooling scheme also had a best case equivalence ratio where the lowest surface temperature, heat flux and convective heat transfer coefficient were observed. The upstream slot scheme offered considerable improvements over the fan-shaped laidback holes alone while cooling in the exhaust of fuel-rich combustion.

In each of the comparison plots, the results for the two upstream gauges and the two downstream gauges were averaged together to produce a single upstream and a single downstream gauge result. Only the results using air in all cooling holes for all schemes is shown.

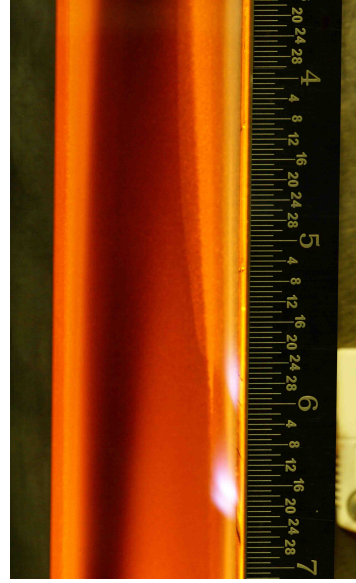
The comparison plots presented in this section show the best case scenario achieved. The comparison plots for all equivalence ratios tested are shown in Ap-



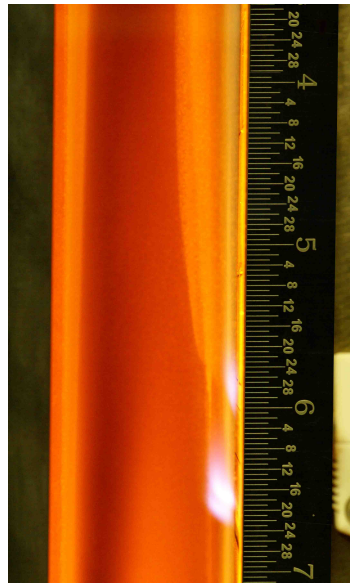
(a) Offset Normal M=1



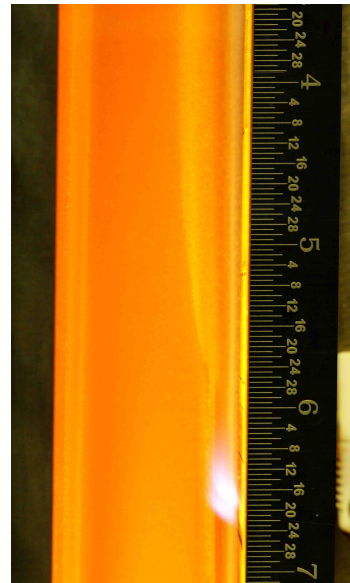
(b) Offset Normal M=2



(c) Offset Normal M=3



(d) Offset Normal M=4



(e) Offset Normal M=4, N₂ in fan-shaped holes

Figure 6.39: Visible burning in offset normal hole and fan-shaped hole film coolant ($\Phi = 1.5$), scale is in inches

pendix E. The best case is defined as the condition that offered the greatest surface temperature, heat flux and heat transfer coefficient reductions compared to the fan-

shaped holes alone. The best case occurred using the slot at $\Phi = 1.1$. As you would expect, the case with the least amount of fuel in the exhaust allowed the slot to cool most effectively. For this condition the slot cooled the upstream surface by 80 degrees and the downstream surface by 35 degrees with a slot blowing ratio of 2 as shown in Figure 6.40. The corresponding heat flux and heat transfer coefficient comparisons shown in Figures 6.41 and 6.42 also report a substantial reduction in both quantities with the addition of the slot compared to the fan-shaped holes alone.

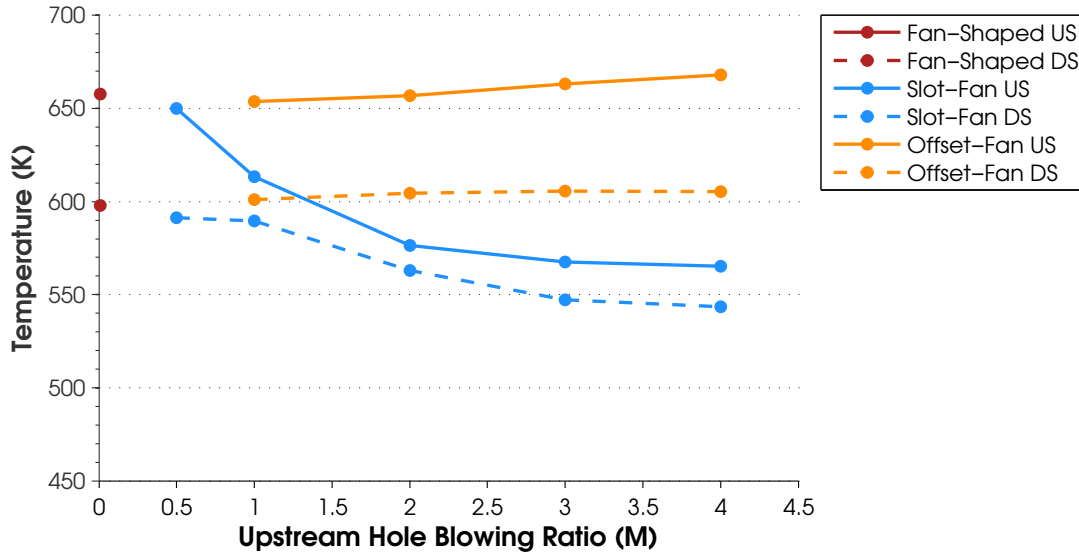


Figure 6.40: Gauge surface temperature comparison, $\Phi = 1.1$, $\dot{m}_{air}=425$ SLPM, US: Blank/Slot/Offset, Coolant=Air, M=Variable, DS: Fan, Coolant=Air, M=2

At higher equivalence ratios (1.3 and 1.5) the cooling provided by the slot was continually reduced as the equivalence ratio was increased. At $\Phi = 1.5$, the slot only provided approximately 10 degrees of cooling on the upstream gauge and heated the downstream gauge approximately 20 degrees compared to the fan-shaped holes alone as shown in Figure E.88 for a blowing ratio of 2 in all cooling holes. Figures E.89 and E.90 show the heat flux and convective heat transfer coefficient across a range of equivalence ratios also for a blowing ratio of 2 in all holes.

A WSR combustion at $\Phi = 1.1$ produced the worst case for the offset normal holes. From the comparisons shown in Figures 6.40 - E.90 it can be seen that there was

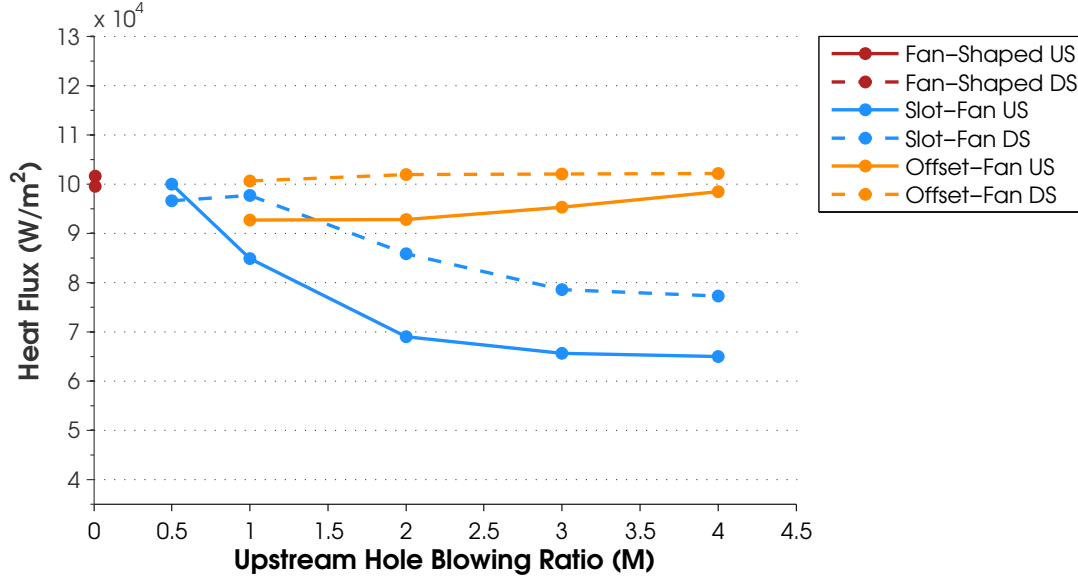


Figure 6.41: Heat flux comparison, $\Phi = 1.1$, $\dot{m}_{air}=425$ SLPM, US: Blank/Slot/Offset, Coolant=Air, M=Variable, DS: Fan, Coolant=Air, M=2

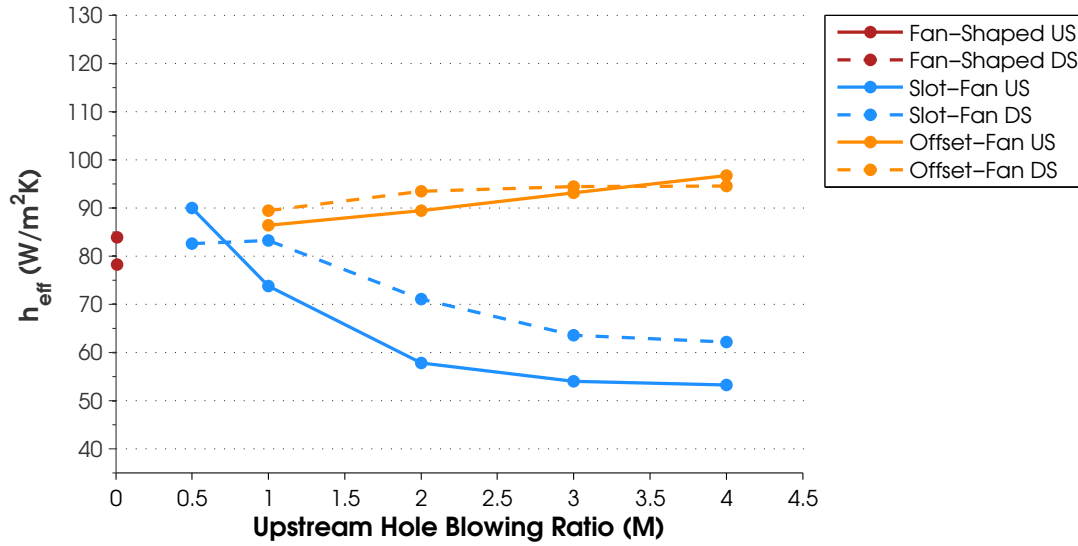


Figure 6.42: Gauge heat transfer coefficient comparison, $\Phi = 1.1$, $\dot{m}_{air}=425$ SLPM, US: Blank/Slot/Offset, Coolant=Air, M=Variable, DS: Fan, Coolant=Air, M=2

no benefit to using the offset normal holes and at this equivalence ratio all calculated quantities showed an increase rather than a reduction for an increased blowing ratio. In fact, at all equivalence ratios tested, the offset normal holes did not offer a benefit

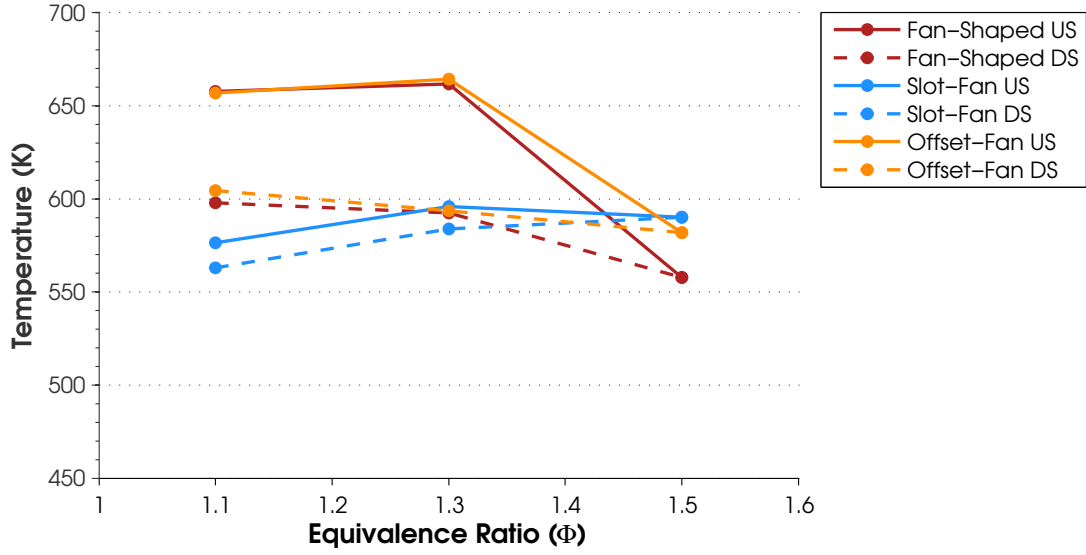


Figure 6.43: Gauge surface temperature comparison, Φ = Variable, $\dot{m}_{air}=425$ SLPM, US: Blank/Slot/Offset, Coolant=Air, M=2, DS: Fan, Coolant=Air, M=2

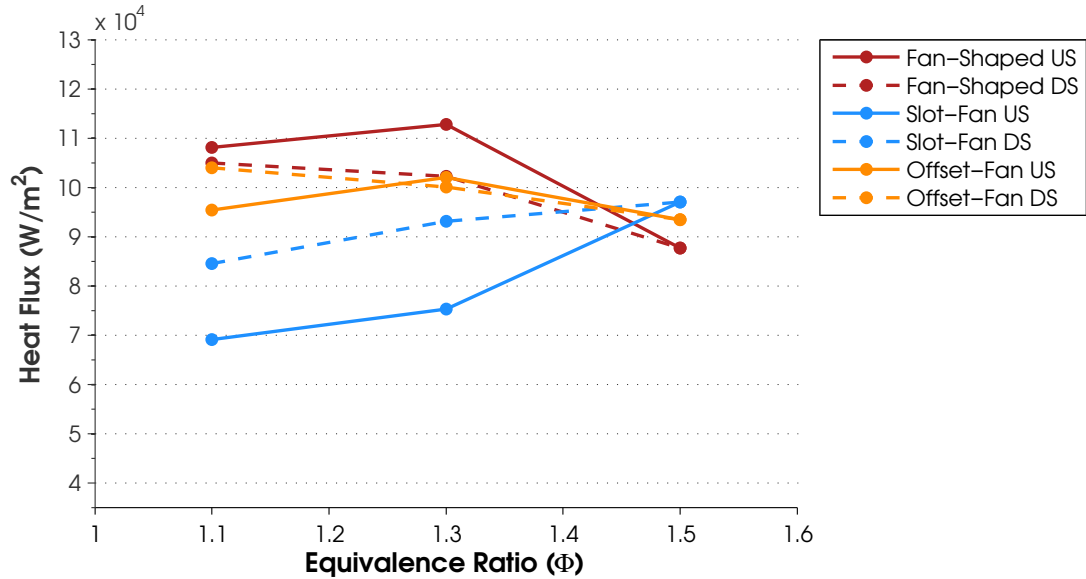


Figure 6.44: Heat flux comparison, Φ = Variable, $\dot{m}_{air}=425$ SLPM, US: Blank/Slot/Offset, Coolant=Air, M=2, DS: Fan, Coolant=Air, M=2

and at all fuel-rich conditions resulted in increases in the calculated quantities for increased blowing ratios.

From these results it can be concluded that it is very important to know the combustion condition upstream of the area to be cooled to choose the appropriate

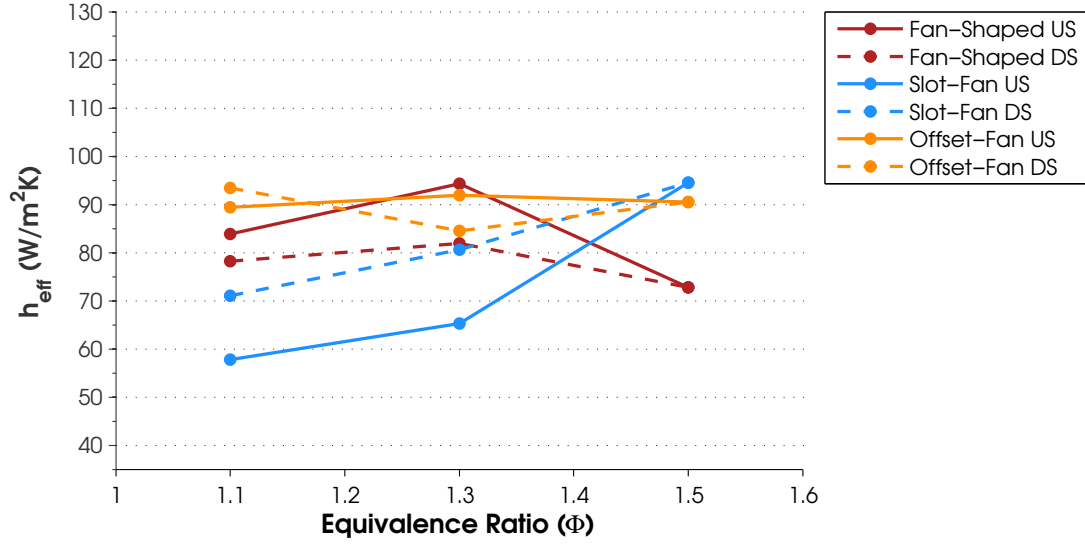


Figure 6.45: Gauge heat transfer coefficient comparison, Φ = Variable, $\dot{m}_{air}=425$ SLPM, US: Blank/Slot/Offset, Coolant=Air, $M=2$, DS: Fan, Coolant=Air, $M=2$

film cooling scheme. For slightly fuel-rich conditions, it has been shown that significant reductions in surface temperature, heat flux and heat transfer coefficient can be achieved using an angled slot with a realistic blowing ratio of 2 upstream from fan-shaped laidback holes also with a blowing ratio of 2. For cooling in the exhaust of very fuel-rich combustion ($\Phi = 1.5$), neither of the cooling schemes in series provided an additional benefit to the fan-shaped laidback holes and in many cases caused an increase in surface temperature, heat flux and heat transfer coefficient. Additional techniques will need to be investigated to improve the film cooling performance at equivalence ratios at or above 1.5.

VII. Conclusions

7.1 *Overview*

This thesis consisted of a two part investigation of concepts related to a fighter-sized ultra-compact combustor. The first investigation was a numerical analysis performed at increasing levels of complexity to quantify the relationships between fluid velocity, temperature and species within the domain to the inlet conditions. Due to the risk of g-load induced blowout, the control of the tangential velocity in the circumferential cavity was an area of particular interest. Additionally, the locations of combustion within the UCC section and the species and temperature profile introduced downstream to the high-pressure turbine are important from a film-cooling and burning-in-the-turbine perspective. The results of the numerical analysis have already been used in the development of a laboratory test rig of the fighter-sized UCC that will provide further understanding of the velocity relationships and flow patterns through the test section. The second area of research was an experimental study which investigated using film cooling schemes in series in an attempt to reduce or eliminate secondary reactions in film cooling jets in the exhaust of fuel-rich combustion. This topic is related to the UCC since the system runs at an equivalence ratio of 2 in the circumferential cavity and the UCC turbine vanes located below the circumferential cavity will require active cooling when the system moves beyond CFD simulations.

7.2 *Numerical Analysis Results Summary*

Based on all levels of numerical analysis complexity, it was found that the circumferential cavity inlet velocity was the primary parameter that controlled the tangential velocity of the fluid in the cavity. Correlations were found between the cavity inlet velocity, tangential velocity and cavity inlet port diameter that allowed a desired tangential velocity (or g-load based on a fixed geometry) to be achieved. Additionally, the cavity cross-sectional area, core mass flow rate and the number of vanes located below the circumferential cavity were found to have a seemingly negligible impact on the tangential velocity.

Using a divider plate offset from the ID endwall allowed cooler air from upstream of the combustor to bypass the combustor section and produce a film-cooling-like effect on the ID endwall, dramatically cooling the surface. Using the divider plate also achieved the desired exit temperature profile of cooler endwall surfaces with the maximum temperature maintained in the center of the engine passage. An additional domain modification that fed the circumferential cavity inlet ports from a bypass duct off the domain inlet showed that the linear relationship of cavity inlet velocity to tangential velocity were maintained when the static pressures were matched between the two inlets.

Using a 12-species combustion model showed that non-negligible amounts of CO and H₂ exited the UCC section into the high-pressure turbine which could potentially result in secondary reactions. The amount of fuel remaining in the exhaust at the end of the UCC section, however, was minimal. Any secondary reactions that occur in the turbine section down stream of the UCC would most likely be the result of reacting intermediate species and not combustion of the fuel itself.

7.3 Film Cooling Analysis Results Summary

Using an angled slot upstream of fan-shaped laidback holes provided the largest reduction in surface temperature, heat flux and convective heat transfer coefficient across a wide range of blowing ratios and equivalence ratios compared to the fan-shaped holes alone. A blowing ratio of 2 in both the slot and the fan-shaped holes was found to provide the best balance between separation of the cooling film that pushed the reactions off the wall, while allowing the least amount of fuel to penetrate the film and react with the fan-shaped hole coolant. Offset normal holes upstream of fan-shaped laidback holes provided a slight reduction in heat flux but caused an increased in surface temperature and the convective heat transfer coefficient across the range of blowing ratios tested.

A review of the visible reactions that occurred in the cooling film of the angled slot show that regardless of the blowing ratio, the visible combustion began approxi-

mately 0.79 centimeters (10/32 inch) downstream of the slot. If the fan-shaped holes could be positioned to eject fluid into this location, the slot film might be pushed off the wall a greater distance, and thus further reduce the impact of the secondary reactions.

7.4 *Conclusions*

Despite the large number of geometry and flow conditions that could influence the tangential velocity in the circumferential cavity, the only condition of consequence was the cavity inlet velocity. The seemingly linear relationship between the cavity inlet velocity and tangential velocity could be used to maintain a constant tangential velocity (or g-load) within the circumferential cavity through the use of variable area inlet ports. By strategically positioning the circumferential cavity and UCC turbine vane in the upstream portion of the diffuser passage, the natural expansion of the flow through this duct significantly aided the migration of the hot gases across the radial span. With the fluid in the circumferential cavity traveling at the ideal tangential velocity, the hot gases easily traversed the radial span of the diffuser. Consequently, additional hardware was required to modify the flow pattern through the UCC section to achieve the desired exit temperature profile and reduce the heat load on the ID endwall.

The slot/fan combination scheme was able to reduce the surface temperature, heat flux and convective heat transfer coefficient compared to the fan-shaped holes alone for equivalence ratios below 1.5. This result is a significant milestone as it suggests that the detrimental effects of secondary combustion in the vane passage may be able to be controlled or at least minimized. This is one of the major obstacles that needs to be overcome if the UCC concept is to be practically implemented in a turbine engine.

7.5 Recommendations for Future Work

While the current numerical analysis took a previously unresearched, open-ended design problem and provided bounds on the flow properties, temperatures and velocities in a UCC in a fighter-scale engine and provided relationships to control the tangential velocity in the circumferential cavity, further analysis is still needed. An additional investigation of the bypass ratio of the duct providing air to the circumferential cavity in the modified engine domain should be performed to determine the geometry requirements to achieve the desired mass flow rate into the circumferential cavity. Alternate cavity inlet configurations such as injection through the side walls of the circumferential cavity should be performed to reduce the circumference of the engine and provide for more direct injection of fluid into the cavity. Additionally, film cooling techniques, such as using film cooling schemes in series, should be integrated into the UCC numerical analysis to determine the effectiveness and optimal locations of the coolant. Experimental studies should be completed using the exact geometry and operating conditions tested in the numerical analysis. The results of the numerical analysis should be compared to the experimental results for validation of the CFD solutions.

With respect to the experimental film cooling study, research should be conducted using a hole-in-slot cooling scheme in both the upstream and downstream film cooling insert locations. This cooling scheme has been shown to provide the benefits of a slot without the loss of structural integrity associated with a slot. The use of laser diagnostics would also provide further insight into the flow patterns and combustion properties in the film coolant. Additionally, since this research will lead to a cooling scheme for the turbine vane in the UCC, flow patterns representative of those around the vane should be used in addition to the flat plate studies.

Appendix A. Numerical Starting Sequences

For numerical stability, the test cases could not be started with the final desired settings and order of accuracy. For this reason, the cases were started first-order and at a reduced level of complexity for the other solver settings. The sections below show the order that solver settings and increased accuracy were added to the solution with the approximate corresponding iteration number that the setting was added. These are averaged numbers, some cases required more time at a specific condition before making a change.

A.1 Preliminary Analysis Solver Starting Sequence

The preliminary analysis test cases were initialized to the domain inlet and started first-order, laminar as an ideal gas. The following changes were made as the solution progressed:

- RNG $k - \epsilon$ Turbulence Model (50)
- Second-order Momentum (100)
- Second-order Energy (200)
- Second-order Density (300)

A.2 Reacting Flow Analysis Solver Starting Sequence

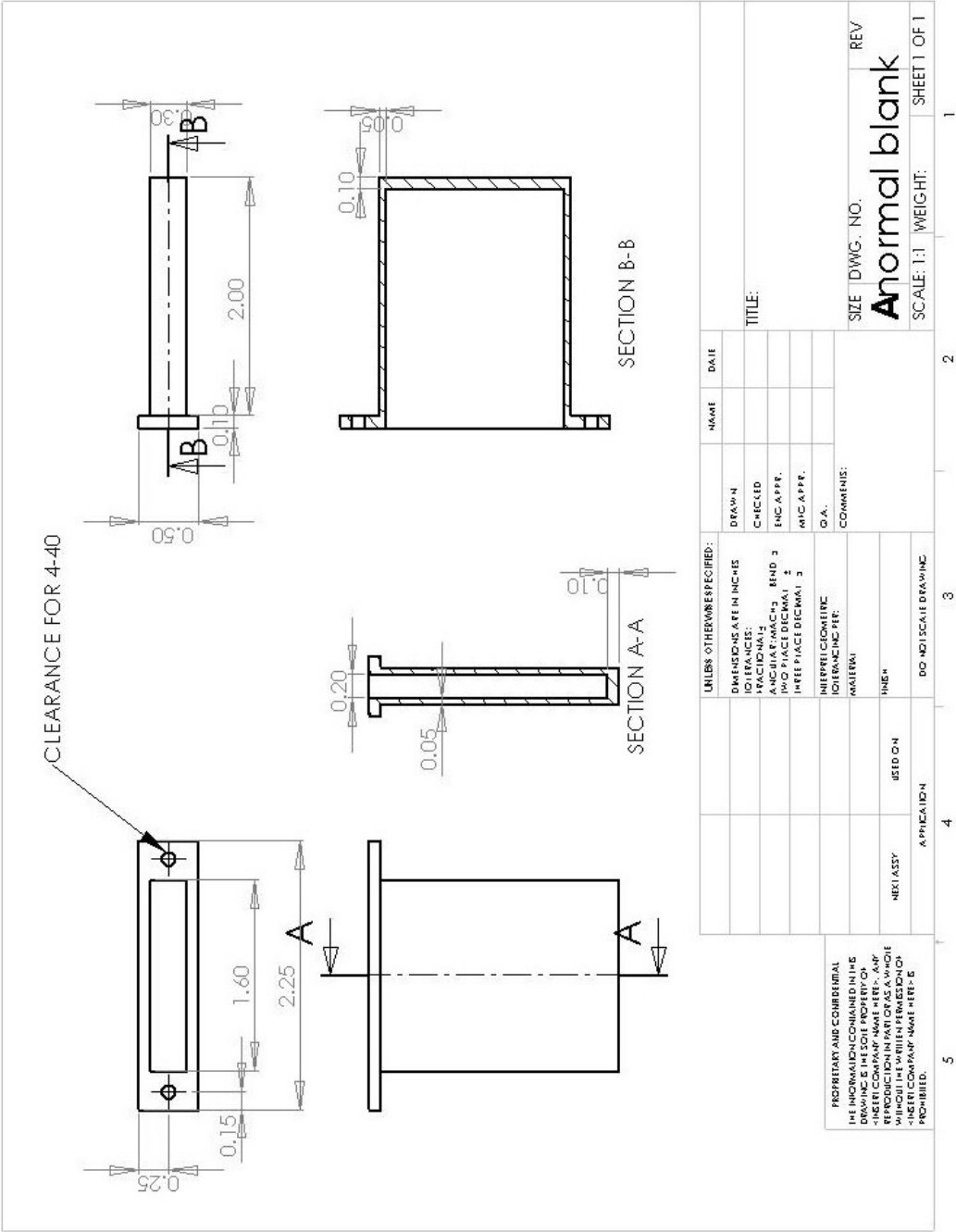
The reacting flow models were more stable when started with a turbulence model; however, they could not be started as an ideal gas. These test cases were initialized to the domain inlet and an x-direction velocity and temperature were patched into the circumferential cavity region. The patch of x-direction velocity was used to get the cavity fluid started in the correct direction while the temperature in the cavity was set to 2,200 K to initiate combustion. The starting settings were: first-order with the RNG $k - \epsilon$ turbulence model, the mixture density set as an incompressible ideal gas and the fluid air density set as ideal gas. For the 12-species combustion analysis

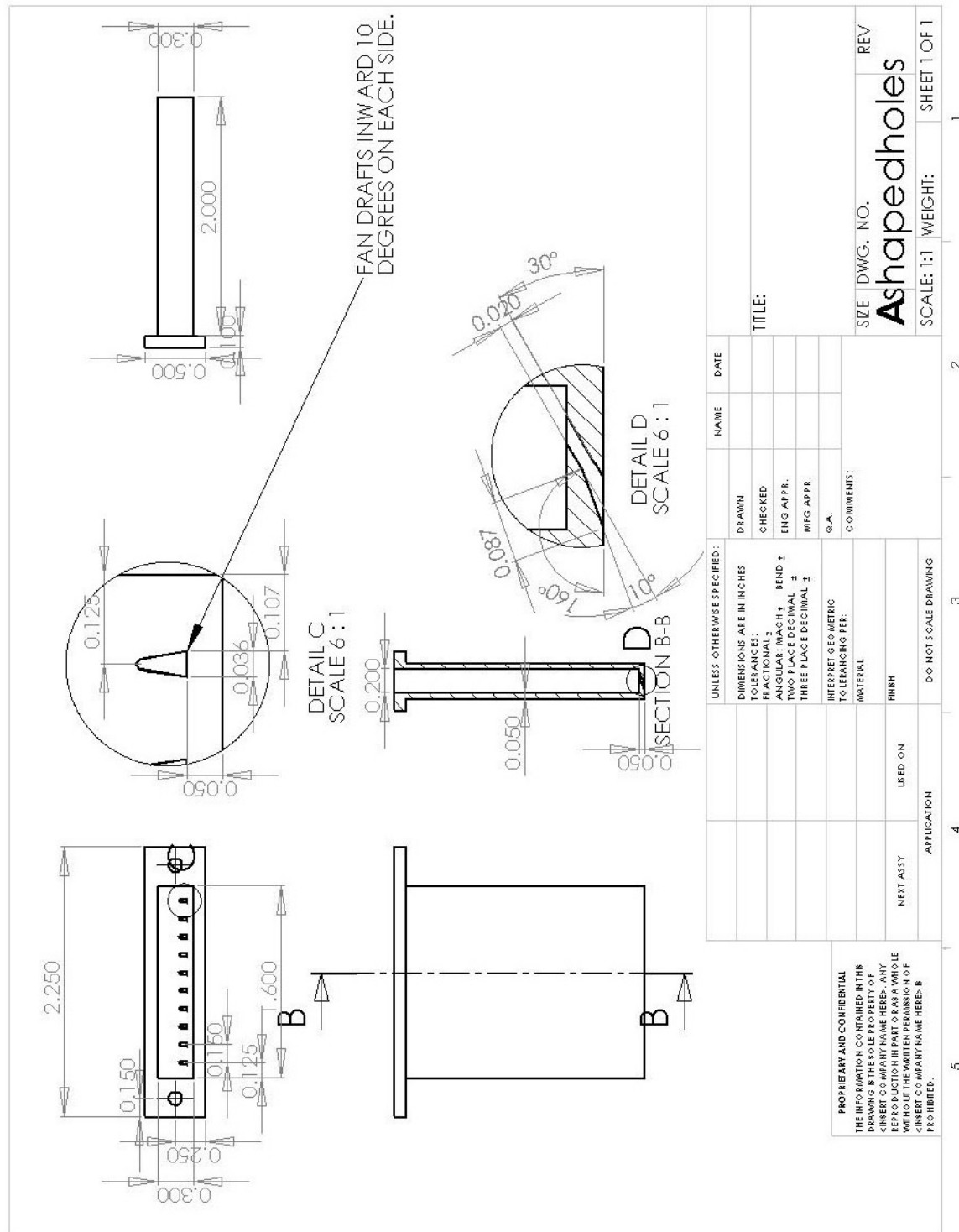
the mixture and fluid air density were started as ‘PDF’. The following changes were made as the solution progressed:

- Second-order Momentum (50)
- Second-order Energy (150)
- Second-order Species (200)
- Mixture changed to Ideal Gas (N/A for 12-species analysis) (300)
- Second-order Density (350)

Appendix B. Detailed Schematic Drawings of Film Cooling Inserts

The following schematics provide detailed specifications of the film cooling inserts created by Evans [8] and used in the current analysis. All dimensions are in inches.





[illegible]

187

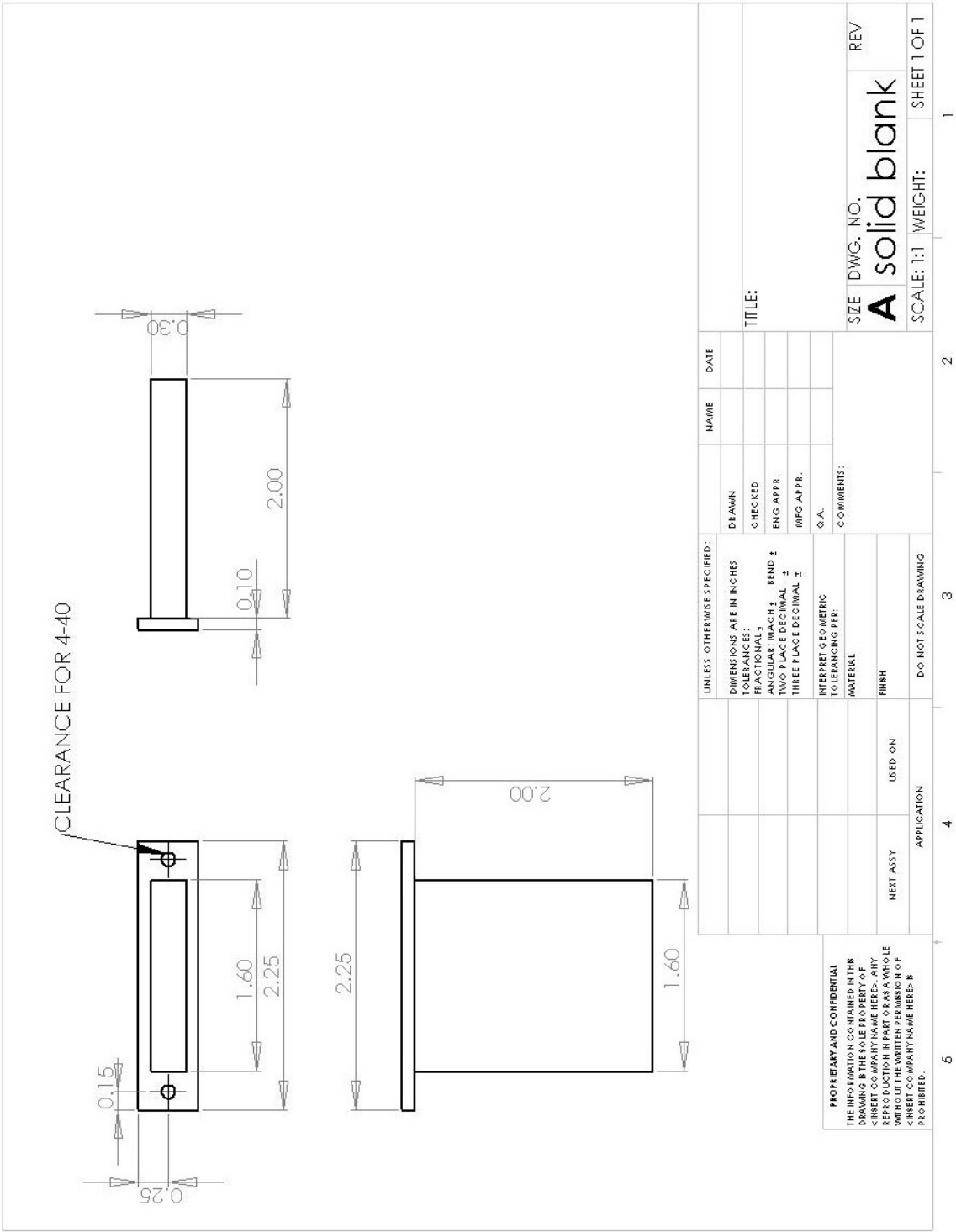


Figure B.5: Solid blank [8]

Appendix C. Detailed Drawing of Design 5 Flow Straightener

The following schematic is the design drawing used to machine the flow straightener.

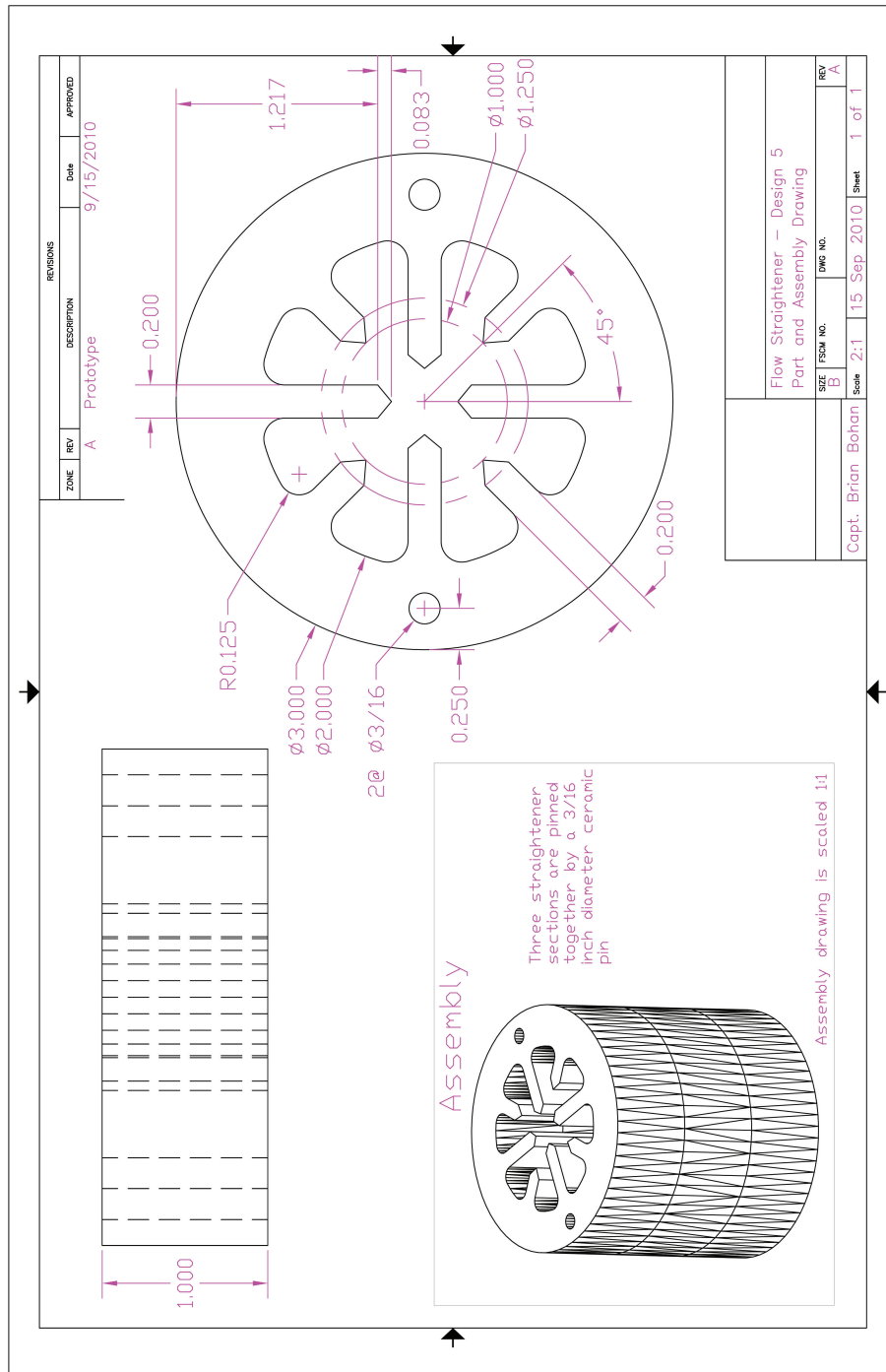


Figure C.1: Design 5 flow straightener (inches)

Appendix D. Numerical Analysis Supporting Results

This appendix provides the supporting results for the analysis presented in Chapter 4. Results are presented in the order they were discussed in Chapter 4.

D.1 Preliminary Analysis

D.1.1 Circumferentially-Averaged Total Temperature Profiles.

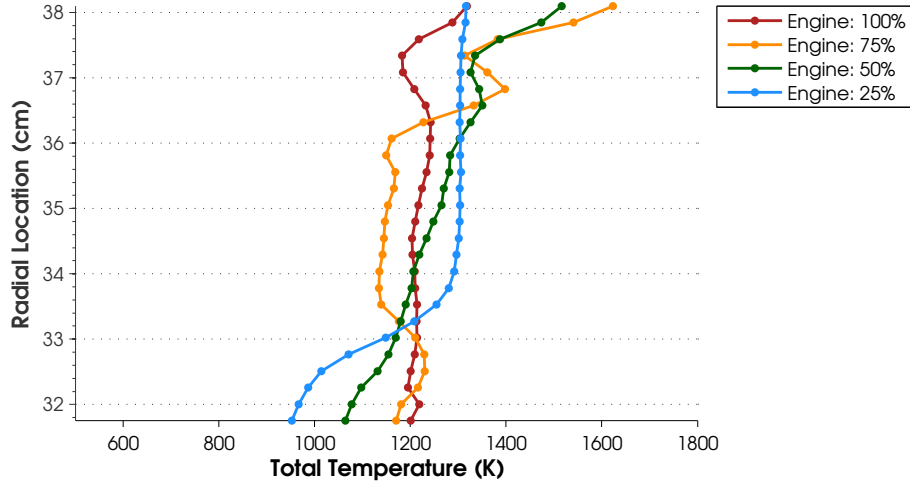


Figure D.1: Circumferentially-averaged total temperatures at combustor section exit for varying cavity inlet mass flow rates for the 0 hybrid vane domain

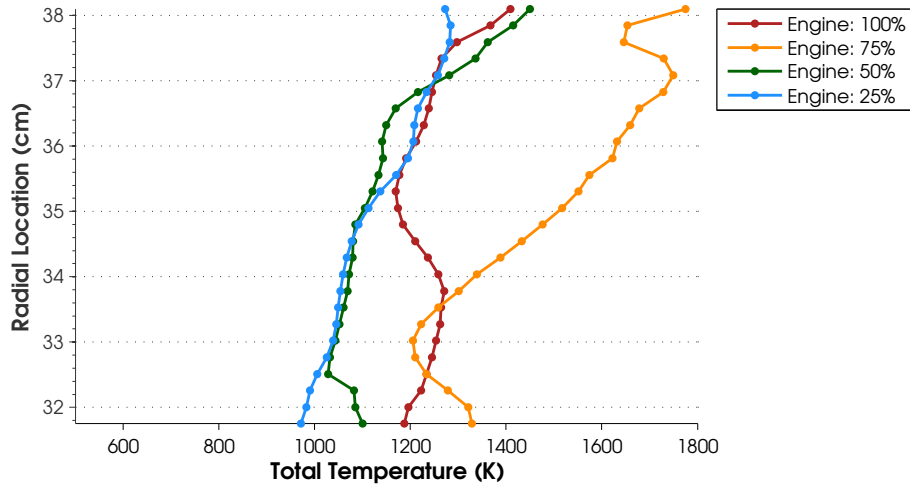


Figure D.2: Circumferentially-averaged total temperatures at combustor section exit for varying cavity inlet mass flow rates for the 0 typical vane domain

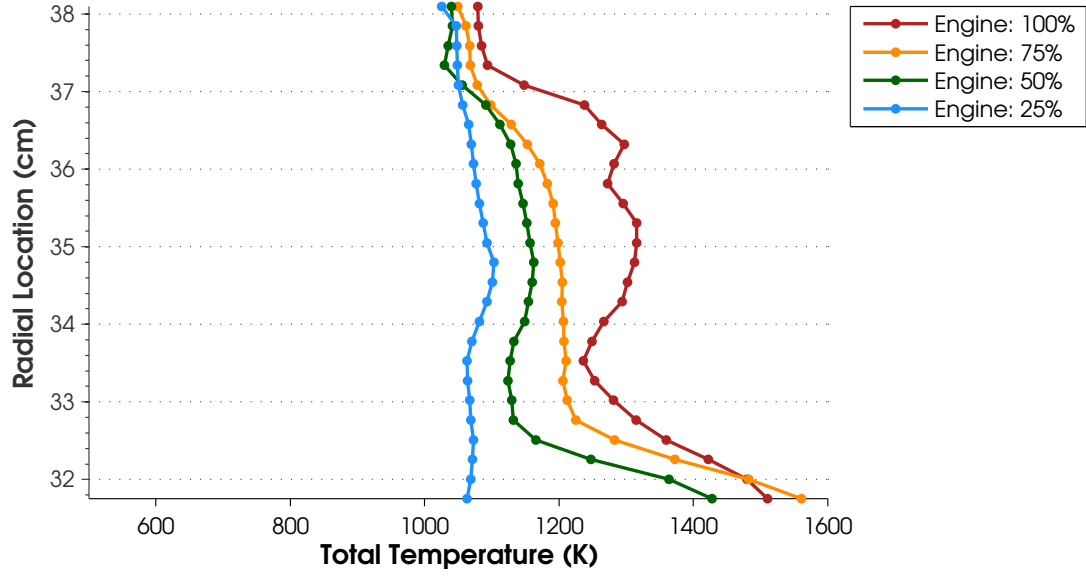


Figure D.3: Circumferentially-averaged total temperatures at combustor section exit for varying cavity inlet mass flow rates for the 20 hybrid vane domain

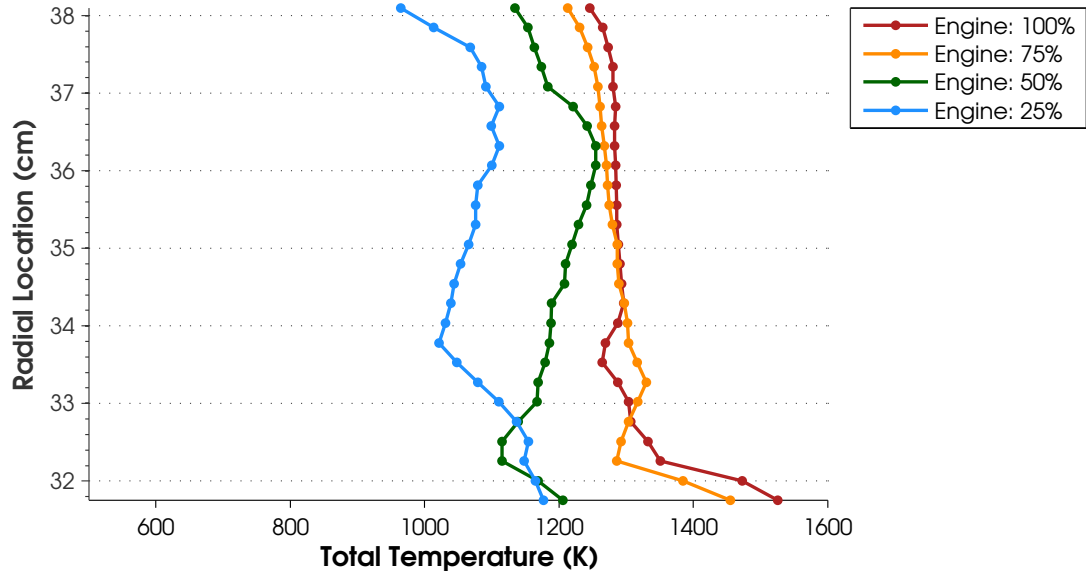


Figure D.4: Circumferentially-averaged total temperatures at combustor section exit for varying cavity inlet mass flow rates for the 20 typical vane domain

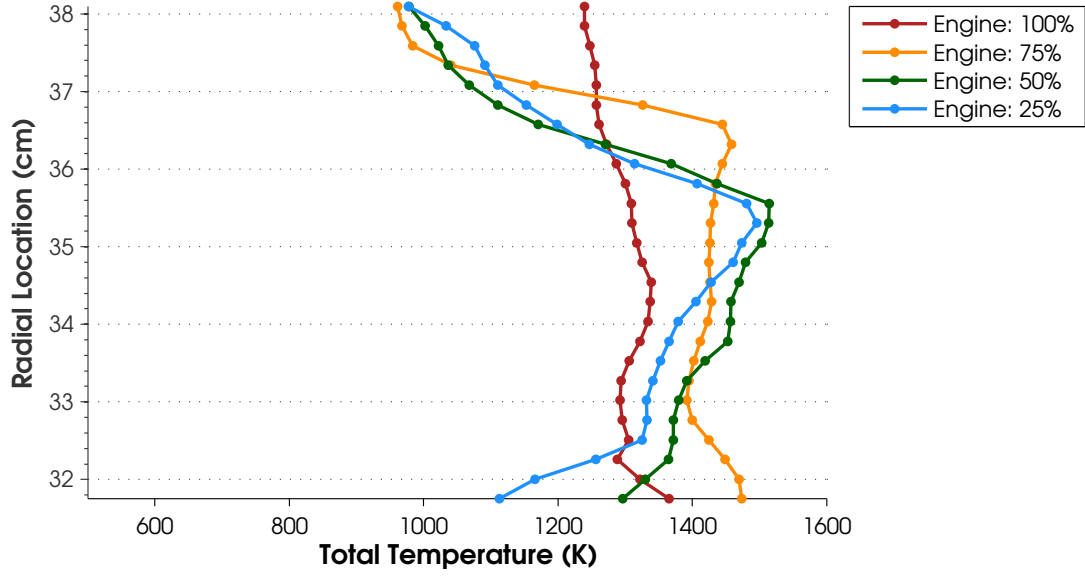


Figure D.5: Circumferentially-averaged total temperatures at combustor section exit for varying cavity inlet mass flow rates for the 30 hybrid vane domain

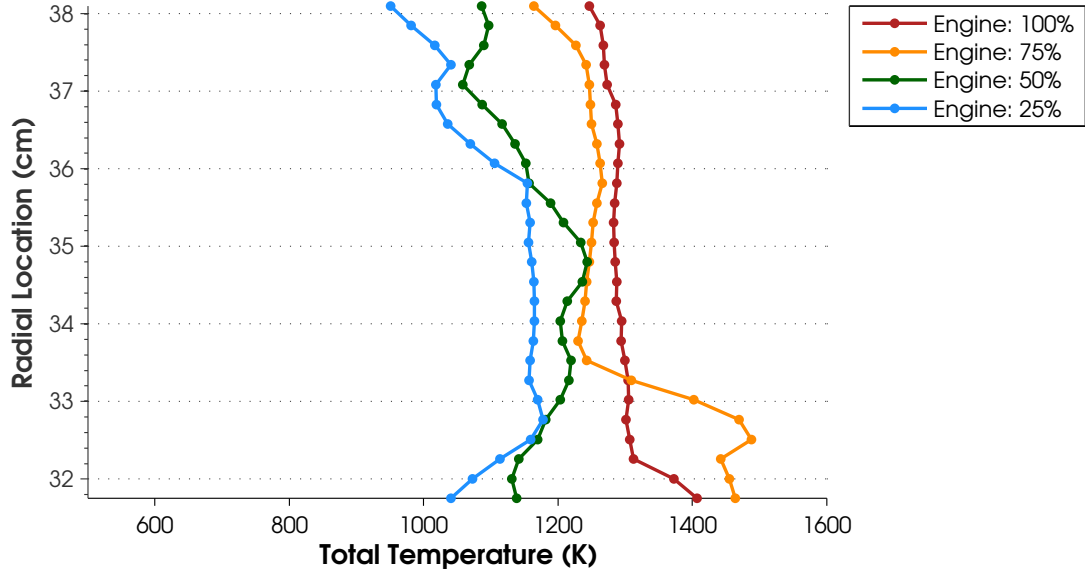


Figure D.6: Circumferentially-averaged total temperatures at combustor section exit for varying cavity inlet mass flow rates for the 30 typical vane domain

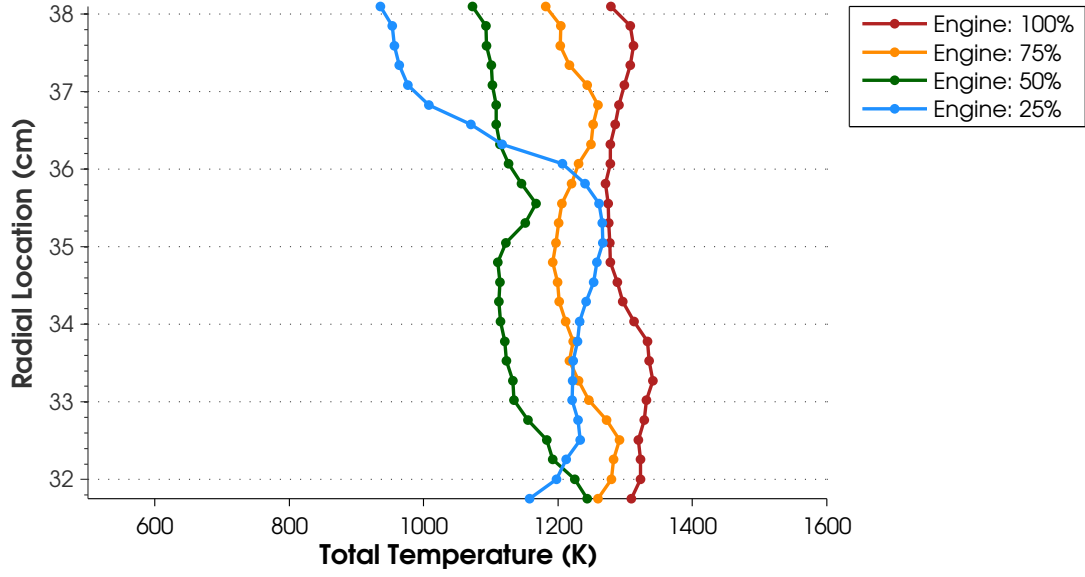


Figure D.7: Circumferentially-averaged total temperatures at combustor section exit for varying cavity inlet mass flow rates for the 45 typical vane domain

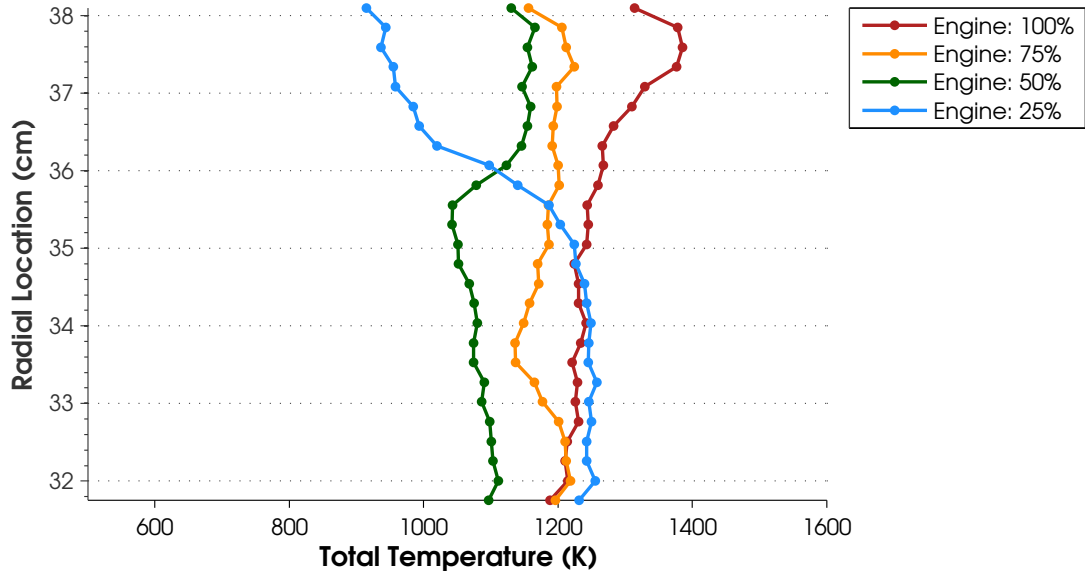
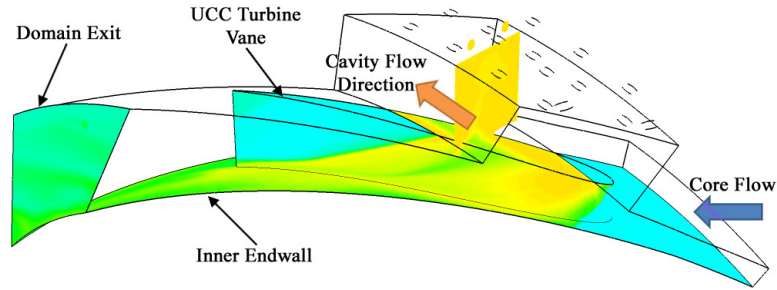
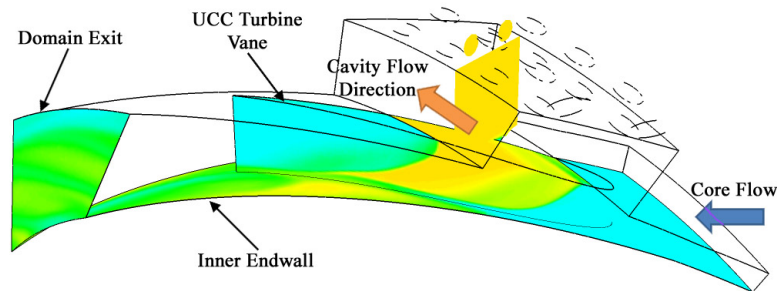


Figure D.8: Circumferentially-averaged total temperatures at combustor section exit for varying cavity inlet mass flow rates for the 60 typical vane domain

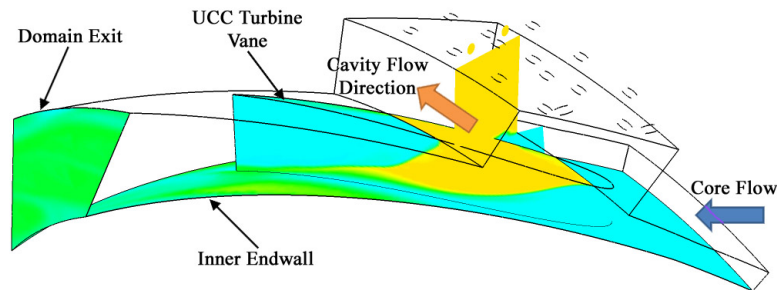
D.1.2 Total Temperature Contour Plots.



(a) Baseline Inlet



(b) 2x Area Inlet



(c) Top Wall Inlet

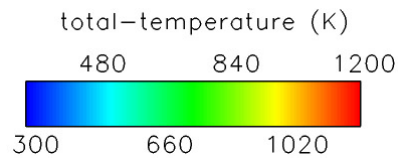
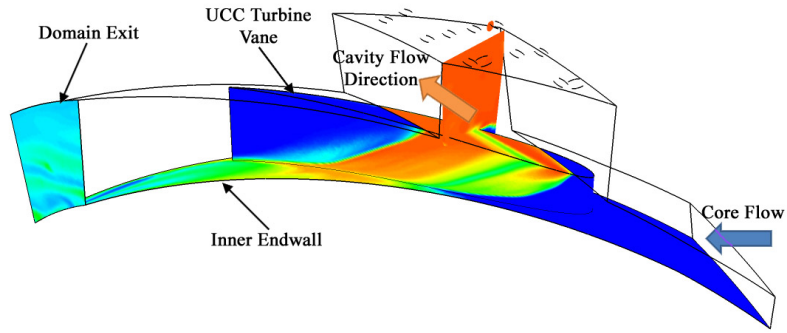
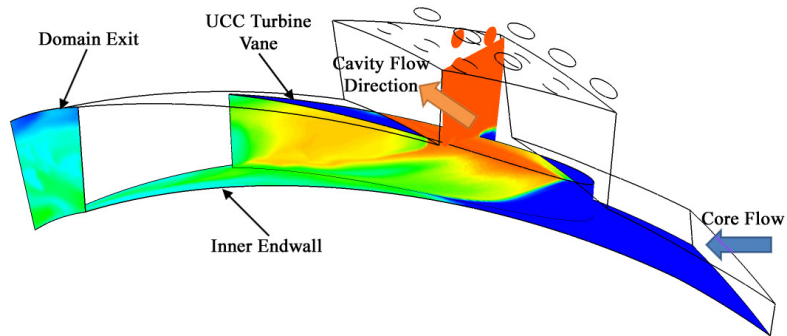


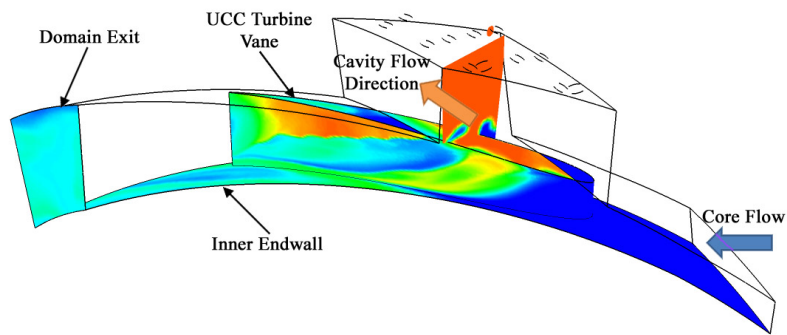
Figure D.9: Total temperature contours on UCC components using 100% cavity inlet mass flow, 20 hybrid vane domain, rig conditions



(a) Baseline Inlet



(b) 2x Area Inlet



(c) Top Wall Inlet

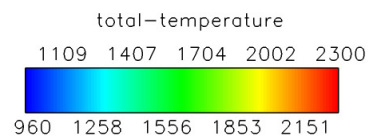
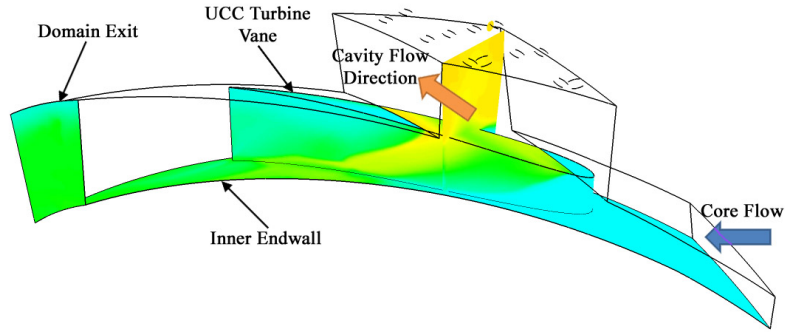
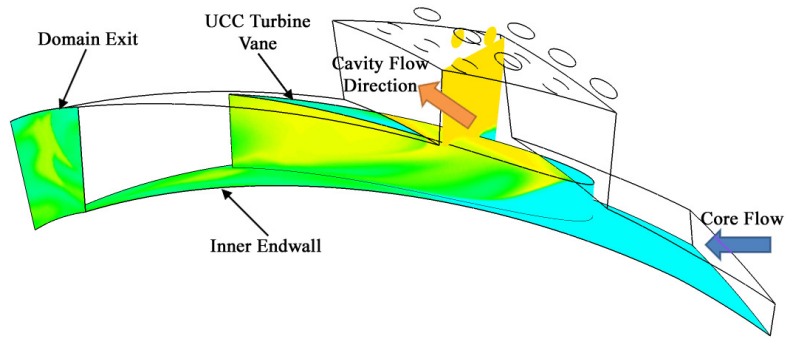


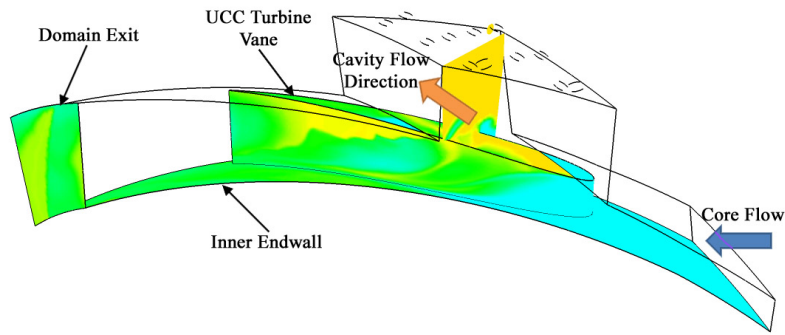
Figure D.10: Total temperature contours on UCC components using 100% cavity inlet mass flow, 30 hybrid vane domain, engine conditions



(a) Baseline Inlet



(b) 2x Area Inlet



(c) Top Wall Inlet

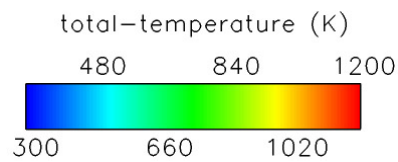


Figure D.11: Total temperature contours on UCC components using 100% cavity inlet mass flow, 30 hybrid vane domain, rig conditions

D.2 12-Species Reacting Flow Analysis

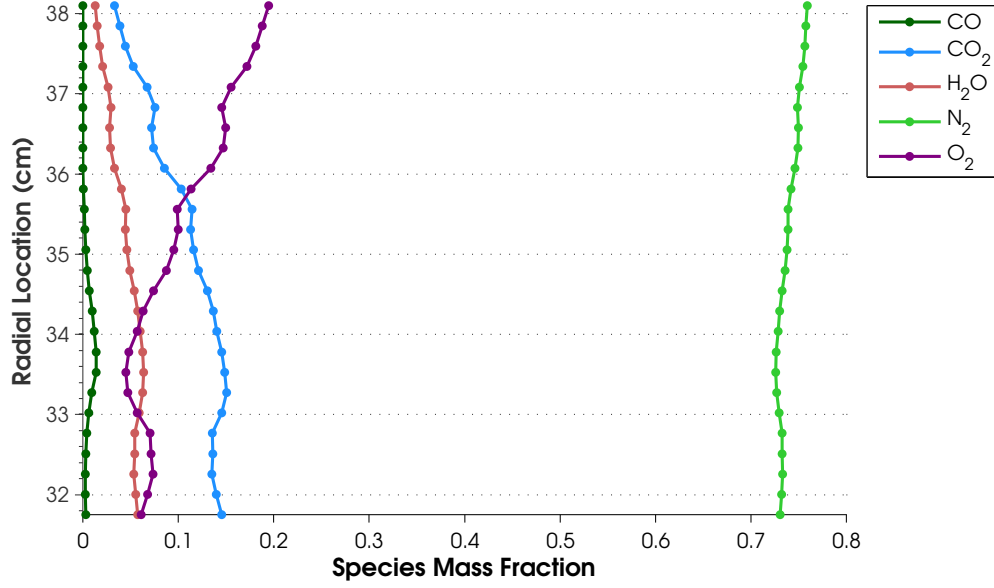


Figure D.12: Circumferentially-averaged mass fractions of species at combustor section exit using the 12-species combustion model and ideal air inlet diameters with a 30 hybrid vane engine configuration

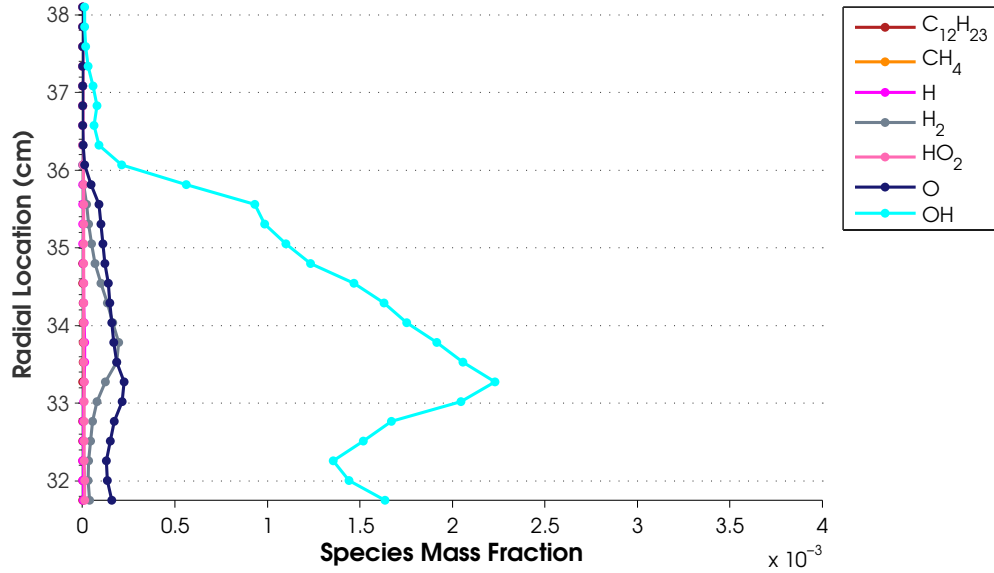


Figure D.13: Circumferentially-averaged mass fractions of species at combustor section exit using the 12-species combustion model and ideal air inlet diameters with a 30 hybrid vane engine configuration

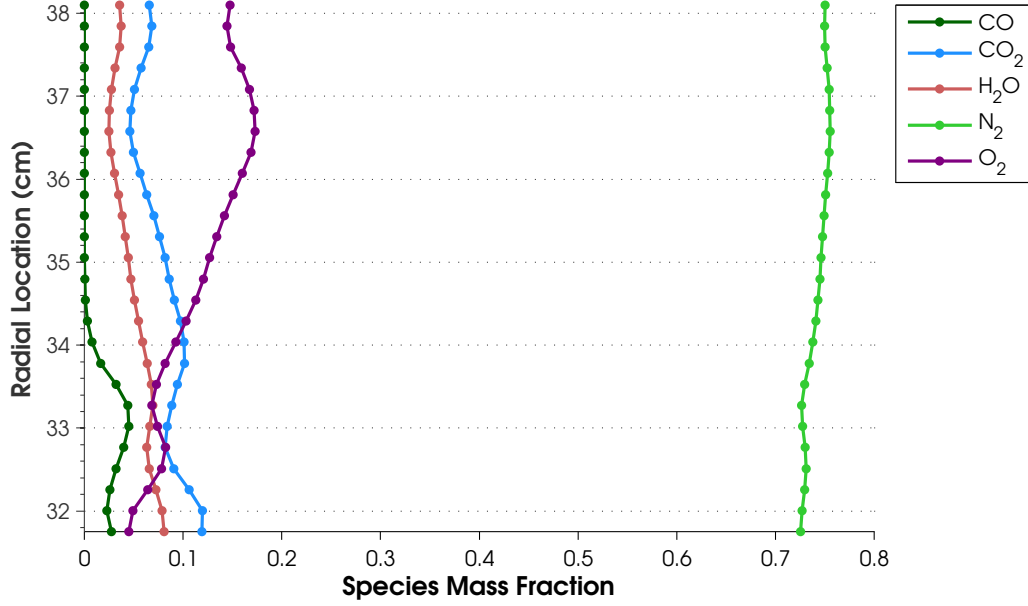


Figure D.14: Circumferentially-averaged mass fractions of species at combustor section exit using the 12-species combustion model and ideal air inlet diameters with a 30 hybrid vane rig configuration

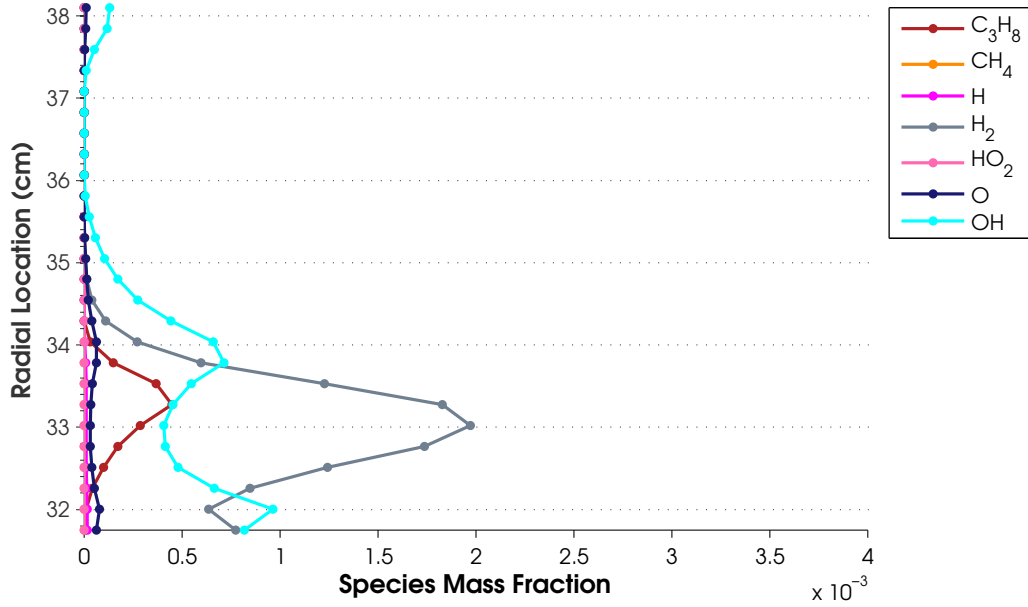


Figure D.15: Circumferentially-averaged mass fractions of species at combustor section exit using the 12-species combustion model and ideal air inlet diameters with a 30 hybrid vane rig configuration

Appendix E. Experimental Film Cooling Supporting Results

This appendix provides the results from all film cooling test cases conducted. The plots are grouped by result type (surface temperature, heat flux, heat transfer coefficient and comparison plots) and arranged within each section in order from lowest to highest equivalence ratio. Within each subsection, the results are presented for the fan-shaped holes alone, the slot upstream of the fan-shaped holes then the offset normal holes upstream of the fan-shaped holes. The order remained consistent with the order the data was presented in Chapter 6. The captions show the film cooling configuration including the cooling gas used in each hole. The results using nitrogen in the slot are shown immediately following the slot results using air as the cooling gas for all fuel-rich equivalence ratios.

E.1 Surface Temperature

E.1.1 $\Phi = 0.6$.

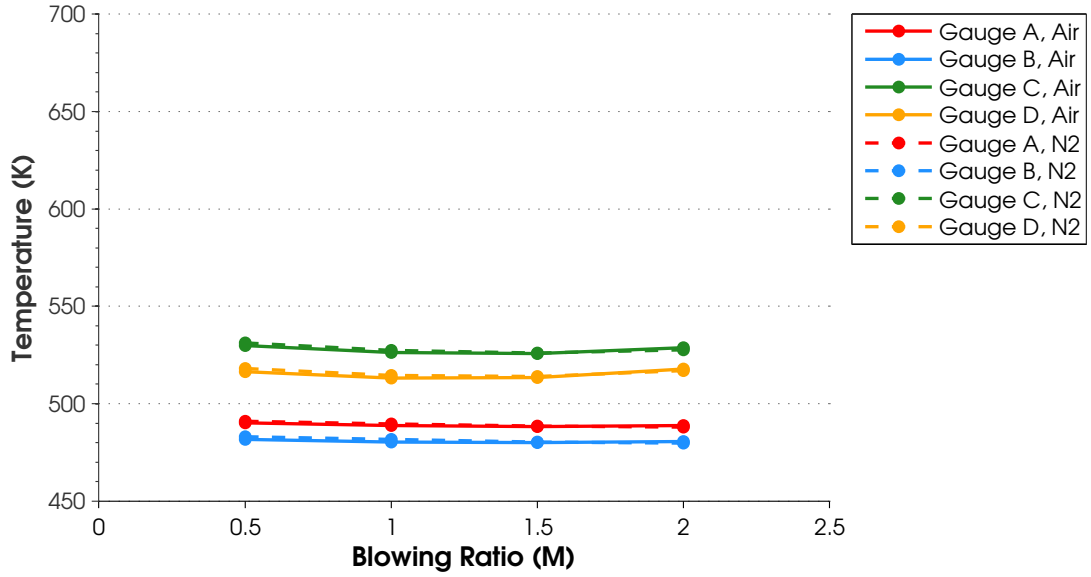


Figure E.1: Gauge surface temperature, $\Phi = 0.6$, $\dot{m}_{air}=425$ SLPM, US: Blank, Coolant=N/A, M=N/A, DS: Fan, Coolant=Air/N₂, M=Variable

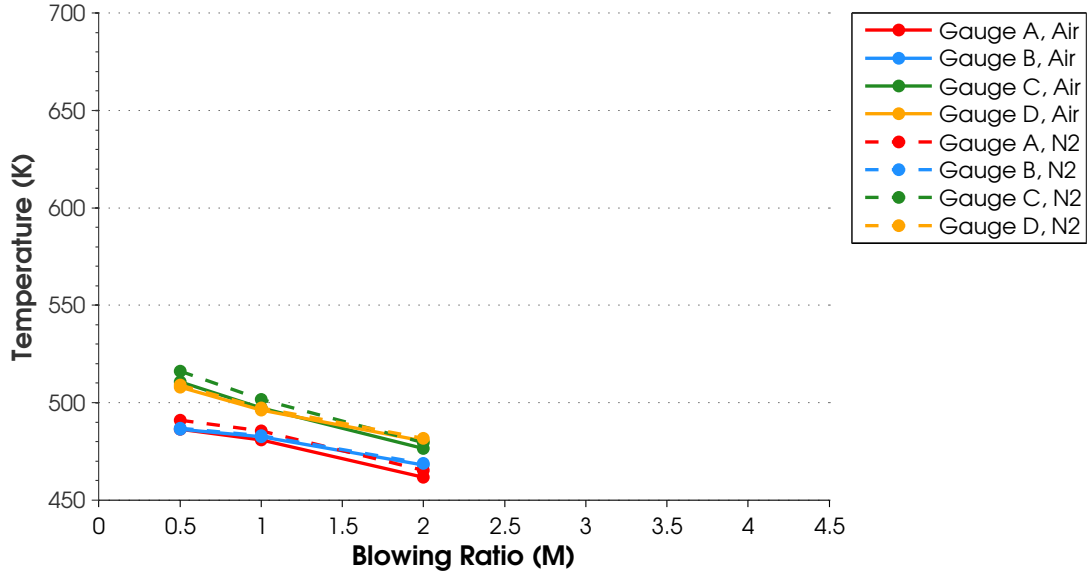


Figure E.2: Gauge surface temperature, $\Phi = 0.6$, $\dot{m}_{air}=425$ SLPM, US: Slot, Coolant=Air, M=Variable, DS: Fan, Coolant=Air/N₂, M=2

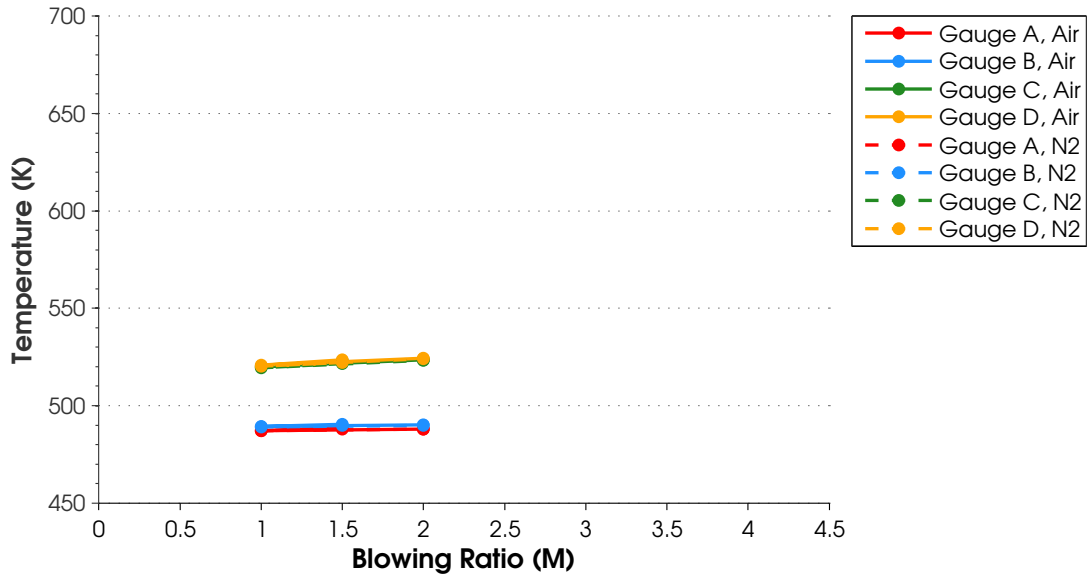


Figure E.3: Gauge surface temperature, $\Phi = 0.6$, $\dot{m}_{air}=425$ SLPM, US: Offset Normal, Coolant=Air, M=Variable, DS: Fan, Coolant=Air/N₂, M=2

E.1.2 Surface Temperature, $\Phi = 1.1$.

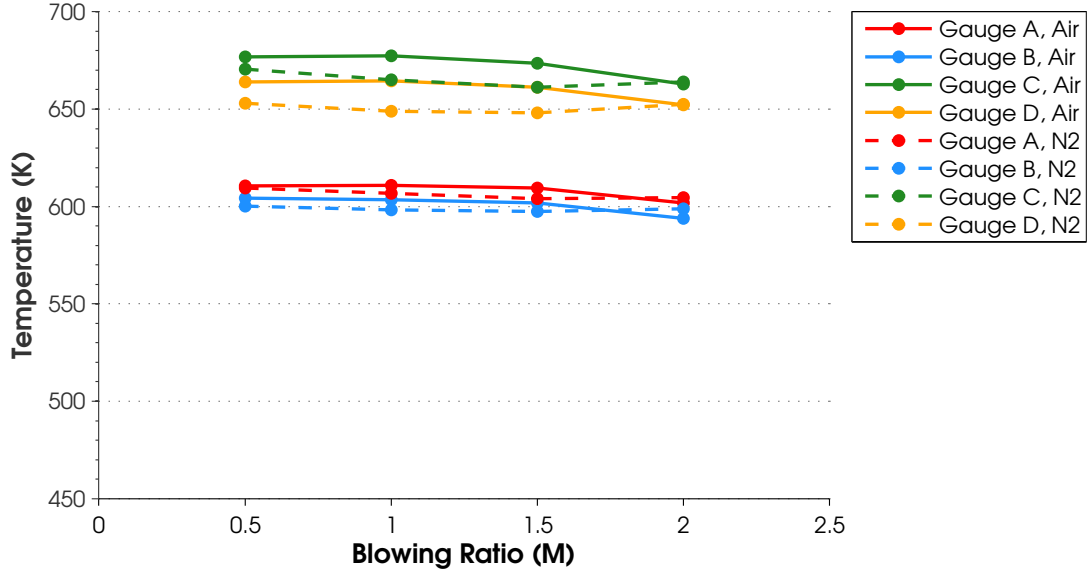


Figure E.4: Gauge surface temperature, $\Phi = 1.1$, $\dot{m}_{air}=425$ SLPM, US: Blank, Coolant=N/A, M=N/A, DS: Fan, Coolant=Air/N₂, M=Variable

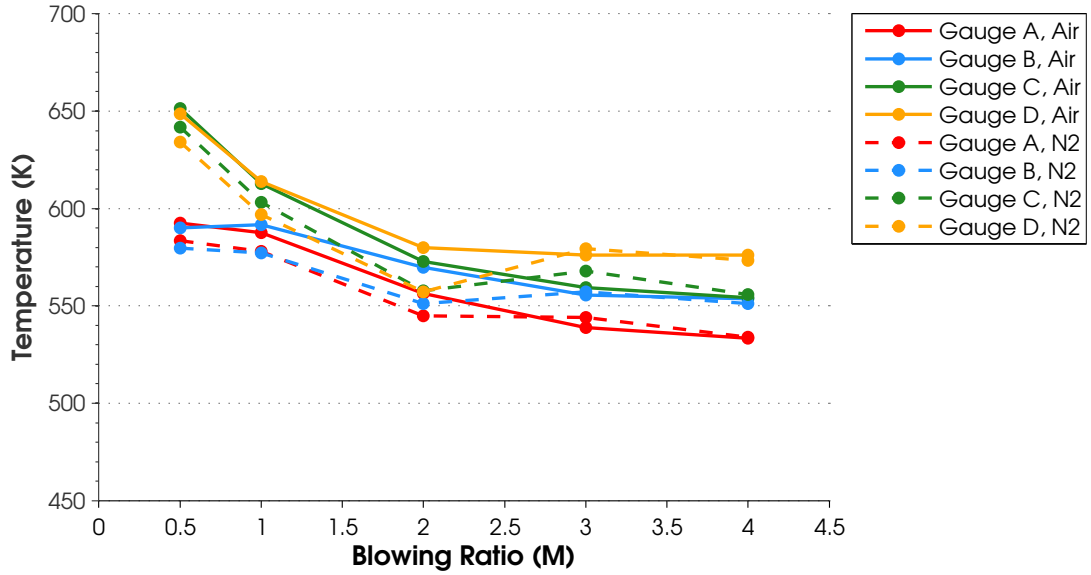


Figure E.5: Gauge surface temperature, $\Phi = 1.1$, $\dot{m}_{air}=425$ SLPM, US: Slot, Coolant=Air, M=Variable, DS: Fan, Coolant=Air/N₂, M=2

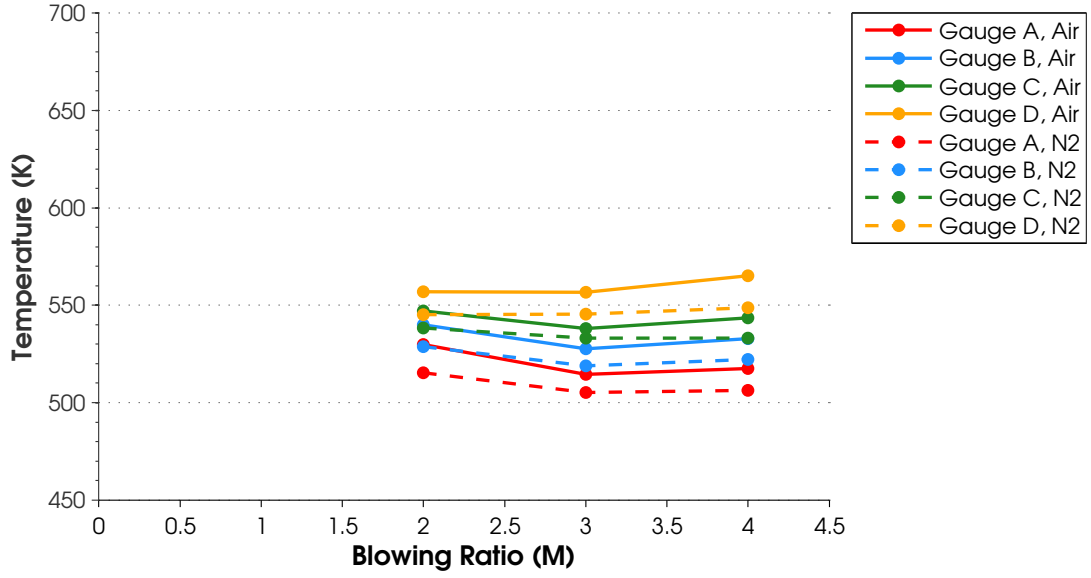


Figure E.6: Gauge surface temperature, $\Phi = 1.1$, $\dot{m}_{air}=425$ SLPM, US: Slot, Coolant= N_2 , M=Variable, DS: Fan, Coolant=Air/ N_2 , M=2

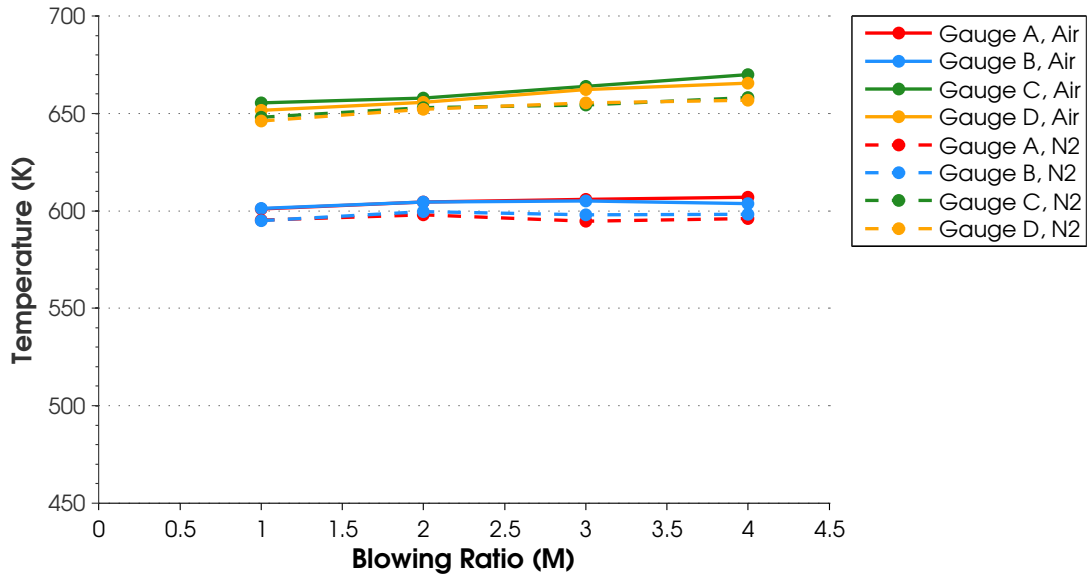


Figure E.7: Gauge surface temperature, $\Phi = 1.1$, $\dot{m}_{air}=425$ SLPM, US: Offset Normal, Coolant=Air, M=Variable, DS: Fan, Coolant=Air/ N_2 , M=2

E.1.3 Surface Temperature, $\Phi = 1.3$.

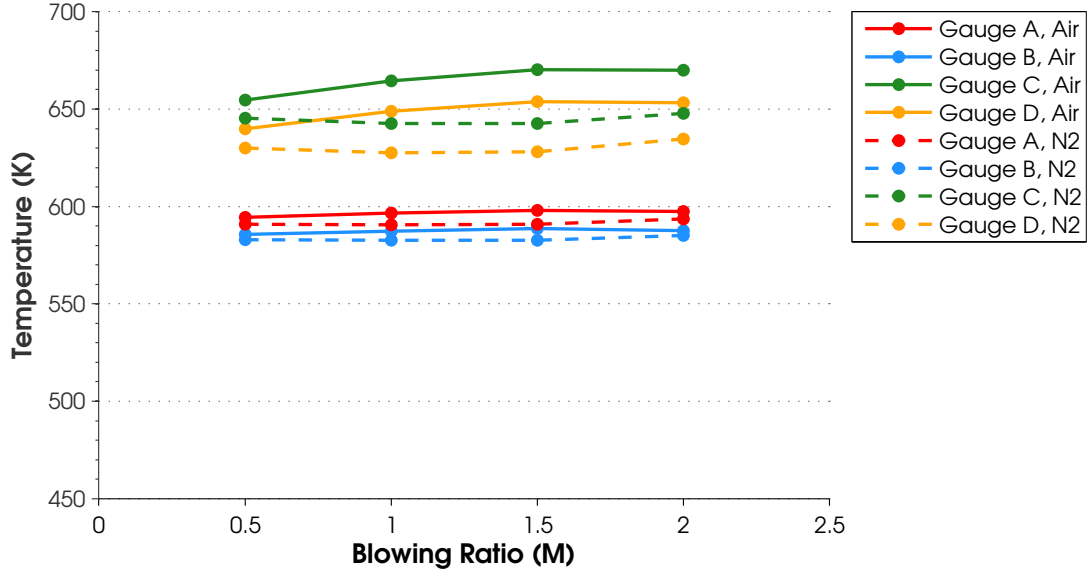


Figure E.8: Gauge surface temperature, $\Phi = 1.3$, $\dot{m}_{air}=425$ SLPM, US: Blank, Coolant=N/A, M=N/A, DS: Fan, Coolant=Air/N₂, M=Variable

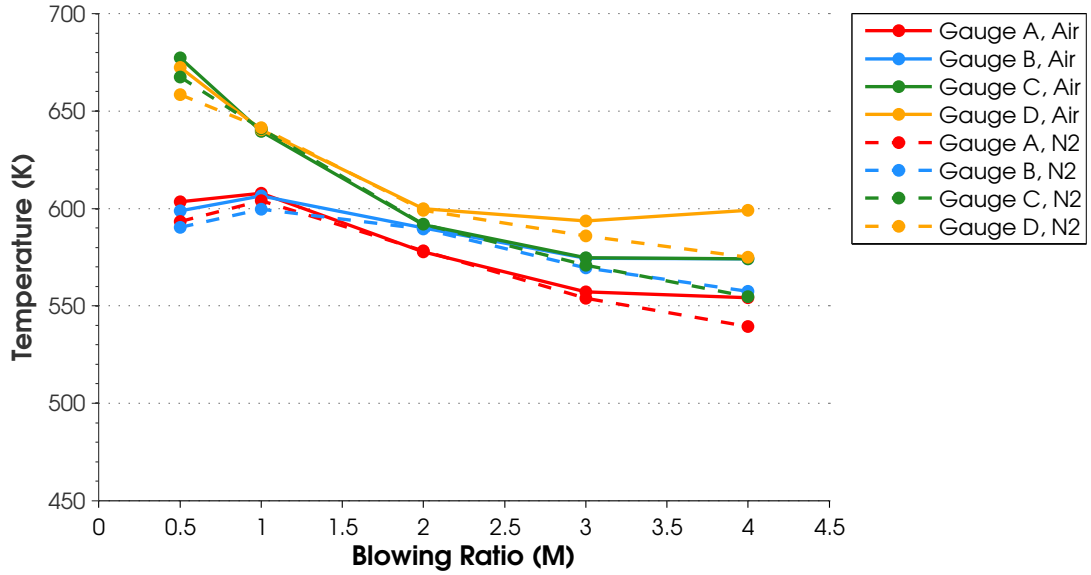


Figure E.9: Gauge surface temperature, $\Phi = 1.3$, $\dot{m}_{air}=425$ SLPM, US: Slot, Coolant=Air, M=Variable, DS: Fan, Coolant=Air/N₂, M=2

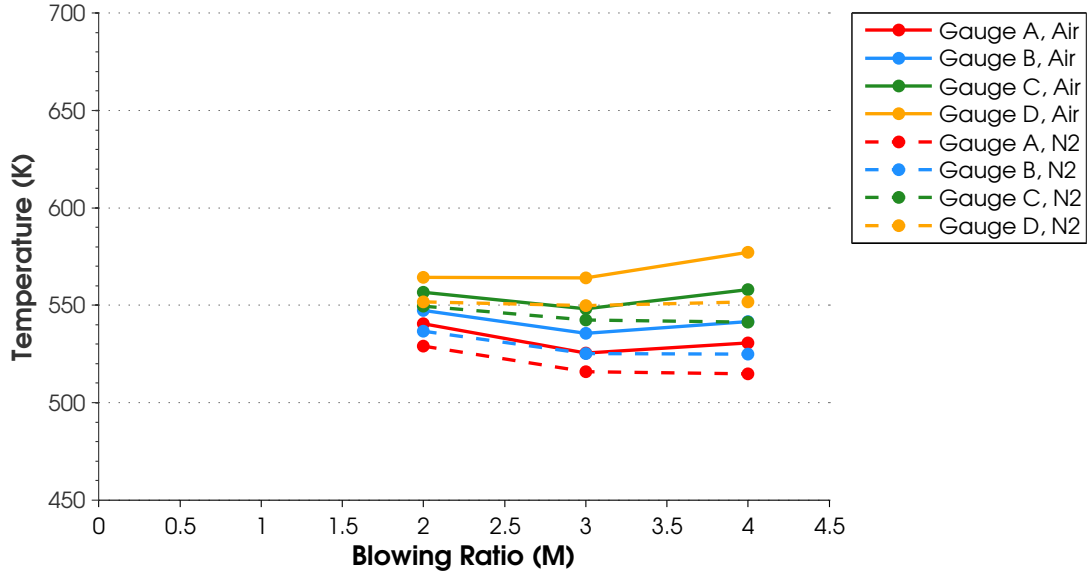


Figure E.10: Gauge surface temperature, $\Phi = 1.3$, $\dot{m}_{air}=425$ SLPM, US: Slot, Coolant=N₂, M=Variable, DS: Fan, Coolant=Air/N₂, M=2

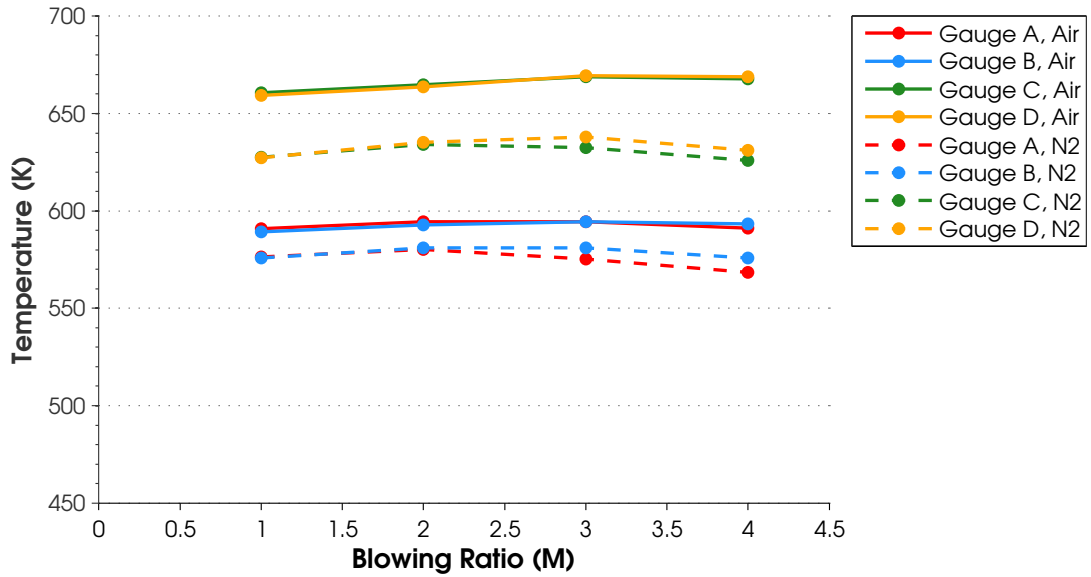


Figure E.11: Gauge surface temperature, $\Phi = 1.3$, $\dot{m}_{air}=425$ SLPM, US: Offset Normal, Coolant=Air, M=Variable, DS: Fan, Coolant=Air/N₂, M=2

E.1.4 Surface Temperature, $\Phi = 1.5$.

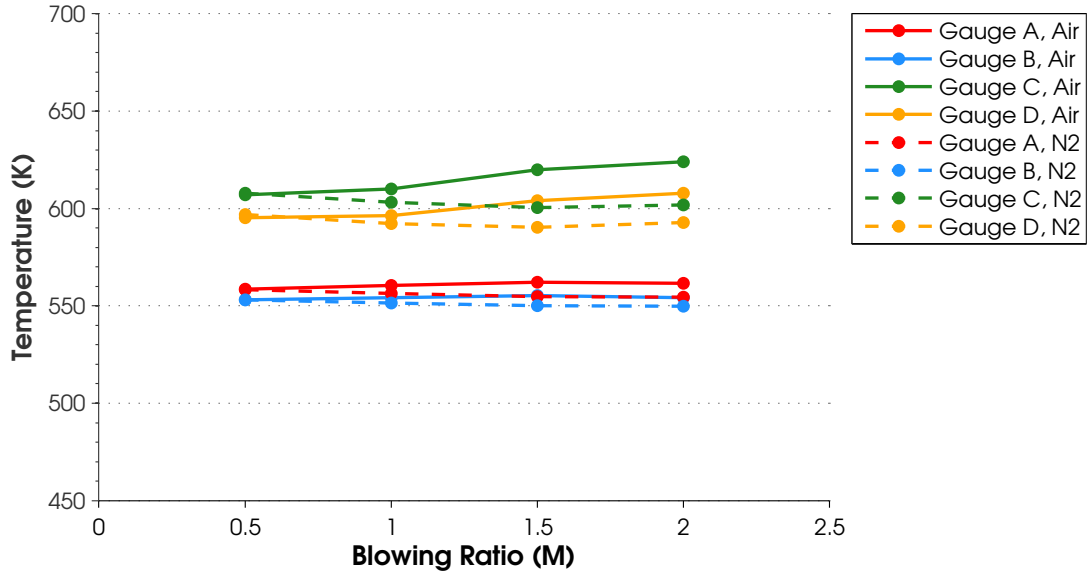


Figure E.12: Gauge surface temperature, $\Phi = 1.5$, $\dot{m}_{air}=425$ SLPM, US: Blank, Coolant=N/A, M=N/A, DS: Fan, Coolant=Air/N₂, M=Variable

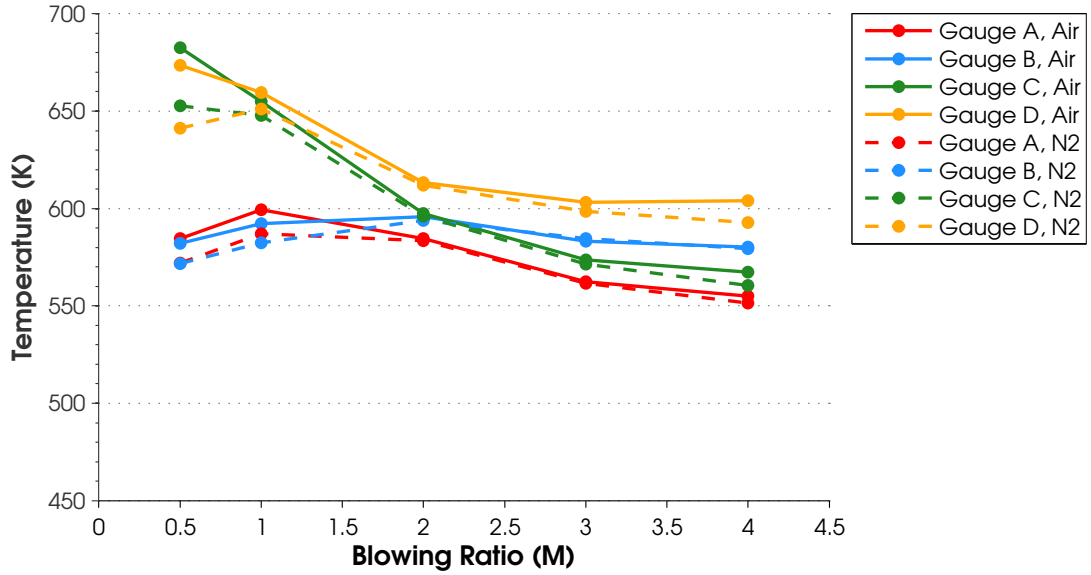


Figure E.13: Gauge surface temperature, $\Phi = 1.5$, $\dot{m}_{air}=425$ SLPM, US: Slot, Coolant=Air, M=Variable, DS: Fan, Coolant=Air/N₂, M=2

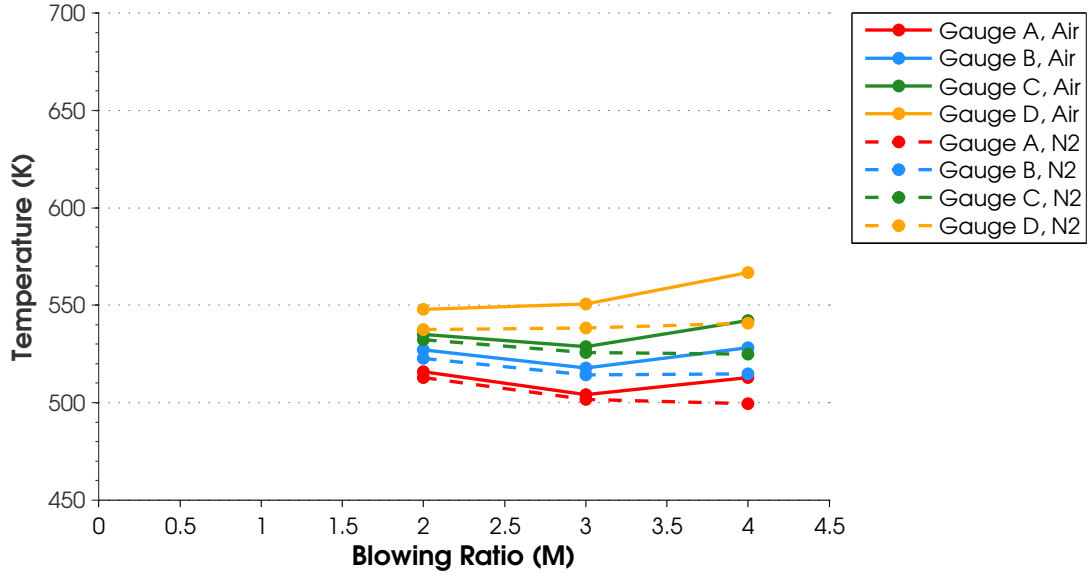


Figure E.14: Gauge surface temperature, $\Phi = 1.3$, $\dot{m}_{air}=425$ SLPM, US: Slot, Coolant=N₂, M=Variable, DS: Fan, Coolant=Air/N₂, M=2

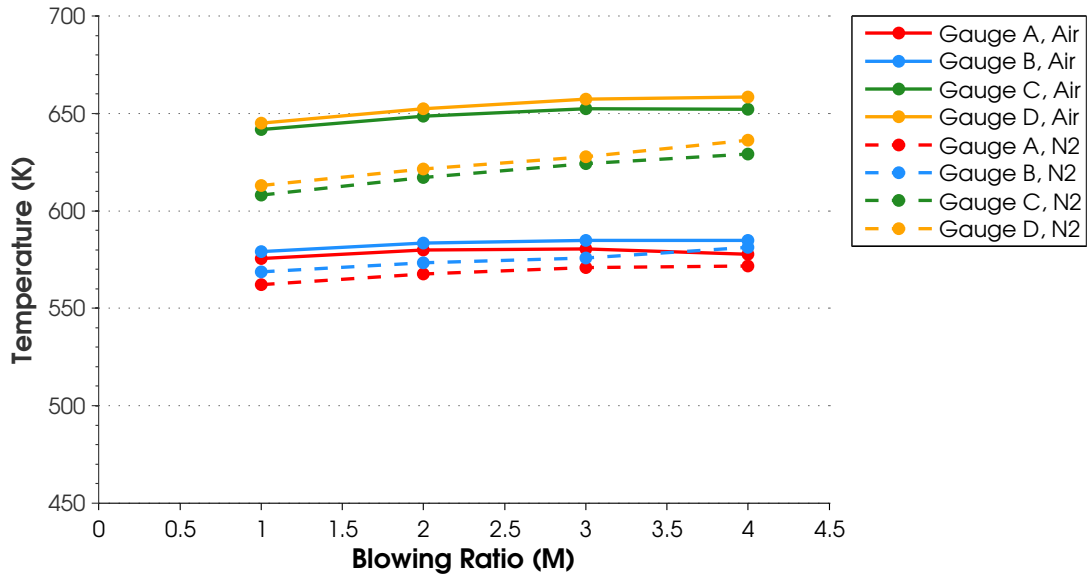


Figure E.15: Gauge surface temperature, $\Phi = 1.5$, $\dot{m}_{air}=425$ SLPM, US: Offset Normal, Coolant=Air, M=Variable, DS: Fan, Coolant=Air/N₂, M=2

E.2 Heat Flux

E.2.1 $\Phi = 0.6$.

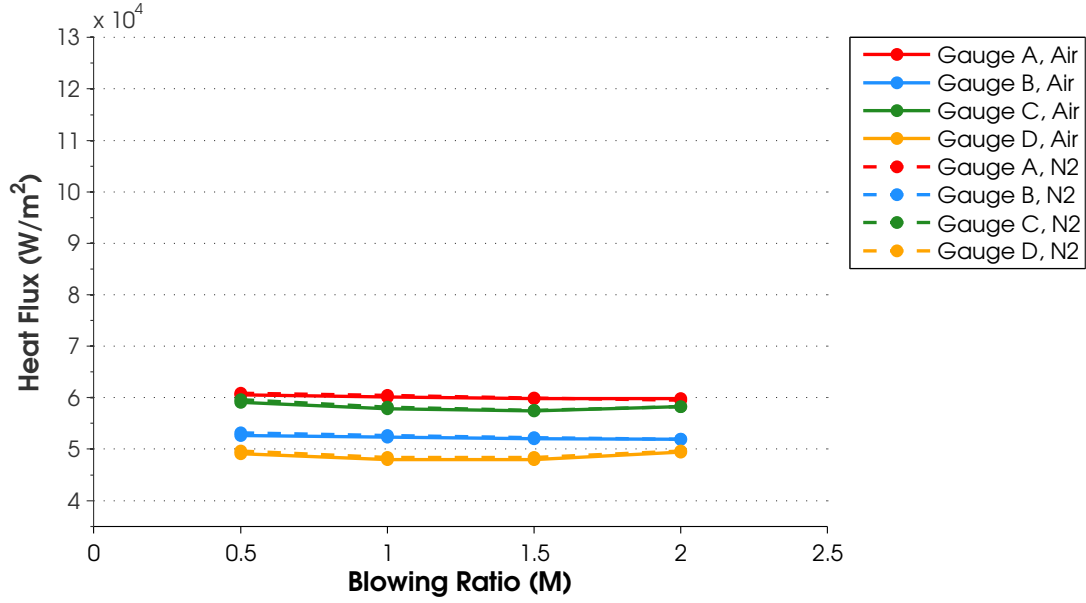


Figure E.16: Gauge heat flux, $\Phi = 0.6$, $\dot{m}_{air}=425$ SLPM, US: Blank, Coolant=N/A, M=N/A, DS: Fan, Coolant=Air/N₂, M=Variable

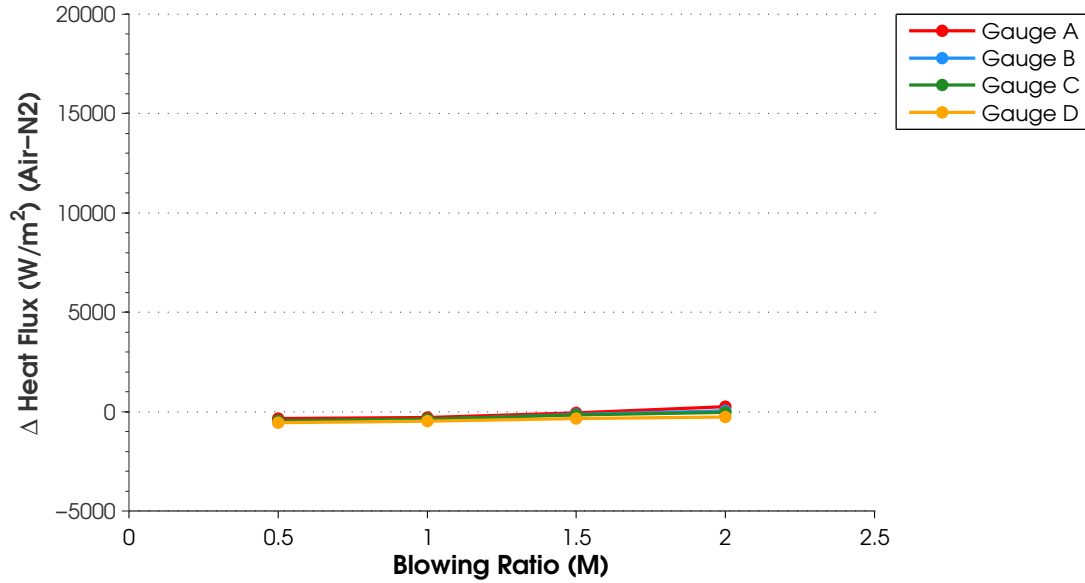


Figure E.17: Gauge heat flux difference, $\Phi = 0.6$, $\dot{m}_{air}=425$ SLPM, US: Blank, Coolant=N/A, M=N/A, DS: Fan, Coolant=Air/N₂, M=Variable

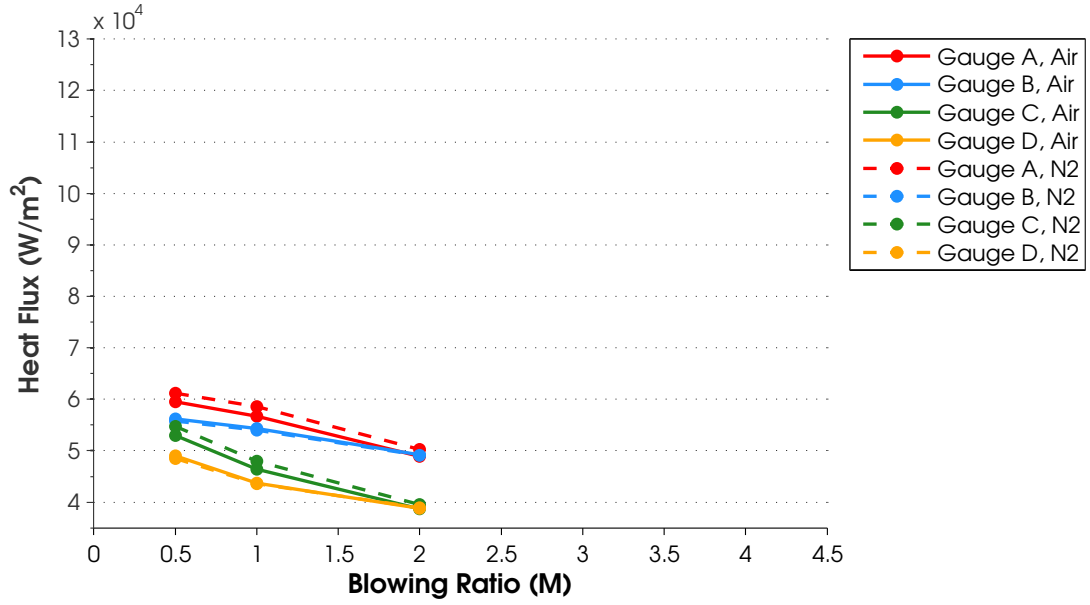


Figure E.18: Gauge heat flux, $\Phi = 0.6$, $\dot{m}_{air}=425$ SLPM, US: Slot, Coolant=Air, M=Variable, DS: Fan, Coolant=Air/N₂, M=2

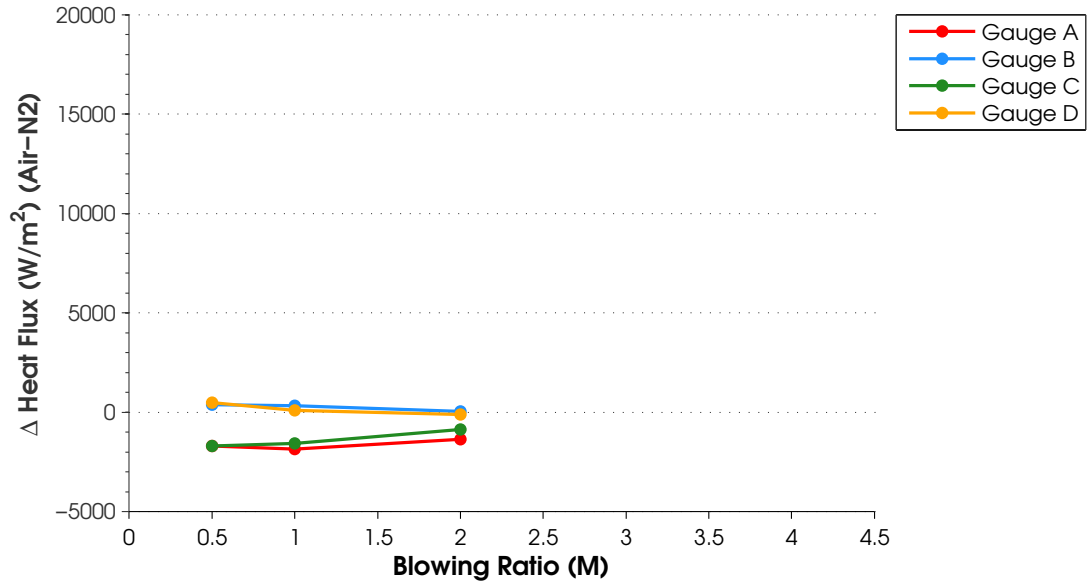


Figure E.19: Gauge heat flux difference, $\Phi = 0.6$, $\dot{m}_{air}=425$ SLPM, US: Slot, Coolant=Air, M=Variable, DS: Fan, Coolant=Air/N₂, M=2

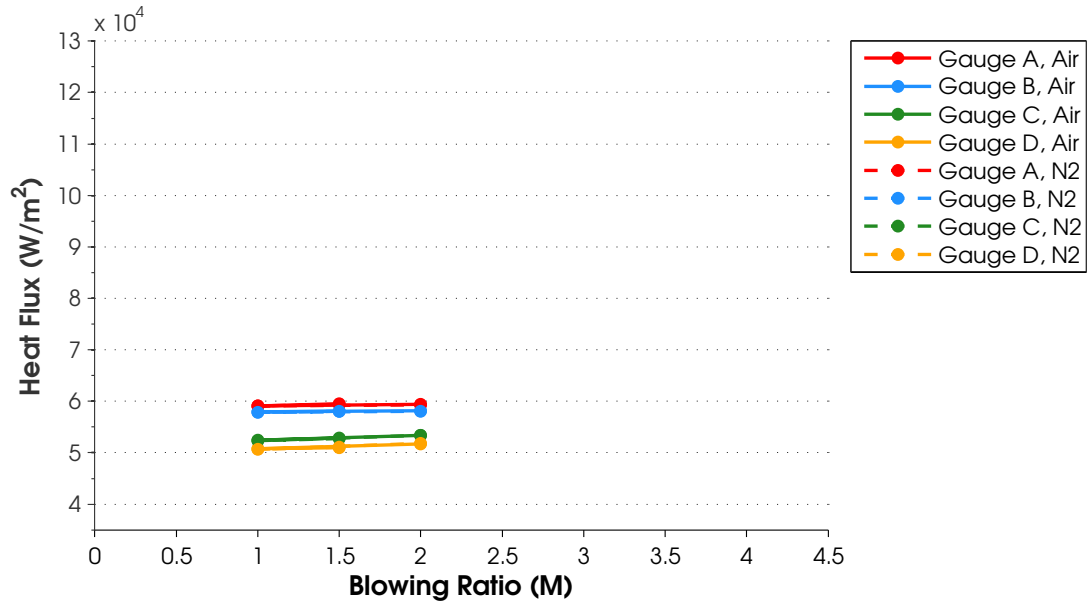


Figure E.20: Gauge heat flux, $\Phi = 0.6$, $\dot{m}_{air}=425$ SLPM, US: Offset Normal, Coolant=Air, M=Variable, DS: Fan, Coolant=Air/N₂, M=2

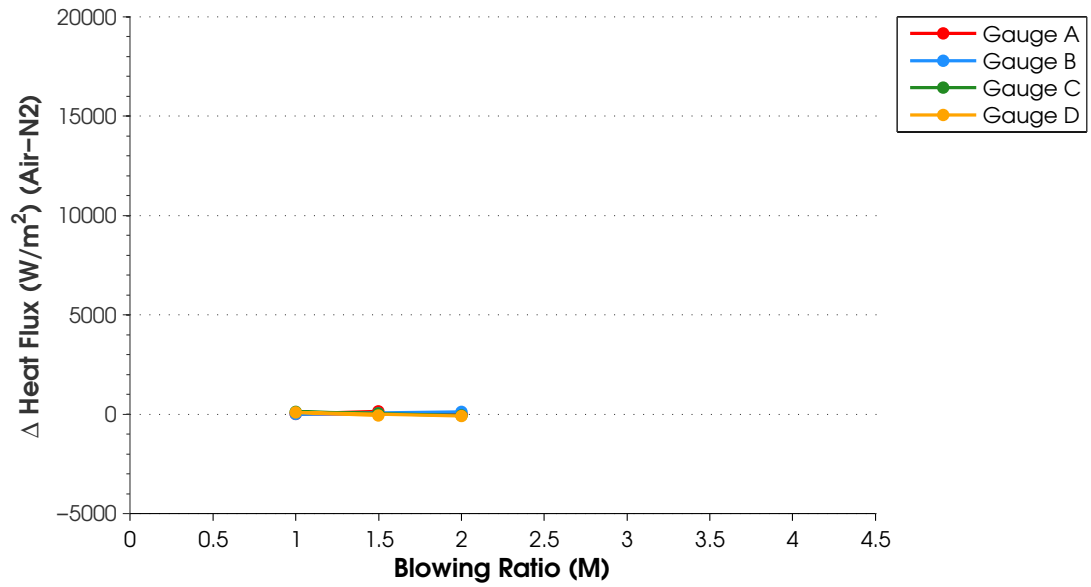


Figure E.21: Gauge heat flux difference, $\Phi = 0.6$, $\dot{m}_{air}=425$ SLPM, US: Offset Normal, Coolant=Air, M=Variable, DS: Fan, Coolant=Air/N₂, M=2

E.2.2 Heat Flux, $\Phi = 1.1$.

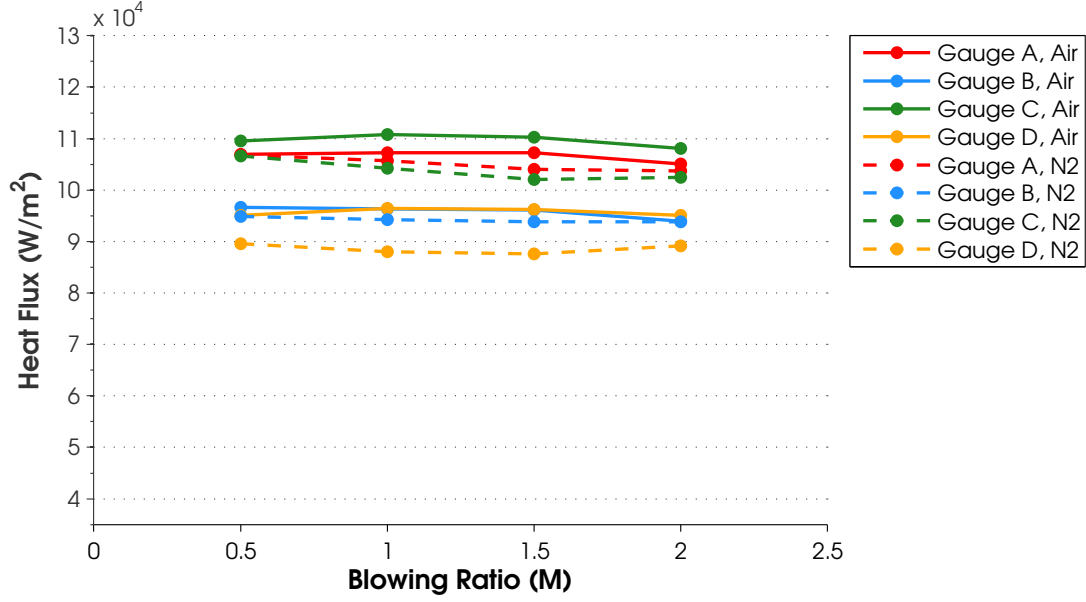


Figure E.22: Gauge heat flux, $\Phi = 1.1$, $\dot{m}_{air}=425$ SLPM, US: Blank, Coolant=N/A, M=N/A, DS: Fan, Coolant=Air/N₂, M=Variable

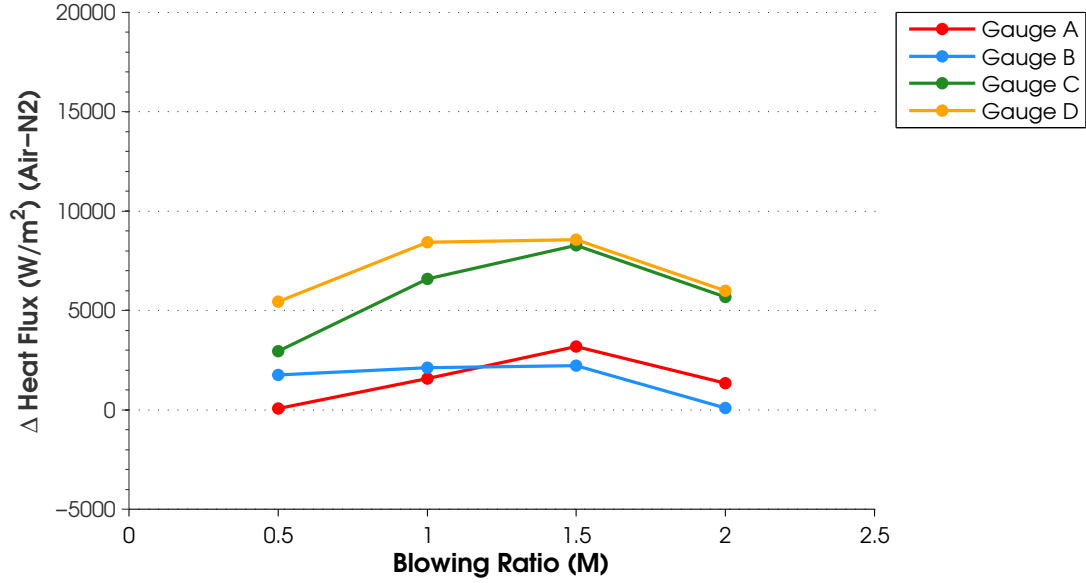


Figure E.23: Gauge heat flux difference, $\Phi = 1.1$, $\dot{m}_{air}=425$ SLPM, US: Blank, Coolant=N/A, M=N/A, DS: Fan, Coolant=Air/N₂, M=Variable

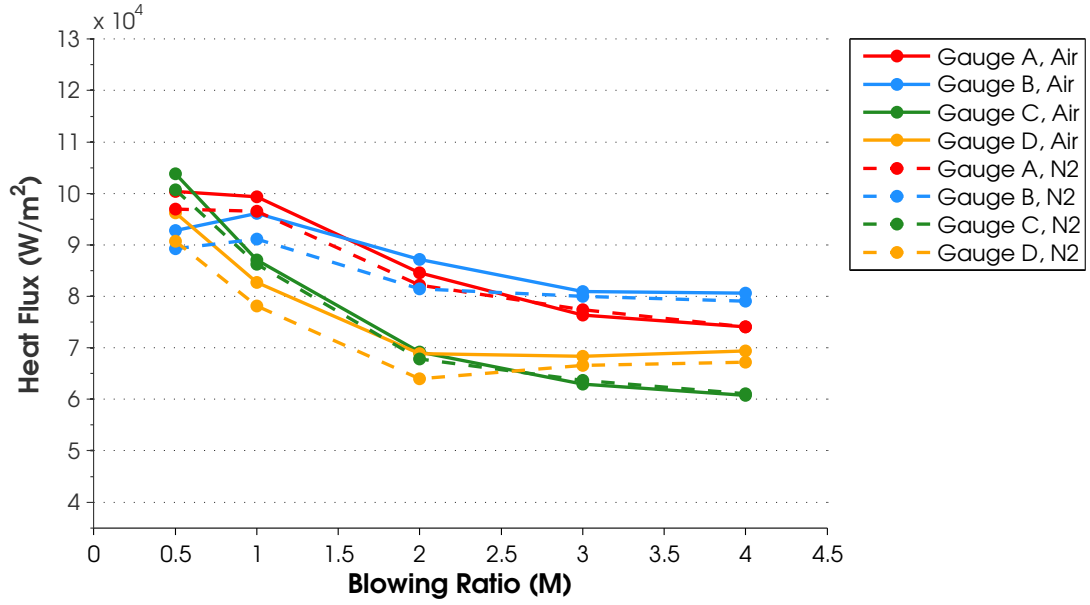


Figure E.24: Gauge heat flux, $\Phi = 1.1$, $\dot{m}_{air}=425$ SLPM, US: Slot, Coolant=Air, M=Variable, DS: Fan, Coolant=Air/N₂, M=2

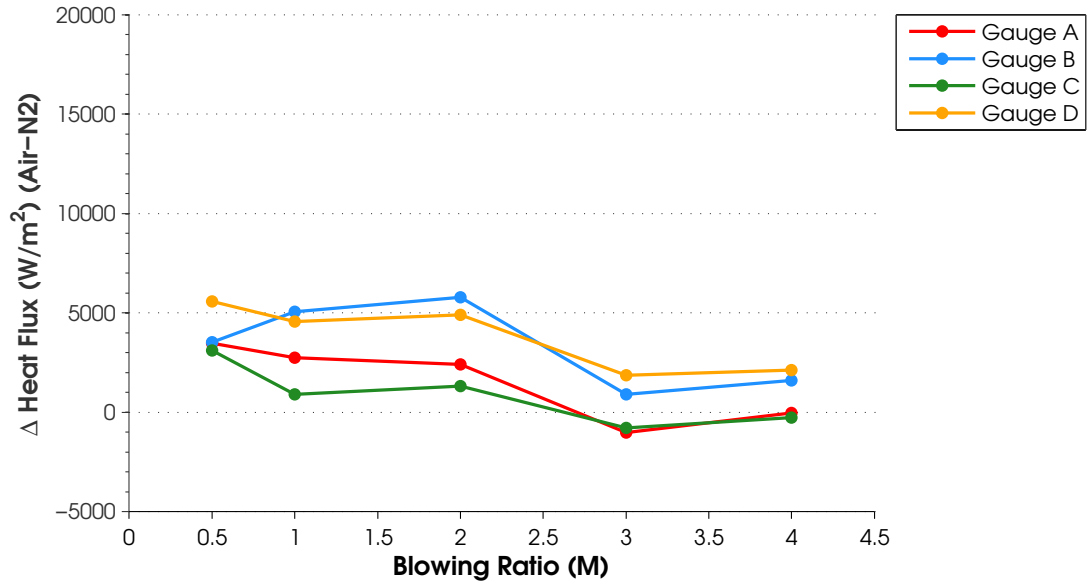


Figure E.25: Gauge heat flux difference, $\Phi = 1.1$, $\dot{m}_{air}=425$ SLPM, US: Slot, Coolant=Air, M=Variable, DS: Fan, Coolant=Air/N₂, M=2

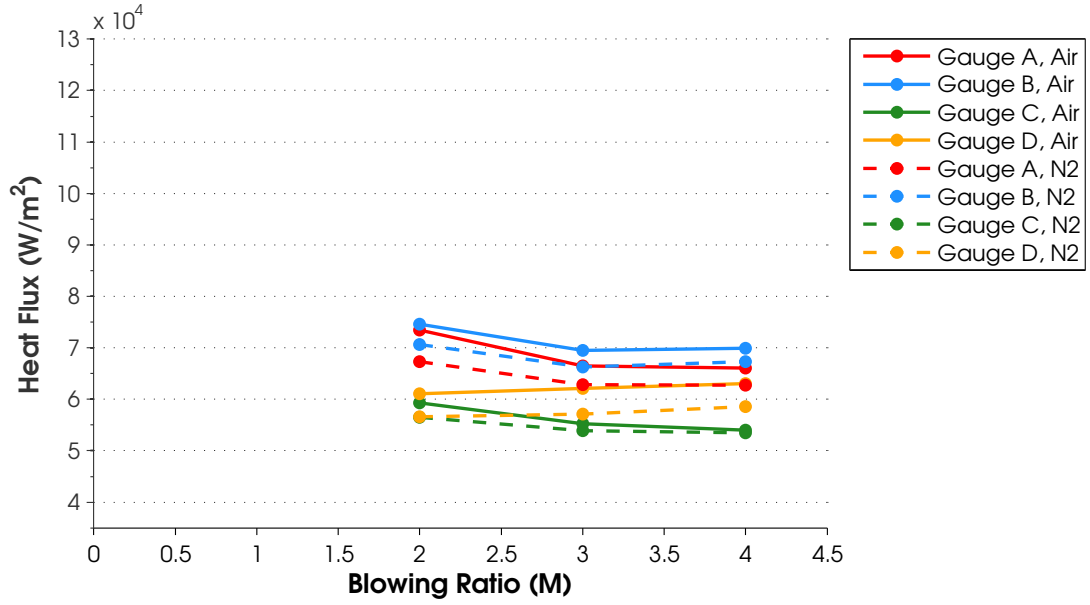


Figure E.26: Gauge heat flux, $\Phi = 1.1$, $\dot{m}_{air}=425$ SLPM, US: Slot, Coolant= N_2 , M=Variable, DS: Fan, Coolant=Air/ N_2 , M=2

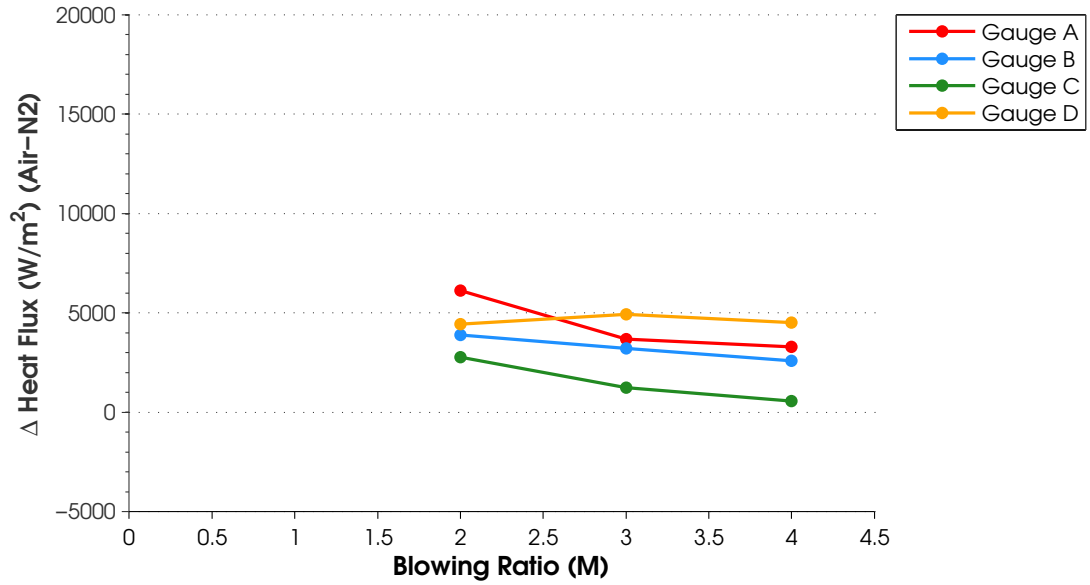


Figure E.27: Gauge heat flux difference, $\Phi = 1.1$, $\dot{m}_{air}=425$ SLPM, US: Slot, Coolant= N_2 , M=Variable, DS: Fan, Coolant=Air/ N_2 , M=2

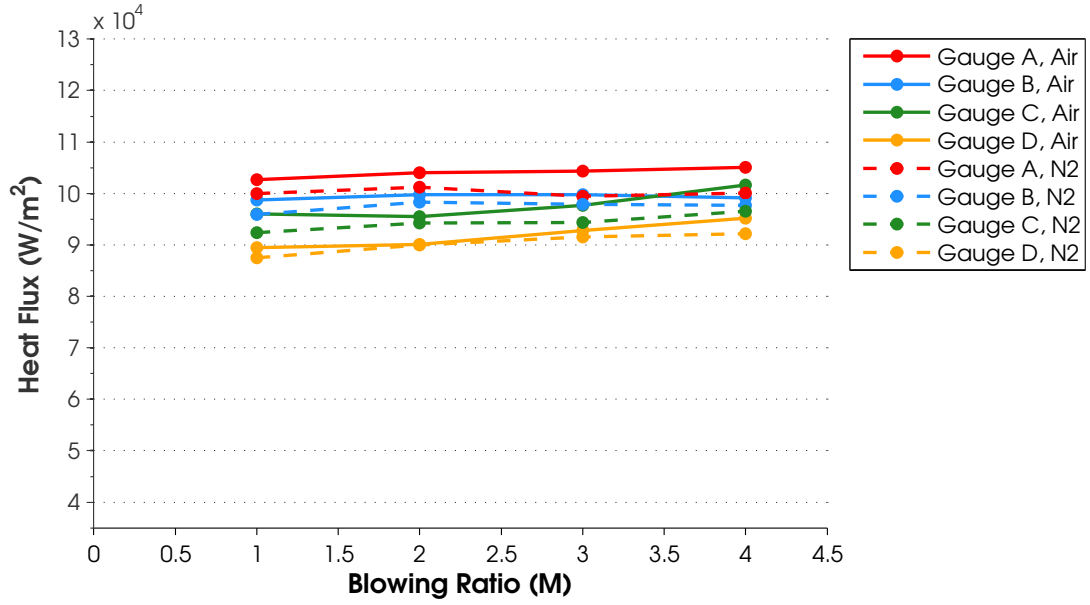


Figure E.28: Gauge heat flux, $\Phi = 1.1$, $\dot{m}_{air}=425$ SLPM, US: Offset Normal, Coolant=Air, M=Variable, DS: Fan, Coolant=Air/N₂, M=2

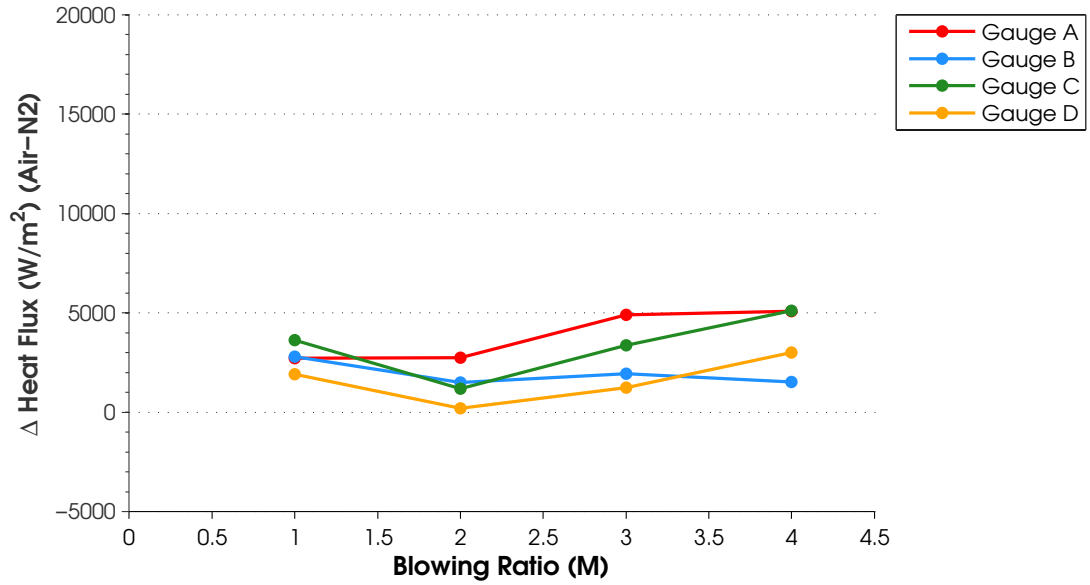


Figure E.29: Gauge heat flux difference, $\Phi = 1.1$, $\dot{m}_{air}=425$ SLPM, US: Offset Normal, Coolant=Air, M=Variable, DS: Fan, Coolant=Air/N₂, M=2

E.2.3 Heat Flux, $\Phi = 1.3$.

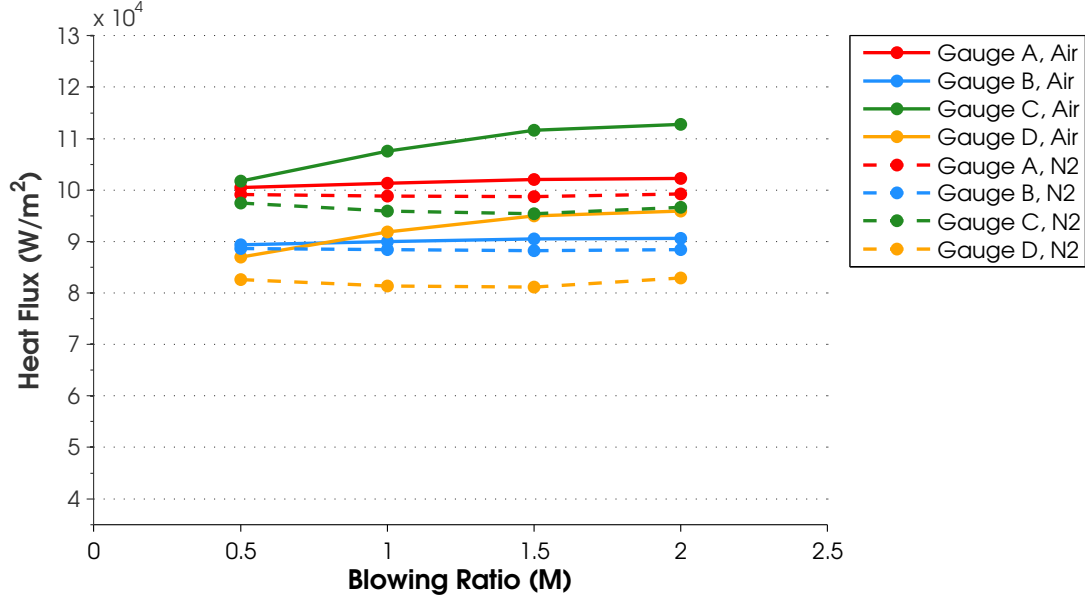


Figure E.30: Gauge heat flux, $\Phi = 1.3$, $\dot{m}_{air}=425$ SLPM, US: Blank, Coolant=N/A, M=N/A, DS: Fan, Coolant=Air/N₂, M=Variable

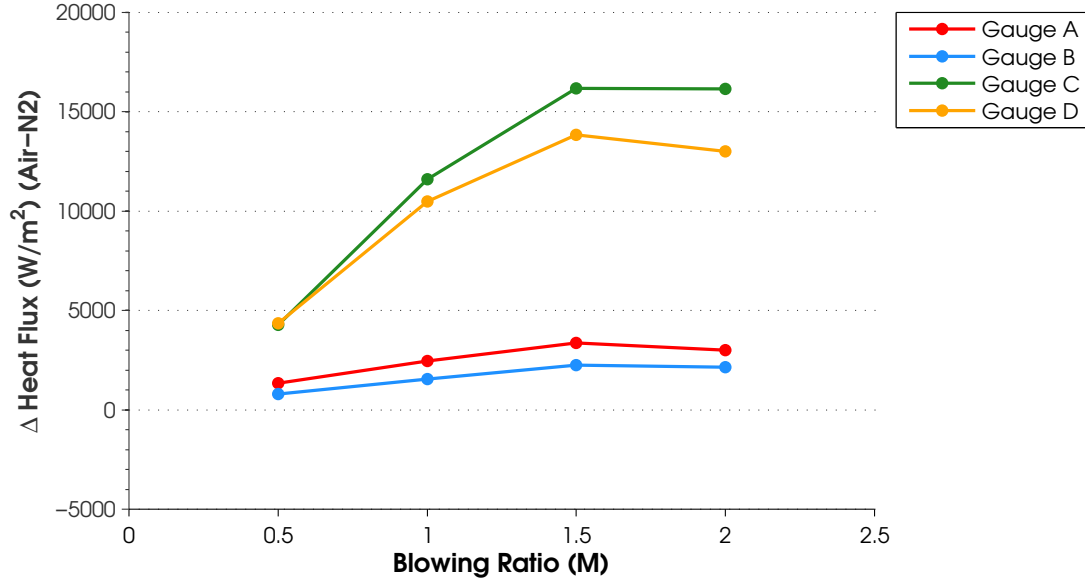


Figure E.31: Gauge heat flux difference, $\Phi = 1.3$, $\dot{m}_{air}=425$ SLPM, US: Blank, Coolant=N/A, M=N/A, DS: Fan, Coolant=Air/N₂, M=Variable

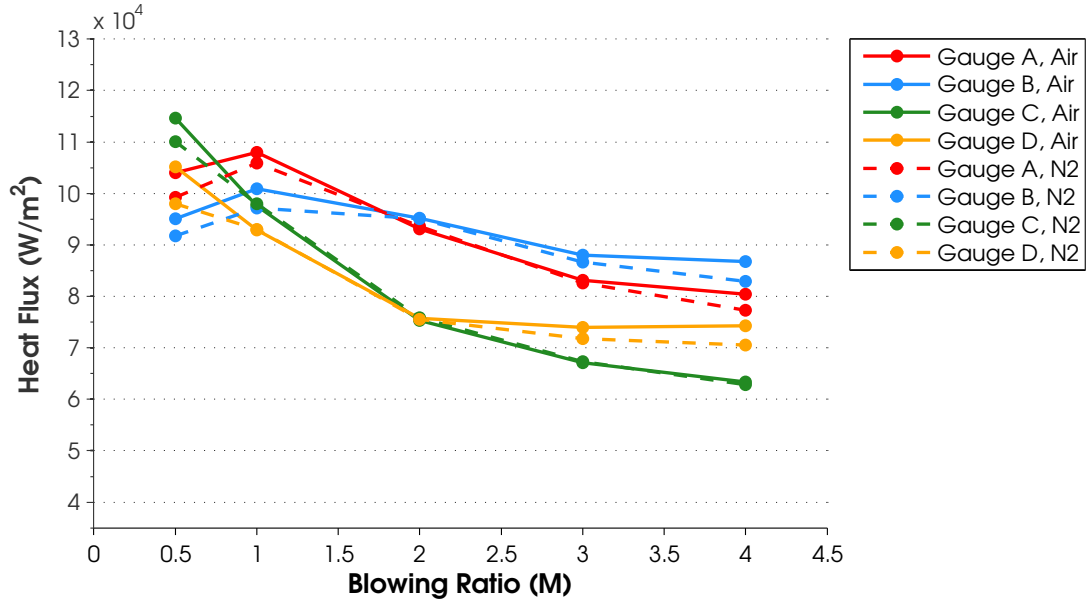


Figure E.32: Gauge heat flux, $\Phi = 1.3$, $\dot{m}_{air}=425$ SLPM, US: Slot, Coolant=Air, M=Variable, DS: Fan, Coolant=Air/N₂, M=2

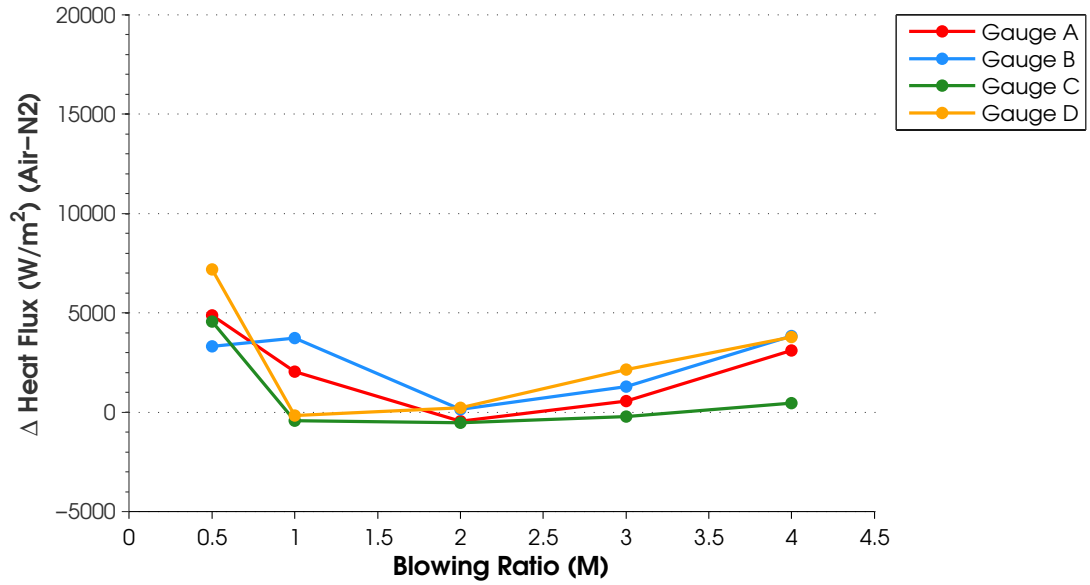


Figure E.33: Gauge heat flux difference, $\Phi = 1.3$, $\dot{m}_{air}=425$ SLPM, US: Slot, Coolant=Air, M=Variable, DS: Fan, Coolant=Air/N₂, M=2

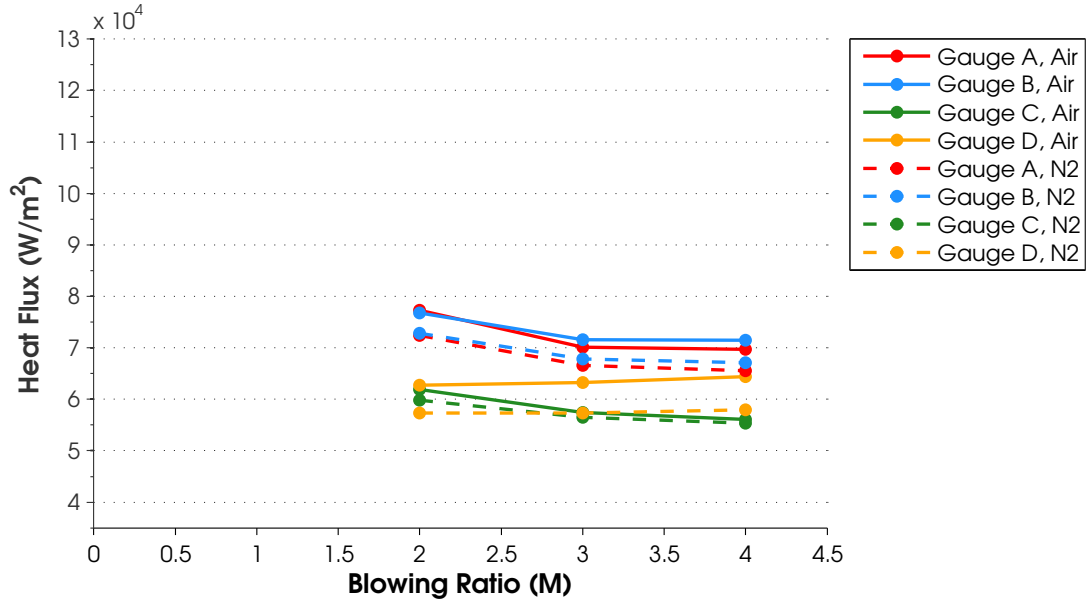


Figure E.34: Gauge heat flux, $\Phi = 1.3$, $\dot{m}_{air}=425$ SLPM, US: Slot, Coolant= N_2 , M =Variable, DS: Fan, Coolant=Air/ N_2 , $M=2$

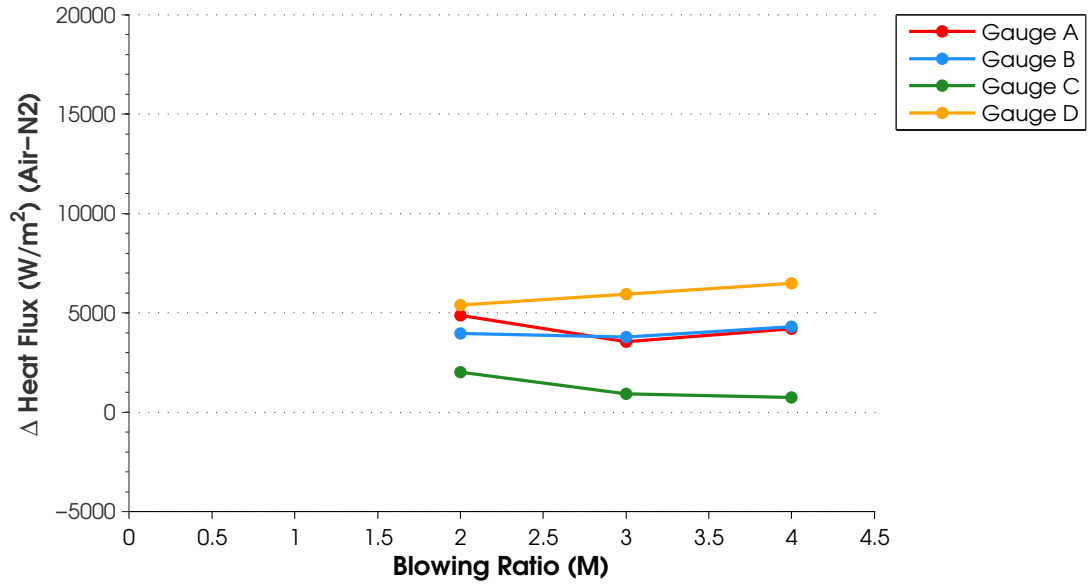


Figure E.35: Gauge heat flux difference, $\Phi = 1.3$, $\dot{m}_{air}=425$ SLPM, US: Slot, Coolant= N_2 , M =Variable, DS: Fan, Coolant=Air/ N_2 , $M=2$

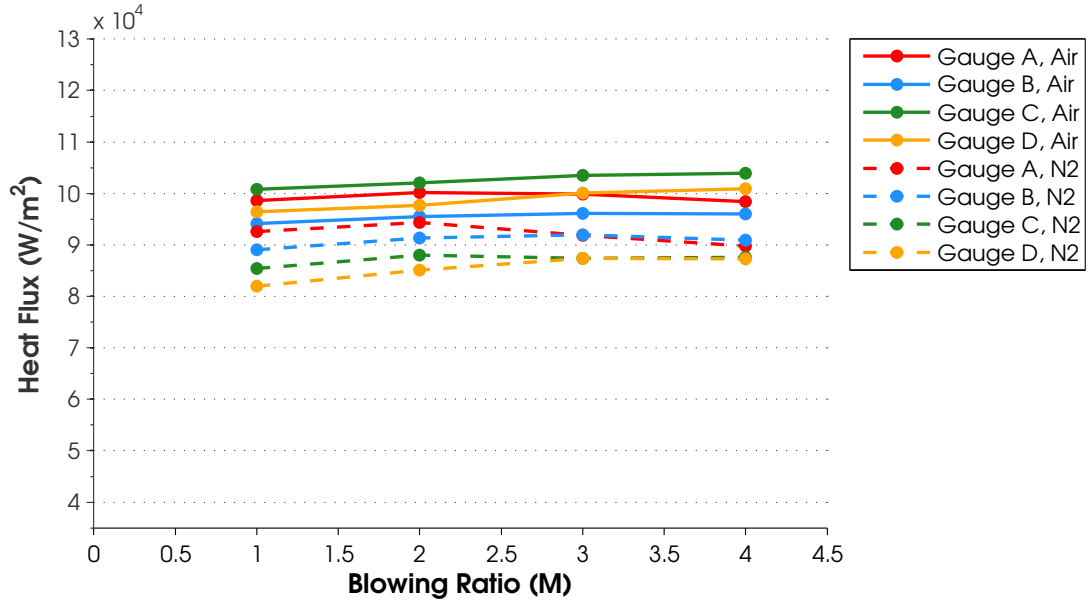


Figure E.36: Gauge heat flux, $\Phi = 1.3$, $\dot{m}_{air}=425$ SLPM, US: Offset Normal, Coolant=Air, M=Variable, DS: Fan, Coolant=Air/N₂, M=2

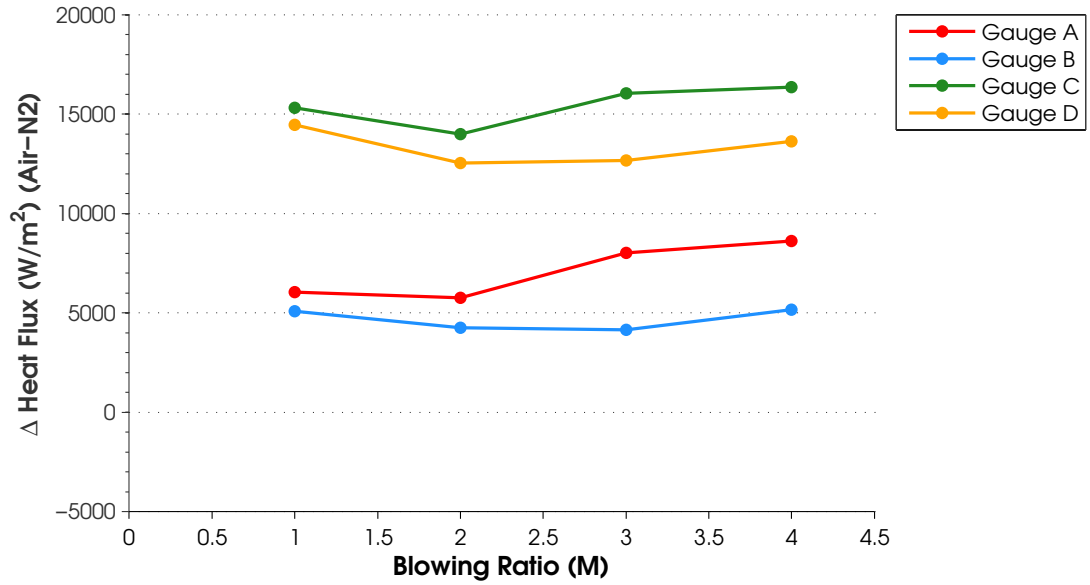


Figure E.37: Gauge heat flux difference, $\Phi = 1.3$, $\dot{m}_{air}=425$ SLPM, US: Offset Normal, Coolant=Air, M=Variable, DS: Fan, Coolant=Air/N₂, M=2

E.2.4 Heat Flux, $\Phi = 1.5$.

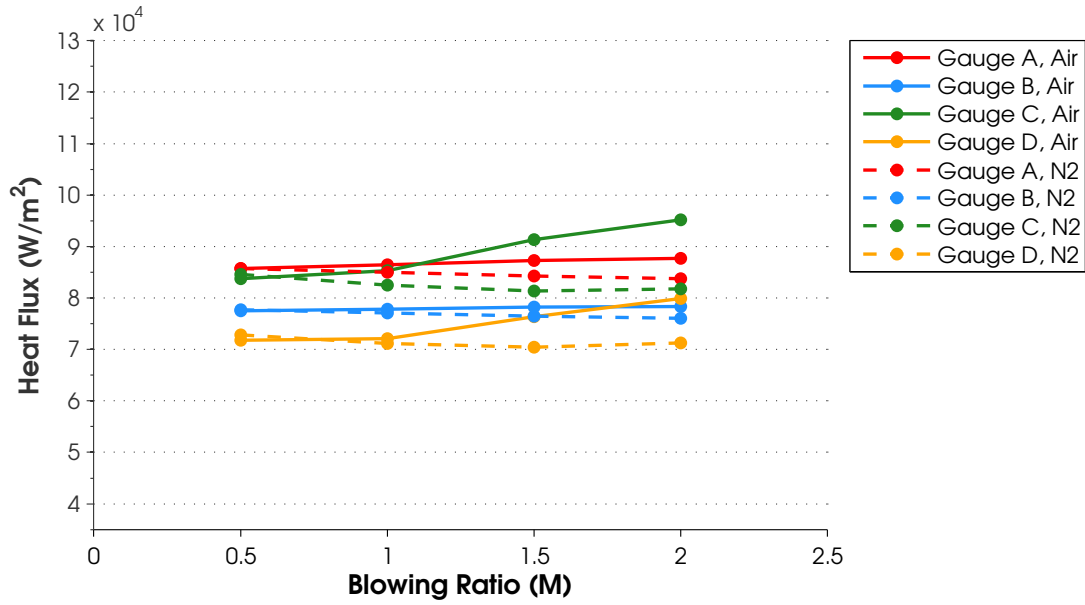


Figure E.38: Gauge heat flux, $\Phi = 1.5$, $\dot{m}_{air}=425$ SLPM, US: Blank, Coolant=N/A, M=N/A, DS: Fan, Coolant=Air/N₂, M=Variable

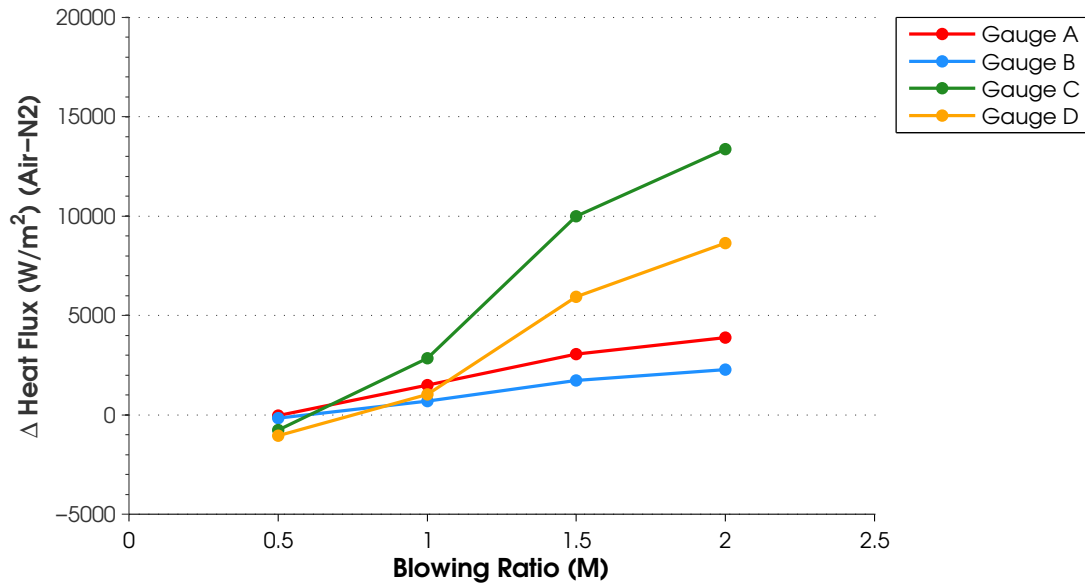


Figure E.39: Gauge heat flux difference, $\Phi = 1.5$, $\dot{m}_{air}=425$ SLPM, US: Blank, Coolant=N/A, M=N/A, DS: Fan, Coolant=Air/N₂, M=Variable

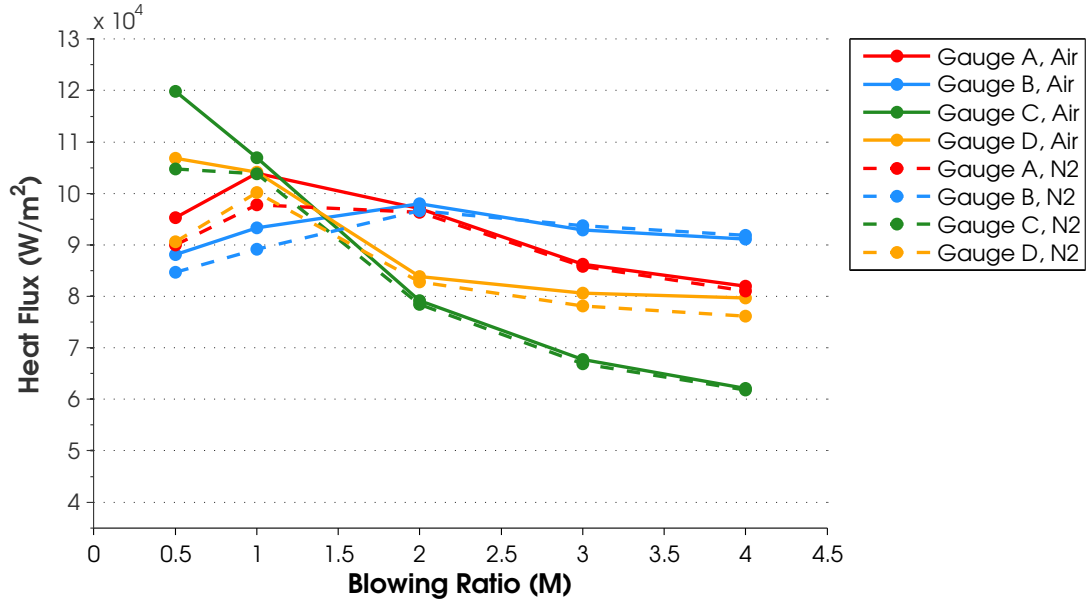


Figure E.40: Gauge heat flux, $\Phi = 1.5$, $\dot{m}_{air}=425$ SLPM, US: Slot, Coolant=Air, M =Variable, DS: Fan, Coolant=Air/ N_2 , $M=2$

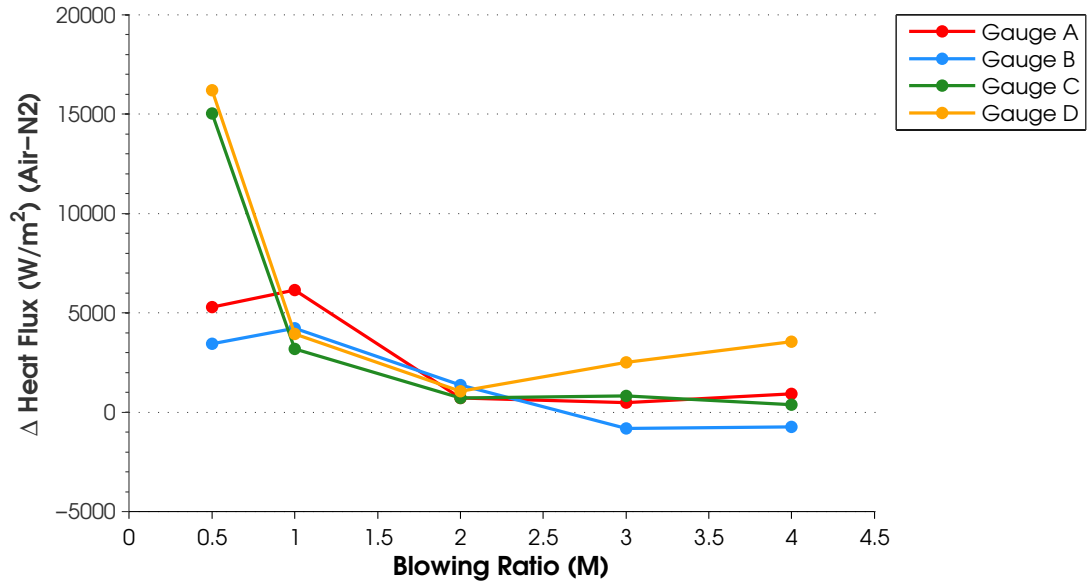


Figure E.41: Gauge heat flux difference, $\Phi = 1.5$, $\dot{m}_{air}=425$ SLPM, US: Slot, Coolant=Air, M =Variable, DS: Fan, Coolant=Air/ N_2 , $M=2$

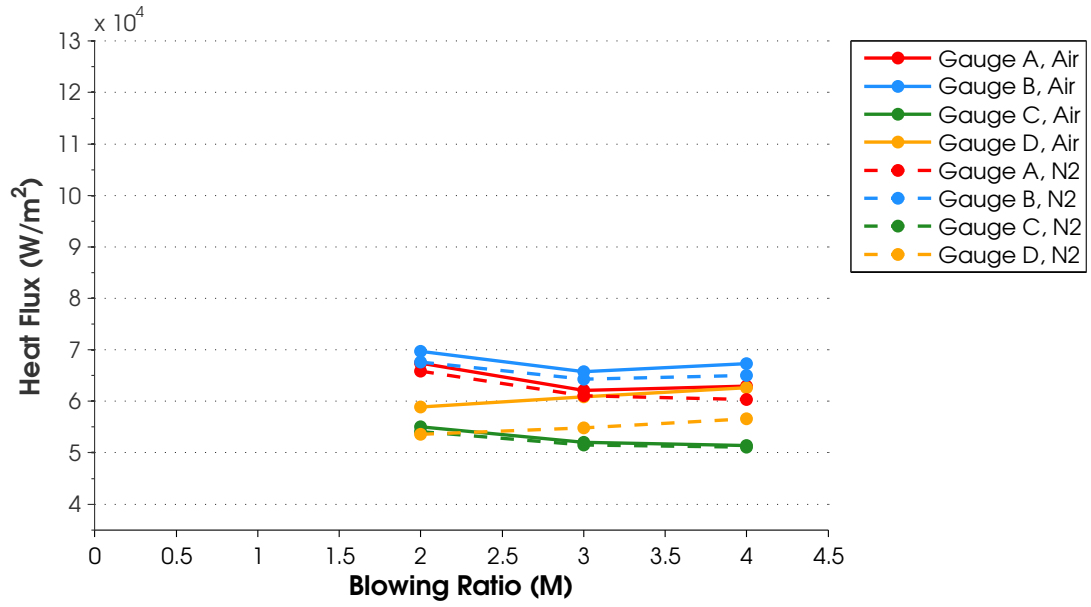


Figure E.42: Gauge heat flux, $\Phi = 1.5$, $\dot{m}_{air}=425$ SLPM, US: Slot, Coolant= N_2 , M =Variable, DS: Fan, Coolant=Air/ N_2 , $M=2$

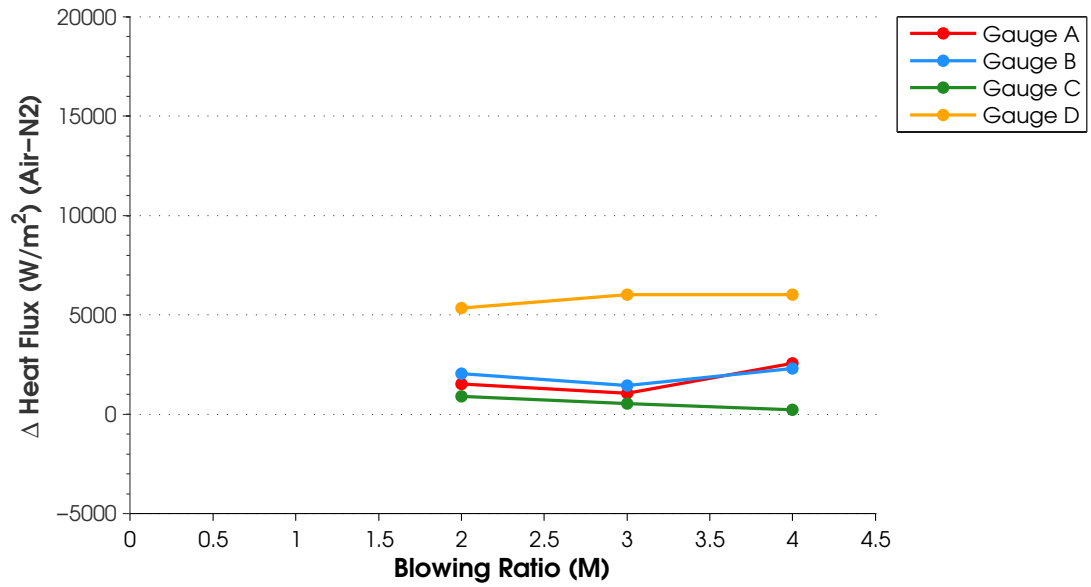


Figure E.43: Gauge heat flux difference, $\Phi = 1.5$, $\dot{m}_{air}=425$ SLPM, US: Slot, Coolant= N_2 , M =Variable, DS: Fan, Coolant=Air/ N_2 , $M=2$

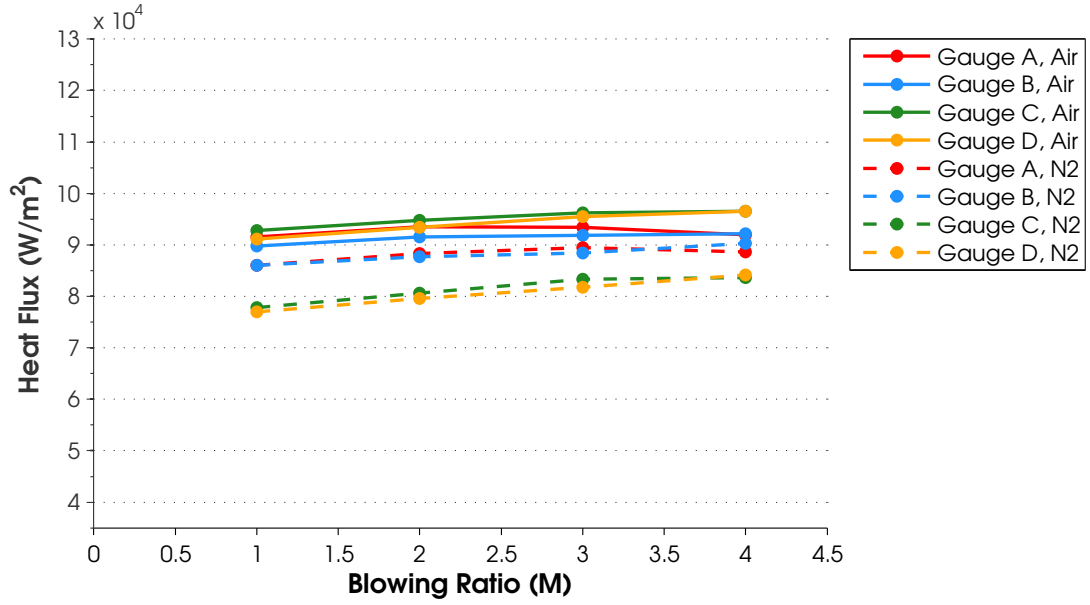


Figure E.44: Gauge heat flux, $\Phi = 1.5$, $\dot{m}_{air}=425$ SLPM, US: Offset Normal, Coolant=Air, M=Variable, DS: Fan, Coolant=Air/N₂, M=2

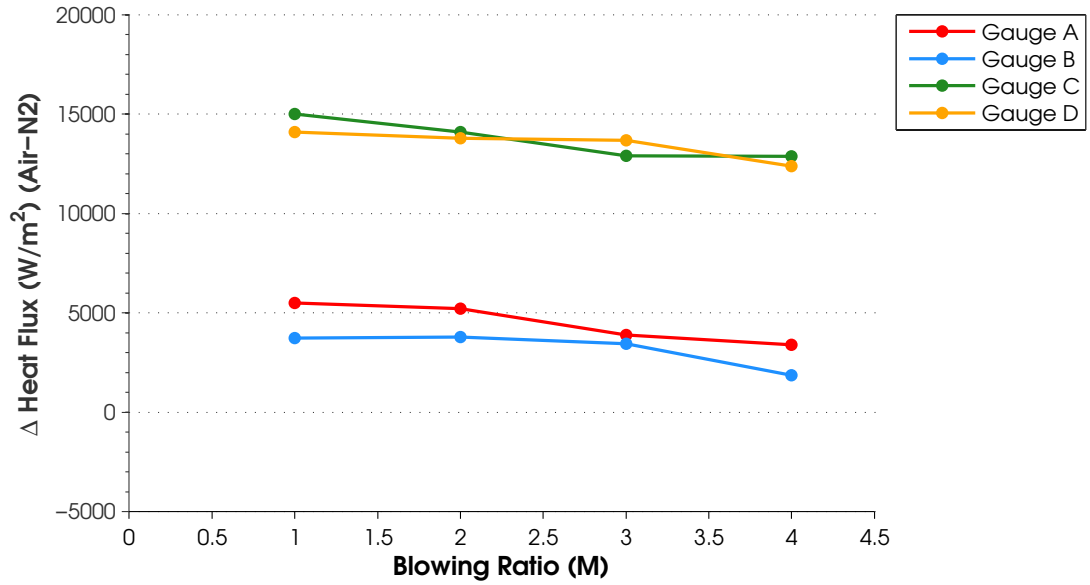


Figure E.45: Gauge heat flux difference, $\Phi = 1.5$, $\dot{m}_{air}=425$ SLPM, US: Offset Normal, Coolant=Air, M=Variable, DS: Fan, Coolant=Air/N₂, M=2

E.3 Heat Transfer Coefficient

E.3.1 $\Phi = 0.6$.

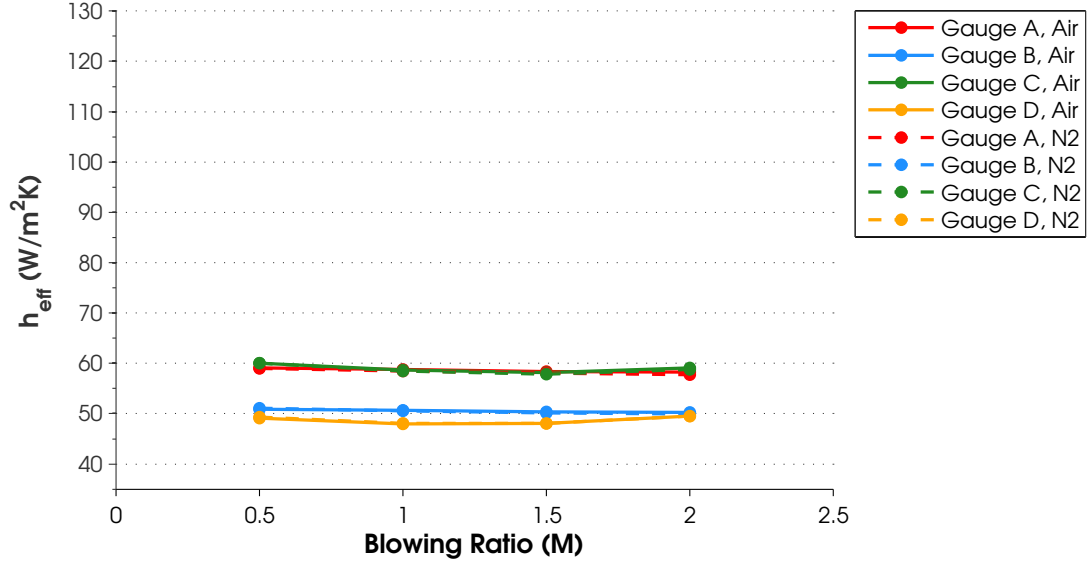


Figure E.46: Gauge heat transfer coefficient, $\Phi = 0.6$, $\dot{m}_{air}=425$ SLPM, US: Blank, Coolant=N/A, M=N/A, DS: Fan, Coolant=Air/N₂, M=Variable

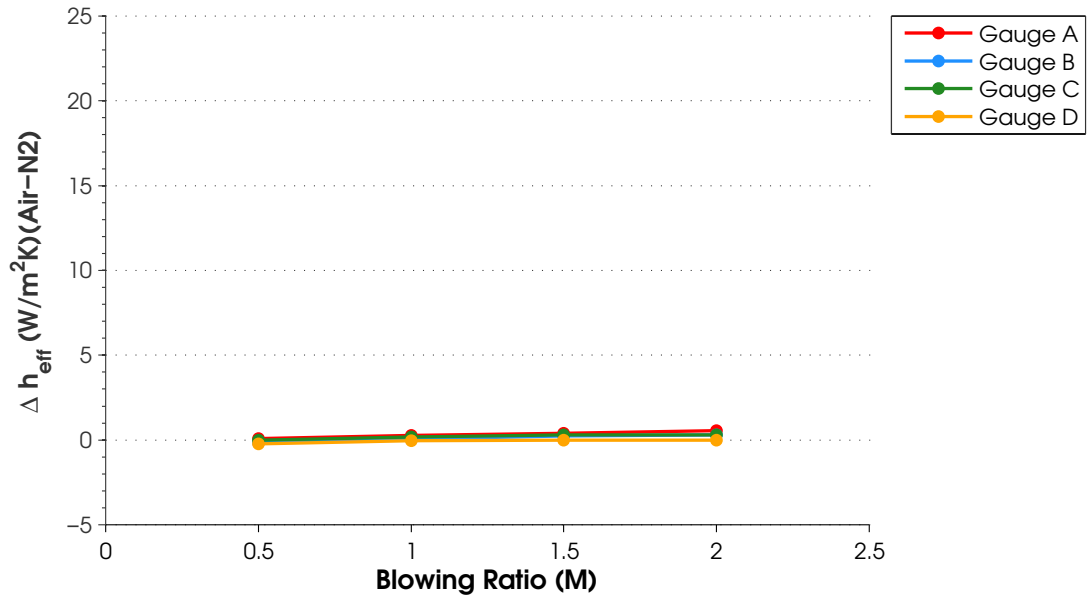


Figure E.47: Gauge heat transfer coefficient difference, $\Phi = 0.6$, $\dot{m}_{air}=425$ SLPM, US: Blank, Coolant=N/A, M=N/A, DS: Fan, Coolant=Air/N₂, M=Variable

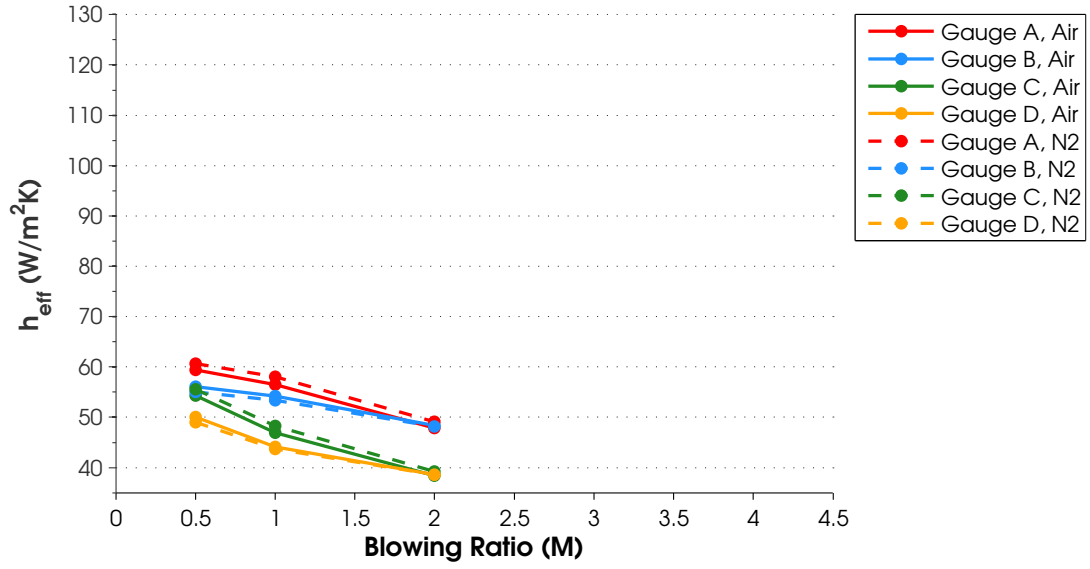


Figure E.48: Gauge heat transfer coefficient, $\Phi = 0.6$, $\dot{m}_{air}=425$ SLPM, US: Slot, Coolant=Air, M=Variable, DS: Fan, Coolant=Air/N₂, M=2

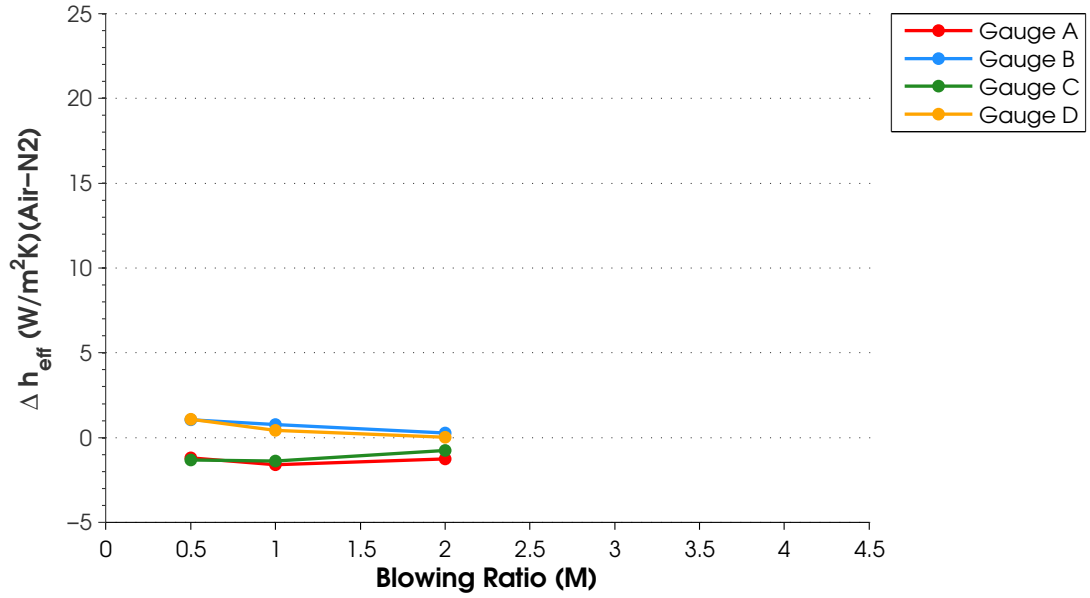


Figure E.49: Gauge heat transfer coefficient difference, $\Phi = 0.6$, $\dot{m}_{air}=425$ SLPM, US: Slot, Coolant=Air, M=Variable, DS: Fan, Coolant=Air/N₂, M=2

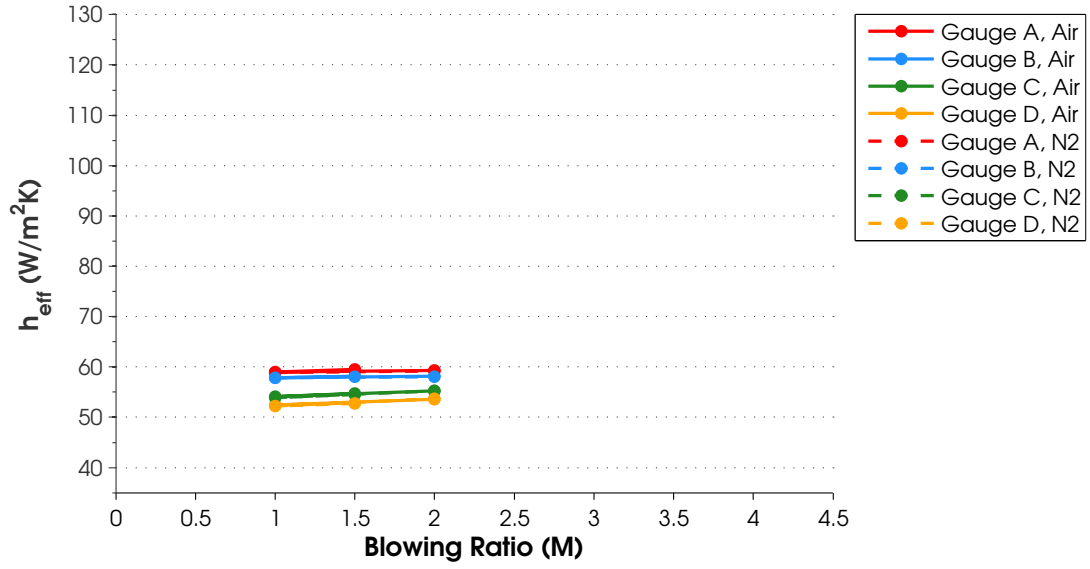


Figure E.50: Gauge heat transfer coefficient, $\Phi = 0.6$, $\dot{m}_{air}=425$ SLPM, US: Offset Normal, Coolant=Air, M=Variable, DS: Fan, Coolant=Air/N₂, M=2

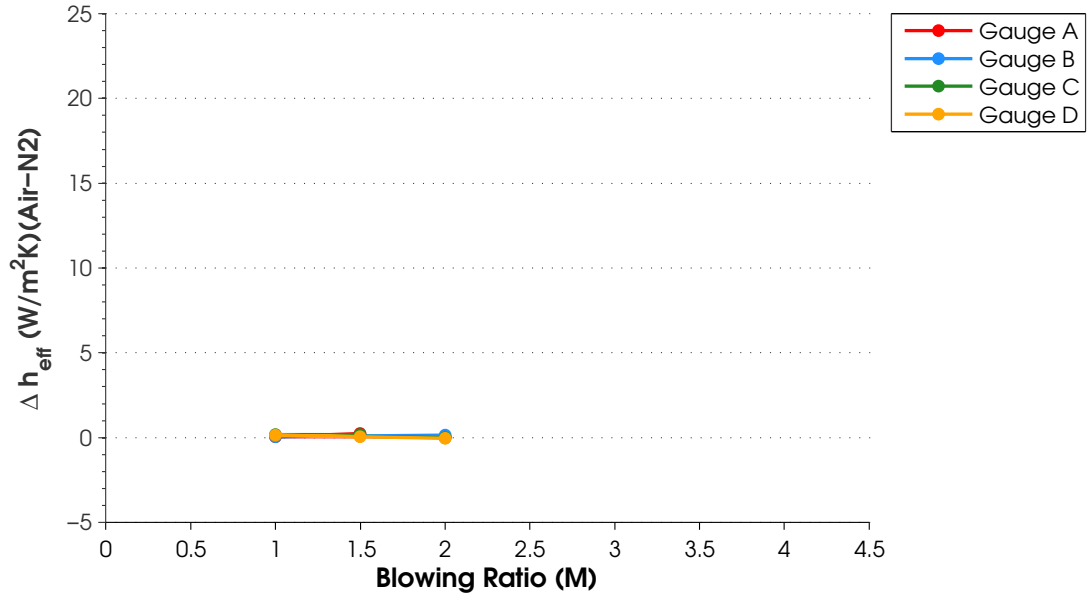


Figure E.51: Gauge heat transfer coefficient difference, $\Phi = 0.6$, $\dot{m}_{air}=425$ SLPM, US: Offset Normal, Coolant=Air, M=Variable, DS: Fan, Coolant=Air/N₂, M=2

E.3.2 Heat Transfer Coefficient, $\Phi = 1.1$.

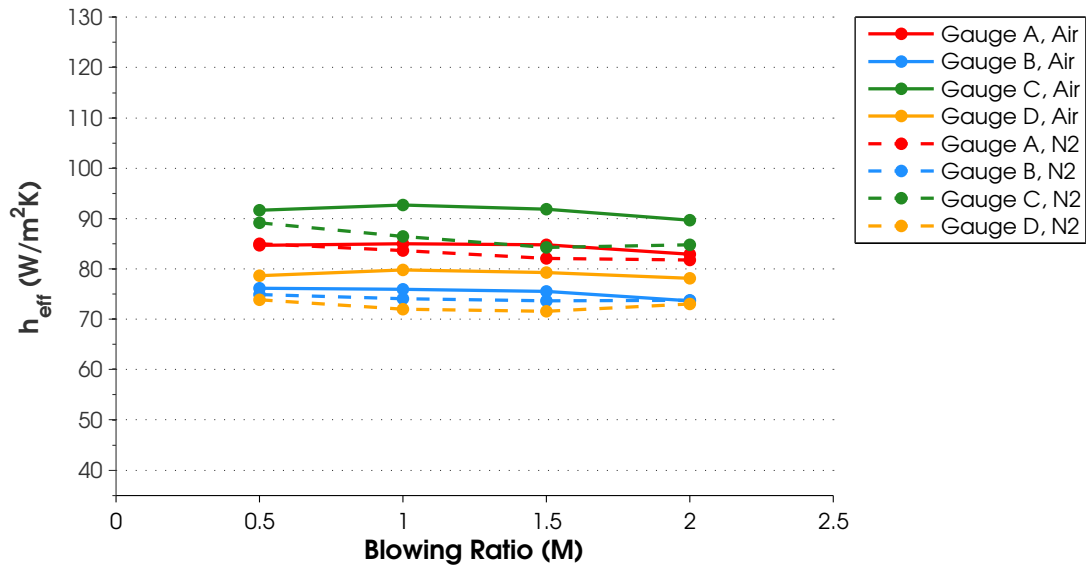


Figure E.52: Gauge heat transfer coefficient, $\Phi = 1.1$, $\dot{m}_{air}=425$ SLPM, US: Blank, Coolant=N/A, M=N/A, DS: Fan, Coolant=Air/N₂, M=Variable

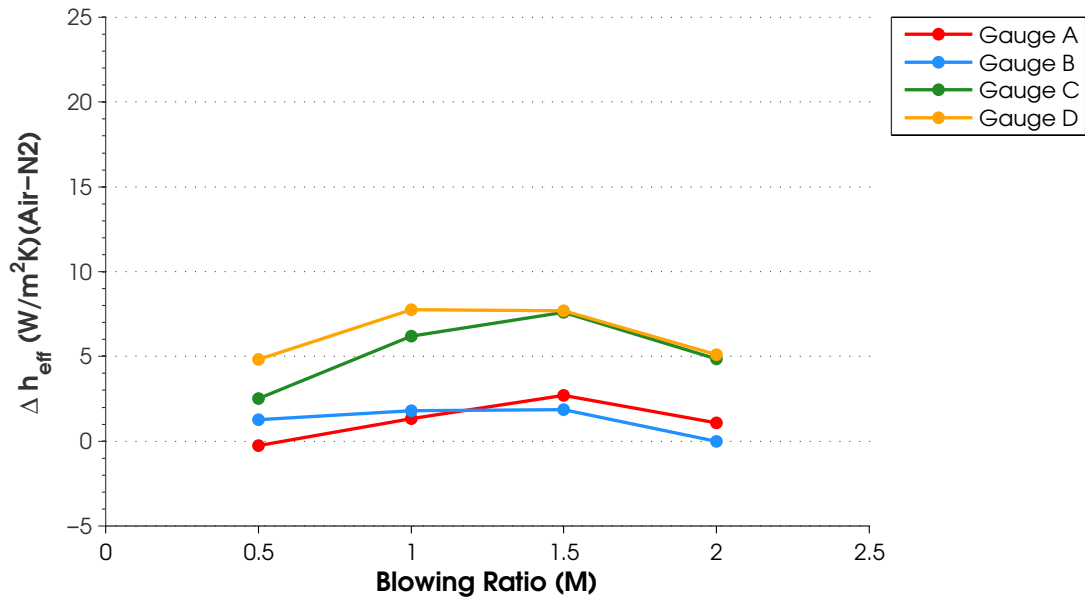


Figure E.53: Gauge heat transfer coefficient difference, $\Phi = 1.1$, $\dot{m}_{air}=425$ SLPM, US: Blank, Coolant=N/A, M=N/A, DS: Fan, Coolant=Air/N₂, M=Variable

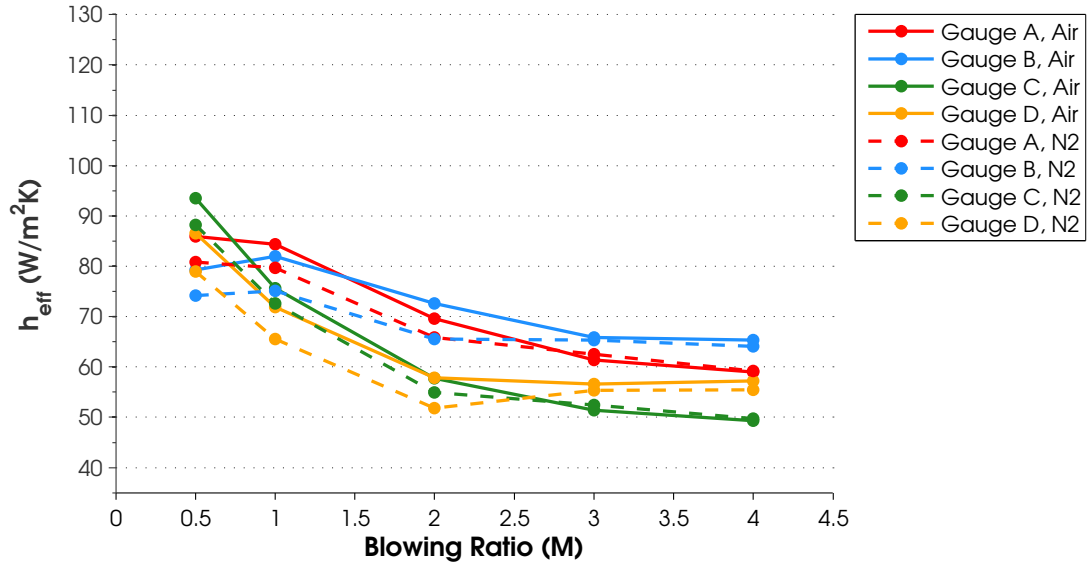


Figure E.54: Gauge heat transfer coefficient, $\Phi = 1.1$, $\dot{m}_{air}=425$ SLPM, US: Slot, Coolant=Air, M=Variable, DS: Fan, Coolant=Air/N₂, M=2

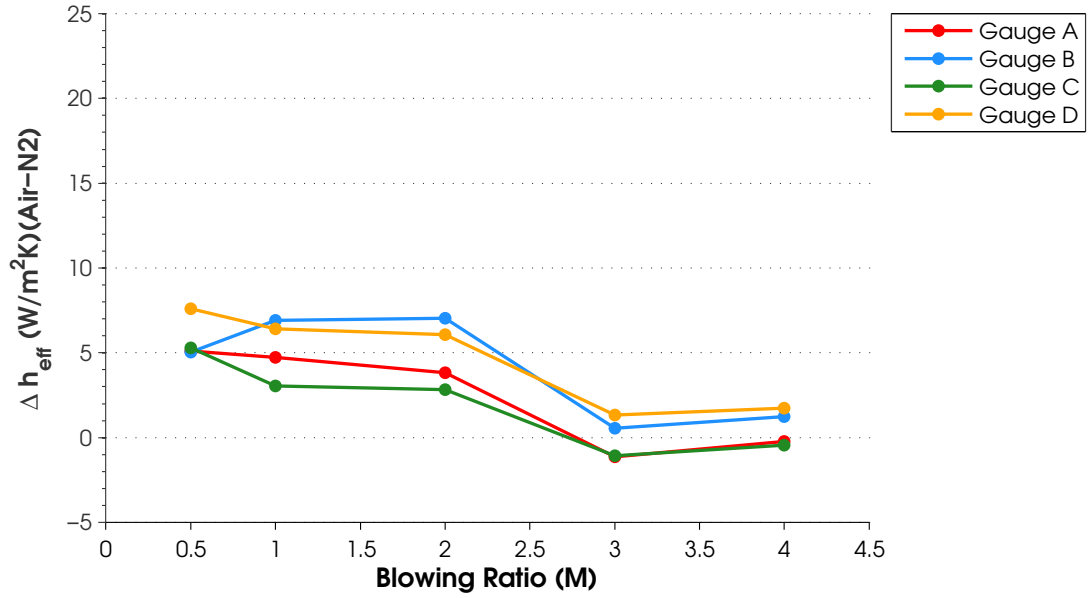


Figure E.55: Gauge heat transfer coefficient difference, $\Phi = 1.1$, $\dot{m}_{air}=425$ SLPM, US: Slot, Coolant=Air, M=Variable, DS: Fan, Coolant=Air/N₂, M=2

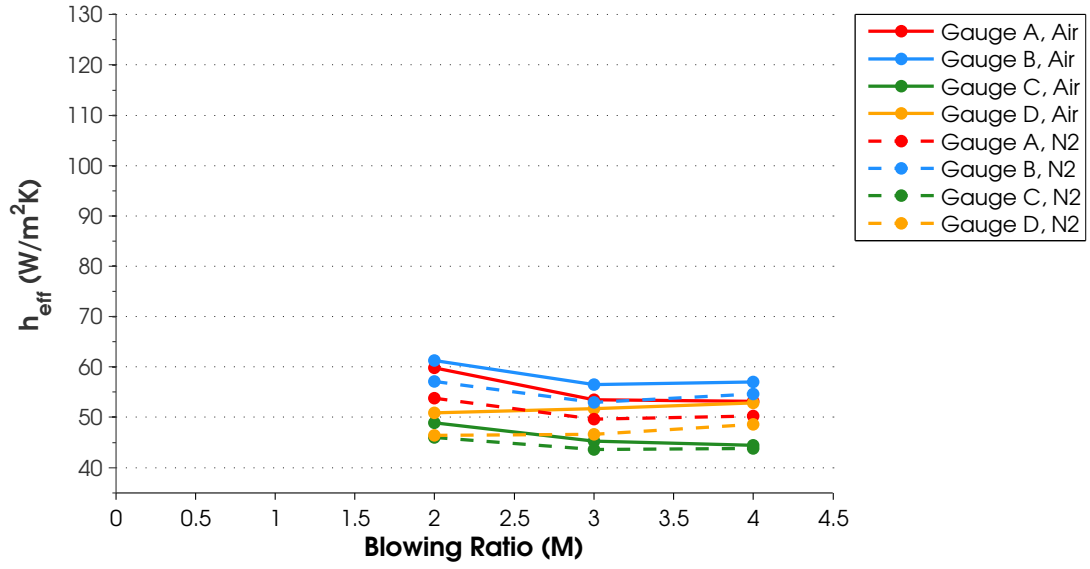


Figure E.56: Gauge heat transfer coefficient, $\Phi = 1.1$, $\dot{m}_{air}=425$ SLPM, US: Slot, Coolant= N_2 , M=Variable, DS: Fan, Coolant=Air/ N_2 , M=2

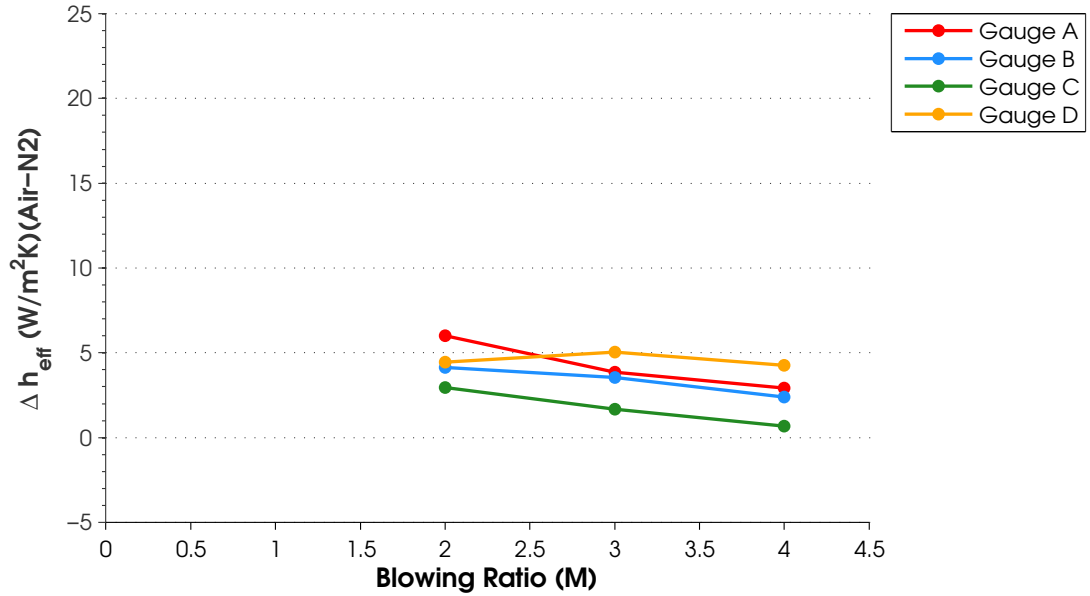


Figure E.57: Gauge heat transfer coefficient difference, $\Phi = 1.1$, $\dot{m}_{air}=425$ SLPM, US: Slot, Coolant= N_2 , M=Variable, DS: Fan, Coolant=Air/ N_2 , M=2

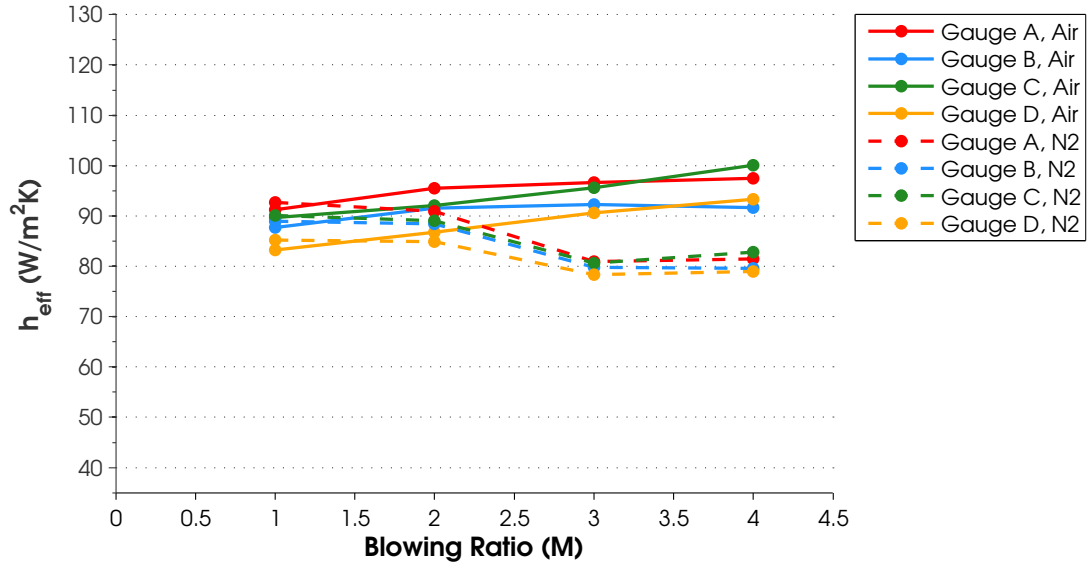


Figure E.58: Gauge heat transfer coefficient, $\Phi = 1.1$, $\dot{m}_{\text{air}}=425$ SLPM, US: Offset Normal, Coolant=Air, M=Variable, DS: Fan, Coolant=Air/N₂, M=2

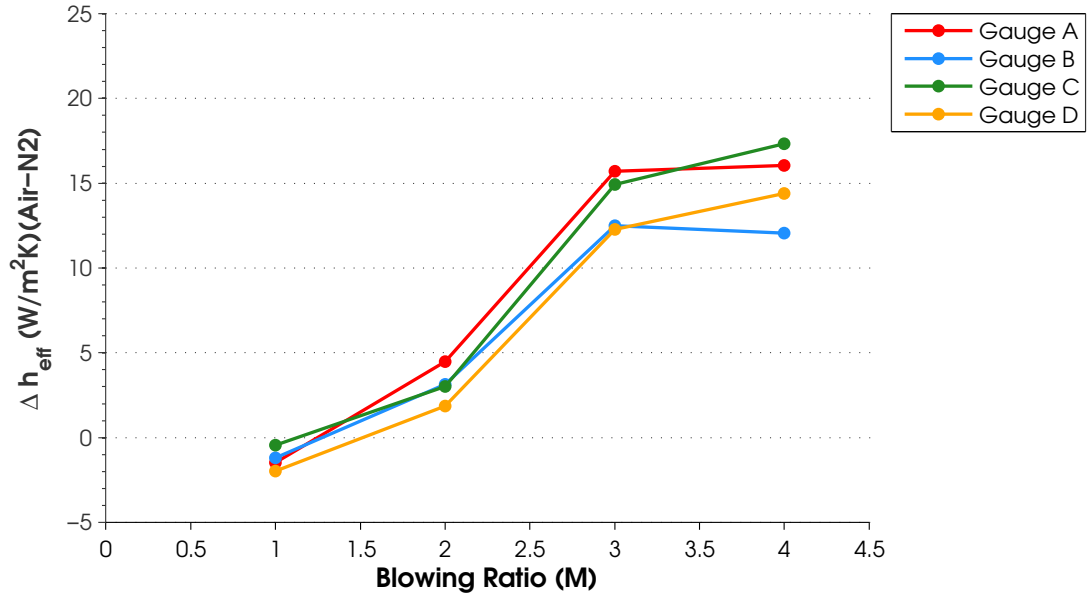


Figure E.59: Gauge heat transfer coefficient difference, $\Phi = 1.1$, $\dot{m}_{\text{air}}=425$ SLPM, US: Offset Normal, Coolant=Air, M=Variable, DS: Fan, Coolant=Air/N₂, M=2

E.3.3 Heat Transfer Coefficient, $\Phi = 1.3$.

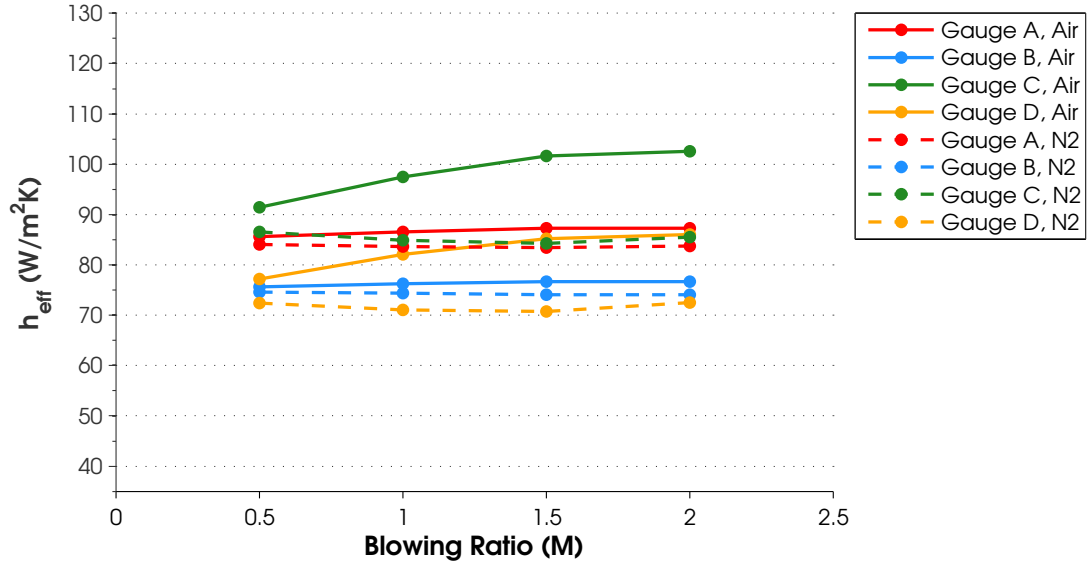


Figure E.60: Gauge heat transfer coefficient, $\Phi = 1.3$, $\dot{m}_{air}=425$ SLPM, US: Blank, Coolant=N/A, M=N/A, DS: Fan, Coolant=Air/N₂, M=Variable

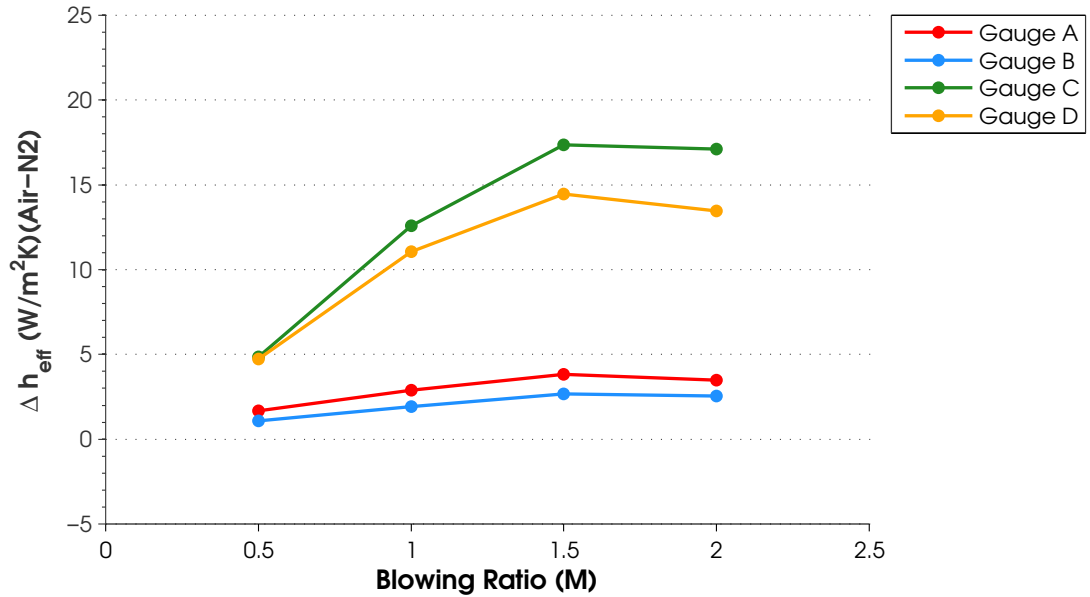


Figure E.61: Gauge heat transfer coefficient difference, $\Phi = 1.3$, $\dot{m}_{air}=425$ SLPM, US: Blank, Coolant=N/A, M=N/A, DS: Fan, Coolant=Air/N₂, M=Variable

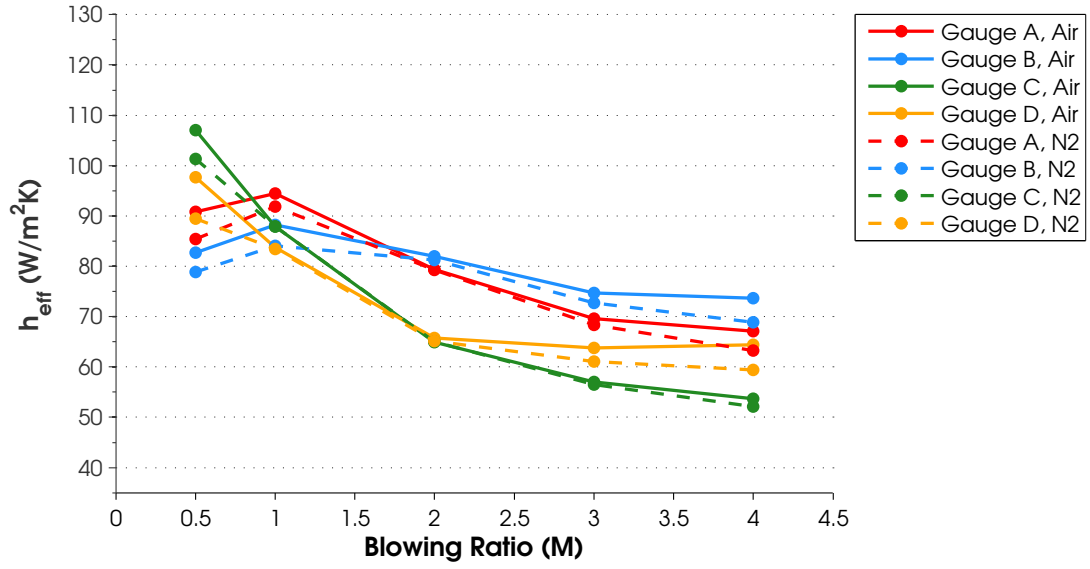


Figure E.62: Gauge heat transfer coefficient, $\Phi = 1.3$, $\dot{m}_{air}=425$ SLPM, US: Slot, Coolant=Air, M=Variable, DS: Fan, Coolant=Air/N₂, M=2

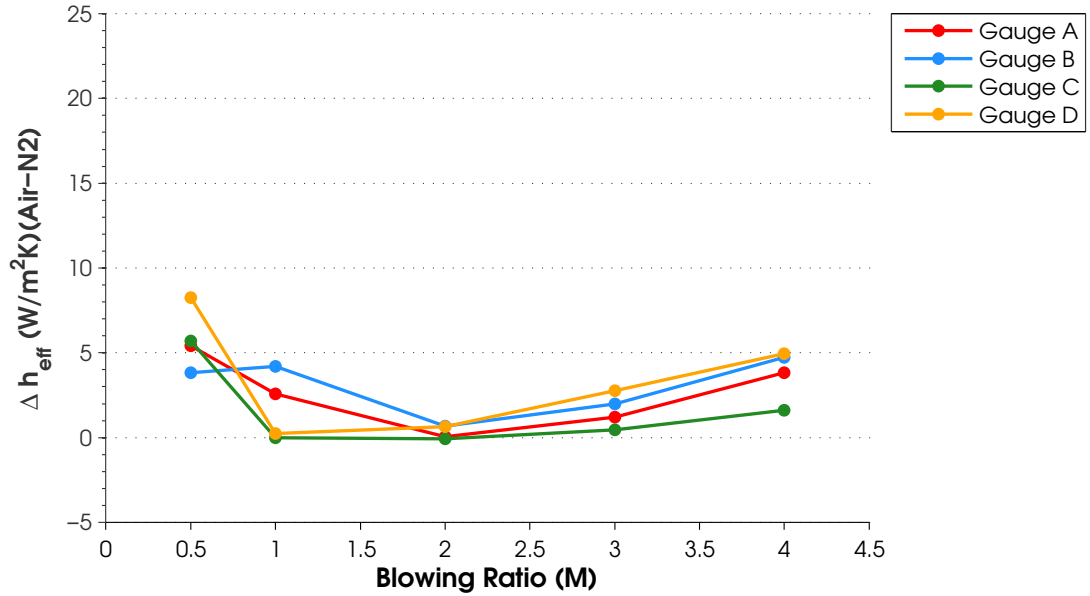


Figure E.63: Gauge heat transfer coefficient difference, $\Phi = 1.3$, $\dot{m}_{air}=425$ SLPM, US: Slot, Coolant=Air, M=Variable, DS: Fan, Coolant=Air/N₂, M=2

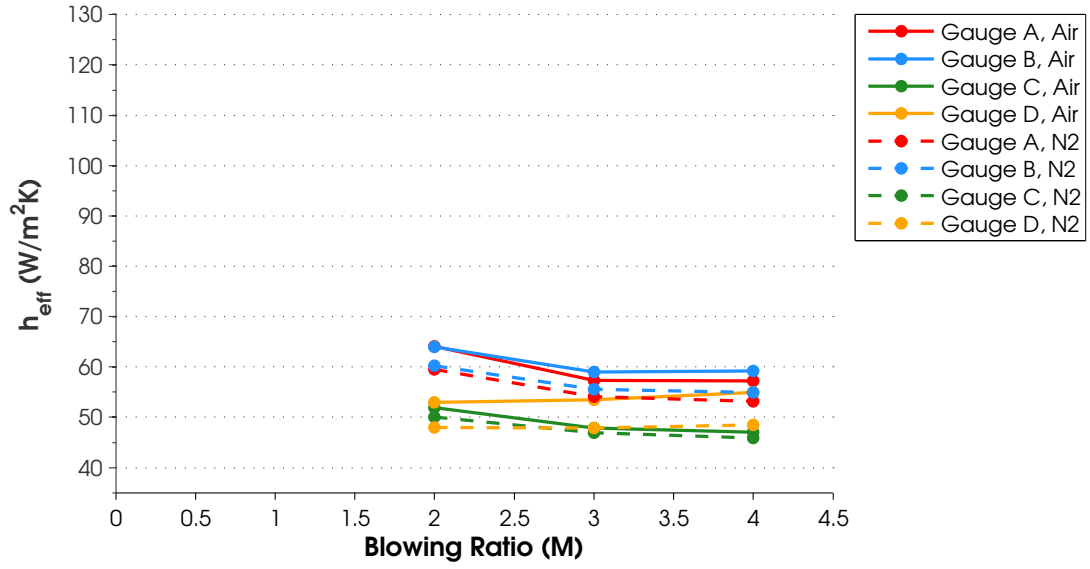


Figure E.64: Gauge heat transfer coefficient, $\Phi = 1.3$, $\dot{m}_{air}=425$ SLPM, US: Slot, Coolant= N_2 , M=Variable, DS: Fan, Coolant=Air/ N_2 , M=2

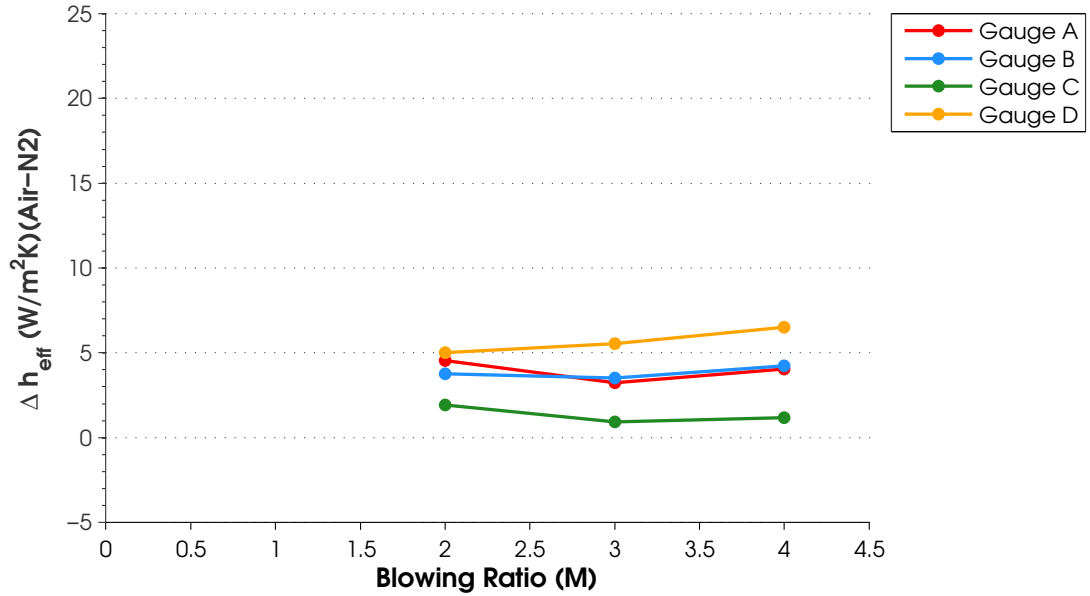


Figure E.65: Gauge heat transfer coefficient difference, $\Phi = 1.3$, $\dot{m}_{air}=425$ SLPM, US: Slot, Coolant= N_2 , M=Variable, DS: Fan, Coolant=Air/ N_2 , M=2

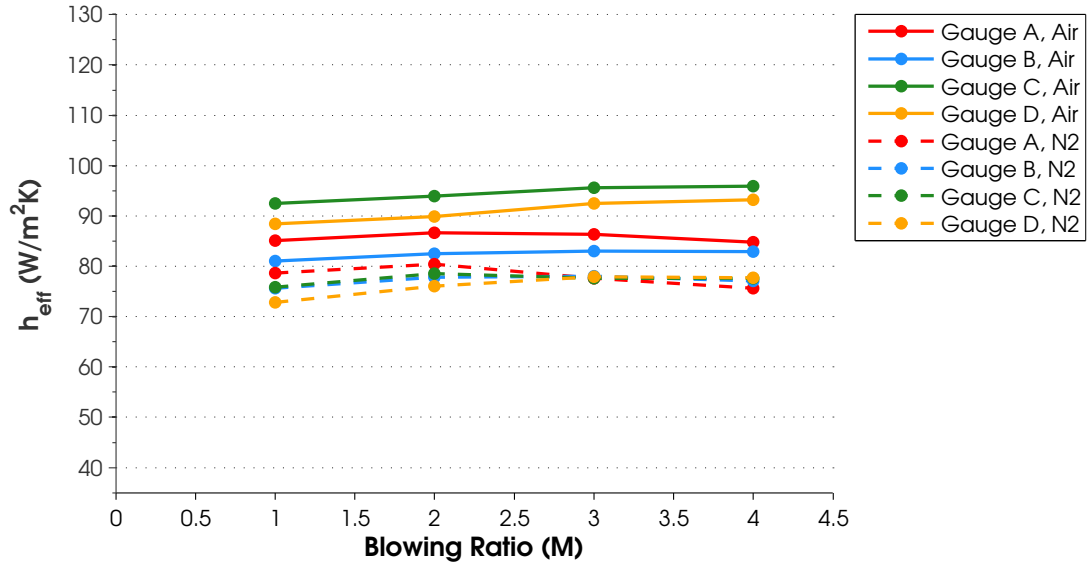


Figure E.66: Gauge heat transfer coefficient, $\Phi = 1.3$, $\dot{m}_{\text{air}}=425$ SLPM, US: Offset Normal, Coolant=Air, M=Variable, DS: Fan, Coolant=Air/N₂, M=2

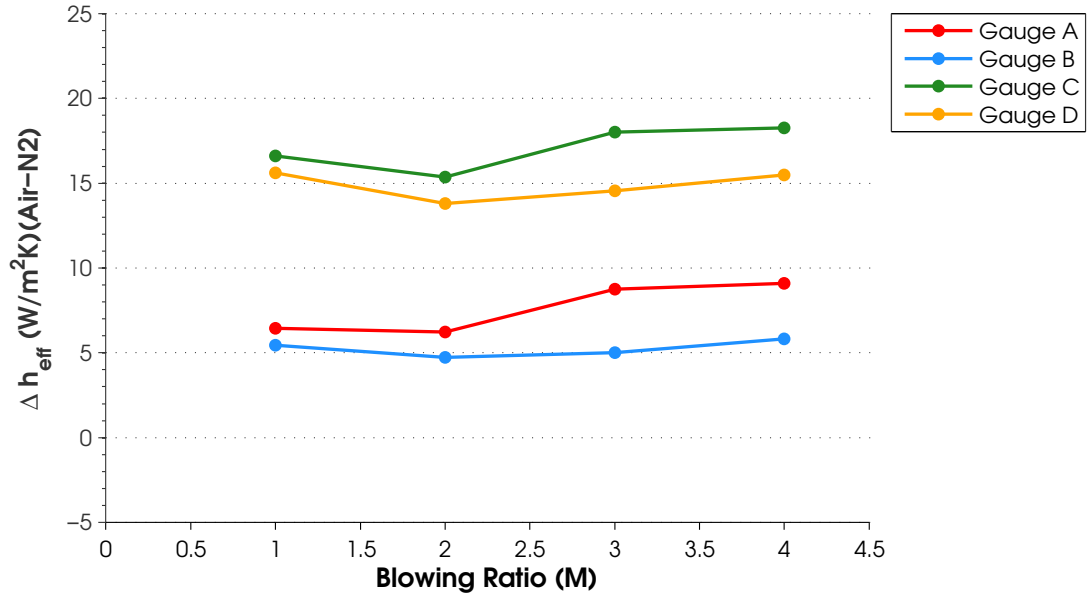


Figure E.67: Gauge heat transfer coefficient difference, $\Phi = 1.3$, $\dot{m}_{\text{air}}=425$ SLPM, US: Offset Normal, Coolant=Air, M=Variable, DS: Fan, Coolant=Air/N₂, M=2

E.3.4 Heat Transfer Coefficient, $\Phi = 1.5$.

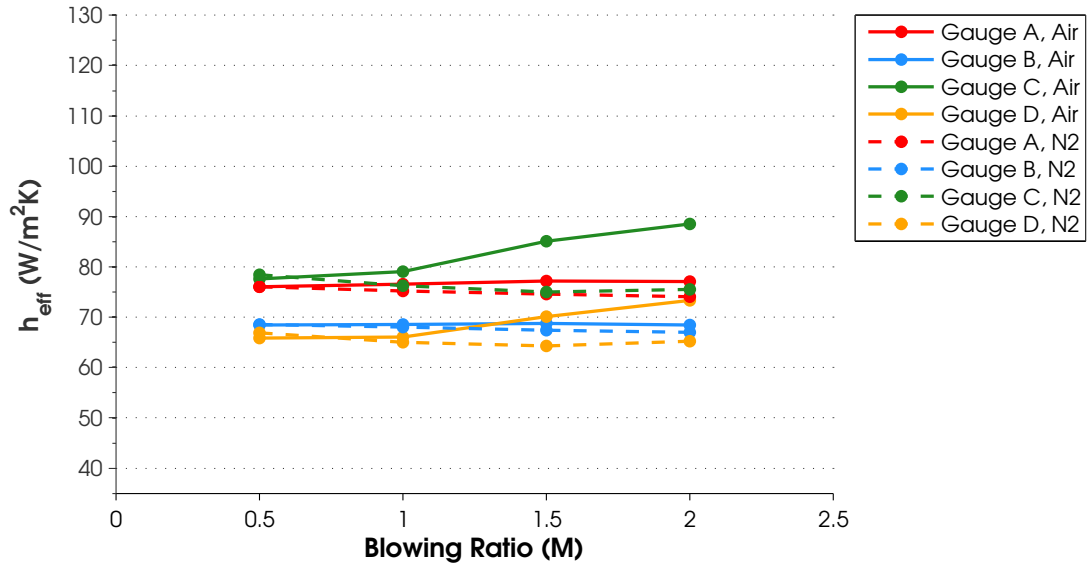


Figure E.68: Gauge heat transfer coefficient, $\Phi = 1.5$, $\dot{m}_{air}=425$ SLPM, US: Blank, Coolant=N/A, M=N/A, DS: Fan, Coolant=Air/N₂, M=Variable

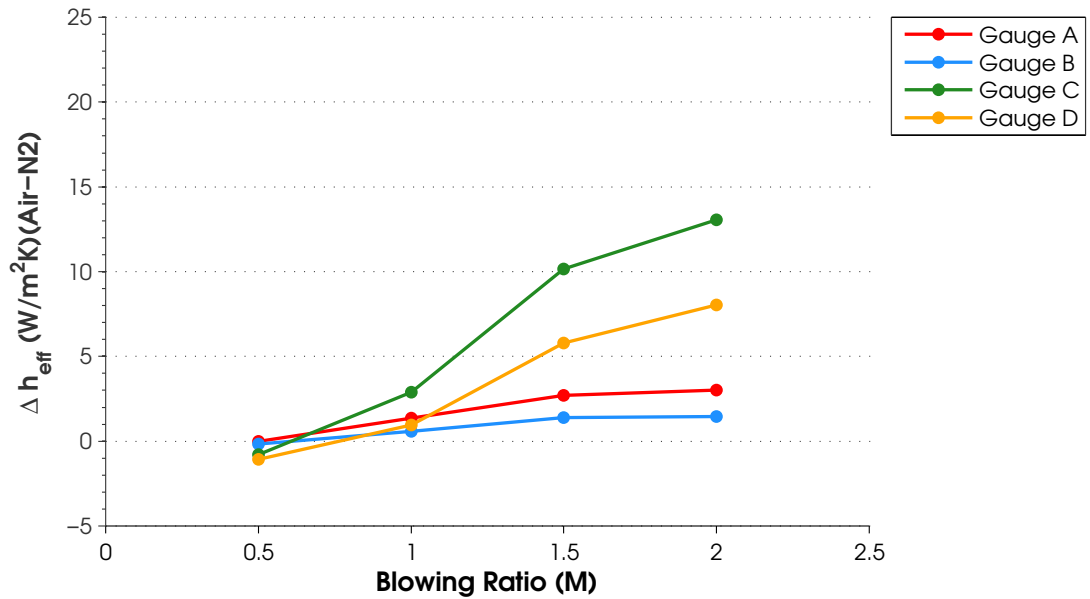


Figure E.69: Gauge heat transfer coefficient difference, $\Phi = 1.5$, $\dot{m}_{air}=425$ SLPM, US: Blank, Coolant=N/A, M=N/A, DS: Fan, Coolant=Air/N₂, M=Variable

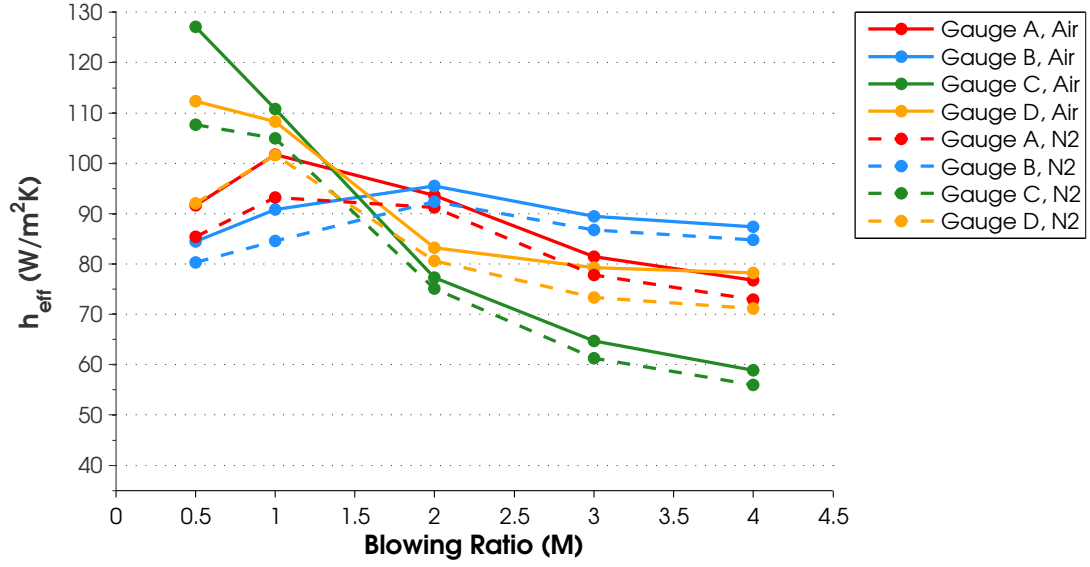


Figure E.70: Gauge heat transfer coefficient, $\Phi = 1.5$, $\dot{m}_{air}=425$ SLPM, US: Slot, Coolant=Air, M=Variable, DS: Fan, Coolant=Air/N₂, M=2

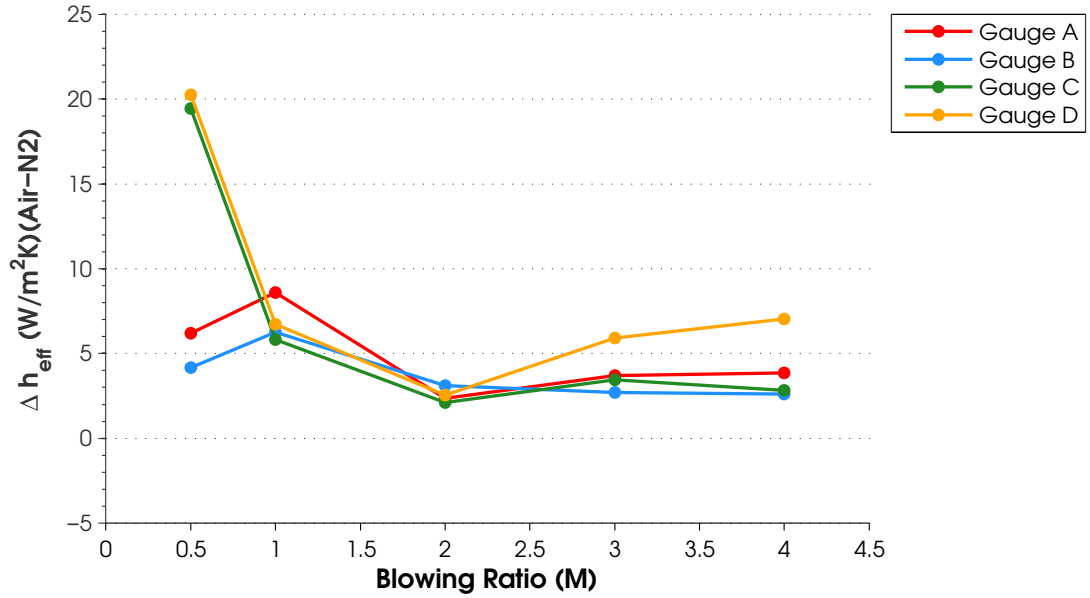


Figure E.71: Gauge heat transfer coefficient difference, $\Phi = 1.5$, $\dot{m}_{air}=425$ SLPM, US: Slot, Coolant=Air, M=Variable, DS: Fan, Coolant=Air/N₂, M=2

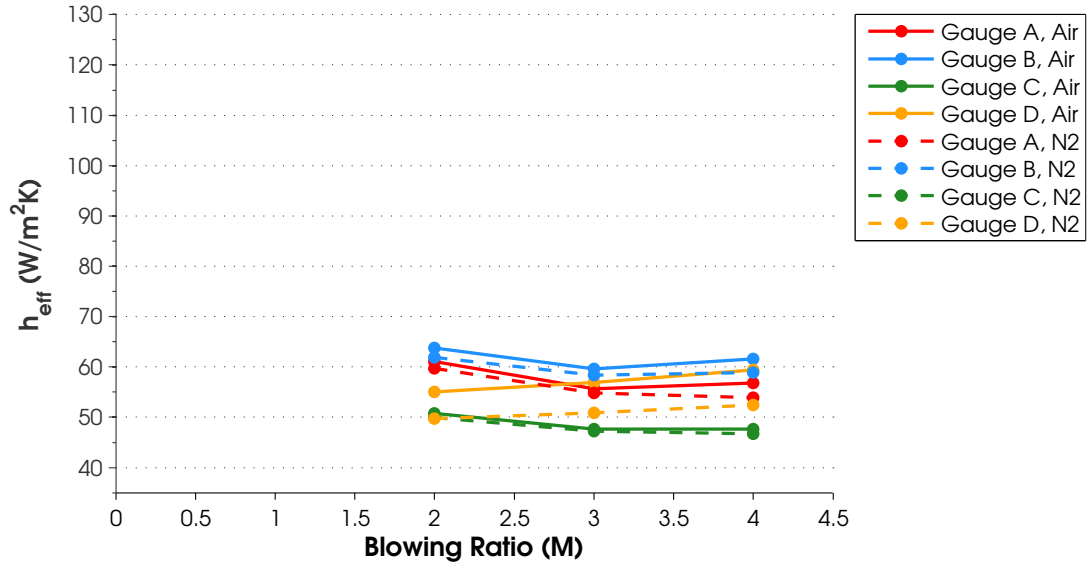


Figure E.72: Gauge heat transfer coefficient, $\Phi = 1.5$, $\dot{m}_{air}=425$ SLPM, US: Slot, Coolant= N_2 , M=Variable, DS: Fan, Coolant=Air/ N_2 , M=2

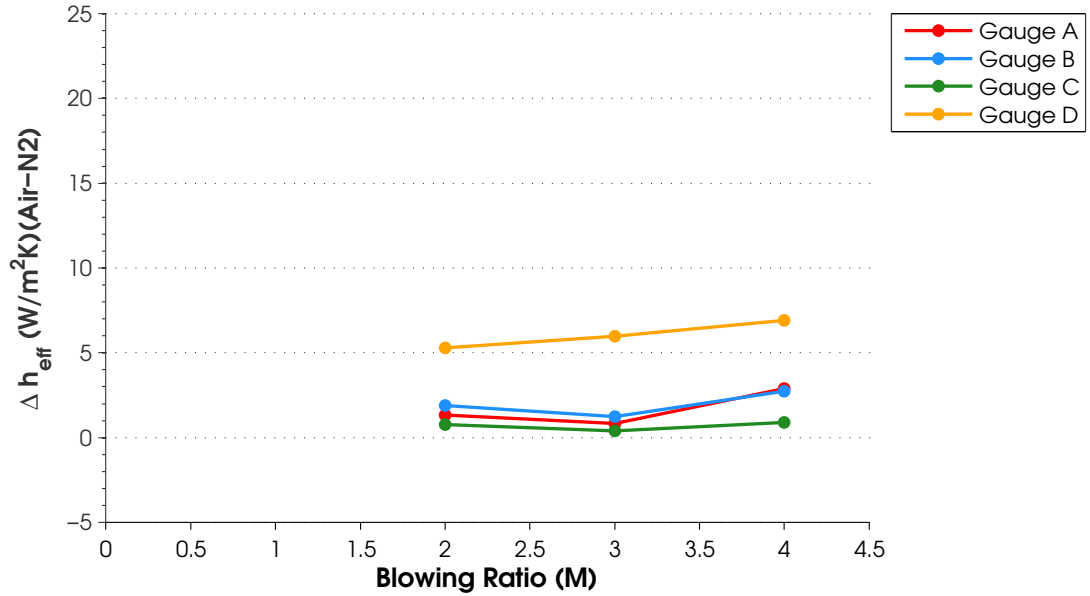


Figure E.73: Gauge heat transfer coefficient difference, $\Phi = 1.5$, $\dot{m}_{air}=425$ SLPM, US: Slot, Coolant= N_2 , M=Variable, DS: Fan, Coolant=Air/ N_2 , M=2

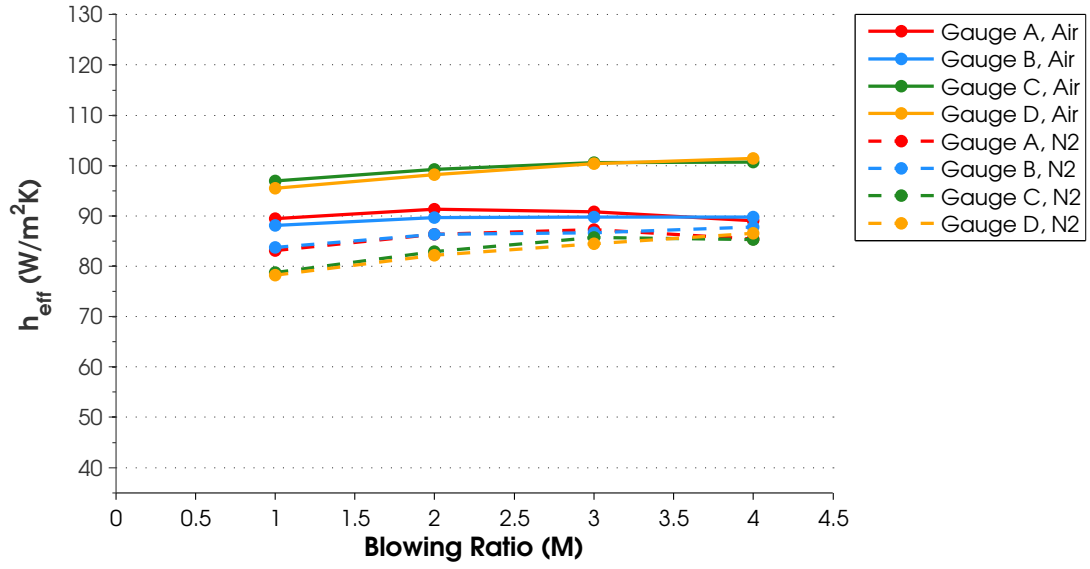


Figure E.74: Gauge heat transfer coefficient, $\Phi = 1.5$, $\dot{m}_{\text{air}}=425$ SLPM, US: Offset Normal, Coolant=Air, M=Variable, DS: Fan, Coolant=Air/N₂, M=2

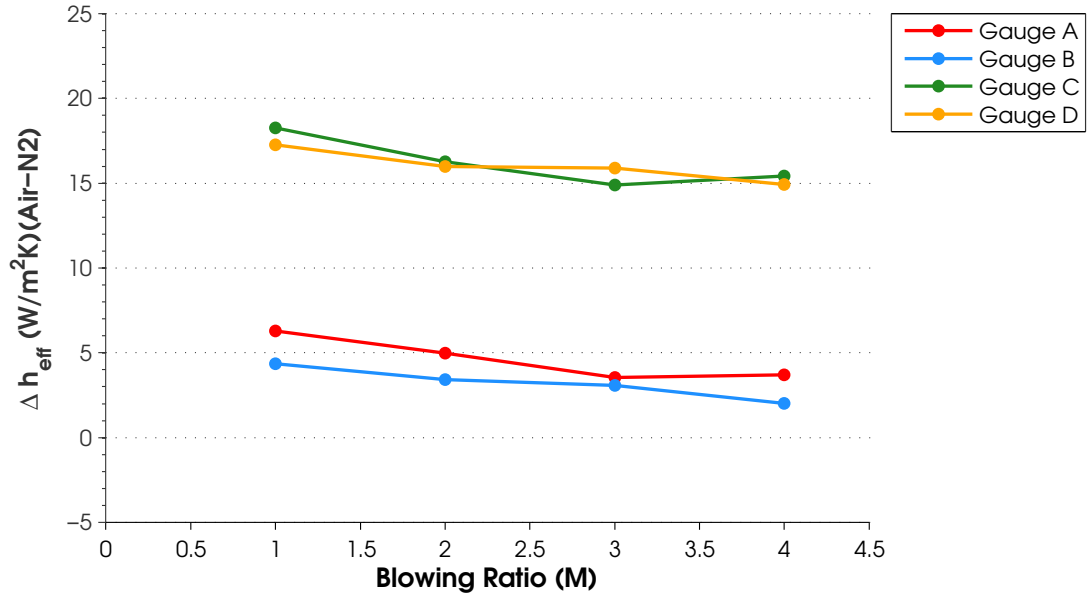


Figure E.75: Gauge heat transfer coefficient difference, $\Phi = 1.5$, $\dot{m}_{\text{air}}=425$ SLPM, US: Offset Normal, Coolant=Air, M=Variable, DS: Fan, Coolant=Air/N₂, M=2

E.4 Comparison Plots

E.4.1 $\Phi = 0.6$.

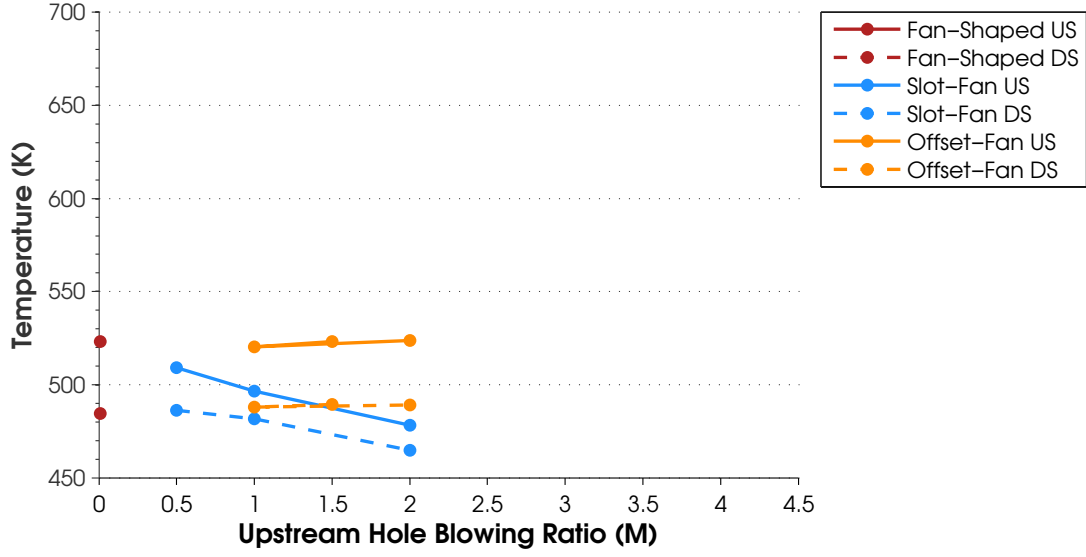


Figure E.76: Gauge surface temperature comparison, $\Phi = 0.6$, $\dot{m}_{air}=425$ SLPM, US: Blank/Slot/Offset, Coolant=Air, M=Variable, DS: Fan, Coolant=Air, M=2

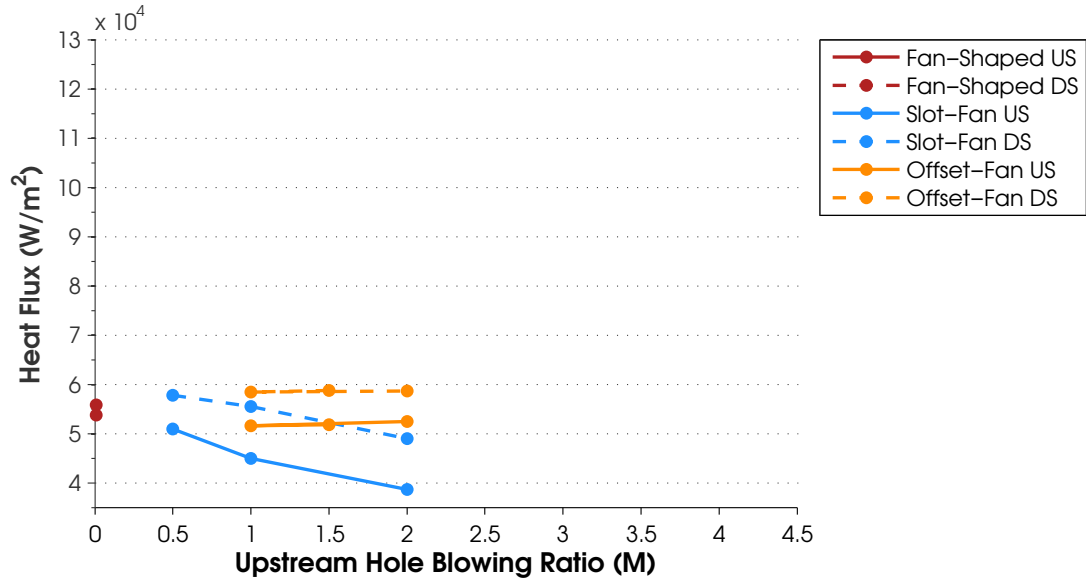


Figure E.77: Heat flux comparison, $\Phi = 0.6$, $\dot{m}_{air}=425$ SLPM, US: Blank/Slot/Offset, Coolant=Air, M=Variable, DS: Fan, Coolant=Air, M=2

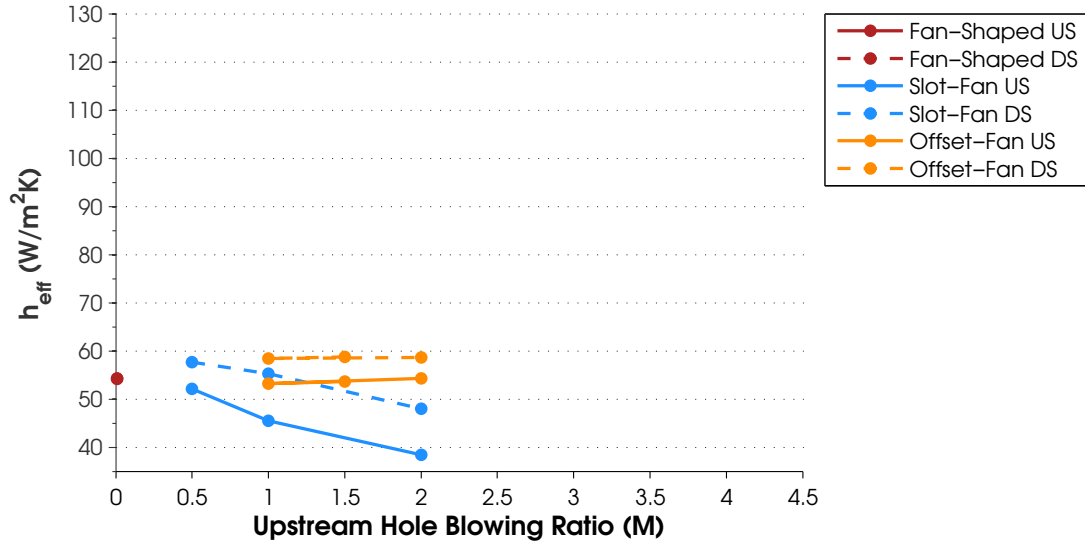


Figure E.78: Gauge heat transfer coefficient comparison, $\Phi = 0.6$, $\dot{m}_{air}=425$ SLPM, US: Blank/Slot/Offset, Coolant=Air, M=Variable, DS: Fan, Coolant=Air, M=2

E.4.2 Comparison Plots, $\Phi = 1.1$.

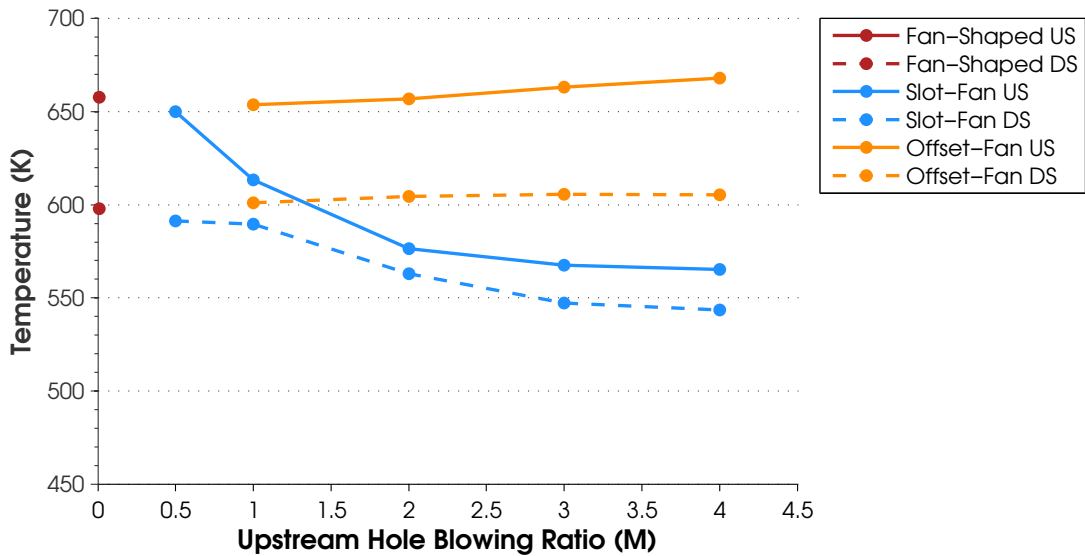


Figure E.79: Gauge surface temperature comparison, $\Phi = 1.1$, $\dot{m}_{air}=425$ SLPM, US: Blank/Slot/Offset, Coolant=Air, M=Variable, DS: Fan, Coolant=Air, M=2

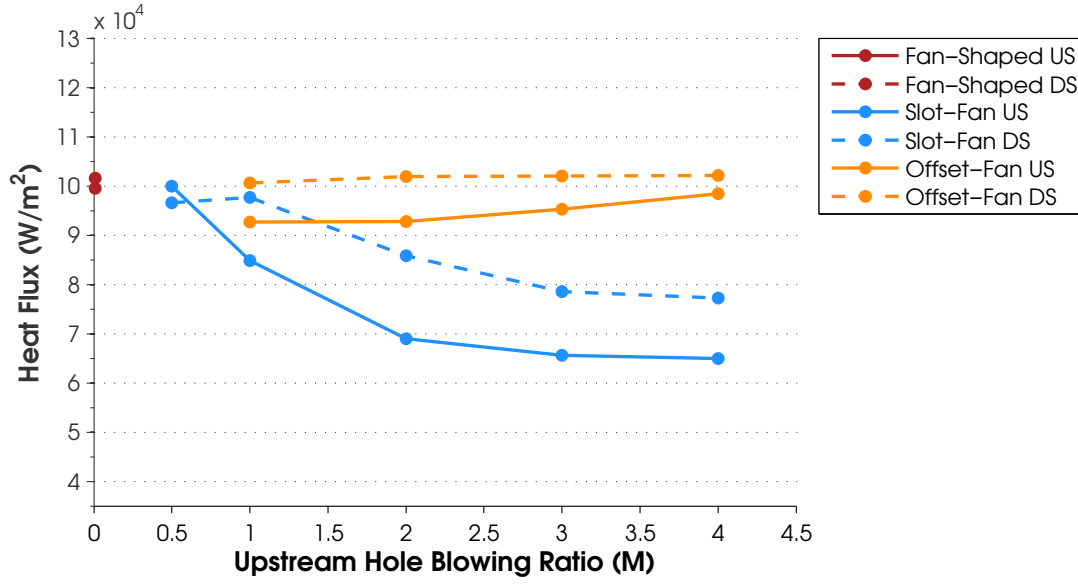


Figure E.80: Heat flux comparison, $\Phi = 1.1$, $\dot{m}_{air}=425$ SLPM, US: Blank/Slot/Offset, Coolant=Air, M=Variable, DS: Fan, Coolant=Air, M=2

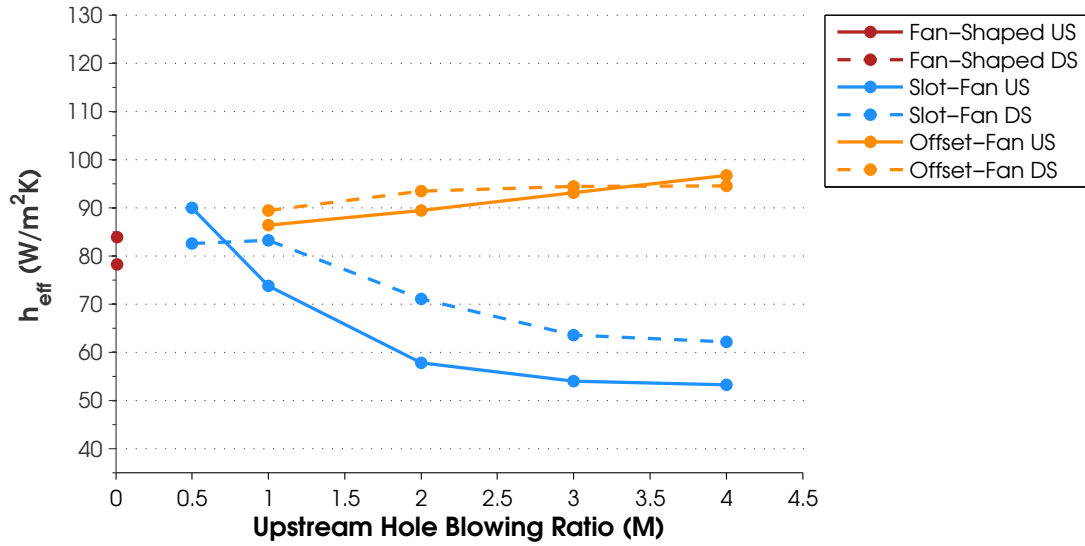


Figure E.81: Gauge heat transfer coefficient comparison, $\Phi = 1.1$, $\dot{m}_{air}=425$ SLPM, US: Blank/Slot/Offset, Coolant=Air, M=Variable, DS: Fan, Coolant=Air, M=2

E.4.3 Comparison Plots, $\Phi = 1.3$.

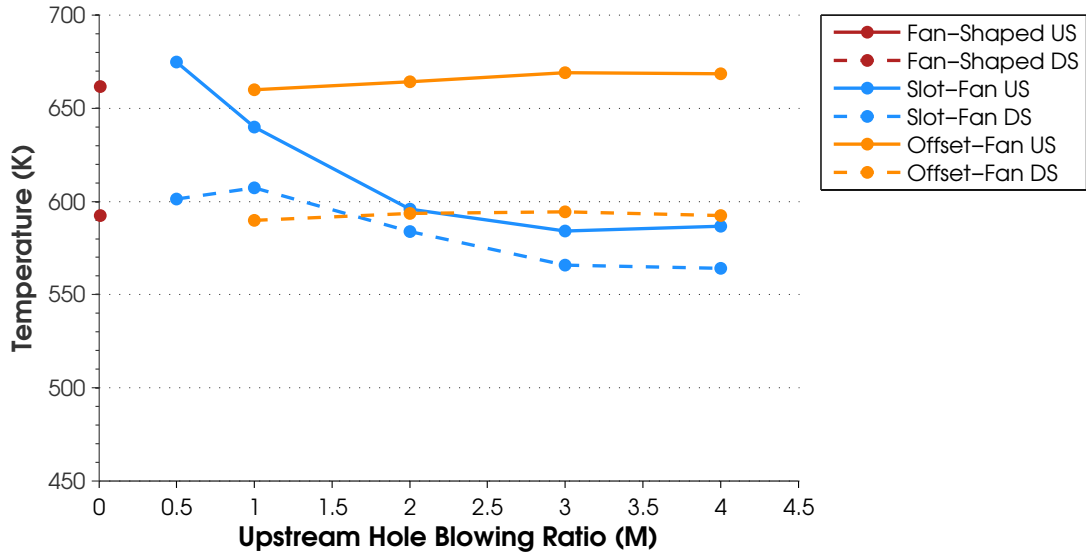


Figure E.82: Gauge surface temperature comparison, $\Phi = 1.3$, $\dot{m}_{air}=425$ SLPM, US: Blank/Slot/Offset, Coolant=Air, M=Variable, DS: Fan, Coolant=Air, M=2

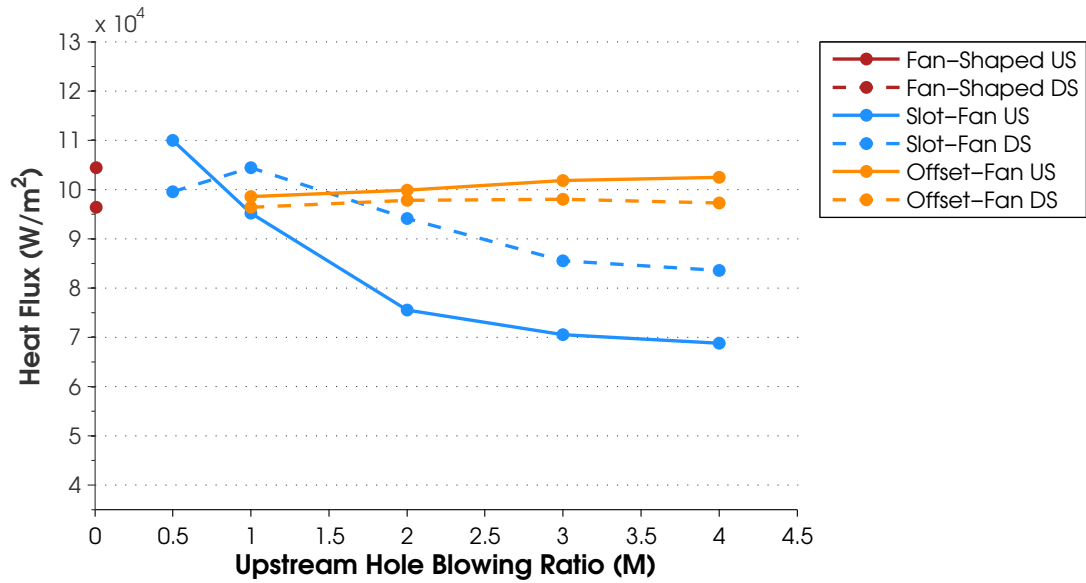


Figure E.83: Heat flux comparison, $\Phi = 1.3$, $\dot{m}_{air}=425$ SLPM, US: Blank/Slot/Offset, Coolant=Air, M=Variable, DS: Fan, Coolant=Air, M=2

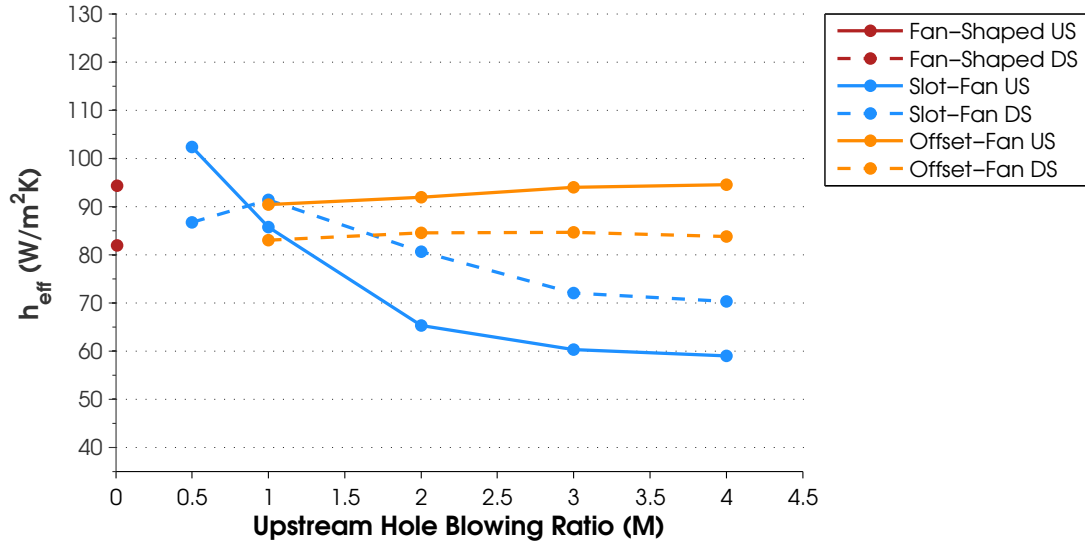


Figure E.84: Gauge heat transfer coefficient comparison, $\Phi = 1.3$, $\dot{m}_{air}=425$ SLPM, US: Blank/Slot/Offset, Coolant=Air, M=Variable, DS: Fan, Coolant=Air, M=2

E.4.4 Comparison Plots, $\Phi = 1.5$.

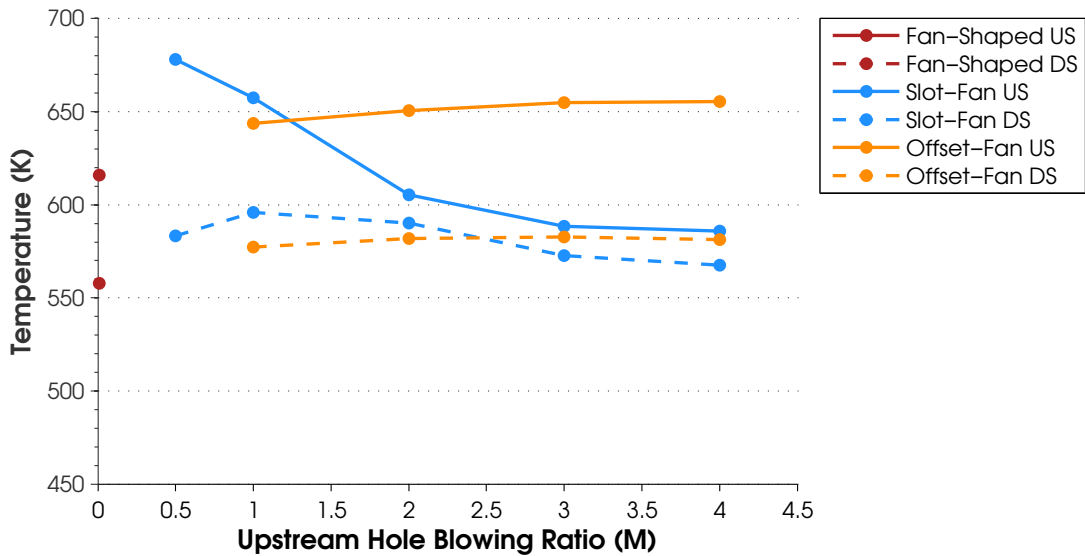


Figure E.85: Gauge surface temperature comparison, $\Phi = 1.5$, $\dot{m}_{air}=425$ SLPM, US: Blank/Slot/Offset, Coolant=Air, M=Variable, DS: Fan, Coolant=Air, M=2

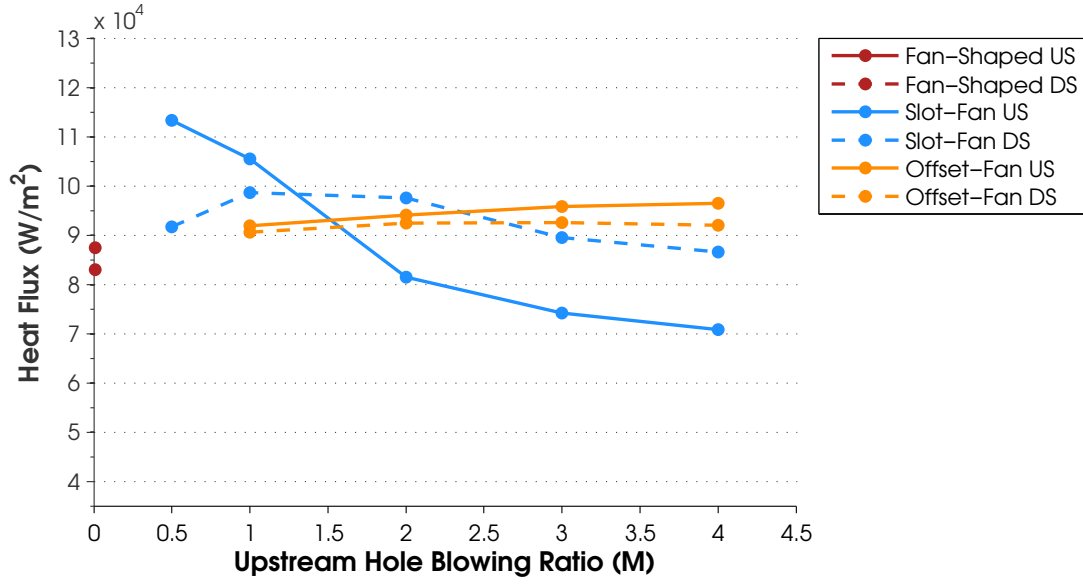


Figure E.86: Heat flux comparison, $\Phi = 1.5$, $\dot{m}_{air}=425$ SLPM, US: Blank/Slot/Offset, Coolant=Air, M=Variable, DS: Fan, Coolant=Air, M=2

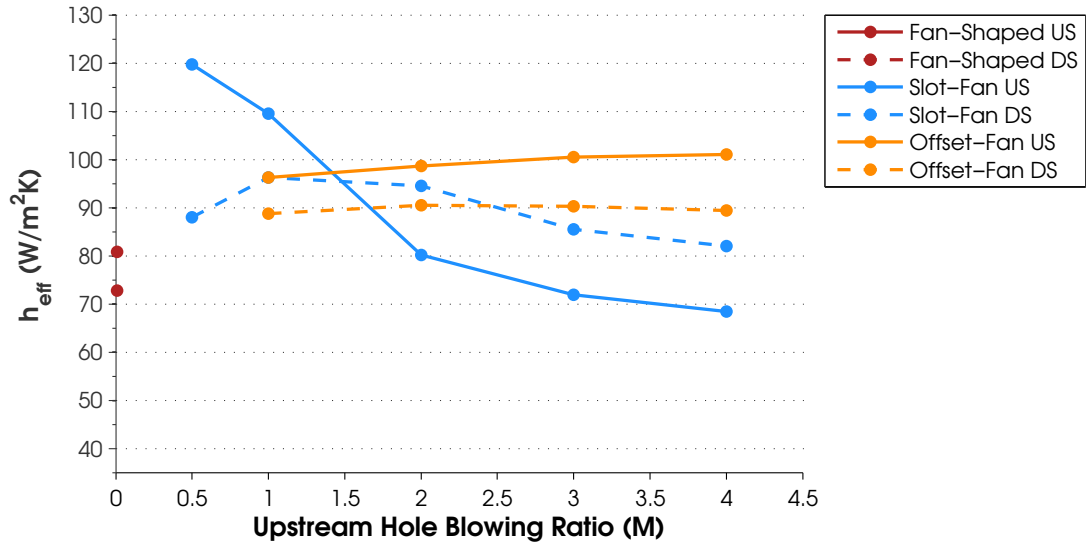


Figure E.87: Gauge heat transfer coefficient comparison, $\Phi = 1.5$, $\dot{m}_{air}=425$ SLPM, US: Blank/Slot/Offset, Coolant=Air, M=Variable, DS: Fan, Coolant=Air, M=2

E.4.5 Comparison Plots as a function of Φ .

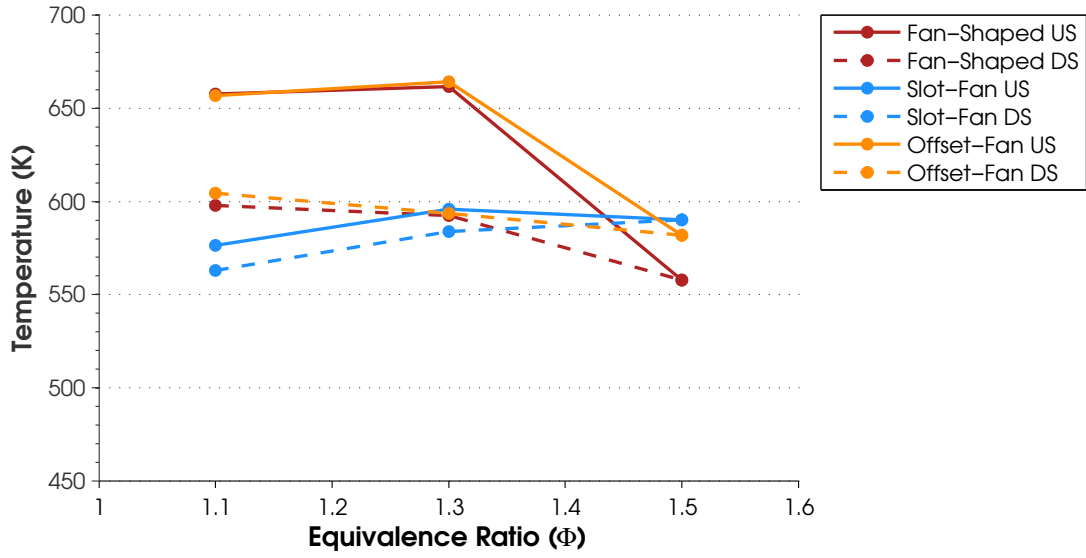


Figure E.88: Gauge surface temperature comparison, Φ = Variable, $\dot{m}_{air}=425$ SLPM, US: Blank/Slot/Offset, Coolant=Air, M=2, DS: Fan, Coolant=Air, M=2

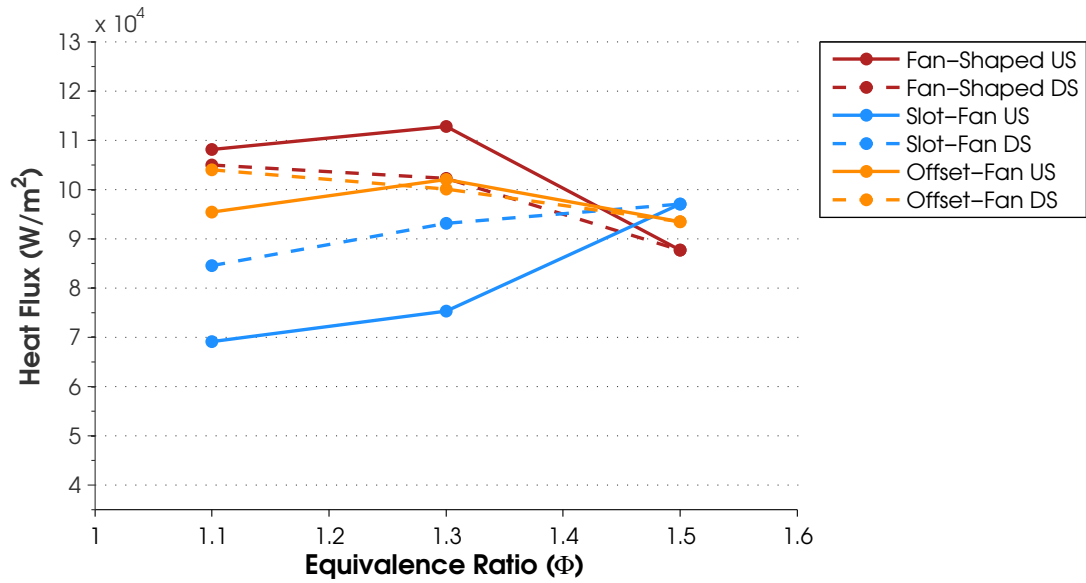


Figure E.89: Heat flux comparison, Φ = Variable, $\dot{m}_{air}=425$ SLPM, US: Blank/Slot/Offset, Coolant=Air, M=2, DS: Fan, Coolant=Air, M=2

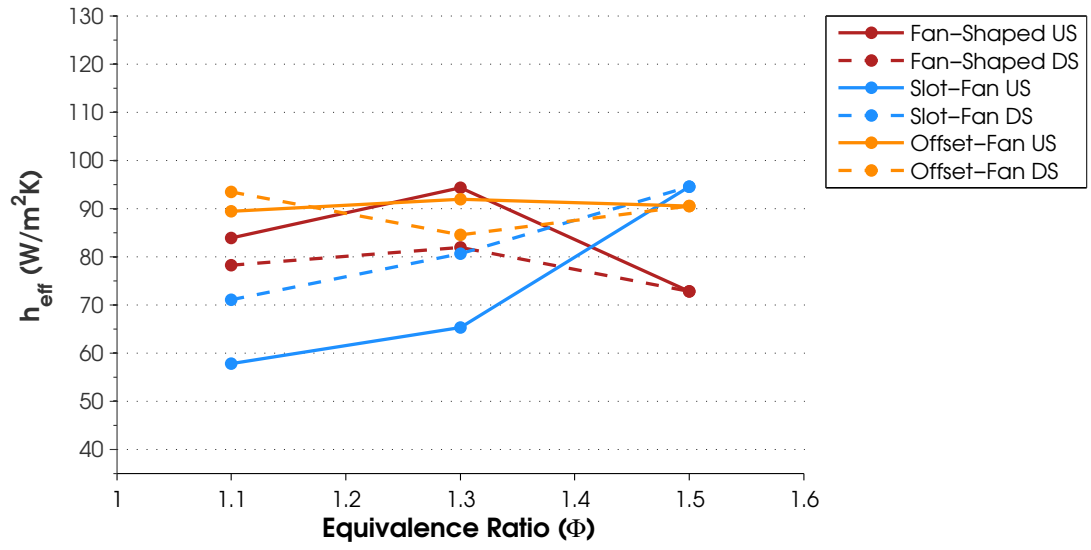


Figure E.90: Gauge heat transfer coefficient comparison, Φ = Variable, $\dot{m}_{air}=425$ SLPM, US: Blank/Slot/Offset, Coolant=Air, M=2, DS: Fan, Coolant=Air, M=2

Bibliography

1. Mattingly, J. D., Heiser, W. H., and Daley, D. H., *Aircraft Engine Design*, AIAA, Washington D.C., 1987.
2. Zelina, J., Sturgess, G. J., and Shouse, D. T., "The Behavior of an Ultra-Compact Combustor (UCC) Based on Centrifugally-Enhanced Turbulent Burning Rates," *AIAA Paper No. 2004-3541*, 2004.
3. Lewis, G. D., "Swirling Flow Combustion - Fundamentals and Application," *Presented at AIAA/SAE 9th Propulsion Conference, Las Vegas, Nevada*, November 1973, AIAA Paper No. 73-1250.
4. Zelina, J., Shouse, D. T., and Hancock, R. D., "Ultra-Compact Combustors for Advanced Gas Turbine Engines," *Proceedings of ASME Turbo Expo '04*, June 2004, 2004-GT-53155.
5. Bogard, D. G. and Thole, K. A., "Gas Turbine Film Cooling," *Journal of Propulsion and Power*, December 2005.
6. Lethander, A. T., *Assessment of Leading Edge Fillet for Decreasing Vane End-wall Temperatures in a Gas Turbine Engine*, Ph.D. thesis, Virginia Polytechnic Institute and State University, Blacksburg, Virginia, 2003.
7. Lukachko, S. P., Kirk, D. R., and Waitz, I. A., "Turbine Durability Impacts of High Fuel-Air Ratio Combustors, Part 1: Potential for Intra-Turbine Oxidation of Partially-Reacted Fuel," *Presented at ASME Turbo Expo 2002: Land, Sea and Air, Amsterdam, The Netherlands*, 2002, GT-2002-30077.
8. Evans, D., *The Impact of Heat Release in Turbine Film Cooling*, Master's thesis, Air Force Institute of Technology, WPAFB, OH, 2008, AFIT/GAE/ENY/08-J02.
9. Sirignano, W. A., Delplanque, J. P., and Liu, F., "Selected Challenges in Jet and Rocket Engine Combustion Research," *33rd AIAA/ASME/SAE/ASEE Joint Propulsion Conference, Seattle, WA*, 1997, AIAA-97-2701.
10. Anderson, W. S., Radtke, J. T., King, P. I., Thornburg, H., Zelina, J., and Sekar, B., "Effects of Main Swirl Direction on High-g Combustion," *AIAA*, 2008.
11. Langston, L. S., "Crossflows in a Turbine Cascade Passage," *Journal of Engineering for Power*, Vol. 102, 1980, pp. 866 – 874.
12. Hermanson, K. S. and Thole, K. A., "Effects of Mach Number on Secondary Flow Characteristics," *Journal of Turbo and Jet Engines*, Vol. 17, 2000, pp. 179 – 196.
13. Hermanson, K. S. and Thole, K. A., "Effects of Inlet Conditions on Endwall Secondary Flows," *Journal of Propulsion and Power*, Vol. 16, No. 2, March-April 2000, pp. 286 – 296.

14. Tannehill, J. C., Anderson, D. A., and Pletcher, R. H., *Computational Fluid Mechanics and Heat Transfer*, Taylor and Francis, Philadelphia, PA, 1997, 2nd Edition.
15. Blazek, J., *Computational Fluid Dynamics: Principles and Applications*, Elsevier Publishing, Oxford, UK, 2005, 2nd Edition.
16. Tu, J., Yeoh, G. H., and Liu, C., *Computational Fluid Dynamics - A Practical Approach*, Elsevier Publishing, Burlington, MA, 2008.
17. Pope, S. B., *Turbulent Flow*, Cambridge University Press, Cambridge, UK, 2000.
18. Baldauf, S., Schulz, A., and Wittig, S., "High-Resolution Measurements of Local Effectiveness From Discrete Hole Film Cooling," *Journal of Turbomachinery*, Vol. 123, 2001.
19. Gritsch, M., Schulz, A., and Wittig, S., "Adiabatic Wall Effectiveness Measurements of Film-Cooling Holes With Expanded Exits," *97-GT-164*, 1997.
20. Dittmar, J., Schulz, A., and Wittig, S., "Assessment of Various Film Cooling Configurations Including Shaped Holes and Compound Angle Holes Based on Large Scale Experiments," *Proceedings of ASME Turbo Expo 2002, June 3-6, 2002 Amsterdam, The Netherlands*, 2002.
21. Saumweber, C., Schulz, A., and Wittig, S., "Free-Stream Turbulence Effects on Film Cooling With Shaped Holes," *Journal of Turbomachinery*, Vol. 125, pp. 65-73, 1993.
22. Thole, K. A., Sinha, A., Bogard, D. G., and Crawford, M. E., "Mean Temperature Measurements of Jets With a Crossflow for Gas Turbine Film Cooling Application," *Rotating Machinery Transport Phenomena*, edited by J. H. Kim and W. J. Yang, Hemisphere, New York, 1992.
23. Teekaram, A. J. H., Forth, C. J. P., and Jones, T. V., "Film Cooling in the Presence of Mainstream Pressure Gradients," *Journal of Turbomachinery*, Vol. 113, 1991, pp. 484 – 492.
24. Liess, C., "Experimental Investigation of Film Cooling With Ejection From a Row of Holes for the Application to Gas Turbine Blades," *Journal of Engineering for Power*, January 1975.
25. Leylek, J. H. and Zerkle, R. D., "Discrete-Jet Film Cooling: A Comparison of Computational Results With Experimental," *Journal of Turbomachinery*, Vol. 116, 1994, pp. 358 – 368.
26. Walters, D. K. and Leylek, J. H., "A Detailed Analysis of Film-Cooling Physics: Part I - Streamwise Injection With Cylindrical Holes," *Journal of Turbomachinery*, Vol. 122, 2000, pp. 102 – 112.
27. McGovern, K. T. and Leylek, J. H., "A Detailed Analysis of Film-Cooling Physics: Part II - Compound-Angle Injection With Cylindrical Holes," *Journal of Turbomachinery*, Vol. 122, 2000, pp. 113 – 121.

28. Hyams, D. G. and Leylek, J. H., "A Detailed Analysis of Film-Cooling Physics: Part III - Streamwise Injection With Shaped Holes," *Journal of Turbomachinery*, Vol. 122, 2000, pp. 122 – 132.
29. Hartnett, J. P., Birkebak, R. C., and Eckert, E. R. G., "Velocity Distributions, Temperature Distributions, Effectiveness and Heat Transfer for Air Injected Through a Tangential Slot Into a Turbulent Boundary Layer," *Journal of Heat Transfer*, 1961, pp. 293 – 306.
30. Bunker, R. S., "Film Cooling Effectiveness Due to Discrete Holes Within a Transverse Surface Slot," *Proceedings of 2002 International Gas Turbine Conference Conference and Exposition, Amsterdam*, 2002.
31. Incropera, DeWitt, Bergman, and Lavine, *Fundamentals of Heat and Mass Transfer*, John Wiley and Sons, Inc, Hoboken, New Jersey, 2007, 6th Edition.
32. Haynes International Inc, "Material Datasheet H-3009a, Hastelloy-X Alloy," 1997, Kokomo, IN.
33. Turns, S. R., *An Introduction to Combustion*, McGraw-Hill, Inc, New York, 1996, 2nd Edition.
34. Polanka, M. D., Zelina, J., Anderson, W., Sekar, B., Evans, D., King, P., Thornburg, H. J., Lin, C. X., and Stouffer, S. D., "Heat Release in Turbine Film Cooling, Part 1: Experimental and Computational Comparison of Three Geometries," *Journal of Propulsion and Power*, 2010.
35. Anderson, W., Polanka, M. D., Zelina, J., Evans, D., Stouffer, S. D., and Justinger, G. R., "Effects of a Reacting Cross-Stream on Turbine Film Cooling," *Journal of Engineering for Gas Turbines and Power*, Vol. 132, 2010.
36. Lin, C. X., Holder, R. J., Polanka, M. D., Zelina, J., Sekar, B., Thornburg, H. J., and Briones, A. M., "Heat Release in Turbine Film Cooling, Part 2: Numerical Simulation of Shaped Hole Secondary Combustion Development and Location," *Journal of Propulsion and Power*, 2010.
37. Baskharone, E., *Principles of Turbomachinery in Air-Breathing Engines*, Cambridge University Press, New York, 1st ed., 2006.
38. Wilson, D. G. and Korakiantitis, T. K., *The Design of High-Efficiency Turbomachinery and Gas Turbines*, Prentice Hall, New Jersey, 2nd ed., 1998.
39. FLUENT® Inc., *FLUENT 6.3 User's Guide*, 2006.
40. LeBay, K. D., Polanka, M. D., and Branam, R. D., "Charactering the Effect of Radial Vane Height on Flame Migration in an Ultra Compact Combustor," *Proceedings of the ASME Turbo Expo 2011*, , No. GT2011-45919, 2011.
41. Nenniger, J. E., Kridiotis, A., Chomiak, J., Longwell, J. P., and Sarofim, A. F., "Characterization of a Toroidal Well Stirred Reactor," *Twentieth Symposium (International) on Combustion*, *The Combustion Institute*, 1984, pp. 473–479.

Vita

Captain Brian T. Bohan graduated from Patchogue-Medford High School in Medford, New York. He entered undergraduate studies at Clarkson University where he graduated with a Bachelor of Science degree in Aeronautical Engineering in May 2005. He commissioned into the Air Force through the Air Force Reserve Officer Training Corps (AFROTC) also in May 2005.

Following a year of casual status and assorted in-residence trainings he was assigned to the 746th Test Squadron at Holloman AFB, NM. The 746th Test Squadron is part of the 46th Test Group which is a geographically separated unit under the 46th Test Wing and Air Armament Center at Eglin AFB, FL. Duties at the 746th included test management of GPS and inertial guidance system test programs, specifically in the areas of GPS vulnerabilities and electronic warfare, as well as program management for a state of the art simulator for a current navigation warfare threat. In June 2008, in addition to test and program management, his duties were expanded to include deputy element chief/acting element chief of the avionics element.

In August 2009 he entered the Graduate School of Engineering and Management at the Air Force Institute of Technology majoring in aeronautical engineering with concentrations in aerodynamics, air breathing propulsion and computational fluid dynamics. Upon graduation he will be assigned to the Air Force Research Lab (AFRL), Propulsion Directorate, WPAFB, OH.

Permanent address: 2950 Hobson Way
Air Force Institute of Technology
Wright-Patterson AFB, OH 45433

REPORT DOCUMENTATION PAGE			Form Approved OMB No. 0704-0188	
The public reporting burden for this collection of information is estimated to average 1 hour per response, including the time for reviewing instructions, searching existing data sources, gathering and maintaining the data needed, and completing and reviewing the collection of information. Send comments regarding this burden estimate or any other aspect of this collection of information, including suggestions for reducing this burden to Department of Defense, Washington Headquarters Services, Directorate for Information Operations and Reports (0704-0188), 1215 Jefferson Davis Highway, Suite 1204, Arlington, VA 22202-4302. Respondents should be aware that notwithstanding any other provision of law, no person shall be subject to any penalty for failing to comply with a collection of information if it does not display a currently valid OMB control number. PLEASE DO NOT RETURN YOUR FORM TO THE ABOVE ADDRESS.				
1. REPORT DATE (DD-MM-YYYY) 24 March 2011		2. REPORT TYPE Master's Thesis		3. DATES COVERED (From — To) 1 September 2010 – 24 March 2011
4. TITLE AND SUBTITLE Analysis of Flow Migration in an Ultra-Compact Combustor			5a. CONTRACT NUMBER	
			5b. GRANT NUMBER	
			5c. PROGRAM ELEMENT NUMBER	
6. AUTHOR(S) Captain Brian Bohan, USAF			5d. PROJECT NUMBER	
			5e. TASK NUMBER	
			5f. WORK UNIT NUMBER	
7. PERFORMING ORGANIZATION NAME(S) AND ADDRESS(ES) Air Force Institute of Technology Graduate School of Engineering and Management (AFIT/ENY) 2950 Hobson Way WPAFB OH 45433-7765			8. PERFORMING ORGANIZATION REPORT NUMBER AFIT/GAE/ENY/11-M02	
9. SPONSORING / MONITORING AGENCY NAME(S) AND ADDRESS(ES) Air Force Research Laboratory Propulsion Directorate, Combustion Branch 1950 Fifth Street, Building 490 WPAFB OH 45433-7251 POC: Dr. Joseph Zelina, Phone: 937-255-7487, Email: joseph.zelina@wpafb.af.mil			10. SPONSOR/MONITOR'S ACRONYM(S) AFRL/RZTC	
			11. SPONSOR/MONITOR'S REPORT NUMBER(S)	
12. DISTRIBUTION / AVAILABILITY STATEMENT APPROVED FOR PUBLIC RELEASE; DISTRIBUTION UNLIMITED This material is declared a work of the United States Government and is not subject to copyright protection in the United States				
13. SUPPLEMENTARY NOTES				
14. ABSTRACT One of the major efforts for turbine engine research is to improve the thrust to weight of the system. One novel concept for accomplishing this is the use of an Ultra-Compact Combustor (UCC). The UCC attempts to shorten the overall combustion length (thereby reducing weight) by performing the combustion in the circumferential direction along the outside diameter of the core flowpath. One of the major benefits of this design is enhanced combustion due to the establishment of a high-g field in the circumferential cavity. AFIT and the Air Force Research Laboratory (AFRL) have been teamed for several years in understanding the fundamental aspects of this design. Prior to the research presented in this report, work has focused around small-scale missile-sized combustors. There is a current push within AFRL to investigate this system for a larger, fighter-sized engine. AFIT has led this push by performing Computational Fluid Dynamic (CFD) simulations to scale the UCC. This thesis outlines this overall effort. Increasing the diameter of the UCC presents several challenges including how to control the fluid velocity in the circumferential cavity and how to turn the centrifugal combustion flow back to the axial direction into the high-pressure turbine rotor while presenting a uniform temperature across the turbine blades. Several numerical parameter studies have been conducted to establish relationships to predict tangential velocity based on cavity inlet conditions and determine a configuration that minimizes pressure losses through the combustor section. As a result of these investigations a 0.75m diameter UCC combustor design has been developed along with a hybrid turning vane which replaces the last compressor vane and high-pressure turbine vane. Furthermore, the issue of cooling the hybrid vane in the exhaust of the UCC, where not all the fuel is combusted within the circumferential cavity causing additional reactions within the vane section, was investigated. A film cooling experimental study was conducted in an effort to reduce or remove the negative effects that result from secondary combustion of unburned fuel with oxygen in the film coolant.				
15. SUBJECT TERMS Jet engines, ultra-compact combustor, UCC, inter-turbine burner, turbine-engine, film-cooling				
16. SECURITY CLASSIFICATION OF:			17. LIMITATION OF ABSTRACT UU	18. NUMBER OF PAGES 283
a. REPORT	b. ABSTRACT	c. THIS PAGE		
U	U	U	19a. NAME OF RESPONSIBLE PERSON Dr. Marc Polanka	
			19b. TELEPHONE NUMBER (Include Area Code) (937)255-3636, ext 4714 Email: marc.polanka@afit.edu	